The Dissertation Committee for Jinguang Cheng Certifies that this is the approved version of the following dissertation:

HIGH-PRESSURE SYNTHESIS OF THE 4D AND 5D TRANSITION-METAL OXIDES WITH THE PEROVSKITE AND THE PEROVSKITE-RELATED STRUCTURE AND THEIR PHYSICAL PROPERTIES

Committee:

John B. Goodenough, Supervisor

Jianshi Zhou, Co-Supervisor

Arumugam Manthiram

Alex De Lozanne

John T. Markert

HIGH-PRESSURE SYNTHESIS OF THE 4D AND 5D TRANSITION-METAL OXIDES WITH THE PEROVSKITE AND THE PEROVSKITE-RELATED STRUCTURE AND THEIR PHYSICAL PROPERTIES

by

Jinguang Cheng, B.S.; M.S.

Dissertation

Presented to the Faculty of the Graduate School of

The University of Texas at Austin

in Partial Fulfillment

of the Requirements

for the Degree of

Doctor of Philosophy

The University of Texas at Austin

May 2010

Dedication

To my wife Yan Li

Acknowledgements

High-Pressure Synthesis of the 4d and 5d Transition-Metal Oxides with the Perovskite and the Perovskite-Related Structure and Their Physical Properties

Jinguang Cheng, Ph. D.

The University of Texas at Austin, 2010

Supervisor: John B. Goodenough

Co-supervisor: Jianshi Zhou

A Walker-type multianvil high-pressure facility is capable of high-pressure syntheses and measurements beyond 10 GPa and has been utilized in my research to synthesize the 4d Ruthenium and Rhodium and the 5d Iridium oxides with the perovskite-related structures. Under high-pressure and high-temperature conditions, these families of oxides can be enlarged to a great extent so that enables us not only to address the long-standing problem about ferromagnetism in the perovskite ruthenates but also explore new phenomena associated with the structural and electronic properties in the iridates and rhodates.

In the perovskite ruthenates $ARuO_3$ (A= Ca, Sr, and Ba), a systematic study of the variations of the ferromagnetic transition temperature T_c and the critical isothermal magnetization as a function of the average A-site cation size and the size variance as well

as external high pressures reveals explicitly the crucial role of the local lattice strain and disorder on T_c and the nature of the localized-electron ferromagnetism. However, such a steric effect is dominated by the electronic effect in another perovskite ruthenate $PbRuO_3$, which is a paramagnetic metal down to 1.8 K and undergoes a first-order structural transition to a low-temperature *Imma* phase at $T_t \approx 90$ K. Bandwidth broadening due to orbital hybridization between Pb-6s and Ru-4d plays an important role in suppressing the ferromagnetism in the $Sr_{1-z}Pb_zRuO_3$ system. The high-pressure sequence of the 9R-$BaIrO_3$ was explored and three more polytypes, *i.e.* 5H, 6H and 3C, were identified under 10 GPa. With increasing fraction of the corner- to face-sharing $IrO_{6/2}$ octahedra, the ground states of $BaIrO_3$ evolve from a ferromagnetic insulator with $T_c \approx 180$ K in the 9R phase to a ferromagnetic metal with $T_c \approx 50$ K in the 5H phase, and finally to an exchange-enhanced paramagnetic metal near a quantum critical point in the 6H phase. In addition to the perovskite $SrRhO_3$, a new 6H polytype was synthesized for the first time under high pressure and a pressure-temperature phase diagram was given for the 6H-perovskite transformation. Restoration of the Curie-Weiss behavior in the high-temperature magnetic susceptibility $\chi(T)$ of the perovskite $SrRhO_3$ resolves the puzzle about unusual dependence of $\chi^{-1} \propto T^2$ reported earlier and highlights the importance of spin-orbit coupling in the 4d and 5d transition-metal oxides.

Table of Contents

List of Tables

List of Figures

xxiii

Chapter 1 Introduction

Since the 1950s, transition-metal perovskite oxides AMO_3 have been extensively investigated. In recent years, the discovery of high-T_c superconductivity in the copper oxides[1] and the observation of a colossal magnetoresistance in the manganites[2, 3] have stimulated a renaissance of broad interest. The perovskite structure,[4] consisting of corner-shared $MO_{6/2}$ octahedra with an A-site cation in a body-center position, can incorporate a wide range of cations at both the 12-coordinate A position and the 6-coordinate M site due to a strong tolerance for mismatch between the equilibrium (A-O) and (M-O) bond lengths. It can also accept up to 0.5 oxide-ion vacancies per formula unit. As a densely packed crystal structure, the perovskite is commonly found as a high-pressure phase,[5] which makes the high-pressure synthesis very effective and critical, in some cases, to synthesize metastable compounds with the perovskite structure.[6] The multianvil high-pressure technique[7, 8] has been well-developed and widely used in the field of geoscience to simulate the conditions reaching the Earth's lower mantle, which is believed to be composed mainly of $(Mg,Fe)SiO_3$ perovskite.[9] Therefore, application of the multianvil high-pressure technique in the field of solid-state synthesis can enlarge the family of perovskite oxides to a great extent, which enables us not only to address long-standing problems, but also to explore new compounds and phenomena.[10]

An excellent example comes from the recent synthesis of the cubic perovskite $BaRuO_3$ under 18 GPa and the new insights it brought to the magnetic behavior of the perovskite ruthenates.[11] The perovskite $Sr_{1-x}Ca_xRuO_3$ system has attracted much attention since 1960s because of the unusual disappearance of ferromagnetism with increasing x;[12, 13] *i.e.* $SrRuO_3$ is ferromagnetic with $T_c \approx 160$ K while the counterpart $CaRuO_3$ does not

show any magnetic ordering down to the lowest temperature. Mazin and Singh[14] have calculated the band structure of $Sr_{1-x}Ca_xRuO_3$ taking into account the cooperative $RuO_{6/2}$ site rotation that bends the Ru-O-Ru bond angle from 163° in $SrRuO_3$ to 148° in $CaRuO_3$; they found that the increased bending of the Ru-O-Ru bond angle reduces the band degeneracy and, therefore, the density of electronic states at the Fermi energy $\rho(\varepsilon_F)$, perhaps to where the Stoner criterion is no longer valid in $CaRuO_3$. This model predicts that the maximum T_c will be achieved as the high symmetry cubic structure is approached since a higher $\rho(\varepsilon_F)$ is created at high-symmetry points in the Brillouin zone.[14] Thus, it is essential to check this model on the cubic $BaRuO_3$ perovskite. Due to a larger Ba-O equilibrium bond length, however, $BaRuO_3$ adopts a 9R polytype at ambient pressure.[15] In 1968, Longo *et al.*[16] have transformed the 9R phase to 4H and 6H polytypes, but they failed to obtain the perovskite phase up to 9 GPa, which was the highest pressure available to them. It was not until 2008 that Jin *et al.*[11] synthesized the cubic $BaRuO_3$ perovskite under 18 GPa and 1000°C for the first time by using a multianvil high-pressure apparatus. Physical-property measurements show that it is also a ferromagnetic metal like $SrRuO_3$, but the $T_c \approx 60$ K is significantly lower than 160 K of $SrRuO_3$, which clearly contradicts the prediction of Mazin and Singh.[14]

The successful synthesis of the cubic $BaRuO_3$ phase makes available the complete magnetic phase diagram of T_c versus $<r_A>$, the average A-cation radius, in the perovskite ruthenates $ARuO_3$ (A= Ca, Sr, Ba). [11] In the phase diagram, T_c peaks out at $SrRuO_3$; both substitutions of smaller Ca^{2+} and larger Ba^{2+} for Sr^{2+} lead to a reduction of T_c in the $Sr_{1-x}Ca_xRuO_3$ and $Sr_{1-y}Ba_yRuO_3$ systems. On the side of Ca^{2+} doping, the inverse susceptibility $\chi^{-1}(T)$ is characteristic of a Griffiths' phase, whereas all compositions of $Sr_{1-y}Ba_yRuO_3$ ($0 \leq y \leq 1$) show a typical Curie-Weiss behavior at $T > T_c$. A comparison

of the magnetic susceptibility of $CaRuO_3$ with those of the $BaRuO_3$ polytypes indicates the importance of spin-orbit coupling $\lambda \mathbf{L \cdot S}$ in suppressing the ferromagnetic ordering in $CaRuO_3$. Taking into account the sharply different $\chi^{-1}(T)$ behaviors found in the $Sr_{1-x}Ca_xRuO_3$ and $Sr_{1-x}Ba_xRuO_3$ systems, the magnetic phase diagram has been interpreted in the context of a Griffiths' phase on the Ca side and of bandwidth broadening on the Ba side. However, it should be noted that changing $<r_A>$ by substituting Ca^{2+} or Ba^{2+} for Sr^{2+} inevitably introduces an A-cation size variance σ^2 $(= <r^2_A> - <r_A>^2)$.[17-19] It has been shown that both the ferromagnetic transition temperature in $AMnO_3$ perovskites[20] and the critical temperature in A_2CuO_4 superconductors[21, 22] decrease linearly with A-cation size variance at constant doping level and average A-cation radius. Therefore, the effect of size variance in the perovskite ruthenates may plague the above interpretation. Moreover, the nature of the ferromagnetism in the perovskite ruthenates remains unclear. Itinerant-electron ferromagnetism has been widely believed to be plausible in $SrRuO_3$; the observations[23] of mean-field critical behavior, *i.e.* nearly parallel linear lines in the Arrott plot M^2 *vs* H/M, and metallic conductivity seem to support this conclusion. However, the unusual high saturation magnetization at the lowest temperature, 1.4-1.6 μ_B/Ru^{4+}, is clearly beyond the criterion of very weak itinerant ferromagnetism.[24] In addition, the ferromagnetic transition in $BaRuO_3$ exhibits significant critical fluctuations as described by the 3D Heisenberg model.[25] The critical fluctuations are significantly enhanced under an external pressure.[25] Moreover, a novel critical exponent, which does not belong to any current universality class, has recently been reported in the $Sr_{1-x}Ca_xRuO_3$ system.[26] Therefore, studies of the evolution of magnetic properties of the system $Sr_{1-x}Ca_xRuO_3$ and the high-pressure system $Sr_{1-y}Ba_yRuO_3$ may help to answer questions about what determines the optimal magnetization and T_c of perovskite ruthenates and whether an itinerant-electron ferromagnetism model is applicable. These issues are addressed in this

work with a systematic study of the effect of the mean A-cation radius and size variance, of hydrostatic versus non-hydrostatic pressure, and of high-pressure synthesis on T_c and the isothermal magnetization on crossing T_c.

According to the magnetic phase diagram of the perovskite ruthenates $ARuO_3$ (A= Ca, Sr, Ba) [11] where T_c peaks out around Sr^{2+}, it is natural to expect that the $EuRuO_3$ and $PbRuO_3$ perovskites, if they exist, should also be ferromagnetic metals because the ionic radii of Eu^{2+} (X: 1.35 Å) and Pb^{2+} (X: 1.40 Å) are close to that of Sr^{2+} (X: 1.36 Å).[27] A literature search shows that $EuRuO_3$ and $PbRuO_3$ both crystallize into the cubic pyrochlore structure $A_2Ru_2O_{7-\delta}$ at ambient pressure.[28, 29] Since no report is available for the perovskite $EuRuO_3$, many attempts have been carried out to synthesize it in this work. However, those attempts were unsuccessful. Fortunately, Kafalas *et al.*[29] prepared the perovskite $Sr_{1-z}Pb_zRuO_3$ ($0 < z \leq 1$) system in 1970 under high pressures up to 9 GPa; their preliminary results indicate that the long-range magnetic ordering disappears around $z = 0.5$ and the perovskite $PbRuO_3$ behaves like $CaRuO_3$. No further characterizations have been made since then. It is difficult to understand the magnetic behavior of the $Sr_{1-z}Pb_zRuO_3$ ($0 \leq z \leq 1$) system based on the knowledge developed for the $ARuO_3$ (A= Ca, Sr, Ba) perovskites. Therefore, further investigations are required in order to gain a comprehensive understanding of the peculiar disappearance of ferromagnetism upon Pb^{2+} doping in the $Sr_{1-z}Pb_zRuO_3$; high-pressure synthesis will play an indispensable role in this study.

During the course of our study of the $Sr_{1-z}Pb_zRuO_3$ system, we noticed a recent report by Kimber *et al.*[30] on the perovskite $PbRuO_3$, which was reported to exhibit a metal-insulator transition at $T_t \approx 90$ K accompanied by a first-order structural transition

from the high-temperature *Pbmn* phase to a low-temperature *Imma* phase. No long-range magnetic ordering was evident down to 1.5 K. The local structural distortions resolved from a neutron diffraction study suggested an orbital ordering on Ru(IV) in the low-temperature *Imma* phase. Moreover, a first-principles calculation in the same report justified the insulator ground state of the *Imma* phase. All the experimental results and the self-consistent justification of an insulator ground state reported by Kimber *et al.*[30] appear to be flawless except for one observation; a temperature-dependent paramagnetic susceptibility shows the presence of a magnetic moment on at least some of the Ru(IV) ions, so it becomes necessary to justify why a magnetic-insulator phase, especially with orbital ordering, does not result in spin ordering. Moreover, the following questions arise based on the above study: (1) How do the T_c and T_t evolve in the phase diagram of the $Sr_{1-z}Pb_zRuO_3$ perovskites from $T_c = 164$ K for $z = 0$ to $T_t = 90$ K for $z = 1.0$? (2) How would the T_t respond to external pressure? Will pressure suppress the T_t and restore the long-range ferromagnetic ordering for heavy Pb^{2+} doping? These problems will be resolved in this work by a detailed characterization of the $Sr_{1-z}Pb_zRuO_3$ system and a systematic comparison with the $Sr_{1-x}A_xRuO_3$ (A = Ca and Ba) systems.

The successful synthesis of the new cubic $BaRuO_3$ follows the general trend of phase transformations of the polytype structures under high pressure, *i.e.* 2H→9R→4H→6H→3C, established during the 1960-1970s.[6] The polytypes are characterized by different stacking sequences of close-paced AO_3 layers, either cubic (C) or hexagonal (*h*) with respect to its two neighboring layers. As a general trend, the number of *h* layer stacking along the *c* axis in a unit cell is reduced as the synthesis pressure increases; *i.e.* the *C:h* ratio increases from 1:2 in the 9R(*hhChhChhC*) phase to 1:1 in the 4H(*hChC*) phase, then to 2:1 in the 6H(*hCChCC*) phase, and finally to ∞ in the

5

3C(CCC) phase. The 9R BaRuO$_3$ is a paramagnetic metal with an unusual temperature dependence of magnetic susceptibility. A calculation [31] that includes a strong spin-orbit coupling can explain the anomalous $\chi(T)$ to a great extent. The evolution from paramagnetic metal to ferromagnetic metal observed in the series of polytypes 9R-4H-6H-3C BaRuO$_3$ indicates an increasing bandwidth W that becomes broad enough to suppress the spin-orbit coupling, but not to eliminate the spin-spin interaction as the population of the *C* layers increases.[11] This study motivated us to explore the evolution of polytypes and the physical properties of BaIrO$_3$ because the ambient phase of BaIrO$_3$ is isostructural with the 9R BaRuO$_3$ except for a monoclinic distortion.[32] In addition, BaIrO$_3$ has attracted much attention due to the observation of charge-density-wave (CDW) formation and weak ferromagnetism at the same temperature $T_c \approx 180K$.[33] The nonmetallic nature of BaIrO$_3$ makes the observation of a CDW quite unusual. Moreover, Longo *et al*.[34] have already reported that the ambient phase of SrIrO$_3$ has the monoclinically distorted 6H structure, which transforms to perovskite structure under high pressure. Therefore, we have explored the high-pressure phases of BaIrO$_3$ and carried out detailed characterizations on these polytypes in this work.

Another important information that we learn from the evolution of BaRuO$_3$ polytypes is that competition between the spin-orbit coupling $\lambda \mathbf{L} \cdot \mathbf{S}$ and the spin-spin exchange interaction can result in an up-turn, or hump-like feature, in the temperature dependence of the inverse magnetic susceptibility, $\chi^{-1}(T)$, at low temperatures.[11, 31] A strong spin-orbit coupling $\lambda \mathbf{L} \cdot \mathbf{S}$ is commonly found in the 4d and 5d transition-metal oxides, especially for the ions with the ground term $^2T_{2g}$ or $^3T_{1g}$.[31] The Curie-Weiss law can only be restored at sufficiently high temperatures, ~400 K for the 9R BaRuO$_3$, for instance, where the spin-orbit coupling becomes dominated by the spin-spin exchange

6

interaction. By loading a mixture of the sample and KClO$_4$ under 6 GPa and 1500ºC, Yamaura et al.[35] in 2002 synthesized a new orthorhombic perovskite SrRhO$_3$, which was found to be a Fermi-liquid metal with enhanced Pauli paramagnetism. However, rather than the conventional linear Curie-Weiss behavior, its $\chi^{-1}(T)$ curve exhibited an upturn at low temperatures and followed an unusual quadratic temperature dependence, i.e. $\chi^{-1}(T) \propto T^2$, up to 400 K, which could not be reasonably explained with the 3D spin fluctuation models in that report.[35] Density-functional calculations [36] for SrRhO$_3$ suggested that it is near a quantum critical point and that the properties are substantially affected by quantum critical fluctuations. However, the effect of spin-orbit coupling has not been invoked to explain the unusual magnetic behavior of SrRhO$_3$; measurements of $\chi(T)$ to much higher temperatures as in 9R BaRuO$_3$ could be helpful to clarify the origin. In addition, we have noticed that although the tolerance factor is t = 0.96 < 1, SrIrO$_3$ adopts at ambient condition a monoclinically distorted 6H polytype,[34] which transforms to an orthorhombic perovskite structure under high pressure. A 6H polytype structure with t < 1 is highly unusual; it could be caused by the strong Ir-Ir bonding in the 6H phase via half-filled a_1^{1} orbitals of the $e_\pi^{4}a_1^{1}e_\sigma^{0}$ configuration in the trigonal site symmetry. As a sister compound with the same electron configuration as SrIrO$_3$ and even larger tolerance factor t, SrRhO$_3$ is also expected to crystallize into a 6H polytype under lower pressures. However, no effort has been made to search for this unknown phase except for the synthesis of perovskite SrRhO$_3$ at 6 GPa and 1500°C. If it exists, evolution of the magnetic susceptibility in the SrRhO$_3$ polytypes would enable us to understand further the peculiar magnetic behavior of the perovskite SrRhO$_3$ as seen in the BaRuO$_3$ polytypes. Therefore, in this work a pressure-temperature phase diagram will be mapped out in order to search for the unknown low-pressure phase of SrRhO$_3$ and detailed characterizations of their

physical properties, especially magnetic susceptibility at high temperatures, will be carried out.

This work on the rhodates underlines another merit of high-pressure synthesis; *i.e.* the ability of incorporating a very high oxygen pressure so as to stabilize an unusually high oxidation state. Some very important perovskite oxides such as $CaFeO_3$,[37] $RNiO_3$,[38, 39] $LaCuO_3$,[40, 41] which are impossible to obtain with conventional methods, have been prepared in this way. The synthesis under high oxygen pressure not only adds many new members to the perovskite-structure family, but also leads to the observations of many interesting properties, including charge disproportionation,[37, 38] metal-insulator transitions,[38, 39] and enhanced Pauli paramagnetism.[40, 41]

The organization of the dissertation is the following. Chapter 2 contains the background knowledge which is the basis to interpret the experimental results. Chapter 3 covers all experimental methods used in this work. A Walker-type multianvil module has been set up at the University of Texas at Austin recently. A detailed description of all procedures such as the pressure and temperature calibrations and how to set up a typical run of high-pressure synthesis is an important document for other users. This part fills up most of the space of Chapter 3. High-pressure synthesis is the essential method to prepare several systems of samples such as the perovkites $Sr_{1-x}A_xRuO_3$ (A = Ca and Ba) and $Sr_{1-z}Pb_zRuO_3$, polytype structures of $BaIrO_3$, and the 6H polytype strucure of $SrRhO_3$. Their characterizations and physical properties are included individually in Chapters 4, 5, 6, and 7.

Chapter 2 Background

This chapter contains the background knowledge on which interpretation of the experimental results in this work will be based. First, I will discuss the crystal structures of the perovskite and the hexagonal polytypes as well as their transformations based on the tolerance factor. Then, I will describe the electronic configurations of transition-metal ions and M-O-M interactions in the AMO_3 perovskites. Finally, some important concepts including the principles of ferromagnetism, size-variance effect, and quantum critical point will be briefly discussed.

2.1 CRYSTAL STRUCTURES

2.1.1 Perovskite structure

The AMO_3 perovskite structure consists of corner-shared $MO_{6/2}$ octahedra with larger A-site cations in a body-center position.[4] Illustrated in Fig. 2.1 is an aristotype cubic perovskite structure with the space group $Pm\overline{3}m$, where the A and M cations are twelvefold and sixfold coordinated by O anions, respectively. In the hard-ball model, the equilibrium (A-O) and (M-O) bond lengths satisfy the geometric relationship $(r_A + r_O) = \sqrt{2}(r_M + r_O)$, where r_A, r_M and r_O are the effective ionic radii obtained empirically from the X-ray data under ambient condition.
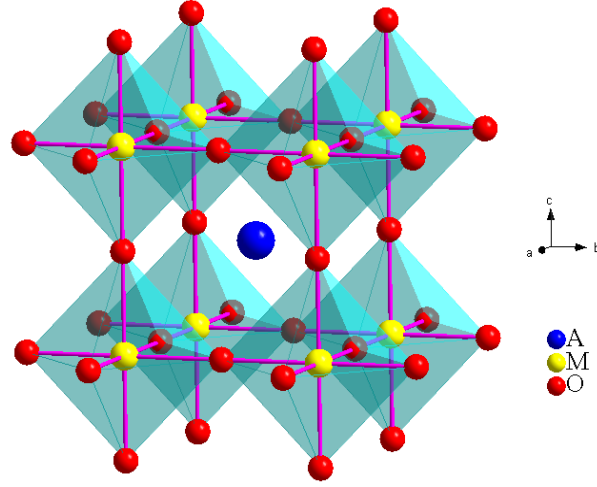
Figure 2.1:   An illustration of the cubic AMO$_3$ perovskite structure.

The perovskite structure also allows a large degree of mismatch between the equilibrium (A-O) and (M-O) bond lengths where the geometric tolerance factor t $[\equiv (r_A + r_O)/\sqrt{2}(r_M + r_O)]$ is smaller than unity.[42] A t < 1 places the (M-O) bond under a compressive stress and the (A-O) bond under a tensile stress, which can be relieved by a cooperative rotation of the MO$_{6/2}$ octahedra and a corresponding shift of the A-cation position. Consequently, the M-O-M bond angle deviates from 180° to (180°- φ) and the coordination number of the A cation decreases from 12 to 10, 9 or 8 depending on t. Cooperative rotations can give rise to as many as 23 Glazer tilt systems;[43, 44] however, the group-theoretical analysis yields only 15 possible space groups for perovskites derived through rigid octahedral tilting.[45] The group-subgroup relationships among the 15 space groups are schematically depicted in Fig. 2.2, where the letters *abc* refer to tilts around the [100], [010], and [001] pseudo-cubic axes, and the superscript, 0, + or −, indicates no tilt around an axis or tilts of successive octahedra in the same or opposite direction according to Glazer's notation.[43] Letters are repeated to indicate equal tilts around the different pseudo-cubic axes. Among the perovskite oxides having t < 1, the orthorhombic *Pbnm* (or *Pnma*)

structure is the most common structure; cooperative rotations of the $MO_{6/2}$ octahedra about a cubic [110] axis, or the *Pbnm* orthorhombic *b* axis, change the cubic lattice parameters from $a_0 \times a_0 \times a_0$ to $a \approx \sqrt{2}\, a_0 < b \approx \sqrt{2}\, a_0$ and $c = 2a_0$.

$$a^0\,a^0\,a^0 \quad \text{Pm-3m}$$

$a^+ a^+ a^+$ Im-3	$a^0 b^+ b^+$ I4/mmm	$a^0 a^0 c^+$ P4/mbm	$a^0 a^0 c^-$ I4/mcm	$a^0 b^- b^-$ Imma	$a^- a^- a^-$ R-3c
$a^+ b^+ c^+$ Immm	$a^+ a^+ c^-$ P4$_2$/nmc	$a^0 b^+ c^-$ Cmcm	$a^+ b^- b^-$ Pnma	$a^0 b^- c^-$ C2/m	$a^- b^- b^-$ C2/c

$$a^+ b^- c^- \quad \text{P2}_1\text{/m} \qquad a^- b^- c^- \quad \text{P-1}$$
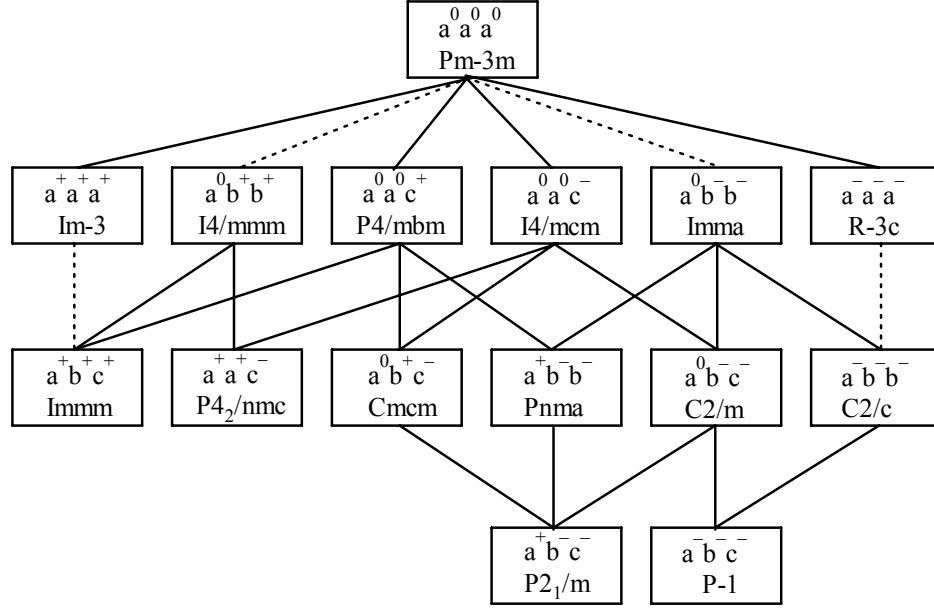
Figure 2.2:   A schematic diagram showing the relationship between the tilting systems. A phase transition between two tilting systems connected by a solid line can be made by eliminating one or more tilting components therefore, it is second order. Otherwise, it is first order for the phase transition between those connected by a dashed line or having no connection. (After Ref. 45)

The above discussions are based on simply tilting rigid octahedral units. However, it is not possible to fill up a real space by corner-shared octahedra with fixed rotation axes as pointed out by O'Keeffe and Hyde.[46] Recently, Zhou and Goodenough have demonstrated that octahedra in the orthorhombic *Pbnm* perovskite structure are not rigid;[42, 47, 48] an octahedral site can distort in two ways: (1) a deviation from 90° of the O-M-O bond angle α that subtends the site edges parallel to the *b* axis and (2) a bond-length splitting. Although the $MO_{6/2}$ octahedral tilting angle γ decreases with increasing average

A-cation size, a deviation of α from 90° increases and can convert $b > a$ to $a > b$ within the *Pbnm* space group. In the orthorhombic perovskite structure, the octahedral-site distortion can be described quantitatively using a polar plot of $\rho = \sqrt{Q_2^2 + Q_3^2}$, the magnitude of the octahedral-site distortion versus the angle $\phi = \tan^{-1}(Q_3 / Q_2)$, where the octahedral-site distortion modes, the orthorhombic $Q_2 = l_x - l_y$ and the tetragonal $Q_3 = (2l_z - l_x - l_y)/\sqrt{3}$, are calculated from the M-O bond lengths l_x, l_y, and l_z defined along [100], [010], and [001] pseudo-cubic axes within an octahedron. Along a circle with a given ρ in this plot, the octahedron with one long and two equal short bonds appears three times with a rotation of the long axis in different directions, *i.e.* at 0° (it is along the z axis), at 120° (along x axis), and at 240° (along y axis). At an angle other than these three angles the bond lengths split into long, medium, and short bonds. The octahedral-site distortion is intrinsic to the orthorhombic perovskites and has been demonstrated to bias strongly the spin and orbital ordering in the $RFeO_3$ and RVO_3 perovskites, respectively. [48]

As a result of both octahedral-site tilting and distortions, the following structural phase transitions are normally observed experimentally in the perovskites oxides with increasing tolerance factor t:

(1) For $A^{3+}M^{3+}O_3$, Orthorhombic *Pbnm* ($b > a$) $\rightarrow$ Orthorhombic *Pbnm* ($a > b$) $\rightarrow$ rhombohedral $R\bar{3}c \rightarrow$ Cubic $Pm\bar{3}m$;

(2) For $A^{2+}M^{4+}O_3$, Orthorhombic *Pbnm* ($b > a$) $\rightarrow$ Orthorhombic *Pbnm* ($a > b$) $\rightarrow$ Orthorhombic *Imma* $\rightarrow$ Tetragonal *I4/mcm* $\rightarrow$ Cubic $Pm\bar{3}m$.

2.1.2 Hexagonal-perovskite polytypes

When t > 1, the (M-O) bond is under tensile stress and the (A-O) bond is under compressive stress. No cooperative rotations of the corner-shared $MO_{6/2}$ octahedra can

relieve these stresses; instead, larger A cations can be accommodated in the space formed by face-shared $MO_{6/2}$ octahedral columns at the expense of the M-M electrostatic Madelung energy across the shared octahedral-site face. As a result, various hexagonal-perovskite polytypes are normally formed for AMO_3 compounds with t > 1. When all $MO_{6/2}$ octahedra share faces to form one-dimensional columns along the c axis, a 2H polytype is formed as typified in $CsNiF_3$ and $BaNiO_3$, for example. The cubic perovskite structure is labeled 3C where all $MO_{6/2}$ octahedra share corners. In between 2H and 3C, polytypes having mixed corner- and face-shared $MO_{6/2}$ octahedra have been identified, including 9R, 4H and 6H. The arrangements of the $MO_{6/2}$ octahedra along the hexagonal c axis in these polytypes are schematically shown in Fig. 2.3. These polytypes are designated by the number of the $MO_{6/2}$ layers in the cell, and a letter indicating the symmetry, R standing for rhombohedral (space group $R\overline{3}c$) and H for hexagonal (space group $P6_3/mmc$). These polytypes changes in the sequence 2H-9R-4H-6H-3C as (t - 1) decreases.
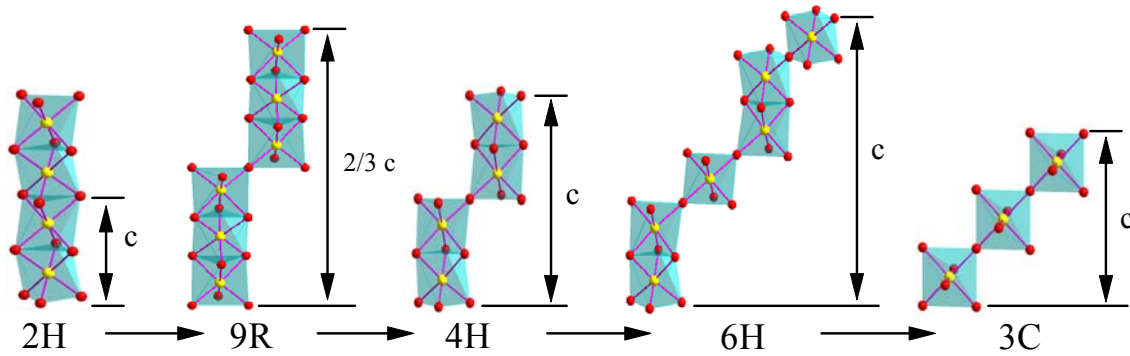
Figure 2.3: Arrangements of the $MO_{6/2}$ octahedra along c axis in the hexagonal-perovskite polytypes.

Since the compressibility of the (A-O) bonds is normally larger than that of the (M-O) bonds, a dt/dP < 0 is expected and the above polytype sequence can also be realized under high pressure. One of the classical examples is the phase transformations

of the ambient 9R BaRuO$_3$ as illustrated in Fig. 2.4. The structural transformations of these hexagonal-perovskite polytypes have been extensively studied in the 1960-1970s in the AMX$_3$ compounds, where X is an anion such as oxygen, fluorine, or chlorine (For a review, see Ref. 6).
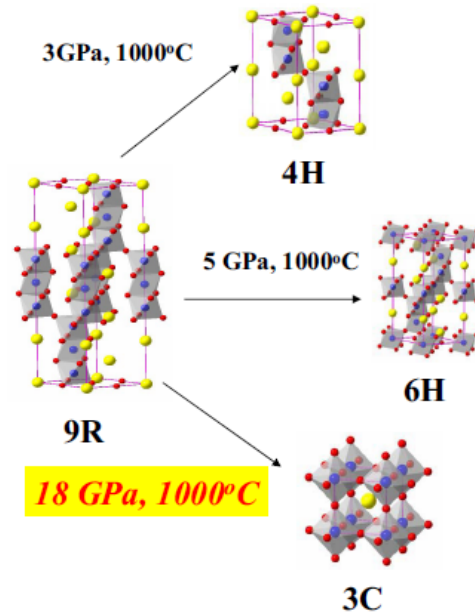
Figure 2.4: Evolution of the crystal structures of the BaRuO$_3$ polytypes as a function of high pressures. (After Ref.11)

2.1.3 A guideline for high-pressure synthesis

In general, the high-pressure and high-temperature (HPHT) synthesis of AMO$_3$ perovskite-related oxides is realized through the following routes: (1) pressure prefers the phase with smaller cell volume in a phase transition, (2) high-pressure synthesis can stabilize some oxidation states or electronic states that are not achievable by a procedure at ambient pressure in the perovskite structure.

14

The above-mentioned pressure-induced phase transformations among the hexagonal polytypes are consistent with the general rule (1); *i.e.* pressure stabilizes preferentially the denser phase with smaller volume, since in the 3C perovskite A cation has twelvefold oxygen coordination whereas in the hexagonal polytypes this coordination is reduced to (6 + 6) or lower. Another example is the transformation under HPHT from the ambient hexagonal phase to the orthorhombic perovskite structure in the $RMnO_3$ (R = Ho, …, Lu, Y or Sc).[49] The hexagonal $RMnO_3$ consists of close-packed layers of bi-pyramidal MnO_5 sites sharing corners in the (001) planes. When it transforms to the perovskite structure the coordination number of Mn^{3+} increases from 5 to 6 with a corresponding improvement of the crystallographic density, for example, from 2.56 a.w./$Å^3$ for the hexagonal phase to 3.39 a.w./$Å^3$ for the perovskite phase in $YMnO_3$.[49]

The essential roles that high-pressure plays in the second route include the following. (1) It can improve the thermal stability of the precursors. For example, the high-pressure synthesis of perovskite $(Ca,Sr)CrO_3$[50, 51] attributes to the stabilization of CrO_2 as a precursor under high pressure because Cr(IV) is not stable at ambient condition due to the thermal decomposition to Cr(III). (2) It can maintain a high-oxygen pressure so as to stabilize unusual formal oxidation states in oxides. By incorporating an oxygen source, for instance $KClO_4$, in the high-pressure cell, unusual high oxidation states can be stabilized in the $MO_{6/2}$ octahedral site, giving rise to a number of new perovskites such as $CaFe^{4+}O_3$,[37] $RNi^{3+}O_3$,[38, 39] $LaCu^{3+}O_3$,[40] and $SrRh^{4+}O_3$.[35] (3) It helps to minimize the electronic anisotropy induced by the lone pair electrons, *e.g.* $Se^{4+}(4s^2)$. As a consequence, a strongly distorted perovskite structure has been stabilized in the $SeMO_3$ with M^{2+} = Mn, Co, Ni, Cu and Zn,[52] characterized by a small tolerance factor and an abnormally high tilting effect of the $MO_{6/2}$ octahedra with M-O-M angles of ~124-130°.

2.2 ELECTRONIC CONSIDERATIONS

2.2.1 Overview

The main-group elements have only s and p electrons in partially filled shells and only these valence electrons are active in bonding. With the exception of $5s^2$ and $6s^2$ lone-pair core electrons, the s and p electrons are itinerant and occupy primarily O^{2-}: $2p^6$ bonding bands that are stabilized by the ionic Madelung energy of an AMO_3 perovskite and are separated from empty antibonding, primarily cation s and p bands by a large (~ 6 eV) energy gap. Transition-metal M cations have d^n configurations with energies that fall within this energy gap. Cations with $5s^2$ and $6s^2$ lone-pair electrons have an intermediate-size gap between bonding and antibonding s and p bands; an overlap of these electronic energies and a transition-metal redox couple may play an important role in broadening the d-electron band or, as in the Tl copper oxides, providing a charge reservoir for the transition-metal redox couple.

The $4f^n$ configurations at the lanthanide atom R are localized, and the intraatomic electron-electron Coulomb energies between 4f electrons are large, $U_f^n > 6$ eV. Consequently, the R atoms can have only a single valence state unless a $4f^n$ configuration falls in the energy gap between the filled O-2p bands and the empty, antibonding R-5d bands.

In the AMO_3 perovskites containing a 3d-block transition-metal atom M, the antibonding electrons of M 3d parentage may be either localized or itinerant. To understand this phenomenon, it is convenient to begin with the construction of crystal-field 3d orbitals; this construction introduces the oxygen component into antibonding orbitals that arises from M-O bonding. The on-site electron-electron Coulomb energy U

that separates successive redox couples is responsible for localizing electrons in single-valent compounds; the interatomic M-O-M interactions are responsible for suppressing U and converting the localized-electron configurations into itinerant electrons occupying an energy band of width W. In comparison with the 3d orbitals, the wavefunctions of 4d and 5d orbitals in the AMO_3 perovskite have a much larger spatial extension, which enhances crystal-field splitting and the 4d- or 5d-2p hybridization between the transition metal and the ligand oxygen. In the following, I briefly review the crystal-field considerations and M-O-M interactions developed based upon the 3d orbitals.[53]

2.2.2 Crystal-field considerations [53]

The five 3d orbitals of a free atom are degenerate; but with more than one electron or hole in the 3d manifold, the spin degeneracy is removed by the ferromagnetic direct-exchange interaction between electron spins in orthogonal atomic orbitals. The energy splitting between a high and a lower localized spin state will be designated Δ_{ex}.

The atomic orbitals f_m with azimuthal orbital angular momentum operator L_z, where $L_z f_m = -i\hbar(\partial f/\partial\phi) = \pm m\hbar f_m$, have the angular dependences

$$\begin{cases} f_0 \sim (3\cos^2\theta - 1) \sim (3z^2 - r^2)/r^2 \\ f_{\pm 1} \sim \sin 2\theta \exp(\pm i\phi) \sim 2(yz \pm izx)/r^2 \\ f_{\pm 2} \sim \sin^2\theta \exp(\pm i2\phi) \sim [(x^2 - y^2) \pm i2xy]/r^2 \end{cases} \quad (2.1)$$

In an isolated octahedral site, the xy and $(yz \pm izx)$ orbitals only overlap the neighboring O-$2p_\pi$ orbitals while the $(3z^2-r^2)$ and (x^2-y^2) orbitals only overlap the O-$2p_\sigma$ and 2s orbitals. The resonance integrals $b^{ca} \equiv (f_m, H'\phi_0) \approx \varepsilon_{m0}(f_m, \phi_0)$ describing the energy of a virtual charge transfer to an empty M-3d orbital from the same-symmetry sum of near-neighbor oxygen orbitals ϕ_0 contain both an overlap integral (f_m, ϕ_0) and a one-electron

17

energy ε_{m0} that are larger for σ-bonding than for π-bonding. Therefore, the antibonding states of a σ-bond are raised higher in energy than those of a π-bond and, as a consequence, the cubic symmetry of the octahedral site raises the twofold-degenerate pair of σ-bonding e orbitals, the $(3z^2-r^2)$ and (x^2-y^2) orbitals, above the threefold-degenerate set of π-bonding t orbitals xy, $(yz \pm izx)$ by an energy Δ_c and quenches the orbital angular momentum associated with m = ±2.

If the empty 3d orbitals of a degenerate manifold lie an energy ΔE_p above the O-2p orbitals and ΔE_s above the O-2s orbitals, the antibonding d-like states may be described in second-order perturbation theory to give the crystal-field wave functions

$$\begin{cases} \psi_t = N_\pi \left(f_t - \lambda_\pi \phi_\pi \right) \\ \psi_e = N_\sigma \left(f_e - \lambda_\sigma \phi_\sigma - \lambda_s \phi_s \right) \end{cases} \tag{2.2}$$

provided the covalent-mixing parameters are $\lambda_\pi \equiv b_\pi^{ca}/\Delta E_p \ll 1$ and $\lambda_\sigma \equiv b_\sigma^{ca}/\Delta E_p \ll 1$. A large ΔE_s keeps $\lambda_s \ll 1$ where Eq. (2.2) is applicable. If ΔE_p becomes too small or b^{ca} too large, the perturbation expansion breaks down, and an isolated MO_6 complex must be described by molecular-orbital theory, an array of corner-shared octahedra by band theory. According to the second-order perturbation theory, the antibonding states are raised by the M-O interactions energy

$$\Delta \varepsilon = \left| b^{ca} \right|^2 / \Delta E_i \tag{2.3}$$

and the cubic-field splitting is

$$\Delta_c = \Delta \varepsilon_\sigma - \Delta \varepsilon_\pi = \Delta_M + \left(\lambda_\sigma^2 - \lambda_\pi^2 \right) \Delta E_p + \lambda_s^2 \Delta E_s \tag{2.4}$$

where Δ_M is a purely electrostatic energy that is small and of uncertain sign due to the penetration of the O^{2-}-ion electron cloud by the cation wave functions.

The cubic splitting Δ_c is the same order of magnitude as the intraatomic exchange energy Δ_{ex}, and the d^4-d^7 configurations may be either high-spin t^3e^1, t^3e^2, t^4e^2, t^5e^2 where $\Delta_c < \Delta_{ex}$ or low-spin t^4e^0, t^5e^0, t^6e^0, t^6e^1 where $\Delta_c > \Delta_{ex}$. The covalent mixing of O-2p wavefunctions into ψ_t and ψ_e lowers the intraatomic exchange splitting Δ_{ex} and increases Δ_c. Therefore, stronger covalent mixing stabilizes low-spin relative to high-spin configurations; the 4d and 5d transition-metal ions in the AMO$_3$ perovskites always take the low-spin states due to strong d-p hybridization.

2.2.3 M-O-M interactions [53]

In the perovskite AMO$_3$ oxides, the dominant interactions between d-like orbitals centered at neighboring M atoms are the $(180° - \phi)$ M-O-M interactions. The spin-independent resonance integrals describing charge transfer between M atoms at R_i and R_j are

$$\begin{cases} b_\pi^{cac} \equiv \left(\psi_{ti}, H'\psi_{tj}\right) \approx \varepsilon_\pi \lambda_\pi^2 \\ b_\sigma^{cac} \equiv \left(\psi_{ei}, H'\psi_{ej}\right) \approx \varepsilon_\sigma \lambda_\sigma^2 \cos\phi \end{cases} \tag{2.5}$$

where λ_π varies with the acidity of the A cations as well as with the bending angle ϕ and H' describes the perturbation of the potential at R_j caused by the presence of an M atom at R_i. The smaller term $\varepsilon_s \lambda_s^2$ is omitted from b_σ^{cac} for simplicity.

In the absence of localized spins on the M atoms, the tight-binding bandwidth for these interactions is given by

$$W = W_b \approx 2zb^{cac} \tag{2.6}$$

where the number of like nearest neighbors is $z = 6$ for an MO$_3$ array.

Where there are localized spins on neighboring sites, it is necessary to introduce spin-dependent resonance integrals; with an angle θ_{ij} between spins at R_i and R_j, these integrals are

$$t_{ij}^{\uparrow\uparrow} = b^{cac} \cos(\theta_{ij}/2) \text{ and } t_{ij}^{\uparrow\downarrow} = b^{cac} \sin(\theta_{ij}/2) \tag{2.7}$$

for parallel and antiparallel coupling of near-neighbor spins. The spin angular momentum is conserved in an electron transfer. Rules for the sign of the interatomic exchange interactions follow:

(1) Direct exchange between spins in orthogonal orbitals is a potential exchange as it does not involve electron transfer; like the intraatomic interactions, it is ferromagnetic.

(2) Superexchange interactions between spin **S** on like atoms is a kinetic exchange that involves virtual charge transfers between orbitals on neighboring atoms. These orbitals may be either

- Both half-filled, in which case spin transfers are constrained by the Pauli exclusion principle to be antiferromagnetic; in second-order perturbation theory,

$$\Delta\varepsilon_{ex}^s \sim -\left|t_{ij}^{\uparrow\downarrow}\right|^2 / U_{eff} = Const + J_{ij} S_i \bullet S_j \tag{2.8}$$

where $J_{ij} \sim \left(2b_{ij}^2 / 4S^2 U_{eff}\right)$, or

- half-filled and empty or half-filled and full, in which case Δ_{ex} stabilizes a ferromagnetic charge transfer

$$\Delta_{ex}^s \approx Const - J_{ij}(S_i \bullet S_j) \tag{2.9}$$

where $J_{ij} \sim \left(2b_{ij}^2 \Delta_{ex} / 4S^2 U_{eff}\right)$ follows from third-order perturbation theory.

20

(3) Double exchange is also a kinetic exchange; this interaction involves a real charge transfer between two different valence states of the same M atom, each carrying a localized spin **S**, in a time τ_h that is short relative to the period ω_O^{-1} of the optical-mode lattice vibrations that would dress the charge carrier as a small polaron. Like molecular orbital or band theory, the real charge transfer is treated in first-order perturbation theory with Δ_{ex} stabilizing a ferromagnetic charge transfer:

$$\Delta_{ex}^D \sim czt_{ij}^{\uparrow\uparrow} = -c(1-c)b_{ij}\cos(\theta_{ji}/2) \tag{2.10}$$

where c is the fractional occupancy of the M sites by a mobile charge carrier and z is the number of like nearest neighbors within a cluster or in a three-dimensional array.

(4) Indirect exchange is a coupling of localized spins at M atoms by a partially occupied broad band where Δ_{ex} is not large enough to remove totally the spin degeneracy of the broad band. The interaction is ferromagnetic at small separation, becomes antiferromagnetic at larger separation, and oscillates as the separation of the M atoms increases.

2.3 OTHER IMPORTANT CONCEPTS

2.3.1 Localized- versus itinerant-electron ferromagnetism

Ferromagnetism has been described for two limiting cases: Heisenberg localized-electron magnetism and Stoner-Wohlfarth itinerant-electron magnetism.[54]

(1) In the Heisenberg localized-electron model, a quantum-mechanical exchange interaction between the electrons in neighboring atoms was introduced in terms of the atomic spin operators:

$$H_{ex} = -2\sum_{j,k} J_{jk}\left(\vec{S}_j \cdot \vec{S}_k\right) \tag{2.11}$$

where j, k specify the nearest neighbors in the lattice. From the Heisenberg model, the Weiss molecular field can be simply expressed as

$$H_{mf} = 2\left(g\mu_B\right)^{-1}\sum_{k} J_{jk}\left\langle S_k \right\rangle \tag{2.12}$$

and the Curie-Weiss law above T_c is given by

$$\chi = Ng^2\mu_B^2 S(S+1)/3k_B(T-T_c) \tag{2.13}$$

with a Curie temperature $T_c = 2J(0)S(S+1)/3k_B$.

The Heisenberg model is actually justified from a microscopic point of view where well-defined local atomic moments exist in both magnetic insulators and metals. In the former, the mechanism of exchange interaction is the superexchange interactions whereas the double exchange or indirect exchange interactions via the conduction electrons dominates in the latter. In these cases, the observed saturation magnetic moments are usually close to the expected spin-only values. Another characteristic feature of the Heisenberg ferromagnets is the concave curvature in the Arrott plot, *i.e.* M^2 *vs* H/M, or a linearity in the modified Arrott plot of $M^{1/\beta}$ *vs* $(H/M)^{1/\gamma}$ with critical exponents $\beta \sim 0.365$ and $\gamma \sim 1.386$. [55, 56] This relationship has been observed in a broad range of ferromagnetic systems such as Ni,[56] CrO_2,[57] Sr_2FeMoO_6,[58] $La_{1-x}A_xMnO_3$.[59]

(2) The Stoner-Wohlfarth itinerant-electron theory describes ferromagnetism in metallic systems where the splitting of the energy bands for up- and down-spin electrons is small.[24, 60] The total energy of such systems can be given by:

$$E = \frac{1 - IN(\varepsilon_F)}{N(\varepsilon_F)} M^2 + \frac{1}{4N(\varepsilon_F)} F_1 M^4 + ... \tag{2.14}$$

from which a ferromagnetic state is realized for $IN(\varepsilon_F) > 1$. This is usually called the Stoner criterion for ferromagnetism.[60] Although ferromagnetism is not realized for $IN(\varepsilon_F) < 1$, the magnetic susceptibility is enhanced by a factor of $1/(1 - IN(\varepsilon_F))$ compared with the Pauli paramagnetism χ_p. Based on the Stoner theory, Wohlfarth[24] has derived the relationship

$$M(H,T)^2 = M(0,0)^2 \left[1 - (T/T_c)^2 + 2\chi_0 H / M(H,T) \right] \tag{2.15}$$

which gives parallel lines of the isothermal M^2 *vs* H/M in the vicinity of T_c. $ZrZn_2$ is a typical example that fulfills such a mean-field universality class.

However, the Stoner theory fails to explain the observed Curie-Weiss magnetic susceptibility above T_c in almost all of the itinerant ferromagnets, for instance, MnSi. This itinerant-electron picture can be improved considerably if spin fluctuations are taken into account in the model of self-consistent renormalization studied by Moriya and others.[54]

2.3.2 Size-variance effect on magnetic ordering temperature

In the AMO_3 perovskite oxides, the electronic and magnetic properties result primarily from the M cations, but are tuned by the cation(s) at the A sites through three dominant factors: the average charge $<q_A>$, average size $<r_A>$, and size variance $\sigma^2(r_A)$. The average charge $<q_A>$ controls the mean oxidation state of the transition metal, or the electron- or hole-doping concentration. The mean A cation radius $<r_A>$ is incorporated into the tolerance factor t controlling the M-O-M interactions through bending of the M-

O-M bond angle. The cation size variance describes the effect of disorder due to disparity or mismatch of individual A cation radii and is defined as

$$\sigma^2 = \sum_i x_i r_i^2 - \left(\sum_i x_i r_i\right)^2 = \left\langle r_A^2 - \langle r_A \rangle^2 \right\rangle \tag{2.16}$$

where x_i are the proportions of each ion present ($\sum x_i = 1$). The first two factors have been well recognized and studied for a long time, the third one was investigated systematically recently by Attfield *et al.* [17-19]

The strategy in studies of $\sigma^2(r_A)$ effects is to fix both $\langle q_A \rangle$ and $\langle r_A \rangle$ but to vary $\sigma^2(r_A)$ by mixing three or more cations at the A sites in homogenous samples. Systematic studies [17-19] have shown that both the ferromagnetic Curie temperature of the CMR manganites and the superconducting transition temperature in the copper oxides decreases linearly with the size variance, *viz.*

$$T_c = T_c^0 - p\sigma^2 \tag{2.17}$$

where T_c^0 is the extrapolated critical temperature at zero variance (no size disorder) for a given $\langle r_A \rangle$ and the slope p of $dT_c/d\sigma^2$ is of magnitude $\sim 10^3 - 10^4$ K Å^{-2}. In addition, it has also been found [21] that the variation of T_c^0 with $\langle r_A \rangle$ can be described by a quadratic form, *viz.*

$$T_c^0 = T_c^m - q(r_A^m - \langle r_A \rangle)^2 \tag{2.18}$$

where the maximum T_c^m is found for the optimal A-cation radius r_A^m.

24
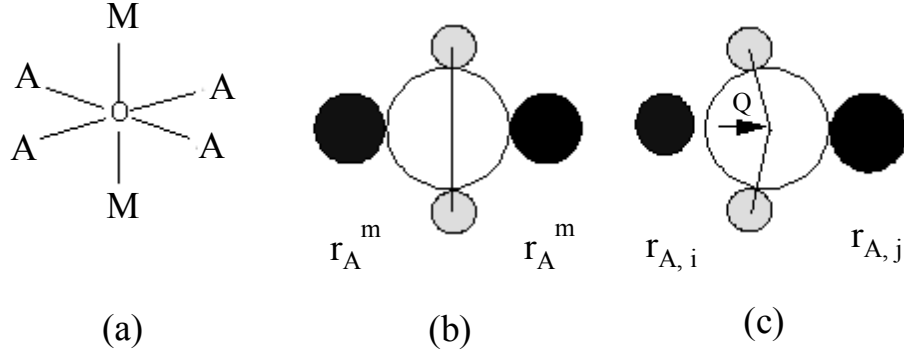
Figure 2.5:   Hard sphere model for local oxygen displacement in AMO_3 perovskites. The ideal oxygen environment with A cations of radii $r_A{}^m$ is shown schematically in (a) and as spherical ions in (b) (with only one of the two pairs of A cations displayed for clarity). (c) The displacement $Q = r_A{}^m - r_{A,j}$ of the oxygen atom when the neighboring cations i and j have radii unequal to $r_A{}^m$. (After Ref. 18)

An empirical hard-sphere ionic model has been proposed to explain the above phenomena based on the lattice strains resulting from the local displacements of the oxygen from the ideal position.[18] As shown in Fig. 2.5(a) and (b), each oxygen atom in an ideal AMO_3 perovskite with A cation radius $r_A{}^m$ is coordinated by four A cations and two M cations with a straight M-O-M bridge. In a real perovskite, Fig. 2.5(c), the A cations generally have $r < r_A{}^m$ and are not all of equal size. If the hard sphere oxide anion remains in contact with one of the two A cations of the radius r_A, then it undergoes a lateral displacement $Q = r_A{}^m - r_A$. If it is assumed that an electronic transition temperature T_c is reduced from a maximum value of $T_c{}^m$ by strain interactions from oxygen displacement Q, then the transition energy $\kappa_B T_c$ becomes

$$\kappa_B T_c = \kappa_B T_c{}^0 - C\langle Q^2 \rangle \qquad (2.19)$$

where C contains the average force constant for the strain term and $\langle Q^2 \rangle$ is split into incoherent and coherent terms by

$$\langle Q^2 \rangle = \left\langle \left(r_A^m - r_A \right)^2 \right\rangle = \sigma^2 + (r_A^m - \langle r_A \rangle)^2 . \qquad (2.20)$$

25

Thus,

$$\kappa_B T_c = \kappa_B T_c^{\ 0} - C\sigma^2 - C(r_A^m - \langle r_A \rangle)^2 \tag{2.21}$$

explains the experimental observation that T_c decreases linearly with σ^2 at constant $\langle r_A \rangle$ and with $(r_A^m - \langle r_A \rangle)^2$ at constant σ^2.

2.3.3 Quantum critical point

As illustrated in Fig. 2.6, a quantum critical point (QCP) is a special class of continuous phase transitions that take place at the absolute zero of temperature, typically in magnetic materials where the transition temperature for long-range magnetic order has been driven to zero by the application of external pressure, magnetic field, or chemical doping.[61-65] Different from the thermal-driven critical fluctuations that are developed over a narrow temperature range in a conventional second-order phase transition, the critical fluctuations at a QCP are quantum mechanical in nature and can influence the physical properties over a wide range of temperature, even up to room temperature. In the vicinity of QCPs, quantum fluctuations can generate new ground states such as an unconventional superconductivity. The Landau Fermi-liquid theory also breaks down near a QCP and gives way to non-Fermi-liquid behaviors,[63, 65] *i.e.*

$$\Delta\rho \propto T^n \ (1 \leq n < 2), \tag{2.22}$$

$$C/T \propto \ln T, \tag{2.23}$$

$$S/T \propto \ln T. \tag{2.24}$$

where ρ, C, and S represent resistivity, specific heat, and thermoelectric power, respectively.
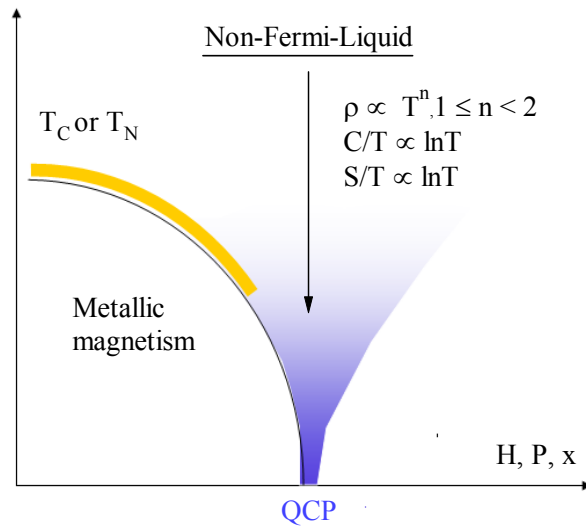
Figure 2.6: An illustration of a quantum critical point (QCP) approached by suppressing the magnetic transition temperatures, T_c or T_N, to absolute zero temperature through application of external magnetic field (H), high pressure (P), or chemical substitution (x). Non-Fermi-liquid behaviors occur in the vicinity of a QCP.

Chapter 3 Experimental Methods

This chapter contains the experimental methods used in this dissertation to prepare and characterize my samples. First, I will present a detailed description of the high-pressure and high-temperature synthesis utilizing a Walker-type multianvil technique. All aspects, including the setup, calibrations, and synthesis procedures, will be covered in this part. Then, I will briefly survey the measurement techniques generally used to characterize various physical properties, including structural, transport, and magnetic properties.

3.1 HIGH-PRESSURE AND HIGH-TEMPERATURE SYNTHESIS

3.1.1 Overview

High-pressure and high-temperature (HPHT) synthesis has became an important part of the field of solid-state synthesis of transition-metal oxides with perovskite-related structures.[6] It has the merits not only of increasing the rate of solid-sate reactions at high temperature, but also of stabilizing many metastable phases to ambient pressure. Beginning in the 1960-1970s, the HPHT synthesis continues to grow steadily in recent decades with more than 60 new compounds prepared.[66] Accordingly, new phenomena have emerged and advanced our understanding of condensed-matter physics.

However, the conventional HPHT techniques, including the piston-cylinder, belt, tetrahedral, and cubic anvil apparatus, can only reach pressures up to 10 GPa. Such a limit prevents us from obtaining compounds that require much higher pressure. In this respect, the multianvil HPHT technique, that is well developed and widely used in the

field of geoscience, is more promising because it can reach pressure as high as 20-30 GPa with considerable sample volume. Therefore, it has been introduced into the field of solid-state synthesis in quite recent years and has been proved to be efficient and critical.[10] An excellent example is the HPHT synthesis of cubic $BaRuO_3$ perovskite under 18 GPa and 1000°C with a Kawai-type multianvil apparatus.[11] Based on the same octahedron-within-cubes geometry, David Walker [7, 8] developed a simplified multianvil system using sliding, split-cylindrical steel wedges to back eight carbide cubic anvils with truncated corners, which has proved to be cost-effective, reliable, and more importantly, the module can be loaded into many existing hydraulic presses used for piston-cylinder devices.

3.1.2 HPHT system

All the HPHT synthesis work in this dissertation was carried out in a Walker-type multianvil module (Rockland Research Corp.) retrofitted to an existing 500-ton Clifton hydraulic press, which has been used previously with a belt apparatus. A pressure/temperature controlling system purchased from the Rockland Research Corp. was also installed in order to achieve smooth, slow compression and decompression at high loading forces. The temperature and pressure values can be recorded with a PC during the experiments.

(1) The Clifton hydraulic press

The Clifton hydraulic press, Fig. 3.1, has a massive four-pole steel frame able to support loads up to 500 US tons exerted from a large hydraulic cylinder, which has a main ram with a diameter of 13″ (33.02 cm), or an area of 132.73 in^2 (856.34 cm^2). An internal oil reservoir under the ram is connected to a large external oil tank through a

relief valve and a fast pump. When the relief valve is closed, the main ram can be raised rapidly by pumping in oil from an external tank, while the main ram will be retracted by draining the oil back to the external tank when the relief valve is open. The conversion from the US Tons of load to the oil pressure is 1 US Ton = 2000 lbs = 15.07 psi ×132.73 in^2, so the limit of 500 US Tons corresponds to a maximum oil pressure in the internal reservoir of ~ 7500 psi. The fast pump is only used for rapid advance of the main ram to close up the gap between the top plates of the module and the press at the beginning of a run and to retract the ram to lower the module at the end of the run.

Figure 3.1:   The 500-ton Clifton hydraulic press.

(2) The pressure control system

The pressure control system is on the left side of the Clifton press. It was designed to produce pressure up to 8800 psi and consists of a hydraulic cylinder, a screw jack that drives the piston into and out of the cylinder, a Servo motor connected to a two-level gear reducer. Motor speed is controlled by a potentiometer in the pressure control panel; the full speed is 1800 RPM. The motor stops when the over-travel limit switches are activated by the screw jack traveling plate; we normally end each run by retracting the

piston all the way down until the bottom limit switch is triggered. A pressure transducer connected to the hose near the top of the hydraulic cylinder monitors the system pressure, which is displayed in units of psi in the Panel View screen. A pressure-relief valve next to the pressure transducer opens if pressure exceeds 9000 psi.
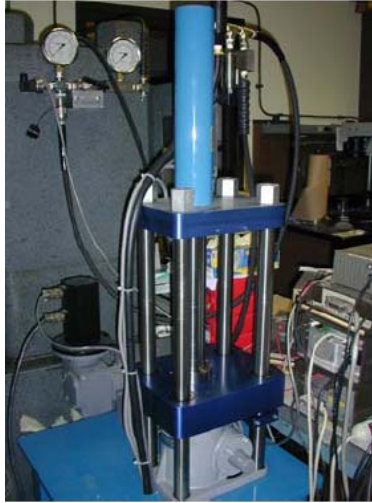
Figure 3.2:   The pressure control system from Rockland Research.

The pressure control system tees in the hydraulic presss by a high-pressure valve. When the valve is open, the oil is pumped directly from the external tank into the internal reservoir to advance the ram and also to refill the cylinder of the pressure control system; when the valve is closed, the fast pump and the relief valve are isolated and the advance of ram will be controlled by the pressure control system. In case that worm-gear driven piston activates the top travel limit switch before achieving the desired pressure, the pressure control system can be separated from the Clifton press; the cylinder is refilled and pressed before reconnecting to the system. However, this procedure has not been used so far to achieve pressures up to 7000 psi.

(3) Pressure and temperature control panel

Figure 3.3 shows the pressure and temperature control panel. The main switch located on the top right controls power to the panel. In case of an emergency, push the read STOP button to shut down the system. The red FAULT pilot light next to the STOP button indicates that an alarm or a warning has occurred. Panel View displays the status of the system and provides access to many other screens in order to change setting points and configurations. In the first row of PRESSURE CONTROLS there are four pilot lights: (1) Amber light indicates that the decrease full-travel-limit switch has been activated and the system has stopped; (2) Blue light indicates that motor is driving piston down to decrease pressure; (3) Green light indicates that motor is driving piston up to increase pressure; (4) Red light indicates that the increase full travel limit switch has been activated and the system has stopped. In the second row there are three selector switches and one PRESSURE START button: (1) MODE switch selects manual, automatic, or remote operation; (2) AUTO PRESSURE switch selects decrease, off, or increase/hold in the auto mode; (3) MANUAL PRESSURE switch selects decrease, off, or increase/jog in the manual mode; and (4) Green illuminated PRESSURE START push button is used to start pressure. A motor-speed potentiometer is used to adjust the motor speed in percentage; the full speed 1800 RPM is 100%.

The high temperature is generated by delivering current through the driver blocks and anvils to the heating element inside the high-pressure cell. The temperature controller provides 0 to 240 Volts AC power to the primary side of either transformer T-1 or T-2, which provides a 1-20 step-down ratio, delivering 0-12 V AC power, or a 1-5 step-down ratio, delivering 0-48 V AC power, to the heating element. The OUTPUT switch is used to select between 12 V and 48 V modes, which are normally used for the graphite and

LaCrO$_3$ heaters, respectively. After selecting the correct output voltage, push the green illuminated START TEMPERATURE button and then turn HEAT selector switch to on with HEAT ADJUST potentiometer turned to 100%. The system is now ready to deliver current to the heating element. The temperature measured with a Type-B or K thermocouple and the Voltmeter should increase steadily with increasing heat percent on the Eurotherm 2404 temperature controller. The HEAT potentiometer is useful to reduce the heating power slowly by turning from 100% to 0% before turning off the HEAT selector switch. But the HEAT selector switch should always be OFF except during the heating step of an experiment.

Figure 3.3:   The pressure and temperature control panel.

(4) Multianvil module

Figure 3.4 illustrates the internal configuration of a Walker-type multianvil module. Inside the containment ring, a split-cylindrical cluster of 6 wedges, 3 on top and

3 at bottom, forms an interior cube-shaped cavity that is used to seat a nest of 8 cubic tungsten-carbide (WC) anvils with 1 inch in edge length. In our setup, we use Toshiba Grade F carbide, which is commonly chosen for a multianvil device due to its higher yield strength (6 GPa) and lower axial strain (2.7) at failure. An octahedral pressure medium containing the sample is placed within the nest of WC cubes with the truncated corners facing the octahedron. A uniaxial compressive force applied through the pressure distribution plates is delivered to the sample inside the octahedron through the converging movement of the wedges and anvils. The containment ring is jacked by the safety ring, inside of which the cooling water is included. The massive module sits on a carriage, *i.e.* an aluminum plate, with wheels on the bottom; it will only roll when the weight of the module is supported by the wheels. There are two retaining pins to keep the aluminum plate locked in position.
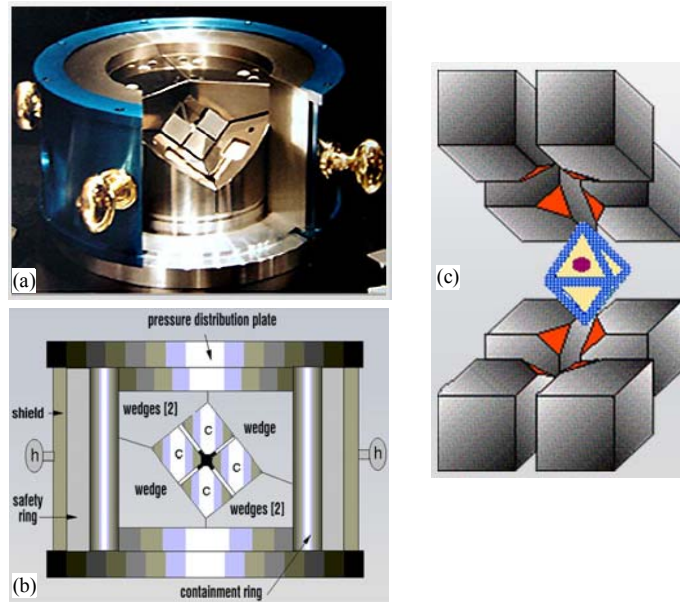
Figure 3.4:   Illustrations of the configuration of a Walker-type multianvil module.

In such a sliding, split-cylindrical wedge system, lubrication between the sliding interfaces is very important in order to improve the pressure efficiency.[8] The interface between the wedges and the bore of the containment ring is filled with a double layer of glossy polyester sheet of thickness 0.002″ with PTFE mold-release agent sprayed on the plastic to plastic interface; one layer is coated on the interior surface of the containment ring with T9 and the other is stuck to the wedges with superglue. The lubricated interfaces between the polyester sheets provide not only a sliding surface to accommodate motion of the wedges, but also an electrical isolation of the ring from the wedges. Between the wedges and the pressure distribution plates is one layer of similar polyester sheet that is used to provide electrical isolation. Epoxy-filled fiberglass (G10) pads are used to separate the wedges and to fill interfaces between the wedges and the anvils. In order to pass heating current to the heater, two WC anvils facing the opposite side of the heater are connected to the wedges with copper electrodes fitted into holes of 0.5″ in diameter on the G10 pads; the corresponding wedges are connected to the top and bottom pressure distribution plates with thin copper sheets of 0.002″ thickness.

(5) Recording temperature and pressure in a HPHT experiment

During a routine HPHT experiment, the pressure and temperature values are always recorded as a function of duration time with a software written with LabView. The pressure reading in psi is converted from the voltage value obtained by a pressure transducer that is located near the two-stage pumping valve. At the very beginning, the voltage value was calibrated to pressure with respect to the pressure reading on the Panel View screen. Figure 3.5 shows the calibration data and corresponding fitting curve and formula. The communication with the Eurotherm 2404 temperature controller was realized with the "iTools" software, which is used as a sub VI in the main program of

Labview to record parameters such as the percent power and temperature. This software is free to download from Eurotherm with a product key: 042-662-9523. In addition, we also made a software to monitor the resistivity as a function of pressure and/or temperature. This measurement is realized by communication with a Keithley 224 Current Source and a Keithley 181 nanovoltmeter.
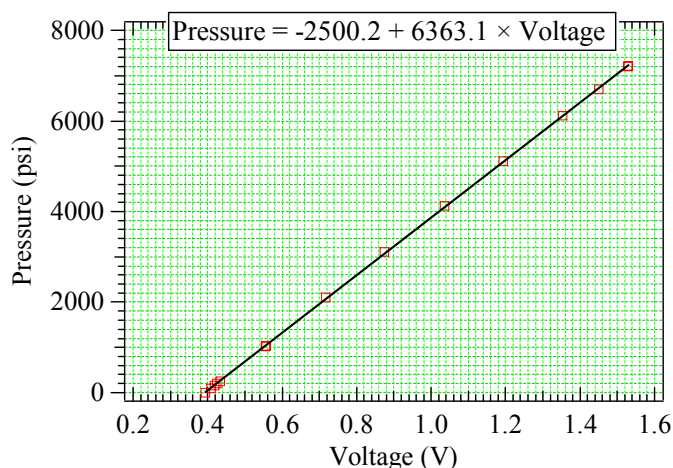
Figure 3.5:   Calibration curve for the conversion of voltage to pressure.

3.1.3 Components for high-pressure synthesis

The HPHT experiments are very costly because some components such as the octahedral pressure medium and G10 pads can only be used once while other parts like the WC anvils also have a high chance of failure. In order to make the high-pressure experiement affordable, Dr. Zhou has developed procedures to prepare all components, including the carbide anvils, in the lab. Some components that are easy to prepare will not be described; these include, for example, BN crucibles, graphite sleeves, G10 pads, Balsa wood spacer, polyester sheet, and copper electrodes. Here, I will only describe in

detail the procedures: (1) to grind the WC anvils from the raw pieces, (2) to cast the octahedral pressure medium (TEL = 8mm), and (3) to fabricate the pyrophyllite gaskets used for 8/3 octahedra. During the past three years, I have been trained to be not only a scientist but also a mechanical engineer.

3.1.3.1 WC cubic anvils

In our setup, we use WC cubic anvils (Toshiba Grade F) with L = 25.4 mm, which is ~\$70-100/piece if ready-to-use ones are purchased from a commercial company. The setup requires 8 pieces of WC anvils. Intrinsic defects, stresses, and blowouts always cause failure of the WC anvils. Once all eight carbide anvils were crushed in a blowout. Therefore, we turn to order the raw pieces, which are \$30/piece. These raw pieces are nearly cubic with L ≈ 26 mm; what we need to do is to grind six surfaces to make an exact cube with L = 25.4 mm and then grind one or more corners with designed truncated edge length (TEL). For this purpose, we use an ACER Supra 818AHD Surface Grinder system equipped with a diamond grinding wheel to control precisely the dimensions of the WC anvils. A stepping motor on the down-feeding system ensures an accurate vertical movement, which can be as small as 0.002 mm/step. Displayed in Fig. 3.6 are pictures of the WC anvils (a) before and (b) after grinding.
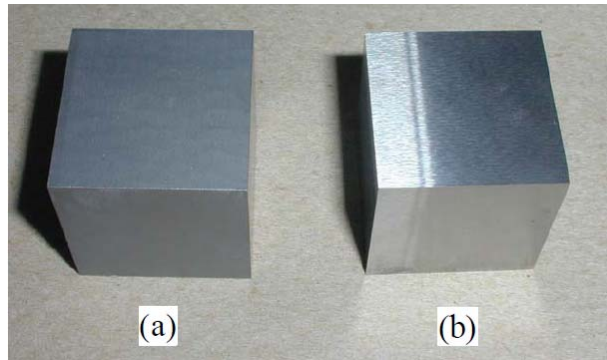
Figure 3.6: Pictures of the WC anvils (a) before and (b) after grinding.

In order to demonstrate clearly the procedure of grinding the raw WC anvils in Fig. 3.8, I first define the six surfaces of a raw piece of WC anvil as shown in Fig. 3.7. These surfaces are ground in the order 1 to 6. Starting from surface 1, four pieces of raw WC anvils are mounted on a flat steel plate, which is then magnetically attached to the grinding plate, Fig. 3.8(a, b). After polishing off ~ 0.3 mm, we turn to the 2nd surface. With the same method as surface 1, monitor the down-feeding amount to ensure precisely the length of 25.4 mm between surfaces 1 and 2. Then, hold up to 6 pieces of WC anvils firmly with a steel chuck with their surface 1 and 2 facing the chuck, Fig. 3.8(c), and then grind off ~ 0.3 mm. The purpose of using the steel chuck is to guarantee that the surface 3 is perpendicular to the surfaces 1 and 2. The surface 4 is ground the same way as surface 2. In order to get surface 5 normal to surfaces 1 to 4, we use two V-blocks inside the chuck to hold up the WC anvil, Fig. 3.8(d). After grinding off ~ 0.1mm of the surface 5, we finally turn to the surface 6, which is ground the same way as surfaces 2 and 4. After these procedures, we get perfect WC cubes with shinning surfaces as shown in Fig. 3.6(b). The key points in grinding these WC anvils are: (1) make sure the surfaces are totally attached to the flat steel plate without any tilting angle; (2) slow down the speed of hydraulic movements in the *xy* plane when approaching the target value.

Finally, the WC cubes are ready for grinding off one corner. In order to make an equilateral triangle for the truncated corner, a holder with an accurate angle of 35.264° is developed, Fig. 3.8(e, f). To get an anvil with TEL = x mm, a total of vertical displacement h of the diamond wheel is calculated by $h = x/\sqrt{6}$ mm; *i.e.* 1.225 mm for TEL = 3 mm and 3.266 mm for TEL = 8 mm. However, it is difficult to determine the position where the wheel touches a carbide cube initially . In practice, I first grind off an unknown amount h' to get an edge length of x', which can be measured under a microscope and used to determine h' by $h' = x'/\sqrt{6}$. In order to get the targeting TEL, the diamond wheel needs to further move down the amount of $(h - h')$ mm.
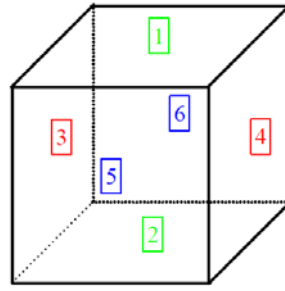
Figure 3.7:   Definition of the six surfaces of a raw WC anvil.
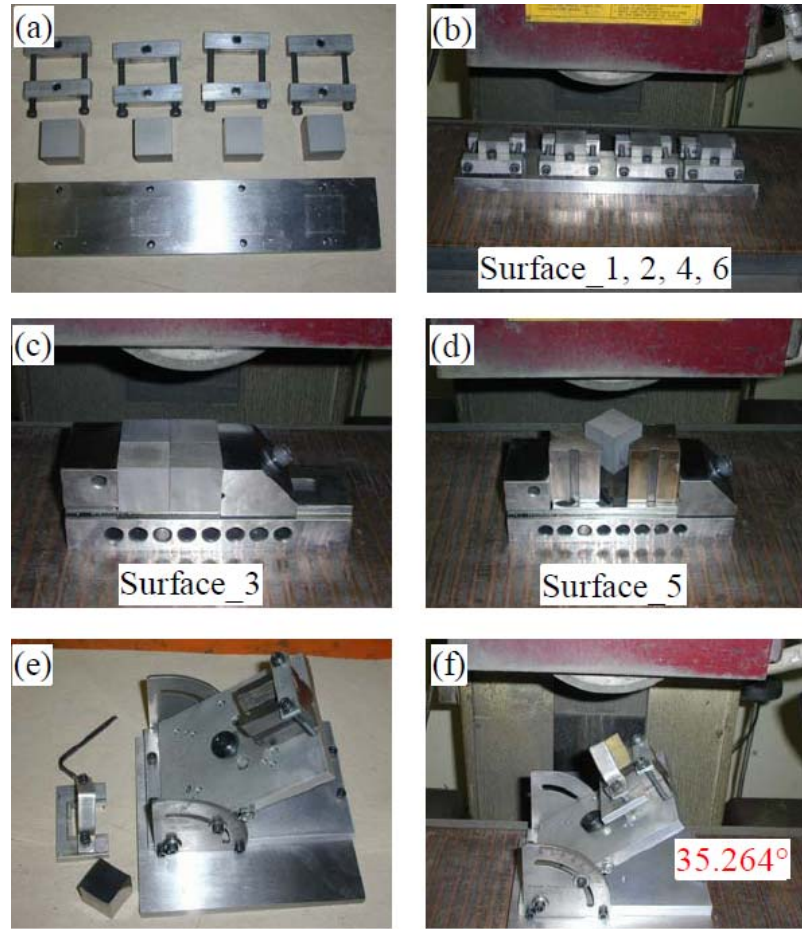
Figure 3.8   Procedures of grinding raw WC anvils.

3.1.3.2 Casting a MgO Octahedron (TEL = 8 mm)

Depending on the gaskets, there are two kinds of octahedral pressure medium: one is the castable octahedron with integrated fin gaskets invented by Walker and the other is the octahedron with preformed pyrophyllite gaskets. These examples are shown in Fig. 3.9. For the former, gaskets are already included as part of the octahedron and are usually referred to as fins. The thickness and the width of the fins need to be considered at the beginning of design; only the truncation edge length (TEL) is used to denote this

kind of octahedron. For the HPHT experiments under 10 GPa, we use this kind of castable octahedron with TEL = 8 mm, Fig. 3.9(a). They are made from a mixture of Ceramacast 584 powder and liquid (Aremco Products, Inc.); the detailed procedure will be given below. An octahedron used in high-pressure synthesis is measured by the octahedron edge length (EL) and the truncated edge length (TEL) on the matched WC anvil in millimeter, *e.g.* 25/15, 18/11, 14/8, 10/5, 8/3, 7/2. For the HPHT experiments above 10 GPa, we use the 8/3 octahedra, Fig. 3.9(b), which are available commercially from Japan Ceramic Engineering CO. LTD with a price of $30/piece. But we have to fabricate the pyrophyllite gaskets in the lab; detailed procedures will be given below.

(a) (b)
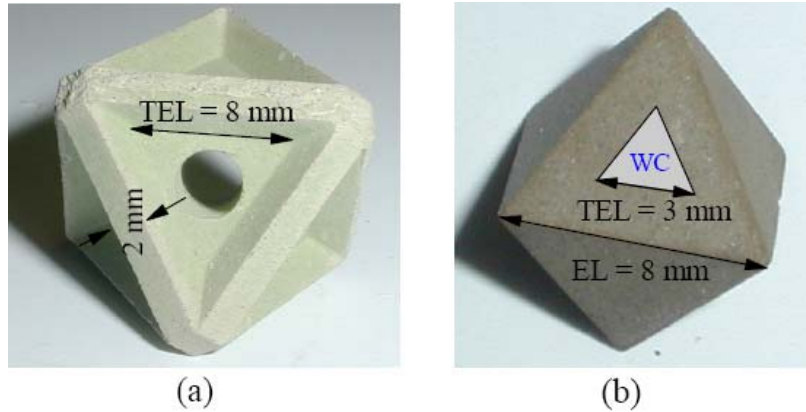
Figure 3.9:   (a) Walker-type castable 14/8 octahedron with integrated fin gaskets and (b) 8/3 octahedron that is used with preformed gaskets. They are used in our lab to reach pressure below and above 10 GPa, respectively.

As pointed out by Walker,[7, 8] reduction of initial porosity is beneficial for pressure generation efficiency because less compressive stroke is wasted in closing the initial porosity present. However, the commonly used injection method to make an octahedral pressure medium always gives rise to high porosity due to the lack of compressive force.

41

To overcome this problem, we cast a half-octahedron under certain pressure and then complete a whole one by combining two half-pieces together. In the following, a detailed procedure to make an octahedron is illustrated.

Step 1: Casting a half-octahedron

The required materials and tools for casting a half-octahedron are shown in Fig. 3.10. They are:

(1) Ceramacast 584 power: from Aremco Products, Inc.;

(2) Chromium (III) oxide (Cr_2O_3): 98+%, ~325 mesh, from Alfa Aesar;

(3) Ceramacast 584 liquid: from Aremco Products, Inc.;

(4) MS-260 Cleaner: from Miller-Stephenson;

(5) MS-122XD PTFE release agent: from Miller-Stephenson;

(6) An agate mortar;

(7) A dropper pipet;

(8) An electronic balance: 0-120g, from TANITA Corp.;

(9) A Teflon container consisting of a two-end opened cylinder with a free-moving piston;

(10) A wood applicator;

(11) A spatula;

(12) A 2 kg donut-shaped block;

(13) A mold set consisting of an adjustable square frame, four cubes with truncated corners, a "plus" spacer insert, two V blocks and a pushing pin;

(14) A ¼'' Allen wrench.

Figure 3.10: Materials and tools required to cast an octahedral pressure medium.

We normally add 5% Cr_2O_3 to the 584 powder, which has been found to improve the ability to resist moisture and to reduce the porosity with respect to the pure 584 power. To prepare the mixed powder of Ceramacast 584 powder with 5% Cr_2O_3, I usually mix 60 g Ceramacast 584 with 3 g Cr_2O_3 power by grinding them in an agate mortar for 20-30 min until a uniform green color is achieved. The mixture is kept in a refrigerator and can be used to cast ~25 pieces of half-octahedra. However, we found no difference between the Cr_2O_3 doped and pure Ceramacast 584 octahedron in terms of the pressure efficiency.

Displayed in Fig. 3.11 is the procedure of casting a half-octahedron. (a) Wipe clean each piece of the mold set with the MS-260 Cleaner and assemble the mold set. Apply the MS-122XD PTFE release agent to the interior of the mold set and one end of

the pushing pin in order to prevent the mixture from sticking to the mold set. (b) Weigh about 2.2-2.4 g mixed powder of 584 (5% Cr_2O_3) with the Teflon container. Using a dropper pipet, add 9-10 drops of 584 liquid into the Teflon container and stir the mixture quickly with a wood applicator until all the lumps of the power disappear. (c) Transfer quickly all the mixture into the mold set by pushing forward the bottom piston of the Teflon container. (d) Place the pushing pin in position with the 2 Kg donut-shaped block on top. The above processes should be done as quickly as possible because the mixture hardens in about 120 seconds including the mixing time. Keep the half octahedron in the mold set to cure for 2 hours. (e, f) Finally, take out of the octahedron and leave in air 2-4 weeks before polishing and attaching two pieces into a whole octahedron.
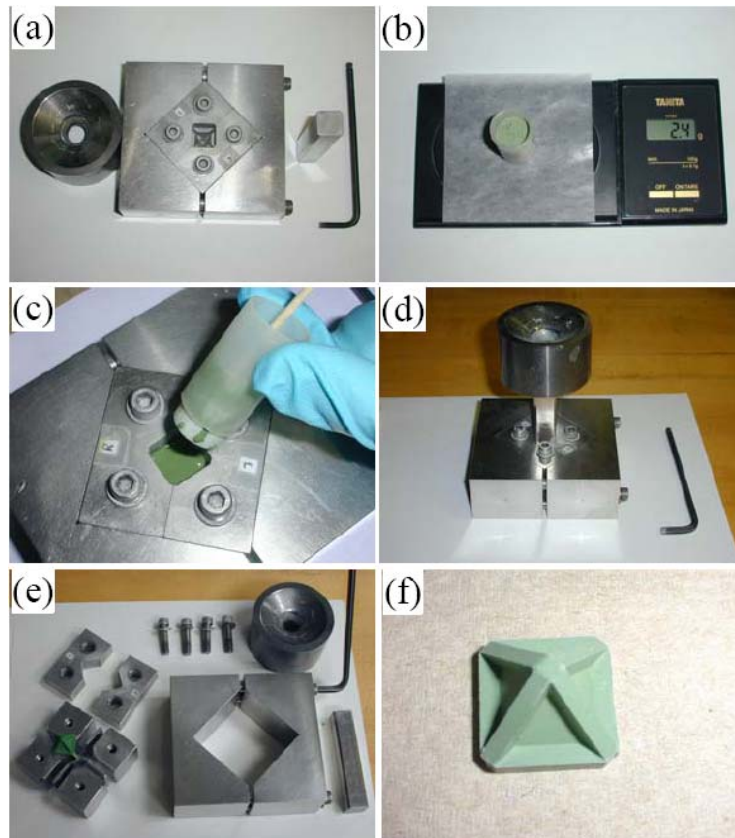
Figure 3.11: Procedures to cast half octahedron.

Step 2: Making a whole octahedron

In order to prevent blowouts, it is important to make an octahedral pressure medium with 12 fins of equal thickness. *i.e.* 2 mm. In our method of casting a half-octahedron, however, we can only confine the thickness of 4 out of (4+4*) fins by the "plus" spacer insert. The other 4* fins at the interface between the two pieces of a half-octahedron have to be thinned down to around half the thickness of a fin before attaching them together to make a whole octahedron.

The procedures of polishing half-octahedra and attaching them together to make a whole one are shown in Fig. 3.12. A Teflon adapter, Fig. 3.12(a), was developed to hold a half-octahedron and fit it onto the bottom of the sample holder of a lapping and polishing machine (Southbay Technology Inc.). After trial and error, it turns out the ideal thickness after polishing should be 0.90 ± 0.02 mm. The binder used to combine the two pieces of half-octahedron is the same material as the octahedron, but it is a much diluted one, *i.e.* ~ 0.2 g 584(5% Cr_2O_3) powder mixed with 2 drops of 584 liquid. After attaching them together, fill the gaps with the binder and remove the excess. Discard the octahedra with fin thickness greater than 2.0 ± 0.1mm. This requirement can be achieved simply by taking practice; $\sim 90\%$ percent of octahedra should be in this range after making ~ 30 octahedra. Leave the octahedra in air overnight in order to dry the binder.
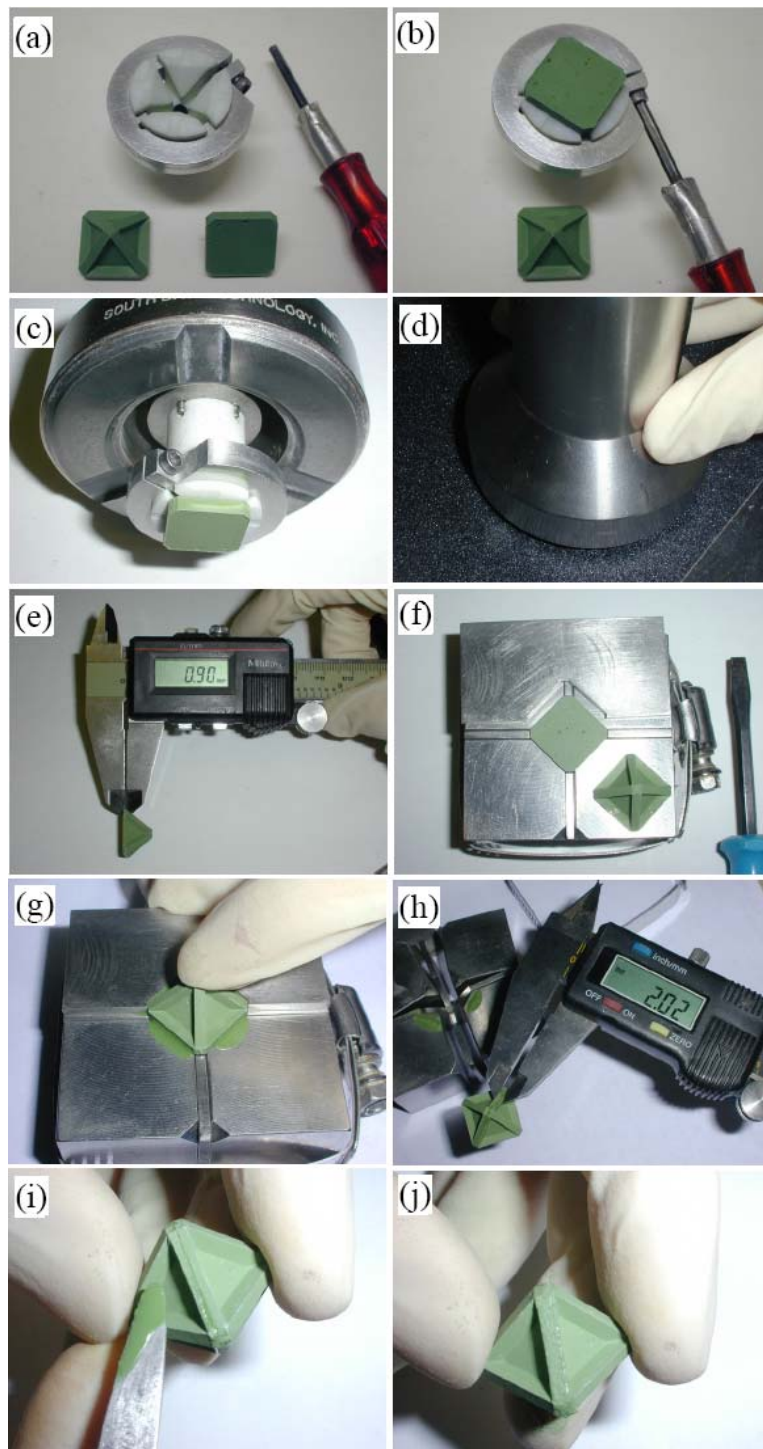
Figure 3.12: Procedures to make a whole octahedron by attaching two half pieces together.

Step 3: Sintering octahedra

Sintering is required to drive off the water and binder residues contained in the ceramic. Place the octahedra in a box furnace and fire at 200°C for 2 hours and then at 1000°C for 2-5 hours. After firing, the octahedra harden and show a light green color.

Step 4: Drilling a hole in the octahedron

After sintering, the octahedron is ready for drilling a hole through the opposite faces. For the TEL = 8 mm octahedral pressure medium, we drill a hole 3.26 mm in diameter. The hole should be well cantered on the octahedron's triangular face; otherwise, the sample assembly will be messed up during pressurization and there will be a great chance of blowout if BN or graphite heater is squeezed into the fins. To accomplish this task, a sample holder shown in Fig. 3.13(c) has been developed in our lab. An octahedron is fixed on this holder with one of its faces sitting exactly on a triangular plate having the same length as TEL. Corresponding to the center of the triangular face, there is a 1/8″ central hole at the bottom of the holder. By adjusting the *xy* position of a 1/8″ drill bit until it fits into this hole smoothly, we can align accurately the drill bits and the center of the triangular face. If the octahedron is not perfectly even, we can also adjust the angle with the three long screws. The drill bits are always solid tungsten carbide and can be resharpened with a Drill Doctor; the drilling task is accomplished with a tabletop Sherline milling machine (Model 540), Fig. 3.13(a). After a hole is drilled, the octahedral pressure medium is ready for the HPHT experiments.
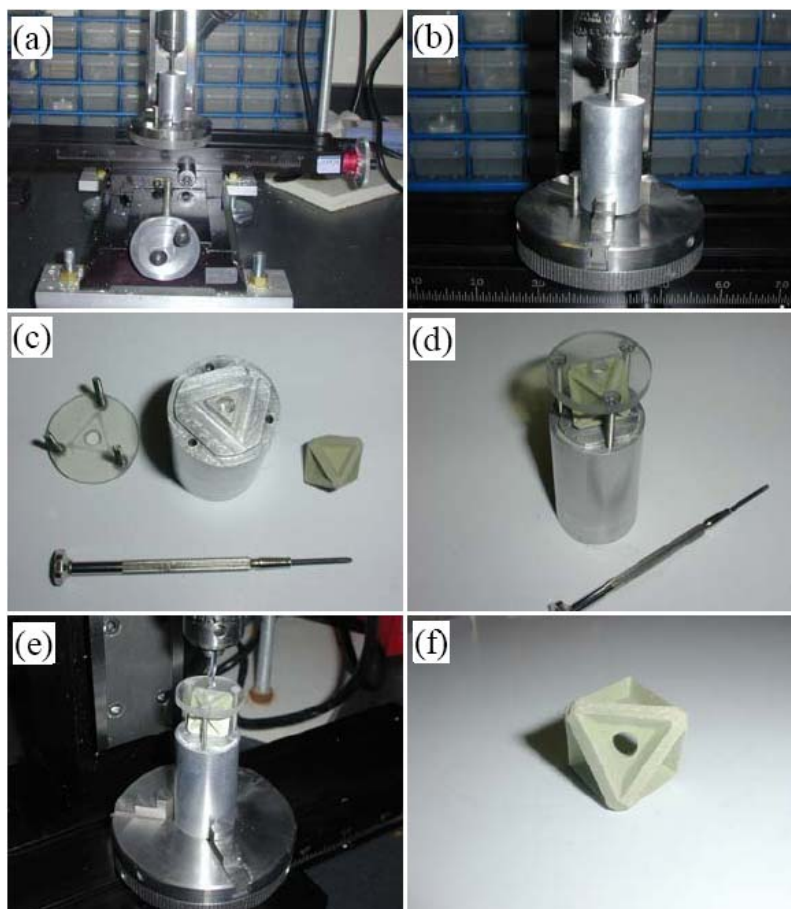
Figure 3.13: Procedures to drill a hole in the castable octahedral pressure medium with TEL = 8mm.

3.1.3.3 Preformed pyrophyllite gaskets for an 8/3 octahedron

The HPHT synthesis with an 8/3 octahedron in Fig. 3.9(b) requires 12 pieces of gasket, trapezoidal in shape, including a longer and a shorter set of 6 each. The common gasketing material is pyrophyllite (often called "lava rock"). Most of the dimensions of the gaskets are fixed by the EL/TEL values. As shown in Fig. 3.14, the length for the inner edge of the longer gasket is equal to EL, while the equivalent length for the shorter gasket is (2TEL+EL)/3. The height perpendicular to the trapezoid is fixed by the formula

$h = \sqrt{2}(EL - TEL)/3$. The only dimension that can be adjusted is the width of the trapezoidal part of the gasket. We choose 2 mm for the width. Therefore, the dimensions of the gaskets are determined and given in Table 3.1.
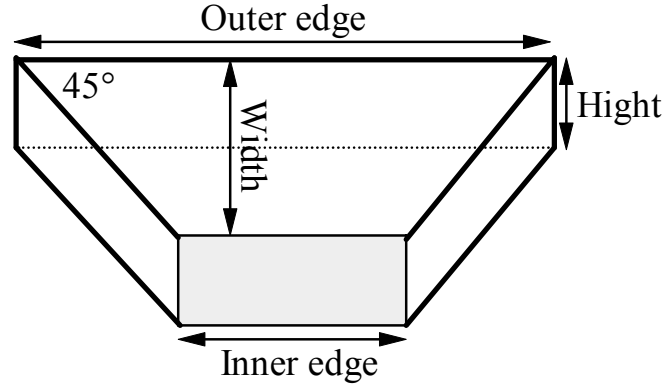
Figure 3.14: A schematic drawing of the trapezoidal shaped gasket.

Table 3.1:   Dimensions of the performed gaskets for the 8/3 and 14/8 octahedra.

	8/3		14/8	
	Longer	Shorter	Longer	Shorter
Inner edge (mm)	8.0	4.67	14.0	10.0
Outer edge (mm)	12.0	8.67	18.0	14.0
Height (mm)	2.36		2.83	
Width (mm)	2.0		2.0	

We use a CNC milling machine (model 5410, Sherline Products, Inc.) for a mass production of pyrophyllite gaskets, Fig. 3.15. First, a pyrophyllite plate is thinned down to 2.36 mm and then made into a pattern by a tungsten-carbide end mill according to the

49

dimensions in Table 3.1. The pyrophyllite gaskets are hardened before use by firing at 500°C for 15 hours.

Figure 3.15: Preformed pyrophyllite gaskets with different size produced with a CNC milling machine.

The pyrophyllite gaskets sealing the octahedral pressure medium are glued to the truncated corners of the WC anvils. The 12 pieces of gasket, including a longer and a shorter set of 6 each, are arranged as shown in Fig. 3.16, where Top and Bottom refer to the clusters of four WC anvils above and below the octahedral pressure medium. Only two out of four anvils for both Top and Bottom need to be glued with the gaskets.
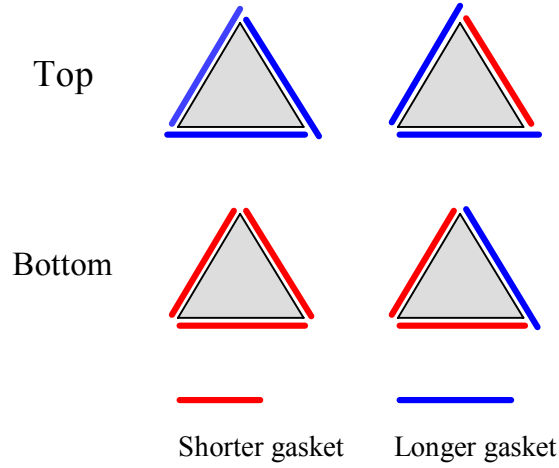
Figure 3.16: Attaching pyrophyllite gaskets to the truncated corners of the WC anvils.

3.1.4 Pressure calibration

Room-temperature pressure calibrations as a function of the uniaxial loading force were carried out by measuring the electrical resistance of well-known materials having pressure-induced phase transitions as shown in Table 3.2.[67] Metals like Bi and Pb with small resistivity are first rolled into a thin sheet of ~ 0.2 mm in thickness and then cut into stripes of ~ 0.2 mm in width; semiconductors or insulators like ZnTe and ZnS (they were used to calibrate pressure with 8/3 octahedra) with huge resistivity at ambient pressure were cut into short bars with dimensions ~ $1\times1\times2$ mm^3. These calibration materials were put into the octahedral pressure medium with the configurations shown in Fig. 3.17; a zigzag configuration (a) is normally used to increase the resistance of the materials exhibiting low resistivity like Pb while configuration (b) can be used for materials showing large resistivity. An h-BN is used to maintain a quasi-hydrostatic pressure condition during the pressurization and slim Indium wires inside the pyrophyllite plugs are used to make electrical contact between the calibration materials

51

and the WC anvil. The electrical resistivity was measured with a two-probe method; the electrical circuit is composed of the calibration material, indium wires, two WC anvils and wedges, and the hydraulic press. A constant current provided by the Keithley 224 Current Source flows through the circuit and a Keithley 181 nanovoltmeter was used to monitor the voltage change that was recorded with a LabView Program.

Table 3.2: Pressure-induced phase transitions that can be used in the fixed-point pressure calibrations at room temperature.

Materials	Pressure (GPa)
Bi (I-II)	2.55(1)
Tl (II-III)	3.68(3)
Ba (I-II)	5.5(1)
Bi (III-IV)	7.7(2)
Sn	9.4(3)
Ba (upper)	12.3(5)
Pb	13.4(6)
ZnTe (I-M)	13.5
ZnS (I-M)	15.5
GaAs(I-M)	18.0
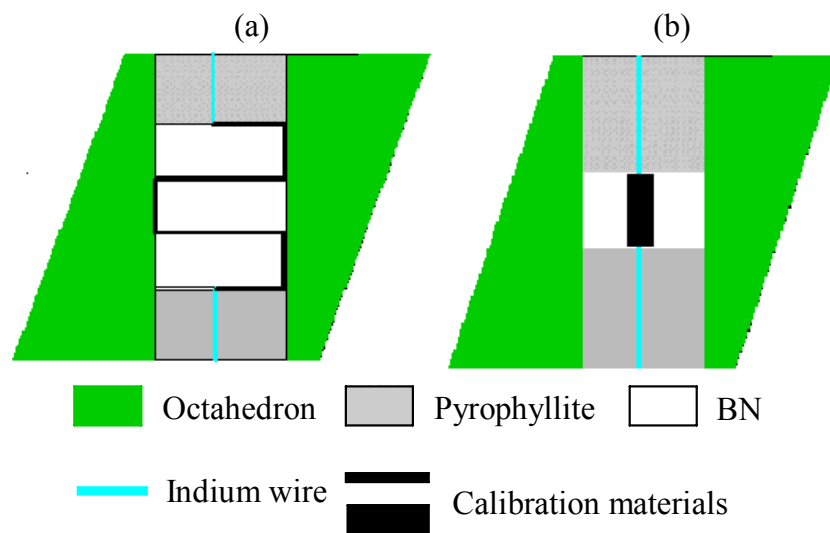
Figure 3.17: Cross-section views of the sample assemblies for pressure calibration against the materials with (a) low resistivity and (b) high resistivity.

Figure 3.18 displays the representative calibration resistance curves as a function of the loading forces for (a) the castable octahedra with TEL = 8 mm and (b) 8/3 octahedra with preformed gaskets. The phase transitions can be easily recognized from the sharp changes of resistance and are also given in Fig. 3.18. The calibrations on the castable octahedra have been carried out 5 times and are found to be well reproducible; *i.e.* the Bi(I-II) and Bi(III-IV) transitions fall into the range of 56 ± 4 Tons and 182 ± 5 Tons. The Pb transition at ~ 13 GPa was only observed once; a blowout occurred before reaching such high pressure in another calibration. Thus, the castable octahedra with TEL = 8 mm can be used to pressures < 13 GPa; this problem has also been observed by most multianvil users. It is worthwhile to mention that our setup shows much higher pressing efficiency compared to that reported in the literature; for example, 71 ± 5 and 267 ± 11 Tons are required to observe the Bi transitions in the original Walker setup.[8] We attribute the higher pressure efficiency to the lower porosity of the octahedral pressure medium that we have cast under certain compressive force. For the 8/3 octahedra with preformed

gaskets, we have only calibrated once on three materials, Fig. 3.18(b). As shown in Fig. 3.19, the calibration pressures are consistent with those reported in the literature.[68] But we failed to find the phase transition at 18 GPa of GaAs in a run to 400 US Tons, which corresponds to over 20 GPa according to the dashed curve.
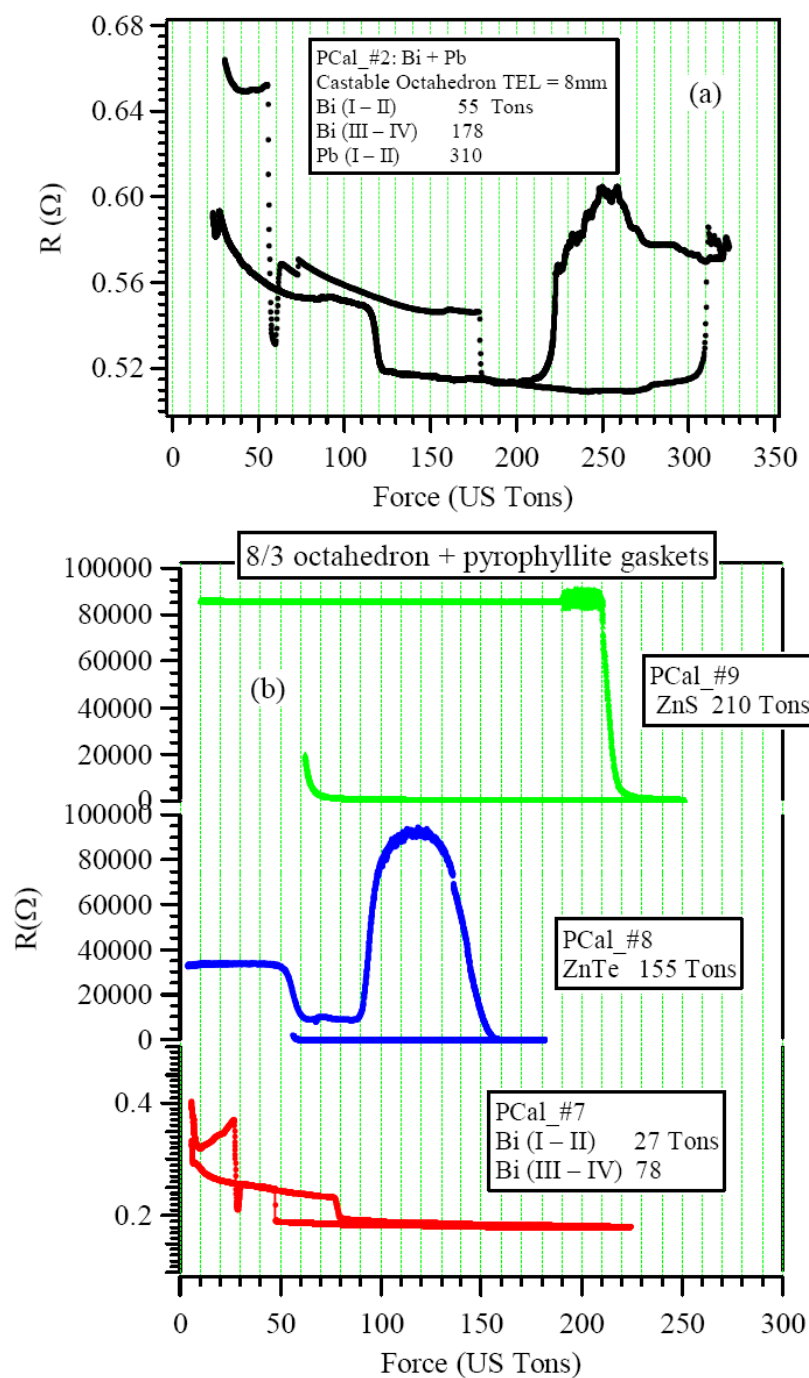
Figure 3.18: Representative calibration resistance curves as a function of the uniaxial loading forces for (a) castable octahedra with TEL = 8 mm and (b) 8/3 octahedra with performed gaskets.
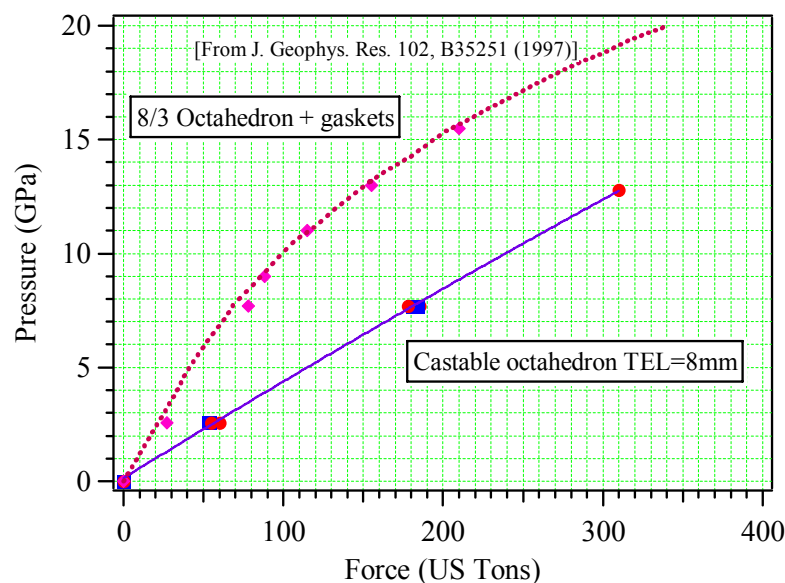
Figure 3.19: Pressure calibration curves for the castable octahedra with TEL = 8mm and 8/3 octahedra with preformed gaskets. The dashed line is from Ref. 68. Diamond symbols are from our fixed-point calibrations.

3.1.5 Temperature calibration

For the purpose of HPHT synthesis, the temperature within the sample cell was not measured directly every time with a thermocouple, but estimated from the calibration curves of temperature versus output power. As already shown by many labs, the temperature distribution inside the sample cell is rather large, ~ 50-100°C/mm from the center;[69] it turns out to be very hard, if not impossible, to accurately control the temperature. For pressures under 10 GPa and temperatures below 1400°C, we have employed a graphite tube as heating element; it is an inexpensive, easily machinable and very stable furnace. The graphite furnace has a length of 8 mm and a wall thickness of

0.5 mm. During temperature calibration, a Type-B (Pt6%Rh-Pt30%Rh) thermocouple is placed in the center of the sample cell and brought out through the fins of the octahedron with either the radial or the axial configurations shown in Fig. 3.20. The temperature in the center of the sample cell is recorded with increasing heat percent and output power; it was calibrated up to ~1400°C for each pressure from 3 to 10 GPa. As shown in Fig. 3.21, more heat power is needed in order to reach the same temperature with increasing pressure. Since the output power has a linear relationship with the heat percent, *viz.* Power = - 229.36 + 39.921 × Heat Percent, the temperature can be monitored with either heat percent or power during the HPHT synthesis according to the calibration curves.
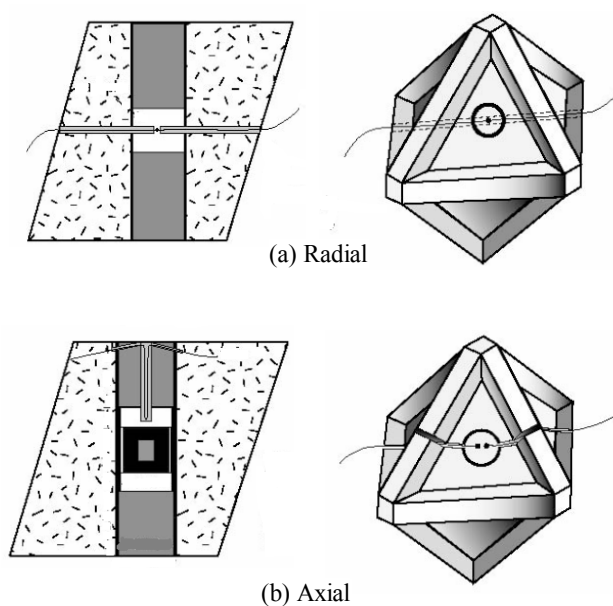
(a) Radial

(b) Axial

Figure 3.20: Cross-section and perspective views of the thermocouple configurations: (a) radial and (b) axial.
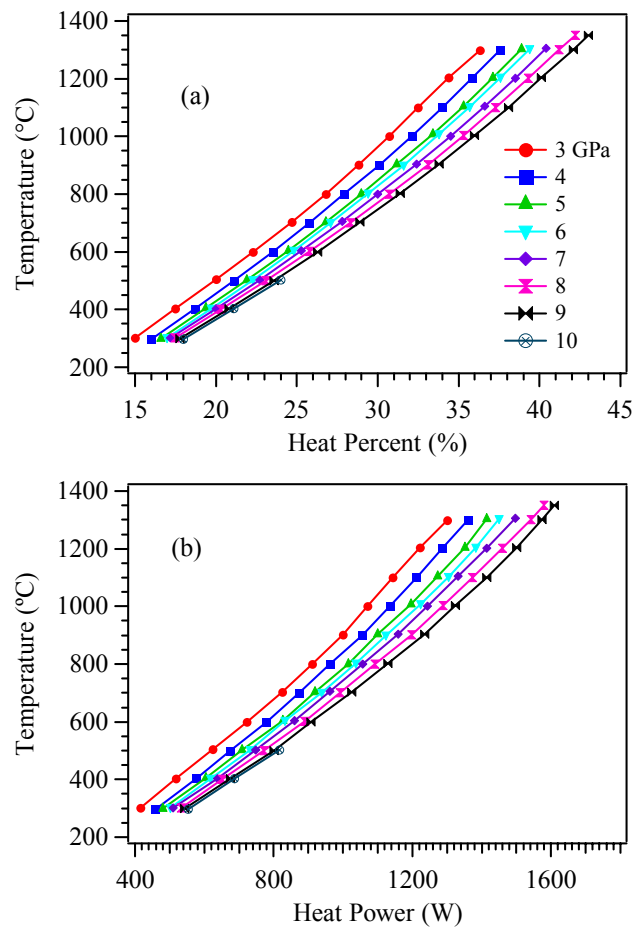
Figure 3.21: Representative temperature calibration curves as a function of (a) heat percent and (b) heat power by using the radial configuration.

The type-B thermocouple shows a negligible pressure effect and is ideal for monitoring the temperature at the sample in a high-pressure synthesis; but the thermocouple is expensive. By placing both a type-B and an inexpensive type-K thermocouples at the same location in a pressure cell, we have obtained the curve of T versus emf under different pressures for a type-K thermocouple. This correction allows us to use a type-K thermocouple to monitor the temperature in the high-pressure

synthesis at T < 1200° C. Figure 3.22 shows the calibrated temperatures measured by a type-K thermocouple against the type-B thermocouple; they were put into the opposite side of the sample cell with the radial configuration. The type-B thermocouple cannot correctly probe temperature below ~ 200°C. As can be seen in Fig. 3.22, the temperature measured by the type-K thermocouple is higher than that given by the type-B thermocouple below 5 GPa, whereas it converts above 5 GPa and the difference enlarges with increasing pressure.
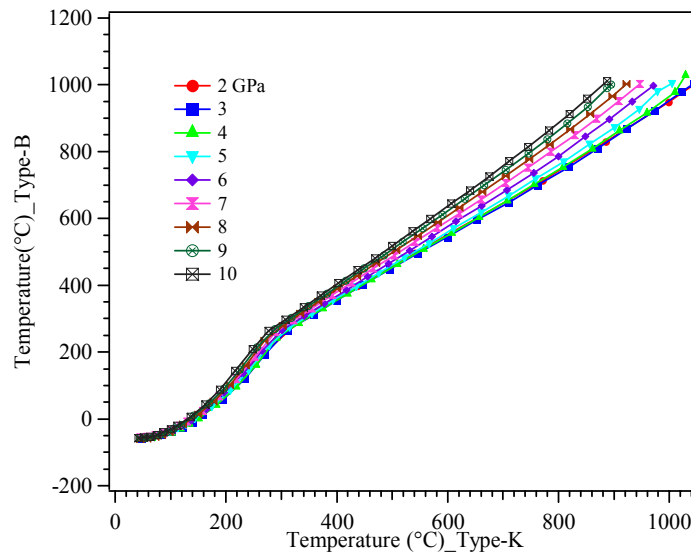
Figure 3.22: Temperature calibration curves of a type-K thermocouple against a type-B thermocouple under high pressures from 2 to 10 GPa.

3.1.6 HPHT experiment

3.1.6.1 Sample assembly

The sample assembly is inserted into a cylindrical hole drilled through the opposite faces of an octahedral pressure medium. For the HPHT synthesis, the sample assembly is composed of a resistance furnace, sample container, electrical and thermal insulation, and spacers. Graphite and lanthanum chromate ($LaCrO_3$) are the most common furnace types. A graphite heater is inexpensive, easily machinable, and stable upto 10 GPa and 1300°C. A graphite heater loses its conductivity due to the formation of the diamond phase under higher temperature and pressure. In this case, $LaCrO_3$ becomes a good alternative, but $LaCrO_3$ is fragile and not as easy to machine as graphite. To save the sample volume in the small pressure cells, *e.g.* TEL = 3 mm or smaller, wrapped metal furnaces are widely used; platinum (Pt) is an effective furnace to 1700°C and Rhenium (Re) to temperatures in excess of 2000°C. To protect the sample from reaction with its surroundings, it should be contained in a capsule, usually made of noble metals (gold or platinum). The metal capsules need to be surrounded by an electrical insulating sleeve in order not to electrically short the furnace, but the sleeve should be thermally conducting to reduce thermal gradient around the sample. h-BN is a good choice to fulfill these requirements and to maintain a good quasi-hydrostatic condition. For temperatures above 1500°C, a thermal-insulation sleeve placed around the outside of the furnace is important in order to prevent excessive heat loss; Zirconia and $LaCrO_3$ are the traditional choices. The other spaces are filled with either pyrophyllite or ceramic plugs.

Figure 3.23 shows a cross-section view of the sample assembly we mostly often used in the TEL = 8 mm castable octahedra. The cylindrical hole is 3.26 mm in diameter and 10 mm in length. Starting materials for the HPHT experiment were sealed in a gold or platinum capsule with a miniature die; the dimensions of the sample capsule are 1.68 mm in diameter and 3 mm in length. The sample capsule is put into an h-BN container with a wall thickness of 0.29 mm and a length of 4 mm. The h-BN container is then inserted into a graphite furnace with a wall thickness of 0.5 mm and a length of 8 mm, both ends of which are stuffed with a Molybdenum foil and a steel ring. Other spaces are filled with pyrophyllite plugs. We have also used the configuration in which the graphite heater is directly contacted with the WC anvils, which was found to consume more power than the above one without direct contact in order to reach the same temperature. Such differences should attribute to the very high thermal conductivity of the graphite with respect to the combination of Mo foil, steel ring and pyrophyllite plug. All the components of the sample assembly are fabricated with a tabletop lathe (Model 4410, Sherline Products, Inc.).

🟩	Octahedron	🟦	Pyrophyllite
⬛	Graphite	⬜	h-BN
🟪	Steel ring	🟨	Gold/Platinum foil
🟥	Mo foil	▦	Sample
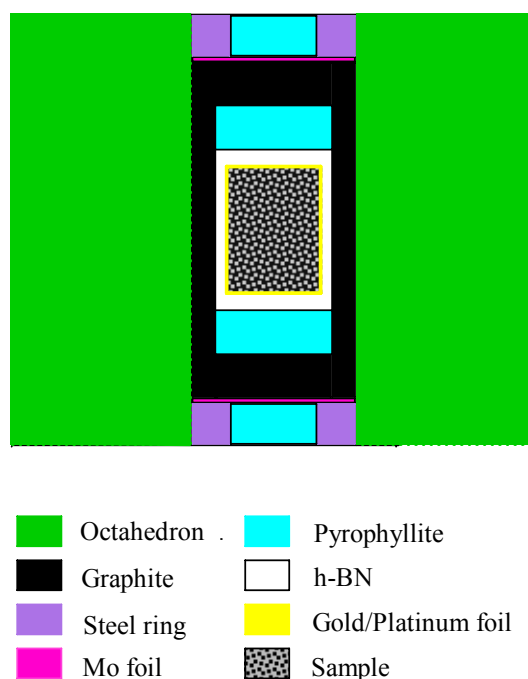
Figure 3.23: A cross-section view of the sample assembly used in the TEL= 8 mm castable octahedra pressure medium.

3.1.6.2 Experiment procedures

After completing all of the above preparation work, we are in a position to perform the HPHT synthesis. In the following, I will present the experimental procedures in a step-by-step manner so that a new user can start the experiment quickly.

Step 1: Prepare the required materials for the HPHT experiment. Figure 3.24 shows the required materials for a HPHT experiment. WC anvils and sample assembly have been described above. G10 pads of 2″×2″ are prepared with a shear cutter in the Machine shop. Some G10 pads are drilled with a ½-inch hole, which is use to hold a copper disk as electrode. Blasa wood spacers are cut from a big piece 2.2 mm in

thickness. Polyester sheets of 0.002″ are used for electrical insulation. All of the G10 pads, Blasa wood spacer and the polyester sheets are stuck to the WC anvils with the Loctite 495 superglue. A type-K thermocouple is used to measure the temperature on the WC anvils.
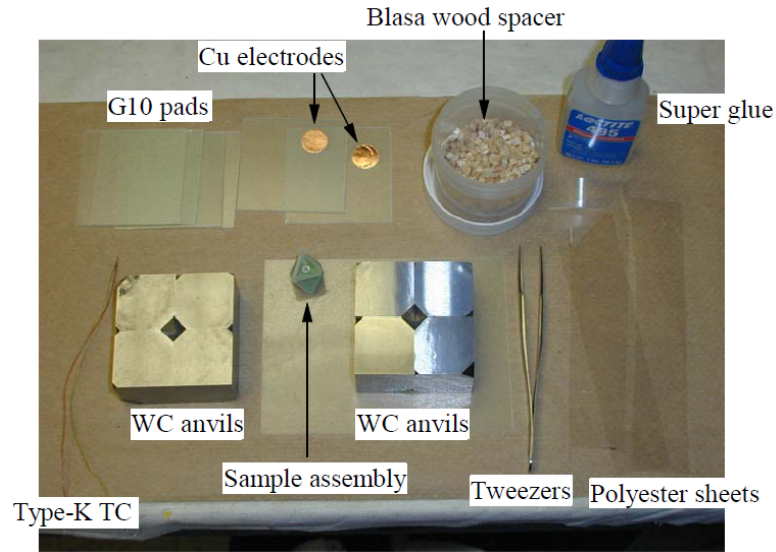
Figure 3.24: Required materials for a HPHT experiment.

Step 2: Glue the polyester insulation and Blasa wood spacer according to Fig. 3.25. The principle is that there should be both polyester insulation and Blasa wood spacer between the 12 interfaces of the WC anvils. For the sake of clarity, I have marked the three surfaces cut by the truncated corner with numbers 1, 2, 3. In practice, it is not necessary to do so.
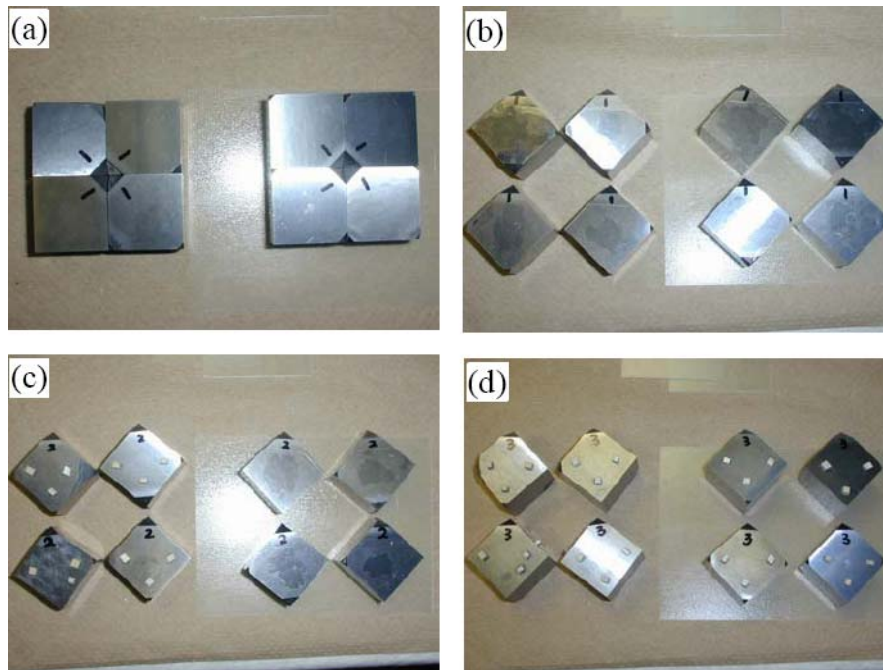
Figure 3.25: Glue the polyester insulation and Blasa wood spacer to the WC anvils.

Step 3: Assemble the WC anvils into a cube according to Fig. 3.26. Remember to mark the two WC anvils that are connected to the opposite ends of the heater inside the pressure medium. The Cu electrodes inside the G10 pads should also fall onto these two anvils. A type-K thermocouple is attached to a WC anvil in a position that is close to the octahedral pressure medium.
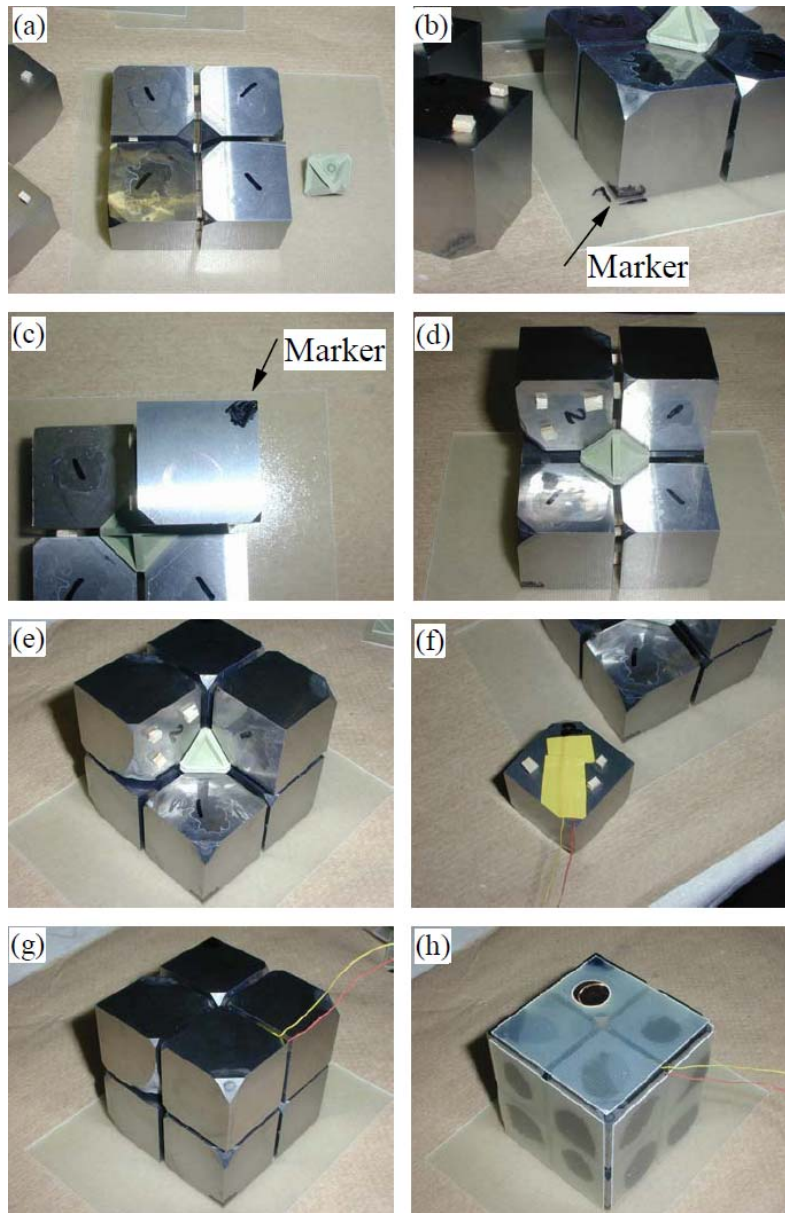
Figure 3.26: Assemble the WC anvils into a cube.

Step 4: Load the WC anvil cube into the pressure chamber according to Fig. 3.27. (a) After thoroughly cleaning the containment ring, T9 is applied to its inner wall, which is then coated with a layer of 0.002″ glossy polyester sheet with the dimensions

22.98 ″× 5 ¼″. (b, c) Remove the air bubbles beneath the polyester sheet and spray PTFE mold-release agent. (d) Put the three bottom wedges into the containment ring carefully. Their outer and bottom surfaces are glued with a layer of 0.002″ polyester sheets except for one wedge whose bottom surface is covered by a layer of copper sheet. Mark this wedge. (e) The interfaces between the wedges are filled with G10 pads. (f) Put the WC anvil cube on top of the three wedges with one Cu electrode facing the wedge having a copper sheet at the bottom. Connect the Type-K thermocouple wires to the connecter. (g) Put the top three wedges with the one having a copper sheet facing another Cu electrode. Insert the G10 pads between the wedges and put the big O-ring on top of the containment ring. (h) Cover the containment ring with the top pressure distribution plate. Push the whole module on the aluminum plate in between the rams of the hydraulic press and lock its position by inserting the two retaining pins into the holes on the bottom plate. Remember to loose the two screws, one in the front and another in the back as marked by the red arrow, in order to prevent damaging the wheels at the bottom of the aluminum plate carrier.
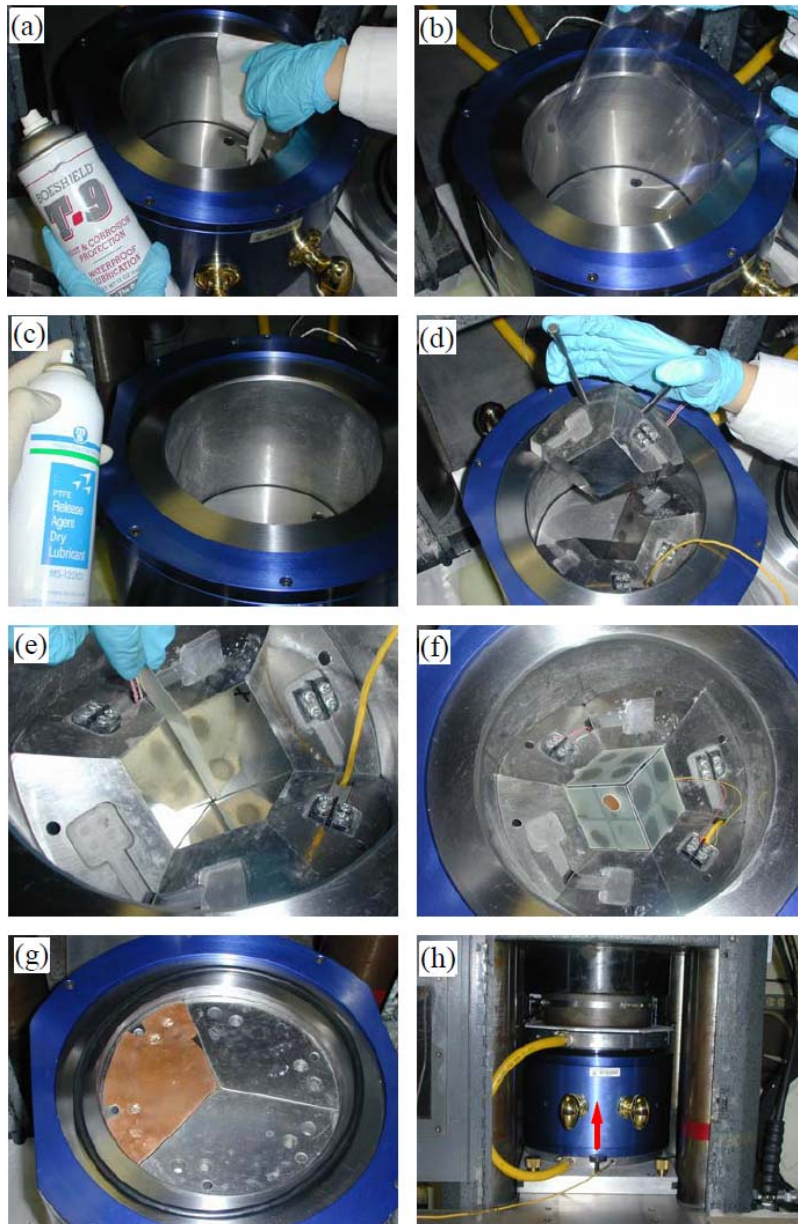
Figure 3.27: Procedures of loading the WC cube into the pressure chamber.

Step 5: Start the monitoring program. Double click the "TempPressLog.vi" on the desktop to open it as shown in Fig. 3.28. The input values are the following:

(1) GPIB K197: 11;

(2) Voltage range (Gauge): 2V;

(3) OPC Server Name: Eurotherm.ModbusServer.1;

(4) Item Name-Read: COM1.ID001-2404.Operator.Main.PV;

(5) Update rate (ms): 1000;

The temperature in °C and loading force in US Tons will be displayed once the program is started. Sometimes, the communication between the Eurotherm 2404 temperature controller and the PC should be established with the iTools software, which is initiated as follows:

(1) Start "iTools" by following the path: "Start" → "All Programs" → "Eurotherm iTools Advanced" → "iTools OPC server";

(2) Select "Start one-shot scan" in the "Network"; "ID001-2404" will appear under COM1;

(3) After selecting "Monitor" in the "Network", "Main", "PV", and "tsp" values will appear under "Operator".
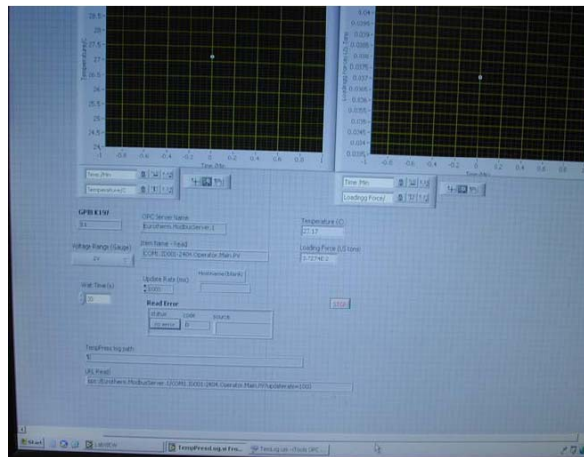
Figure 3.28: LabView program to log temperature and pressure during the HPHT
          experiments: TempPressLog. vi.

Step 6: Start pressure. Before starting pressure, make sure the valve A in Fig. 3.29(a) is open. Push the green "Start" button, Fig. 3.29(b), to start the fast pump of the hydraulic press; close the valve B gradually to advance the main ram until the gap between the top plates of the module and the press is closed. Then, quickly close the valve A and the fast pump and then switch to the pressure control system. Finally, set the target pressure point in the View Panel, (c), and start increasing pressure in the Auto mode, (d). The motor speed should be lowered gradually with increasing pressure; it should be as slow as 54 RPM when reaching 8-10 GPa.

Figure 3.29: Procedures to increase pressure.

Step 7: Start temperature. After reaching the target pressure, it is ready to deliver current to the heating element. As shown in Fig. 3.30, switch the OUTPUT to 12 V and push the green illuminated START TEMPERATURE button and then turn HEAT

selector switch to ON with HEAT ADJUST potentiometer turned to 100%. Manually increase the heat percent by using the up-arrow at the right bottom of the Eurotherm 2404 display to the value corresponding to the calibrated temperature. After heating 30 to 60 min, quench the HPHT experiment by turning the HEAT ADJUST from 100% to 0% and turning off the HEAT selector.

Figure 3.30: Temperature control panel.

Step 8: Release pressure. This process should be as slow as possible, especially at high pressures, in order to prevent blowout. Retracting the piston of the pressure control system all the way down until the bottom limit switch is triggered. Then, open the valve A and B to finally lower the ram by draining the oil into the external tank.

Step 9: Recover the sample.

Step 10: Vacuum clean the pressure chamber and prepare the WC anvils for the next experiments.

3.1.7 Blowouts

Although the intrinsic defect and stress can limit the lifetime of the WC anvils, blowout is the most disastrous cause of the failure of the anvils. In some cases, as many as eight anvils can break. Figure 3.31 shows some broken WC anvils. There are several situations that can result in blowouts.

(1) Pressure is too high to be sealed by the gaskets. Every design of the high-pressure setup has a pressure limit. Avoiding running the experiments beyond the limit can reduce the chance of a blowout. For the castable octahedra made of Ceramacast 584 powder and having TEL = 8 mm, the pressure limit is ~12 GPa as observed by most multianvil users. We have only run one high-pressure experiment exceeding 12 GPa successfully with this kind of octahedron. On the other hand, improving the gasket or configuration is another way to prevent blowout. At pressures higher than 10 GPa, pyrophyllite is the best material for gasketing because it is softer than the ceramic materials. The drawback is that the pressure efficiency is low with the soft pyrophyllite gaskets. Thus, it is recommended to heat the pyrophyllite properly, *e.g.* at 500°C for 15 hours.

(2) Initial gaps among the WC anvils are not uniform. Even though we have used the Blasa wood spacer to confine the initial gaps among WC anvils, an irregular shape of the octahedral pressure medium or some artificial factors can result in non-uniform gaps. In this case, the octahedron will not be pressurized uniformly. The uneven movement

between anvils produces fins with different thicknesses and a blowout takes place easily from the thinner fins. In some cases, flowing of the pressure-medium can mess up the internal sample assembly; disturbing the furnace to give a wrong temperature reading if measuring with the calibrated output power, and squeezing out the BN or graphite into the fins will increase the chance of gasket failure. Therefore, it is very important to make sure that the initial gaps among the WC anvils are uniform and that the octahedra have fins of very close thicknesses.

(3) Contamination of the fins. In the course of preparing the sample assembly, it is very easy to leave BN or graphite powders on the fins. Since the gasketing relies on the friction between the fins and WC anvils, the contamination by some good lubricants like BN and graphite powders reduces the friction and thus the capability of sealing. Therefore, it is important to clean carefully the fins after finishing the sample assembly.

Figure 3.31: Examples of failed WC anvils.

3.2 MEASUREMENT METHODS

3.2.1 Powder X-ray diffraction

The powder X-ray diffraction (XRD) was used to exam the phase purity and to determine the crystal structure. The XRD patterns were collected at room temperature in a Philips X'pert diffractometer equipped with a pyrolytic graphite monochromator and Cu Kα radiation ($\lambda = 1.54059$ Å). Samples were ground into fine powder and coated onto a glass slide with amyl acetate. Silicon was used as the internal standard if necessary. For a routine scan, the XRD pattern is measured from 15° to 80° in 2θ with a step of 0.04° and a dwell time of 2 seconds; while for the purpose of structural refinement, the XRD data were collected from 10° to 120° in 2θ with a step of 0.02° and a dwell time of 10 seconds. The XRD data were analyzed with the program JADE and/or FULLPROF.[70]

3.2.2 Electrical resistivity measurement

Low-temperature resistivity measurements in the interval 4 K < T < 320 K were performed with a four-probe technique on specimens with a rectangular geometry having typical size of $0.5 \times 0.5 \times 3$ mm^3. Four pieces of copper wire are attached to the surface of the specimen via an Indium pad or silver epoxy; the inner two copper wires pick up the voltage while the other two apply a small current. The specimen is mounted on a small piece of mica glass with a very small amount of thermal compound. The whole assembly is put on a round, thin sheet of copper with a copper cap to shield it. The cooling system is a closed-circle refrigerator with He gas as refrigerant. A Lakeshore silicon diode temperature sensor is put on the cooling head. Temperature is monitored and controlled by a Lakeshore temperature controller Model 340. Current is provided with a Keithley Model 224 Current Source and voltage is recorded with a Keithley 181 nanovoltmeter.

Data are recorded under GPIB control of these instruments with a personal computer. To eliminate the contribution of the contact and thermoelectric potentials, voltage is recorded with +/- current at each sampling point.

3.2.3 Thermoelectric power measurement

Thermoelectric power measurements were performed on a home-made setup diagramed in Fig. 3.32. Specimens are mounted between two brass heater stages, each controlled independently by a Lakeshore Model 304 Temperature Controller with DT-470 sensing diodes. The stage is sheltered in a Styrofoam canister and submerged into a liquid-nitrogen Dewar for a measurement to 80 K. The probe is placed in a liquid-helium Dewar if the measurement down to 10 K is required. In a typical run, a constant temperature gradient $\Delta T = 2$ or 4 K is used over the entire temperature range. Without considering the contribution to the thermoelectric power from the copper leads, the thermoelectric power of the specimen is:

$$\alpha = \frac{\Delta V}{\Delta T} = \frac{\Delta V_1 - \Delta V_0}{\Delta T_1 - \Delta T_0} \tag{3.1}$$

However, after making correction for the copper-lead contribution, the thermoelectric power of the specimen becomes

$$\alpha = \alpha_{Cu} - \frac{\Delta V}{\Delta T} = \alpha_{Cu} - \frac{\Delta V_1 - \Delta V_0}{\Delta T_1 - \Delta T_0} \tag{3.2}$$

where α_{Cu} is the thermoelectric power of the copper lead .
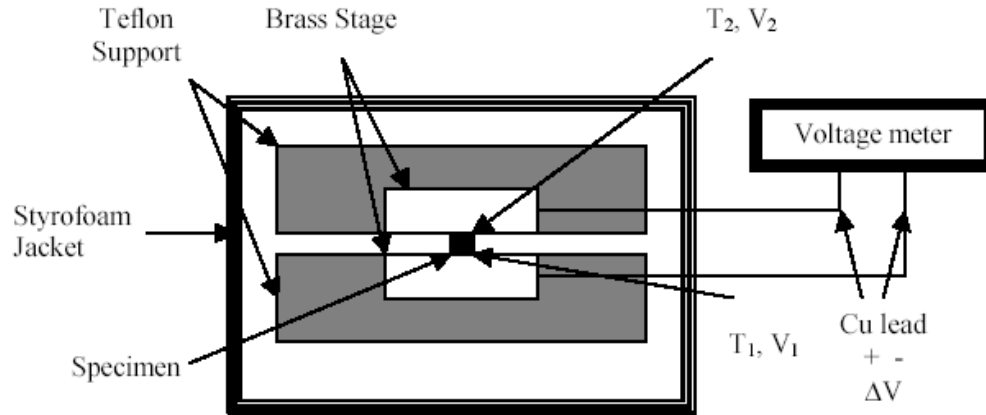
Figure 3.32: Schematic diagram for the measurement of thermoelectric power.

3.2.4 Thermal conductivity measurement

The thermal conductivity was measured with a steady-state longitudinal heat flow method. The principle of the measurement lies with passing a heat flux through a known sample and an unknown sample and comparing the respective thermal gradients, which will be inversely proportional to their thermal conductivities. As shown in Fig. 3.33, thermal conductivity can be obtained with the following equation for adiabatic conditions

$$\kappa = -\frac{q\Delta x_s}{A_s \Delta T_s} = -(\frac{\kappa_r . A_r . \Delta T_r}{\Delta x_r}).\frac{\Delta x_s}{A_s . \Delta T_s} \tag{3.3}$$

where κ is the thermal conductivity, q is the heat flow, Δx is the distance between thermal couples on reference (r) or sample (s), ΔT is the temperature difference along the heat flowing direction across a distance Δx on reference (r) or sample (s), A is the cross-section area of reference (r) or sample (s). The heater is a gold cap wrapped with a thin insulator-coated manganin wire; heat flow is controlled by the current applied to the resistance wire. The reference is a piece of constantan alloy with uniform diameter of

75

0.19 mm^2. Differential thermal couples, a pair of a copper wire and a constantan wire, are glued to the reference and sample with Lake Shore silver epoxy or Stycast epoxy; superglue is used to glue the thermal couples onto the sample with a high electrical conductivity. The resolution of the thermocouples is 0.1 K. Specimens measured are usually rectangular bars with a typical size of 0.5 × 0.5 × 2.5 mm^3. The sample holder was enclosed by a radiation shield of Cu that was thermally anchored to the cold head. The whole sample chamber was evacuated to 1×10^{-6} Torr by a turbo pump (Edwards, EXC 120). The temperature range for the measurement is from 4 K to 320 K. The cooling system, temperature monitor and controller, current supply, and voltage pickup are the same as those used for the electrical resistivity measurement.

1. Thermal sink
2. Specimen
3. Reference
4. Heater
5. Differential thermal couple
6. Copper wire
7. Six-pin connector
8. Two-pin connector to heater
9. Four-pin connector in the cool head
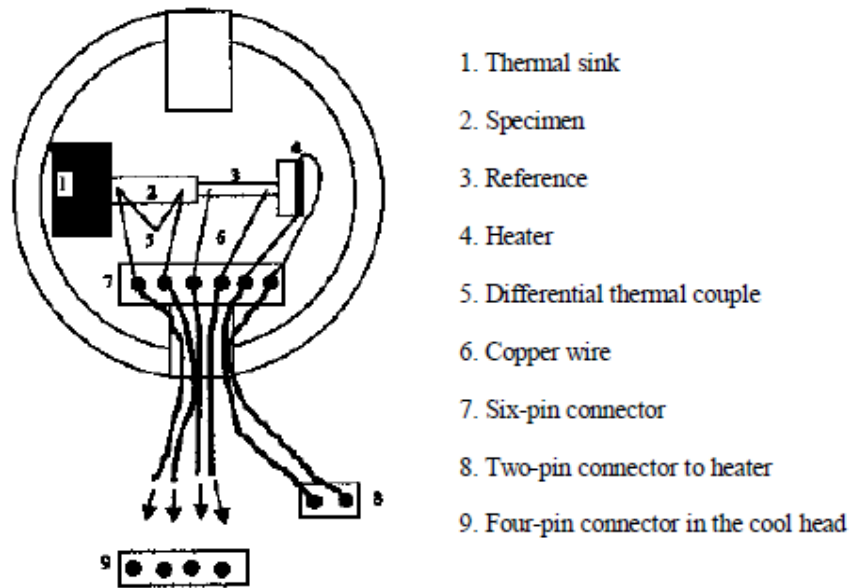
Figure 3.33: Schematic diagram of sample installation for thermal conductivity measurement.

The inevitable lateral heat loss would cause measuring errors at high temperatures. But it is not a major problem for our measurements below room temperature and under high vacuum as well as with the protection of a Cu shield. The measuring error, ~ 20%, mainly comes from the geometrical measurement of the specimen, the distance between thermocouples on both the reference and specimen.

3.2.5 Magnetic properties measurement

Magnetic properties are measured with a SQUID (Quantum Design) magnetometer in the temperature interval 2 K < T < 750 K at magnetic fields from −5 T to 5 T. A miniature Cu-Be cell fitting into the SQUID magnetometer is used to measure magnetization under high pressure. A piece of Pb as the pressure manometer, the sample, and a mixture of 3M Florinert FC77+FC72 as pressure medium are sealed in a Teflon capsule.

Chapter 4 Anomalous ferromagnetism in the perovskite ruthenates $ARuO_3$ (A = Ca, Sr, Ba)

4.1 INTRODUCTION

The orthorhombic perovskite $SrRuO_3$ is a metallic ferromagnet with $T_c \approx 164$ K, whereas the counterpart $CaRuO_3$ does not show any magnetic ordering down to the lowest temperature. The unusual disappearance of ferromagnetism in $SrRuO_3$ upon Ca^{2+} doping has been a subject of extensive investigations since forty years ago.[12-14, 23, 71, 72] As a representation of currently popular models about the disappearance of ferromagnetism in the $Sr_{1-x}Ca_xRuO_3$ system, Mazin and Singh [14] have calculated the band structure taking into account the cooperative $RuO_{6/2}$ site rotation that bends the Ru-O-Ru bond angle from 163° in $SrRuO_3$ to 148° in $CaRuO_3$; they found that the increased bending of the Ru-O-Ru bond angle reduces the band degeneracy and, therefore, the density of electronic states at the Fermi energy $\rho(\varepsilon_F)$, perhaps to where the Stoner criterion is no longer valid in $CaRuO_3$. This model predicts that the maximum T_c will be achieved as the high symmetry cubic structure is approached since a higher $\rho(\varepsilon_F)$ is created at high-symmetry points in the Brillouin zone.[14] However, this viewpoint was challenged recently after the successful synthesis of the cubic $BaRuO_3$ perovskite under 18 GPa and 1000°C,[11] which makes available the complete magnetic phase diagram of T_c versus the average A-cation radius $\langle r_A \rangle$ in the perovskite ruthenates $ARuO_3$ (A= Ca, Sr, Ba). As shown in Fig. 4.1, T_c peaks out at $SrRuO_3$; both substitutions of smaller Ca^{2+} and larger Ba^{2+} for Sr^{2+} lead to a reduction of T_c in the $Sr_{1-x}Ca_xRuO_3$ and $Sr_{1-y}Ba_yRuO_3$ systems. On the side of Ca^{2+} doping ($r_A < r_{Sr}$), T_c decreases quickly and reaches zero near $x \approx 0.7$ and the inverse susceptibility $\chi^{-1}(T)$ is characteristic of a Griffiths' phase.[73] On the side of Ba^{2+} doping

($r_A > r_{Sr}$), T_c decreases gradually and reaches 60 K for the cubic $BaRuO_3$. All compositions of $Sr_{1-y}Ba_yRuO_3$ ($0 \leq y \leq 1$) show a typical Curie-Weiss behavior at $T > T_c$. The suppression of T_c upon Ba^{2+} doping, which increases the Ru-O-Ru bond angle from 163° to 180°, clearly contradicts the prediction of Mazin and Singh.[14] Taking into account the sharply different $\chi^{-1}(T)$ behaviors of the $Sr_{1-x}Ca_xRuO_3$ and $Sr_{1-y}Ba_yRuO_3$ systems, the magnetic phase diagram has been interpreted in the context of a Griffiths' phase on the Ca side and of bandwidth broadening on the Ba side.[11] However, it should be noted that changing $<r_A>$ by substituting Ca^{2+} or Ba^{2+} for Sr^{2+} inevitably introduces an A-cation size variance $\sigma^2 = (<r^2_A> - <r_A>^2)$.[17-19] As discussed in chapter 2.3.2, introducing σ^2 can suppress linearly both the ferromagnetic Curie temperature in CMR manganites [20] and the critical temperature in A_2CuO_4 superconductors[21, 22] with constant doping level and mean A-cation radius. Therefore, the magnetic phase diagram of the perovskite ruthenates cannot be comprehensively understood before the effect of size variance is clarified.

With respect to the nature of the ferromagnetism in $SrRuO_3$, itinerant-electron ferromagnetism has been widely believed to be plausible;[23] the supportive evidences include: (1) a sample-dependent saturation magnetization lower than the spin-only 2 μ_B/Ru^{4+}, (2) the observation of mean-field critical behavior, *i.e.* nearly parallel linear lines in the Arrott plot M^2 *vs* H/M, and (3) the metallic conductivity. However, the nature of itinerant-electron ferromagnetism in perovskite ruthenates becomes questionable when making a comparison between the critical behaviors of $SrRuO_3$ and $BaRuO_3$. As shown in Fig. 4.2, their critical isotherms behave differently. The Arrott plot of $SrRuO_3$ shows nearly parallel straight lines, consistent with the mean-field critical behavior expected from the Stoner-Wohlfarth itinerant-electron ferromagnetism as discussed in chapter

2.3.1. However, a series of uniform curves with concave curvature is evidenced in the Arrott plot of $BaRuO_3$; nearly linear lines can be restored in a modified Arrott plot with critical exponents belonging to the 3D Heisenberg universal class,[25] implying a localized-electron ferromagnetism. The critical fluctuations in $BaRuO_3$ are significantly enhanced under external pressure.[25] As the bandwidth broadens from $SrRuO_3$ to $BaRuO_3$, it does not make sense to attribute itinerant-electron ferromagnetism to $SrRuO_3$ and localized-spin ferromagnetism to $BaRuO_3$. In addition, the unusually high saturation magnetization of $SrRuO_3$ at the lowest temperature, 1.4-1.6 μ_B/Ru^{4+}, is clearly beyond the criterion of very weak itinerant-electron ferromagnetism.[24, 60] Moreover, a novel critical exponent, which does not belong to any current universality class, has been recently reported in the $Sr_{1-x}Ca_xRuO_3$ system.[26] Thus, the nature of the ferromagnetism in the perovskite ruthenates remains unclear.

Therefore, studies of the evolution of magnetic properties of the system $Sr_{1-x}Ca_xRuO_3$ and the high-pressure system $Sr_{1-y}Ba_yRuO_3$ have left unsolved what determines the optimal magnetization and T_c of perovskite ruthenates and whether an itinerant-electron ferromagnetism model is applicable. Here we address all these issues with a systematic study of the effect on T_c and the isothermal magnetization on crossing T_c of the mean A-cation radius and size variance, of hydrostatic versus non-hydrostatic pressure, and of high-pressure synthesis. We conclude that local lattice strains and disorder are the dominant factors determining the magnitude of T_c and that the ferromagnetism of the perovskite ruthenates is associated with localized spins interacting by the Heisenberg model.
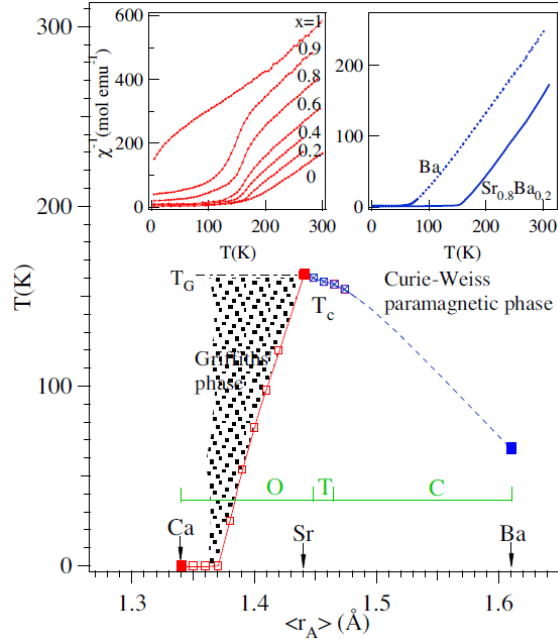
Figure 4.1: Phase diagram of the magnetic transition temperature versus the average A-site cation radius $\langle r_A \rangle$ for $Sr_{1-x}Ca_xRuO_3$ and $Sr_{1-y}Ba_yRuO_3$. Inset shows the temperature dependence of inverse susceptibility of these two systems. (After Ref. 11)
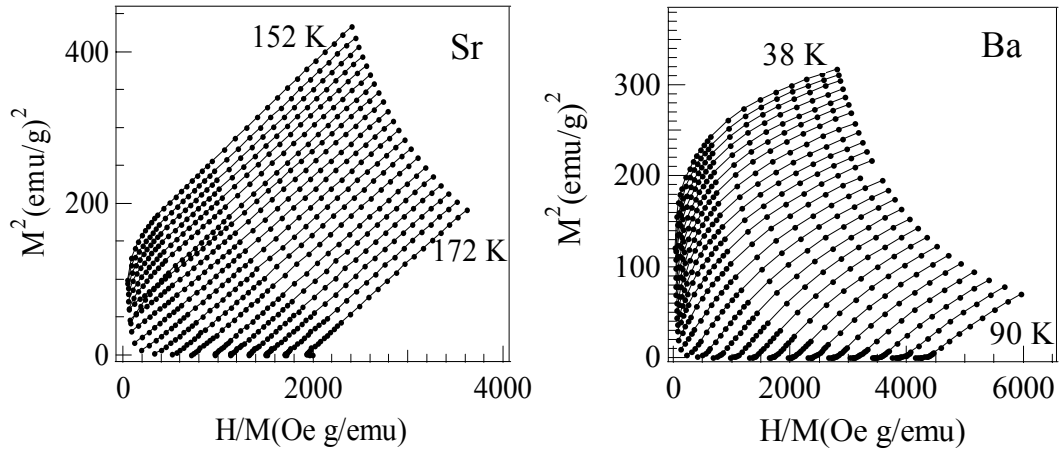
Figure 4.2: Arrott plots of $SrRuO_3$ and $BaRuO_3$ perovskites.

4.2 EXPERIMENTAL DETAILS

All samples in this study were made with starting materials ACO_3 (A = Ca, Sr, Ba) and RuO_2. The well-mixed starting materials were sintered at temperatures 800-1100°C in air with several intermediate grindings. This procedure produced a single phase with the orthorhombic perovskite structure for all compositions of $Sr_{1-x}Ca_xRuO_3$. However, a small amount 9R-phase $BaRuO_3$ was found in all compositions with a Ba component if the synthesis was made under ambient pressure. For these samples, high-pressure synthesis under 3-11 GPa and 1000 °C is required in order to obtain a single phase with perovskite structure; it was carried out in a Walker multianvil module (Rockland Research Corp.). A size variance was introduced into these samples by substituting $(Ca_{.51}Ba_{.49})$ for Sr.

The X-ray powder diffraction was performed with a Philips X'pert diffractometer and the Rietveld refinement on these diffraction spectra was made with FULLPROF.[70] Magnetic properties of the ruthenates were measured in a SQUID magnetometer (Quantum Design). High pressure was created in a home-made self-clamping BeCu cell that fits the chamber of a commercial SQUID magnetometer. Pressure inside the high-pressure cell was checked by the superconductive transition in a small piece of lead. We used two pressure mediums, silicone oil and 3M Fluorinert FC77 +FC72. No noticeable broadening of the superconductive transition was found with these two pressure media. However, these pressure media cause a significant difference of magnetization in the ruthenates. A non-hydrostatic component is generally higher in the silicone oil than in 3M Fluorinert liquid. The sample's demagnetization factor is determined by the magnetization at low field. However, subtraction of the demagnetization field from the external field H_0 does not influence the output of the Arrott plot, so this correction has

not been made in our plot. The correction becomes impossible for measurements with a high-pressure cell since the magnetization at low field includes some contribution from the cell.

4.3 RESULTS AND DISCUSSIONS

4.3.1 Crystal structure
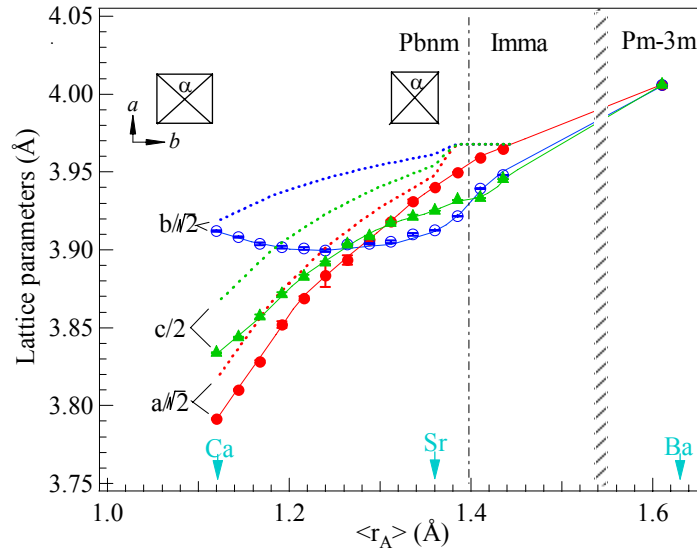
Figure 4.3: Lattice parameters versus the mean A-cation size of perovskites $ARuO_3$. Insets are schematic drawings of the octahedra with $\alpha \approx 90°$ for the compositions with $b > a$ and the octahedra with $\alpha < 90°$ where $b < a$ occurs. Dashed lines are the lattice parameters predicted by using the software SPuDs.[74]

The perovskites $ARuO_3$ undergo a series of phase transitions from the orthorhombic phase with space group *Pbnm* to another orthorhombic phase (*Imma*) and finally to the cubic phase ($Pm\bar{3}m$) as the A-cation size increases from Ca to Ba. In the first orthorhombic phase, the cooperative octahedral-site rotation, which is primarily around the *b* axis of the orthorhombic cell, results in $b > c/\sqrt{2} > a$ for rigid $RuO_{6/2}$

octahedra. The evolution of lattice parameters as a function of the average A-cation size $\langle r_A \rangle$ can be well simulated by the software SPuDs [74], which is shown by dashed lines in Fig. 4.3. The program no longer works where the geometric tolerance factor is t > 1. While the composition $Sr_{0.9}Ba_{0.1}RuO_3$ has the orthorhombic structure, the program predicts a cubic phase for this composition. The problem is that the valance sum values of both Sr^{2+} and Ba^{2+} cations used in the SPuDs are slightly larger than their actual size in crystals.

As illustrated systematically in the $A^{3+}M^{3+}O_3$ perovskites,[47] *b* decreases from the prediction of the SPuDs program as the A-cation size r_A passes a critical value and eventually crosses *a* as r_A further increases. The same situation occurs in $A^{2+}Ru^{4+}O_3$ as is shown in Fig. 4.3. The anomalous lattice parameters are due to the octahedral-site distortion with an α angle less than 90°. There are two important consequences due to this kind of octahedral-site distortion: (a) the formula [46] for calculating the (180° -ϕ) Ru-O-Ru bond angle based on lattice parameters is no longer valid; (b) since the t-orbital degeneracy is lifted by the distortion, the orbital angular momentum of the localized t^4e^0 configuration on the octahedral-site Ru^{4+} is quenched.

4.3.2 The lattice effect on T_c

The A-cation substitution in the perovskite ruthenates introduces a mixture of two effects, a change in the average radius of the A-cation $\langle r_A \rangle$ and the introduction of a size variance $\sigma^2 = \langle r^2_A \rangle - \langle r_A \rangle^2$. Without consideration of the size-variance effect, the phase diagram of T_c versus $\langle r_A \rangle$ of Fig. 4.1 shows that ferromagnetism in the ambient-pressure system $Sr_{1-x}Ca_xRuO_3$ sets in at $\langle r_A \rangle \approx 1.17$ Å (A= $Sr_{.3}Ca_{.7}$) and T_c increases monotonically as $\langle r_A \rangle$ increases until $r_A = r_{Sr}$. In order to extract the sole effect of changing $\langle r_A \rangle$ on T_c,

84

the size-variance effect on T_c must be determined first. It has not been made clear before this study how the size variance influences T_c and other properties of the ferromagnetic phase in the ruthenates. We used the following procedure to study the size-variance effect. The combination A= $(Ca_{.51}Ba_{.49})$ has the same $\langle r_A \rangle$ as r_{Sr} according to the tabulated ionic radii.[27] The substitution of $(Ca_{.51}Ba_{.49})$ for Sr in $Sr_{1-x}(Ca_{.51}Ba_{.49})_xRuO_3$ does not change $\langle r_A \rangle$, but it changes the size variance σ^2 depending on x. Compositions with a Ba component need to be synthesized under pressure regardless of their $\langle r_A \rangle$. In order to have all samples made under the same conditions, we have also made $SrRuO_3$ by high-pressure synthesis. T_c of the high-pressure-synthesized (HP) $SrRuO_3$ increases by 4 K and the moment at 5 K reaches 1.6 μ_B under 5 T, which is equivalent to its value at 44 T for a sample prepared at ambient pressure.[75] As shown in Fig. 4.4, we have determined the T_c of the system $Sr_{1-x}(Ca_{.51}Ba_{.49})_xRuO_3$ prepared under pressure from the minimum of $d\chi/dT$; T_c *vs* σ^2 follows well Eq. (2.17), *i.e.* $T_c = T_c^0 - p\sigma^2$. As shown in Chapter 2.3.2, a similar procedure has been applied to determine the effect of σ^2 on the superconductive transition temperature T_c of the copper oxides and the ferromagnetic Curie temperature T_c of the perovskite manganites exhibiting the colossal magnetoresistance phenomenon.[17-19] The superconductive transition at T_c in the copper oxides and the CMR phenomenon in the manganites are each found where there is a crossover from localized to itinerant electronic behavior, so it is particularly noteworthy that in both cases T_c is sensitive to the bond-length disorder as described by $T_c = T_c^0 - p\sigma^2$ and the lattice sensitivity coefficients *p* for all these cases fall into a narrow range 2000 ~ 2500 KÅ^{-2}.
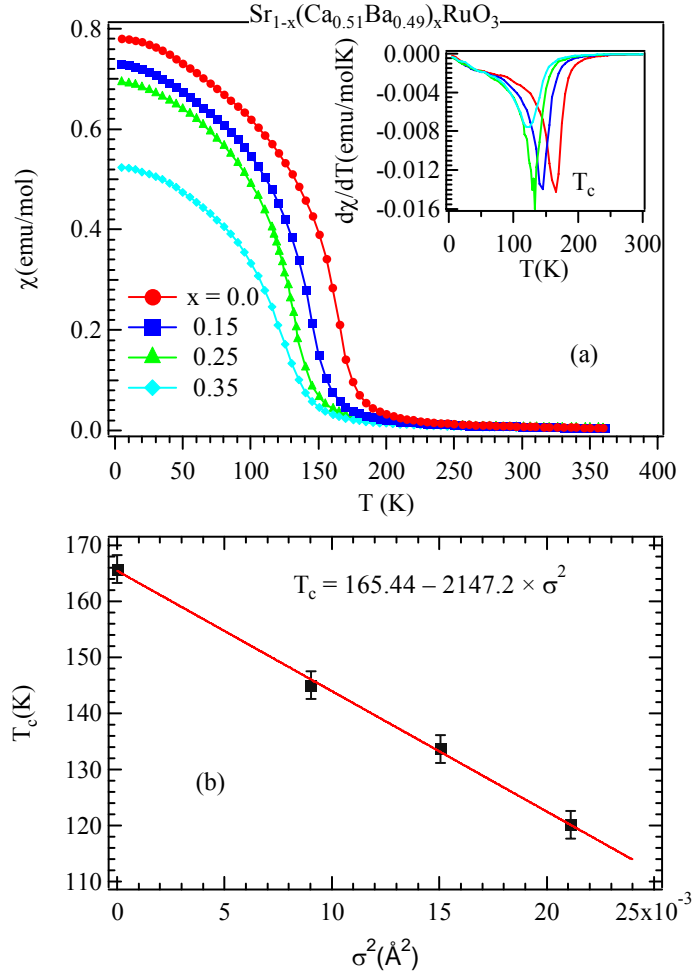
Figure 4.4: (a) Temperature dependence of the magnetic susceptibility $\chi(T)$ of the $Sr_{1-x}(Ca_{.51}Ba_{.49})_xRuO_3$ system. Inset shows that T_c is determined from the minimum of $d\chi/dT$. (b) Variation of T_c with size variance σ^2, which is fitted with Eq. (2.17).

The same procedure was used to determine the effect of A-site size variance on both sides of r_{Sr}. We have covered the $\langle r_A \rangle$ from $A = Sr_{.7}Ca_{.3}$ to $A = Sr_{.7}Ba_{.3}$ in this study. As shown in Fig. 4.5(a), for a given $\langle r_A \rangle$, T_c decreases linearly with σ^2; fitting to the formula $T_c = T_c^0 - p\sigma^2$ gives T_c^0 ($\sigma^2 = 0$) for a given $\langle r_A \rangle$. The fitting parameter p is slightly larger for $\langle r_A \rangle < r_{Sr}$ than for $\langle r_A \rangle > r_{Sr}$, The slope p for $A = Sr_{.7}Ba_{.3}$ was taken from that for $A = Sr_{.8}Ba_{.2}$ and p for $A = Sr_{.7}Ca_{.3}$ was from $A = Sr_{.9}Ca_{.1;}$ they are shown by

dashed lines in the plot. We show in Fig. 4.5(b) the T_c^0 versus $\langle r_A \rangle$ curve obtained from all the high-pressure samples prepared in this study together with a point for $BaRuO_3$ obtained from the previous report.[11] It is striking that the evolution of T_c^0 versus $\langle r_A \rangle$ matches well a formula for T_c reduction due to local lattice strains, *viz.* $T_c^0 = T_c^m - q(r_A^m - \langle r_A \rangle)^2$, in which T_c^m is the maximum T_c obtained for the r_A^m giving equilibrium (A-O) and (M-O) bond lengths.[21] Moreover, T_c^m in Fig. 4.5(b) is reached near the boundary between two orthorhombic *Pbnm* and *Imna* phases where the mean Ru-O-Ru bond angle jumps from 163° to 171°, *i.e.* to where the A-O and Ru-O bond lengths both approach their equilibrium values. The plot of T_c^0 versus $\langle r_A \rangle$ in Fig. 4.5(b) reveals, therefore, two remarkable features: (a) T_c is extremely sensitive to both lattice disorder and local lattice strains instead of the electron bandwidth; it reaches its maximum value where the disorder and local lattice strains are smallest, (b) T_c^0 vanishes at the same composition where T_c is totally suppressed by Ca doping in $Sr_{1-x}Ca_xRuO_3$.

An r_A size variance clearly introduces local, disordered bond-length strains. Where there is no variance, bond-length strains are introduced by a mismatch of the equilibrium (A-O) and (M-O) bond lengths. A measure of this mismatch is the geometric tolerance factor t. A t < 1 places the (A-O) bond under tension and the (M-O) bond under compression. Even though these stresses are relieved by a cooperative rotation of the octahedra to lower the symmetry from cubic, which bends the M-O-M bond angle from 180°, nevertheless octahedral-site and icosahedral-site distortions accompany these rotations to introduce local bond strains. These strains are minimal where the equilibrium bond lengths are most nearly matched at a t = 1 with cubic symmetry. A t > 1 as in cubic $BaRuO_3$ places the (A-O) bond under compression and the (M-O) bond under tension. In this case, the system can only relieve these bond-length strains by a displacement of the

M cation from the center of symmetry of its octahedral interstice as occurs in ferroelectric BaTiO$_3$ with empty d orbitals. But such a displacement is not stable for a Ru(IV): t^4e^0 cation. Therefore, the bond-length strains are present even though the cation octahedra and icosahedra are not distorted.
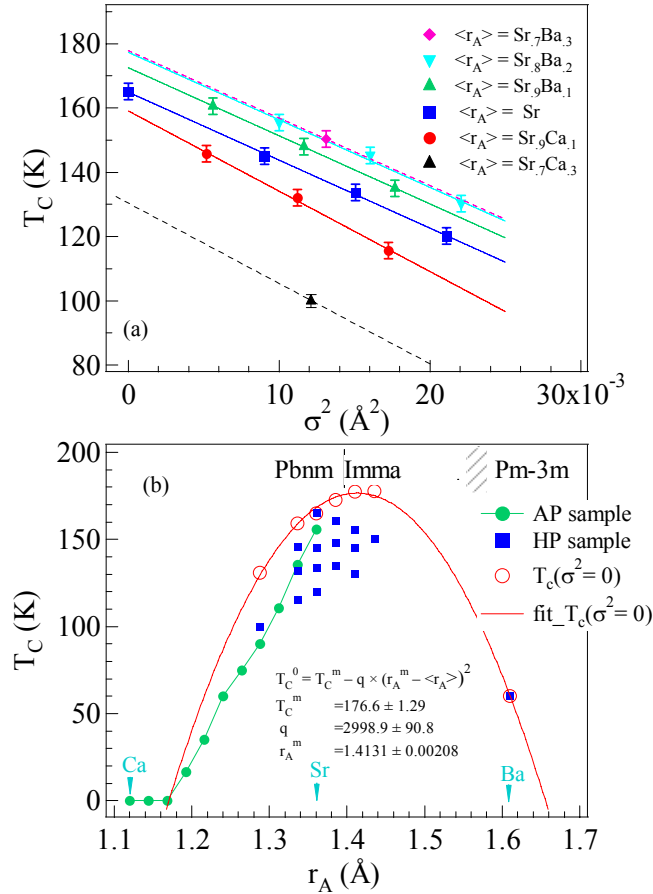
Figure 4.5:   (a) Variation of T_c with σ^2 covering A = Sr$_{.7}$Ca$_{.3}$ to Sr$_{.7}$Ba$_{.3}$ in this study. A linear fitting to the formula $T_c = T_c^0 - p\sigma^2$ gives $T_c^0 (\sigma^2 = 0)$ for a given $\langle r_A \rangle$. The slope p for A = Sr$_{.7}$Ba$_{.3}$ was taken from that for A = Sr$_{.8}$Ba$_{.2}$ and p for A = Sr$_{.7}$Ca$_{.3}$ was from A = Sr$_{.9}$Ca$_{.1}$; they are shown by dashed lines in the plot. (b) T_c *vs* $\langle r_A \rangle$ for all samples in this study were mapped out. Samples made under ambient pressure (AP) and those made under high pressure (HP) are distinguished by different symbols in the plot. $T_c^0 (\sigma^2=0)$ for each $\langle r_A \rangle$ obtained from the linear fitting in (a) are superimposed; these data points fit well the lattice strain formula: $T_c^0 = T_c^m - q(r_A^m - \langle r_A \rangle)^2$.

4.3.3 The lattice effect on magnetization

After clarifying the lattice effect on T_c, we now turn to the lattice effect on the magnetization in perovskite ruthenates. The isothermal M(H) curves were taken over a broad range of temperature around T_c with an interval $\Delta T = 2$ K for most typical ferromagnetic samples in the phase diagram of Fig. 4.5. As in the study of the lattice effect on T_c, we have distinguished the size effect and the size-variance effect on the magnetization in these samples. We first demonstrate in Fig. 4.6 the Arrott plot of M(H) of the samples covering all A-cation substitutions synthesized under high pressure. The ferromagnetic phase on the side of Ca substitution has a lower T_c and exhibits an unusual convex curvature of the Arrott plot. On the other hand, the Arrott plot of M(H) in $BaRuO_3$ shows more uniform lines with a concave curvature, which is typical for a Heisenberg ferromagnet.[25] In general, the convex curvature of the plots for the samples with $\langle r_A \rangle < r_{Sr}$ reduces as $\langle r_A \rangle$ increases; the concave curvature develops at high magnetic field in the plots for samples with $\langle r_A \rangle > r_{Sr}$. The balance between these two opposite curvatures occurs for the sample with $\langle r_A \rangle \approx r_{Sr}$ so that perfect linear lines in the Arrott plot were found. We have still left out the effect of the size variance in these plots. As a matter of fact, two obvious features in the plots evolve as $\langle r_A \rangle$ increases continuously with Ba substitution: (a) the curvature at high magnetic field is toward concave; (b) the curvature at low field is toward more convex. Since an overall concave curvature is seen in the plot of $BaRuO_3$ with $\sigma^2 = 0$, it is likely that the feature (a) is associated with increasing $\langle r_A \rangle$ whereas the feature (b) is caused by the size-variance effect. In order to confirm this conjecture, we have taken isothermal M(H) curves for a series of samples $Sr_{1-x}(Ca_{.51}Ba_{.49})_xRuO_3$ where σ^2 increases with increasing x while $\langle r_A \rangle \approx r_{Sr}$ has no change. Fig. 4.7 shows that increasing σ^2 converts nearly linear lines of the Arrott plot into curves with slightly convex curvature at low fields.
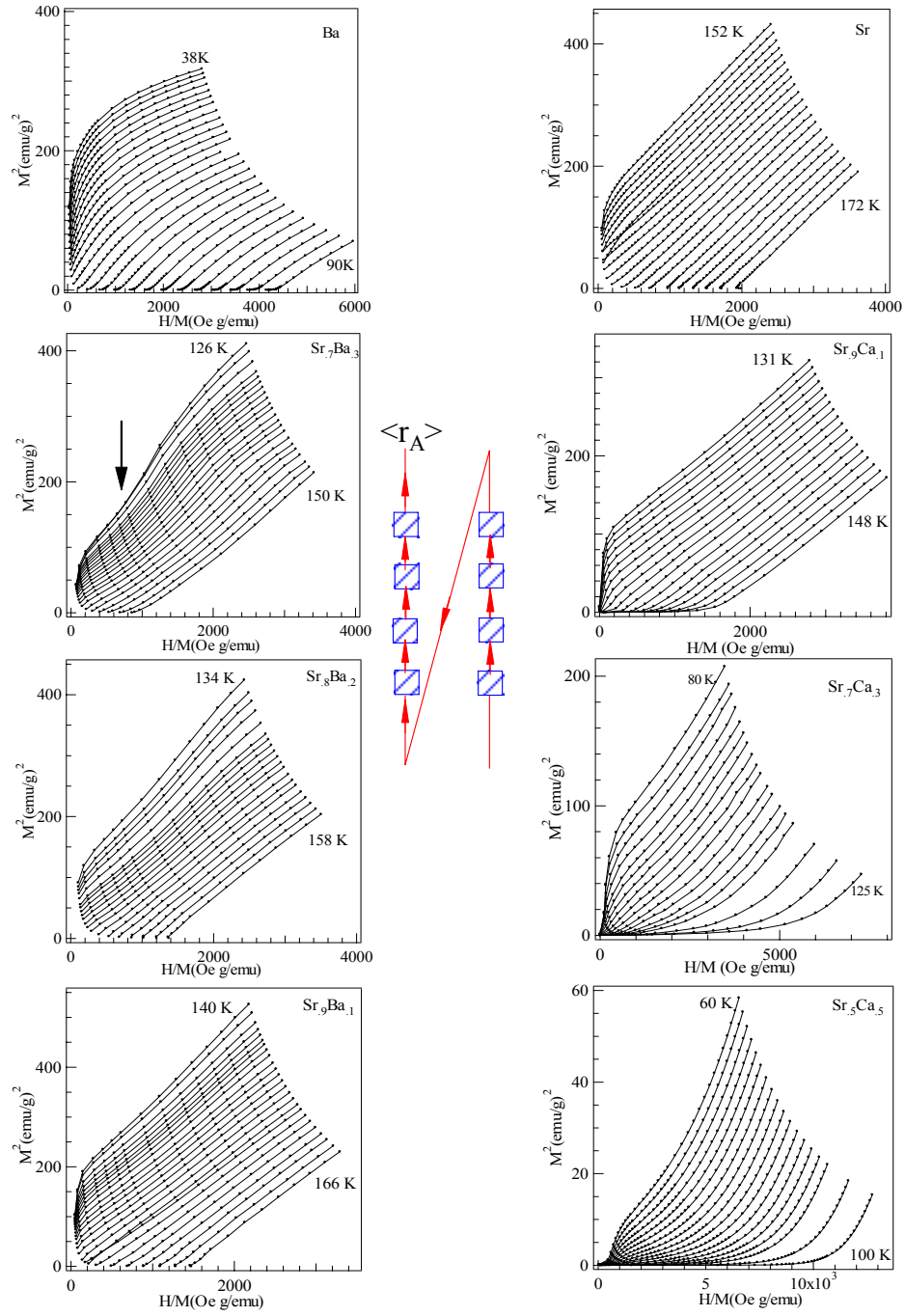
Figure 4.6:   Arrott plots M^2 *vs* H/M for perovskites $ARuO_3$ showing the effect of average A-cation size. These plots are organized according to their A-cation size in the order shown by the schematic diagram in the center of the figure.
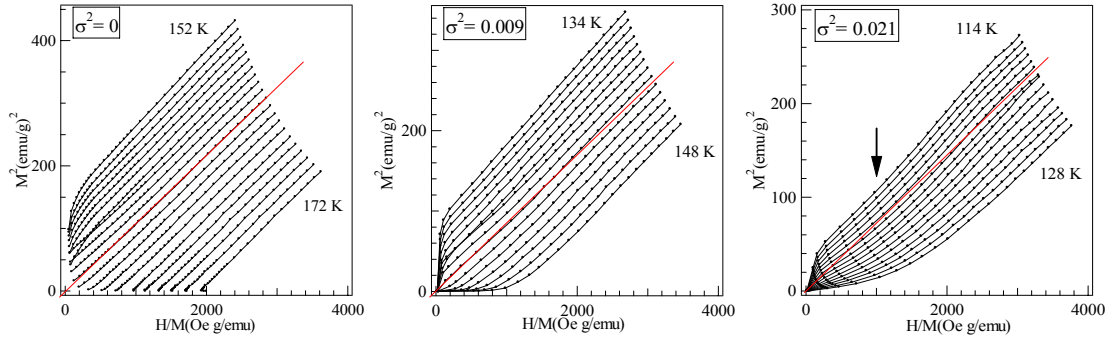
Figure 4.7:   Arrott plots M^2 *vs* H/M for $Sr_{1-x}(Ca_{0.51}Ba_{0.49})_xRuO_3$ showing the effect of size variance. These three samples have an identical $\langle r_A \rangle = r_{Sr}$ but different σ^2 as labeled inside each panel. Lines are a guide to the eyes. The linearity deteriorates as σ^2 increases.

4.3.4 The effect of high-pressure synthesis on magnetization

It is also important to discuss here the effect of high-pressure treatment. All samples used to demonstrate the effects of $\langle r_A \rangle$ and σ^2 on changing the curvature in the Arrott plot were synthesized under high pressure since the synthesis of the samples with a Ba component requires high pressure. We have also applied the same high-pressure synthesis in the samples of $Sr_{1-x}Ca_xRuO_3$ for a comparative study. All ceramic samples of $Sr_{1-x}Ca_xRuO_3$ made under ambient pressure (AP) show curves with generally convex curvature, but the convex curvature is significantly reduced in the high-pressure samples of the corresponding compositions. As shown in Fig. 4.8, the Arrott plot for the ambient pressure $SrRuO_3$ does not show linear lines at all. The plot for a single-crystal $SrRuO_3$ that was digitized from the literature[23] shows lines with a slightly convex curvature. Nearly perfect straight lines were only found in the plot for the high-pressure $SrRuO_3$. High-pressure synthesis brings about no change of lattice parameters in $SrRuO_3$, but it

leads to obvious changes of magnetic properties. It increases the saturation moment at 5 K and 5 T from about 1.2 μ_B to 1.65 μ_B. In summary, the Arrott plots in the perovskite ruthenates show a systematic change from curves with convex curvature to concave curvature as $\langle r_A \rangle$ increases and the curvature changes sensitively with the lattice disorder and the high-pressure treatment. Therefore, the linearity of the Arrott plot found for $SrRuO_3$ is due to a subtle balance between convex and concave curvatures and has little to do with a signature of itinerant-electron magnetism.
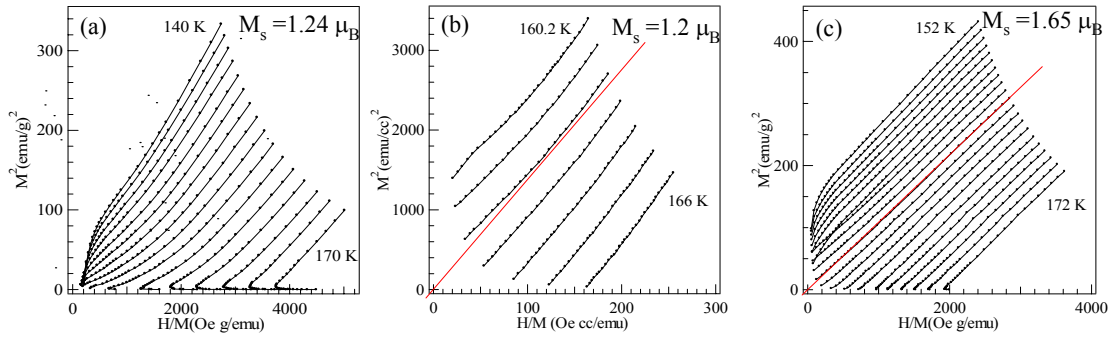
Figure 4.8:   The Arrott plot M^2 *vs* H/M for (a) the ambient-pressure $SrRuO_3$, (b) a single-crystal $SrRuO_3$ (after Ref. 23), and (c) the high-pressure $SrRuO_3$. Lines inside panels are the guide to eyes.

In order to elaborate further how high-pressure treatment can influence so dramatically the linearity of the Arrott plot although the treatment brings no change of σ^2 and $\langle r_A \rangle$, we have studied the crystal structure of these samples. X-ray powder diffraction indicates a very tiny change of the *b* axis and no changes of the *a* and *c* axes within the best resolution of our diffractometer between the AP sample and the HP sample. The major difference between these samples is the full width at half maximum (FWHM) of the diffraction peaks. The FWHM is much wider for the AP samples than the HP sample,

which indicates there is some bond-length disorder in the AP $SrRuO_3$ sample even though it has $\sigma^2 = 0$. Structural disorder and site distortion cause a convex curvature in the Arrott plot in ruthenates. We will further verify this argument by comparing the effect of hydrostatic versus non-hydrostatic pressure.

4.3.5 The pressure effect on T_c

The pressure effect on T_c of $SrRuO_3$ has been measured by several groups;[76-78] T_c decreases with a ratio $-dT_c/dP = 5–7$ K/GPa. However, no study of other magnetic properties under pressure has been made on this material. The primary motivation for us to carry out the high-pressure measurements on the ferromagnetic ruthenates was to answer whether a high-pressure study can help to distinguish localized- versus itinerant-electron magnetism. As shown in Fig. 4.9(a), the dependence of T_c on P for several samples covering the whole ferromagnetic compositional range of $ARuO_3$ is negative, and linear fits on these curves give a coefficient dT_c/dP that varies within a small range around -5 K/GPa. As shown in Fig. 4.9(b), the magnitude of $dlnT_c/dP$, however, jumps dramatically for the samples with $\langle r_A \rangle < r_{Sr}$ whereas it remains small and nearly identical for the other samples with $\langle r_A \rangle \geq r_{Sr}$. A negative pressure dependence of T_c is commonly seen in a single-valent ferromagnet. In Heisenberg ferromagnetic insulators, a negative sign of the pressure dependence is due to the exchange striction. The exchange striction reverses for antiferromagnetic coupling, which normally leads to a positive pressure dependence of T_N in single-valent antiferromagnetic insulators. In the case of itinerant-electron ferromagnetism, a negative pressure dependence can be predicted by analysis of the free energy of the magnetic equation of state,[79] and this conclusion holds for itinerant-electron ferromagnets $ZrZn_2$,[80, 81] $MnSi$,[82] Ni_3Al,[83] but not for Sc_3In [84] where a positive dT_c/dP was found. Therefore, the sign of the dT_c/dP does not provide a decisive

distinction between localized- and itinerant-electron magnetism and we have to turn to the magnitude of $d\ln T_c/dP$.

First of all, the A-cation size variance apparently is not a factor to influence the pressure dependence of T_c since $d\ln T_c/dP$ is nearly identical for $SrRuO_3$ and those with Ba substitution. It is interesting to note that $d\ln T_c/dP$ of these compositions is in line with that of other single-valent ferromagnetic perovskite insulators such as $BiMnO_3$, $LaMn_{0.5}Ga_{0.5}O_3$, $YTiO_3$. Since the bulk modulus varies within a small range for most perovskite oxides, the Bloch ratio $\alpha \equiv d\ln T_c/d\ln V$ for these ferromagnets is close to a constant. The Bloch ratio $\alpha \approx -3.3$ holds for most antiferromagnetic Mott insulators.[85] This rule can be rationalized through the perturbation formula of the superexchange interaction, which means T_N increases due to a gain of the orbital overlap integral under pressure. There appears to be no counterpart for ferromagnetic coupling. Nevertheless, a nearly identical α found in the ruthenates and ferromagnetic Mott insulators would suggest that the ferromagnetic coupling in the ruthenates reflects the presence of a localized-spin system. The increase of $|d\ln T_c/dP|$ for the compositions with $\langle r_A \rangle < r_{Sr}$ seems related to the peculiar magnetic phase with convex curvature of the Arrott plot. We will further elaborate on this problem in the discussion of the pressure dependence of the curvature. In contrast, we cite data for several typical itinerant-electron ferromagnets for comparison. The relation of T_c versus P is system-dependent; it is nearly linear only for $ZrZn_2$ whereas MnSi and Ni_3Al exhibit a curved T_c versus P that is close to the prediction of a model of band ferromagnetism. Although the pressure dependence of T_c in the ruthenates is somewhat different from that of band ferromagnets, we have no clear-cut evidence to distinguish whether the T_c versus P behavior of the ruthenates is typical of

itinerant-electron ferromagnetism based on these data. The change of M(H) under pressure presented below is critical to get insight into the problem.
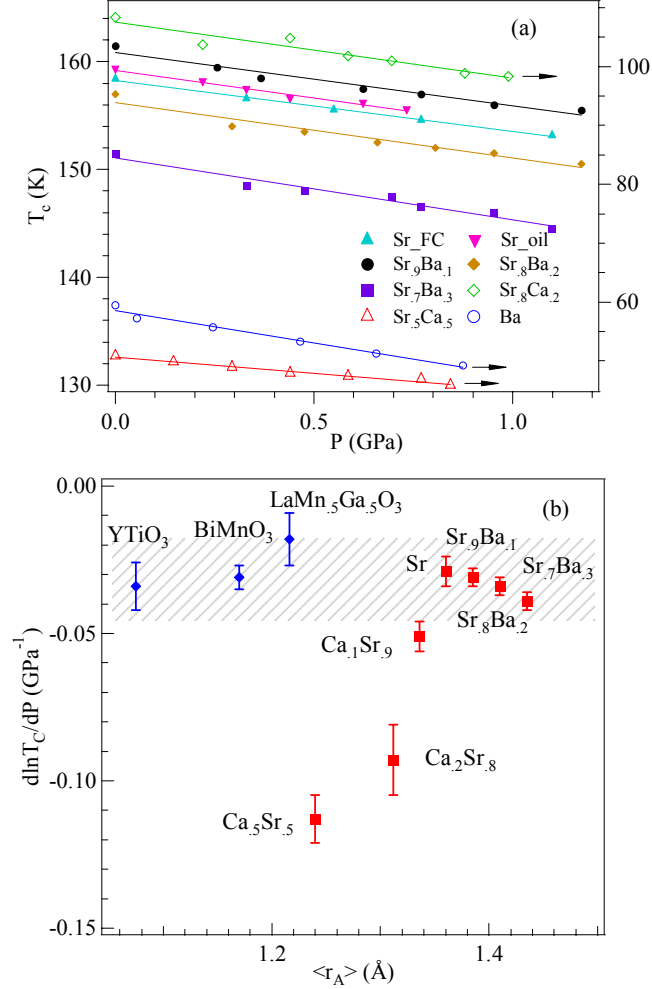
Figure 4.9:   (a) Pressure dependence of the ferromagnetic transition temperature T_c in the perovskites $ARuO_3$. All high-pressure measurements were carried out with silicone oil as the pressure medium. Two pressure media, silicone oil (oil) and a mixture of 3M fluorinert FC77 + FC72 (FC), were used for measurements of HP $SrRuO_3$ for comparison. $dT_c/dP = -4.9$ K/GPa and -5.1 K/GPa were obtained with FC and Oil, respectively. (b) The coefficient $dlnT_c/dP$ *vs* $\langle r_A \rangle$ for ferromagnetic metallic systems of $Sr_{1-x}Ca_xRuO_3$ and $Sr_{1-y}Ba_yRuO_3$ and ferromagnetic insulators $LaMn_{.5}Ga_{.5}O_3$, $BiMnO_3$, and $YTiO_3$.

4.3.6 The pressure effect on magnetization

In the discussion of the lattice effect, we have shown that the Arrott plot of M^2 *vs* H/M changes from convex to concave curvature as $\langle r_A \rangle$ increases from $\langle r_A \rangle < r_{Sr}$. Perfect straight lines in the Arrott plot were obtained in the HP SrRuO$_3$ sample. High pressure should induce some deviation from the perfect linear Arrott plot if it happens at a subtle balance between two opposite curvatures. A recent report[86] has shown that the lattice-parameter difference $a-b$ increases slightly with pressure in the pressure range P < 20 GPa, which is equivalent to the effect of Ba substitution on lattice parameters in Sr$_{1-y}$Ba$_y$RuO$_3$. The structural response to high pressure does not change for different pressure media.[86] However, non-hydrostatic pressure generally broadens up diffraction peaks. To demonstrate the pressure effect on the Arrott plot, we have carried out the measurements of M(H) of HP SrRuO$_3$ and Sr$_{.7}$Ba$_{.3}$RuO$_3$ in different pressure media, *i.e.* 3M Fluorinert FC77 + FC72 (FC) and silicone oil (oil). A more nearly hydrostatic condition can be maintained to higher pressure in the pressure medium FC than in the oil. As shown in Fig. 4.10, the Arrott plot of the HP SrRuO$_3$ sample has no noticeable change under P < 1 GPa with FC as the pressure medium in which hydrostatic pressure remains up to 0.9 GPa. It is remarkable that high pressure causes a significant change to convex curvature if silicon oil, which creates more non-hydrostatic component than 3M Fluorinert, was used as the pressure medium. Hydrostatic pressure would induce a slight change of cooperative octahedral-site rotations and shrink the Ru-O bonds, which play a similar role as changing $\langle r_A \rangle$ without varying σ^2 in many cases. The effect of hydrostatic pressure on the Arrott plot looks negligible since the maximum pressure applied in this study does not induce as much structural change as that by the A-cation substitution x = 0.1 Ca or Ba in Sr$_{1-x}$A$_x$RuO$_3$ regardless which direction pressure drives. The A-site substitution of Ca or Ba in Sr$_{1-x}$A$_x$RuO$_3$ with x = 0.1 does not lead to a significant deviation from the linear

Arrott plot as is shown in Fig. 4.6. On the other hand, non-hydrostatic pressure introduces structural disorder and the structural disorder has the same effect on the Arrott plot as that of increasing the size variance.

It is also worth mentioning that the non-hydrostatic component results in an additional suppression of T_c on top of that due to hydrostatic pressure as demonstrated in Fig. 4.9 by comparison of dT_c/dP of HP $SrRuO_3$ in the pressure media Oil versus FC. This observation also shows that T_c of the magnetic phase with convex curvature in the Arrott plot, whether due to non-hydrostatic pressure or to the size variance, is more sensitive to high pressure, which explains the large magnitude of $dlnT_c/dP$ found in the samples with $\langle r_A \rangle < r_{Sr}$. We have also verified the non-hydrostatic effect on the Ba substituted $Sr_{1-y}Ba_yRuO_3$ samples. Initial Ba substitution increases both $\langle r_A \rangle$ and σ^2. The Arrott plot in Fig. 4.10 does not show straight lines any more in the Ba-substituted sample; curves at low field become more convex, shown by the down arrow, whereas the curvature at high field is increasingly concave, shown by the up arrow. The convex curvature at low field due to the size variance is clearly enhanced by non-hydrostatic pressure. The concave curvature as seen in $BaRuO_3$ of Fig. 4.6 becomes visible in $Sr_{.7}Ba_{.3}RuO_3$ at high magnetic filed as pointed by the up arrows. The non-hydrostatic pressure appears to have little influence on this feature.
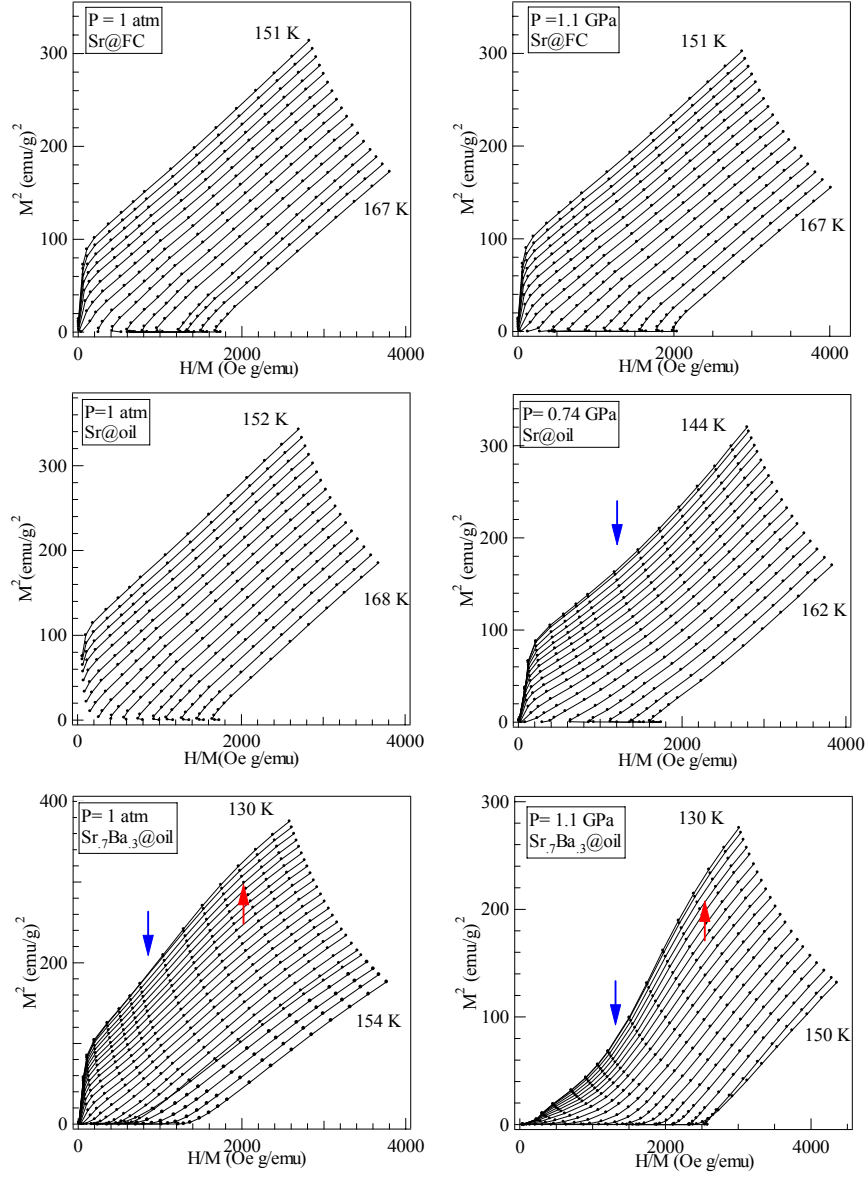
Figure 4.10: Arrott plots M^2 *vs* H/M for HP $SrRuO_3$ and $Sr_{.7}Ba_{.3}RuO_3$ under different pressure media. FC and oil denote 3M Fluorinert (FC77 +FC72) and silicone oil, respectively. A more nearly hydrostatic condition can be maintained to higher pressure in the pressure medium FC than in the oil. The convex and concave curvatures are pointed by the down and up arrows in several panels.

The essential issue in the ferromagnetic perovskite ruthenates is the origin of the convex curvature in the Arrott plot. The same plot has been reported in $Sr_{.3}Ca_{.7}RuO_3$ by another group [26] and in the 9R phase of $BaIrO_3$.[87] A convex curvature is associated with a significantly reduced magnetic moment at zero field and cannot be justified so far by existing magnetic models. This peculiar magnetic phenomenon is enhanced when either the crystal structure becomes more distorted by reducing $\langle r_A \rangle$ or the bond length becomes disordered with increasing σ^2 or under non-hydrostatic pressure. $BaRuO_3$ has the largest $\langle r_A \rangle$ in the family and a $\sigma^2 = 0$; in this sample the peculiar phenomenon gives way to a magnetization typical of a Heisenberg ferromagnet. $SrRuO_3$ exhibits a crossover from the convex curvature to the concave curvature of the Arrott plot; therefore whether the Arrott plot can produce straight lines is sample-dependent and is extremely sensitive to non-hydrostatic pressure. Perfect linearity of the Arrott plot was found in the sample with the highest saturation moment close to the spin-only value, which is fundamentally against itinerant-electron ferromagnetism and the SCR model.

4.4 CONCLUSION

To this point, we have shown that T_c varies sensitively with bond-length strain, a phenomenon that has also been found in two other oxides with perovskite-related structures at the crossover from localized to itinerant electronic behavior. The perovskite ruthenates also appear to be at such a crossover: high pressure transfers $BaRuO_3$ from a ferromagnet to a Pauli paramagnet [25] and the introduction of Ca into $SrRuO_3$ produces an inverse paramagnetic susceptibility typical of a Griffiths phase [73] in which the ferromagnetic Ru-O-Ru spin-spin interactions are diluted. Whereas Ca substitution introduces local lattice strains and the size variance, it also narrows the π^* bandwidth and makes the O-Ru-O bond angle α approach 90°. These two factors would enhance the

99

spin-orbit $\lambda \mathbf{L} \cdot \mathbf{S}$ coupling for a localized $t^4 e^0$ configuration at an octahedral-site Ru(IV). The spin-orbit coupling apparently competes with the intersite spin-spin coupling so as to dilute the ferromagnetic coupling of the array.

We have also shown that the linear behavior of the Arrott plot for $SrRuO_3$ does not signal itinerant-electron ferromagnetism. In fact, the nearly spin-only saturation moment of our HP $SrRuO_3$ clearly signals localization of majority-spin electrons. On the other hand, a single-crystal film of $SrRuO_3$ has been reported [88] to exhibit Fermi liquid transport properties at low temperature whereas photoemission data [89] have shown a broadening of the Ru-4d π^* band due to the presence of strongly correlated electrons in a lower Hubbard band. All these data can be reconciled by the Rozenberg *et al.* [90] model of a coexistence of localized and itinerant electrons at the crossover from a Mott insulator to a Pauli metal. The coexistence of localized and itinerant electronic states may also evolve into a dynamic phase segregation as can be inferred from an NMR study.[91]

The bandwidth W of the antibonding π^* band derived from the π-bonding t^4 configuration would be narrowed by substitution of the more acidic Ca for Sr and broadened by substitution of the more basic Ba atom. Since this A-cation substitution is also accompanied with a change of the mean A-cation size, we can generally say that the bandwidth would increase with $\langle r_A \rangle$. This bandwidth argument alone, however, cannot explain the parabolic dependence of T_c^o versus $\langle r_A \rangle$. Moreover, since the antibonding π^* band is 2/3 filled, Anderson localized states do not appear to be relevant to the size-variance effect on T_c. In the model of a coexistence of localized and itinerant electronic states, more electrons are transferred from itinerant to localized states as the band narrows. Moreover, in a localized-electron configuration, the orbital angular momentum

is associated with the minority-spin electrons, and the majority-spin electrons would occupy the lower Hubbard band before the minority-spin electrons because intraatomic exchange would reduce their radial extension relative to that of the minority-spin electrons. Minority-spin itinerant electrons would couple the localized majority-spin electrons ferromagnetically as in indirect or de Gennes double exchange; they would also suppress any intraatomic spin-orbit coupling. Our findings clearly suggest that the optimum ferromagnetic coupling in the ruthenates occurs at a specific population ratio of the two electronic states. The local lattice strains and disorder would influence the distribution of the two electronic states in real space.

Arrott plots of the magnetization in the perovskite ruthenates show a systematic change from curves with convex curvature to concave curvature as $\langle r_A \rangle$ increases. The linearity of the Arrott plot found for $SrRuO_3$ is due to a subtle balance between convex and concave curvatures and has little to do with a signature of itinerant-electron magnetism. It is due to this subtle balance that the magnetization of $SrRuO_3$ presented in the Arrott plot is extremely sensitive to the local bond-length disorder, non-hydrostatic pressure and how the sample is synthesized. We have argued that developing a convex curvature of the Arrott plot as the orthorhombic distortion or the local lattice disorder increases is caused by an orbital coupling to random local lattice distortion and a spin-orbit $\lambda \mathbf{L} \cdot \mathbf{S}$ coupling that increases with decreasing bandwidth.

Chapter 5 Ferromagnetism in the perovskite $Sr_{1-z}Pb_zRuO_3$

5.1 INTRODUCTION

According to the magnetic phase diagram of the perovskite ruthenates $ARuO_3$ (A= Ca, Sr, Ba), Fig. 4.5, a steric-effect consideration would predict that the perovskite $PbRuO_3$ is a ferromagnetic metal since the ionic radius of Pb^{2+} (1.40 Å) is slightly larger than that of Sr^{2+} (1.36 Å).[27] However, it has been reported [29, 30] that the perovskite $PbRuO_3$ has no magnetic ordering. In an early report, Kafalas and Longo [29] first prepared the perovskite $Sr_{1-z}Pb_zRuO_3$ ($0 < z \leq 1$) system under HPHT in order to prevent the formation of the pyrochlore phase; their preliminary results indicated that the perovskite $PbRuO_3$ is a paramagnetic metal. No characterizations of crystal structure and physical properties at low temperatures were made in that report. However, Kimber *et al.*[30] reported very recently that the perovskite $PbRuO_3$ undergoes a semiconductor-insulator transition at ca. 90 K accompanied by a first-order structural transition from the high-temperature *Pbnm* phase to a low-temperature *Imma* phase. No long-range magnetic ordering was evident down to 1.5 K. The local structural distortions resolved from a neutron-diffraction study suggested an orbital ordering on Ru(IV) in the low-temperature *Imma* phase. Moreover, a first-principles calculation in the same report justified the insulator ground state of the *Imma* phase. All the experimental results and the self-consistent justification of an insulator ground state reported by Kimber *et al.*[30] appear to be flawless except for one observation; a temperature-dependent paramagnetic susceptibility shows the presence of a magnetic moment on at least some of the Ru(IV) ions, so it becomes necessary to justify why a magnetic-insulator phase, especially with orbital ordering, does not result in spin ordering. Kimber *et al.*[30] suggested that the bending of the Ru-O-Ru bond angle from 180° weakens the superexchange interaction.

However, the 159.8° Ru-O-Ru bond angle they reported is too large to suppress magnetic interactions between localized spins; provided that the M-O-M bond angle falls into a range from 142° to 156° in most 3d transition-metal oxides with orthorhombic perovskite structure, most of them exhibit spin-ordering transitions. This inconsistency motivated us to reexamine the transport and magnetic properties of the $PbRuO_3$ perovskite and to study the peculiar *Imma* phase under high pressure. In addition, the orthorhombic $PbRuO_3$ is the end member in the series of $Sr_{1-z}Pb_zRuO_3$. The phase diagram is badly needed in order to demonstrate the evolution from ferromagnetic $SrRuO_3$ to paramagnetic $PbRuO_3$ and how the low-temperature *Imma* phase develops. Kafalas and Longo[29] had mentioned that the Curie temperature T_c falls rapidly with increasing z and vanishes at $z \approx 0.5$. No data of T_c versus z and magnetic and transport properties were provided in that report.

Therefore, we have carried out a systematic study on the whole series of $Sr_{1-z}Pb_zRuO_3$ ($0 \leq z \leq 1$) by measuring the transport, magnetic properties and the crystal structure under ambient and high pressures. We have also made a side-by-side comparison between the effect of Pb substitution and Ca and Ba substitutions; the comparison distinguishes clearly an electronic hybridization from the steric effect in Pb substituted samples. Our results revealed that a metal-metal transition takes place at 90 K for the $PbRuO_3$ and the broadening the bandwidth due to the hybridization between Pb 6s and Ru 4d orbitals plays a leading role in suppression of ferromagnetism in the $Sr_{1-z}Pb_zRuO_3$.

.

5.2 EXPERIMENTAL DETAILS

By firing a stoichiometirc mixture of $SrCO_3$, PbO and Ru powders at 1000°C for 2 days in air, we have always obtained a mixture of perovskite and pyrochlore phases for all compositions of $Sr_{1-z}Pb_zRuO_3$ ($0 < z \leq 1$). The perovskite samples were synthesized from a mixture of perovskite and pyrochlore phases as the starting materials under 9 GPa and 1400°C in a Walker-type multianvil module (Rockland Research). All samples were examined with powder X-ray diffraction (XRD) at room temperature with a Philips X'pert diffractometer (Cu Kα radiation). Lattice parameters were obtained by using either the least-square analysis with the software JADE or the profile fitting with FULLPROF [70]. Magnetic properties were measured with a superconducting quantum interference device (SQUID) magnetometer (Quantum Design). A four-probe method was used to measure the resistivity. Thermoelectric-power measurements were performed in a home-made setup.

5.3 RESULTS AND DISCUSSIONS

5.3.1 Metal-metal transition in perovskite $PbRuO_3$

The XRD profile fitting through the Rietveld refinement shows in Fig. 5.1 that our samples have precisely the same crystal structure as that reported by Kimber *et al.*[30] Fig. 5.2 shows that the XRD at low temperatures on our samples also revealed a phase transition to the *Imma* phase at ca. 80 K. The oxygen stoichiometry is another factor to consider. Kimber *et al.*[30] have verified their sample was close to stoichiometry within 1% by the site occupation obtained from refining their neutron-diffraction data. From electron energy loss spectroscopy (EELS), we have obtained the ratio O/Ru = 3 ±1 from sampling points on scanning across a crystal grain (most points fall on the line of 3) as

shown in Fig. 5.3. All these comparisons indicate that samples from the two groups are identical.
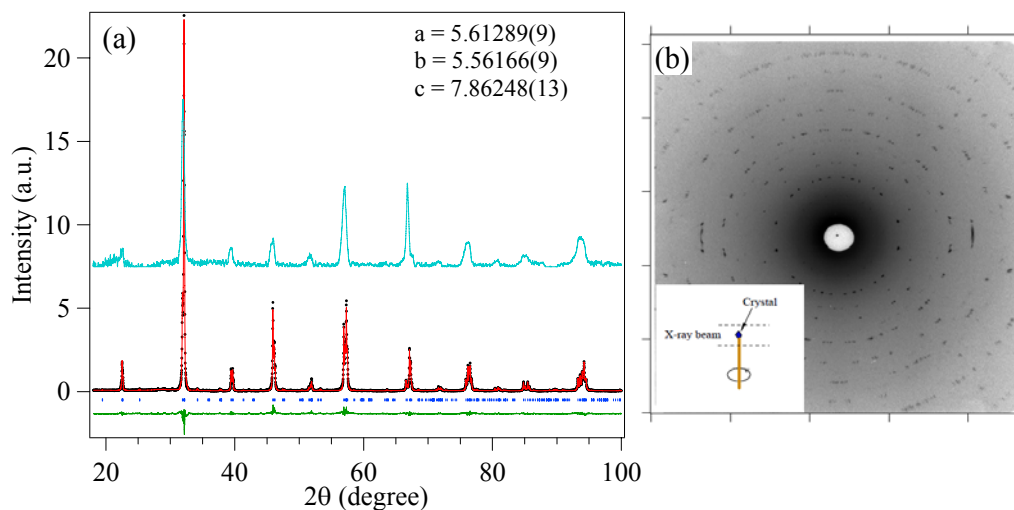
Figure 5.1: (a) X-ray powder diffraction and its profile fitting by Rietveld refinement of the orthorhombic PbRuO₃. The XRD in middle is obtained from integrating the rotation sample X-ray diffraction pattern (b). The inset of (b) illustrates the configuration how the diffraction was performed.
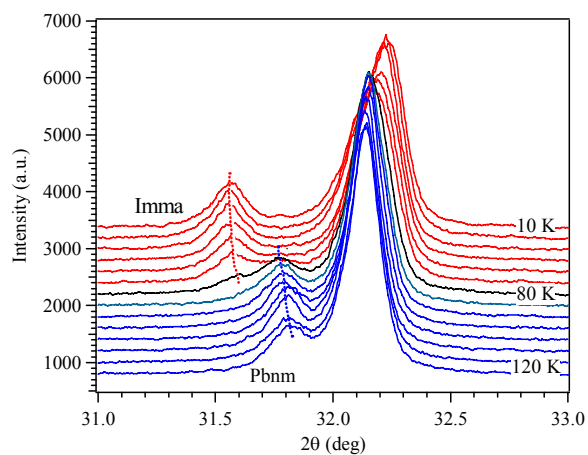
Figure 5.2: XRD profiles in the 2θ range of 31° to 33° at low temperatures from 10 to 120 K. The phase transition from low-temperature *Imma* phase to the high-temperature *Pbnm* phase takes place at ca. 80 K.
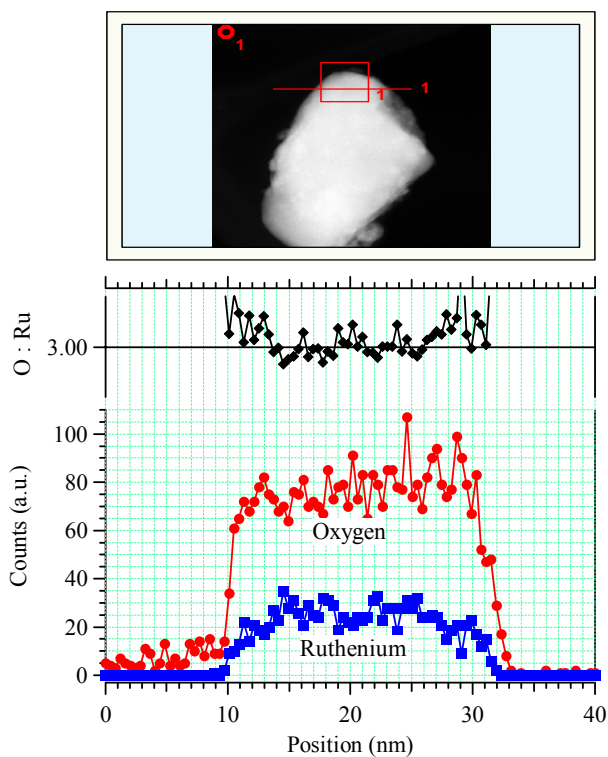
Figure 5.3: Electron energy loss spectroscopy (EELS) obtained on scanning across a crystal PbRuO$_3$ grain.

In order to explain the discrepancy of the transport properties found between our samples and that by Kimber *et al.*,[30] we provide here a detailed description about the procedure of sample characterizations and measurements. The synthesis at T ≈ 1400°C and P > 9 GPa always gives perovskite samples with large grains; the longest dimension is about 200 μm as seen from scanning electron microscopy. These grains are loosely connected and can be separated easily by a pair of tweezers. Cracks were developed during cooling of these high-pressure products, which resulted in a noisy signal and many sharp up-and-down changes in ρ(T) if the measurement was made directly on pellets from high-pressure synthesis. We have chosen to make measurements on single grains separated from the high-pressure products. Selected grains were mounted on a thin glass fiber and then placed in a four-circle diffractometer (Bruker P4) for rotation-sample X-ray diffraction (RSXRD). Diffractions were collected by an image plate from Fuji. The X-ray beam size is about 500 μm and grains were located in the center of the beam, which insures that we have checked the entire part of the grain. Spots in the RSXRD pictures in Fig. 5.1(b) confirm that the grain included large domains. The possible twining and the multidomain character of the selected grains prevented structural determination by single-crystal diffraction. However, as superimposed in Fig. 5.1(a), the intensity versus 2θ from the RSXRD patterns integrated by using the software Fit2d confirms that the structure is the same as that from the XRD of a bulk sample and no impurity phase was found. All measurements of transport properties were made on small single-crystal grains that had been checked by RSXRD. Four Cu leads (12 μm dia.) were attached on a grain with silver epoxy and cured at 150°C for 20 min. The contact resistance is a couple of ohms. Due to the small sample size, a pair of differential thermal couples was attached to two copper leads from a grain; the distance between contact points and the grain is about 100 μm. Therefore, the temperature gradient measured is

slightly larger than that actually applied on the grain; as a result, the magnitude of the thermoelectric power shown is slightly smaller than that we obtained on a polycrystalline pellet by a regular method. However, results from these two methods have the same temperature dependence. Measurements under pressure were made in Be-Cu high-pressure cells; the cell for magnetization measurement fits a commercial SQUID magnetometer from Quantum Design. The samples were placed inside a Teflon cell filled with a 1:1 mixture of 3M Fluorinert FC77 and FC72 as the pressure medium. In the magnetic-susceptibility measurement, a small piece of Pb was used as the pressure manometer whereas the pressure was monitored by a manganin-wire coil in the measurements of transport properties. The same configuration for the RSXRD was also used to study the crystal structure of $PbRuO_3$ under pressure. In this case, a diamond anvil cell was placed in the position of the sample in the P4 diffractometer. A small amount of CaF_2 powder as pressure manometer was mixed with the sample, and a mixture of methanol and ethanol 4:1 was used as the pressure medium.

The temperature-dependent magnetic susceptibility of Fig. 5.4 is nearly identical to that reported by Kimber et al.;[30] on cooling, $\chi(T)$ exhibits an abrupt drop at $T_t = 89$ K followed by a broad maximum near 25 K. A curve fitting to the formula $\chi(T) = \chi_0 + C/(T+\theta)$ in the temperature range $T > T_t$ suggests that the *Pbnm* phase might have become antiferromagnetic below a $T_N < T_t$. Since no classic spin ordering was detected down to 1.5 K,[30] the broad hump in $\chi(T)$ signals AF spin fluctuations at $T < 25$ K. As shown in Fig. 5.4(a), the structural transition, which is monitored by an anomaly of $\chi(T)$ at T_t, is dramatically suppressed under pressure since pressure prefers the *Pbnm* phase, which has a smaller cell volume than the *Imma* phase at low temperatures. Linear fitting of T_t versus P in Fig. 5.4(b) yields a pressure coefficient $dT_t/dP = -0.84(1)$ K/kbar.

108
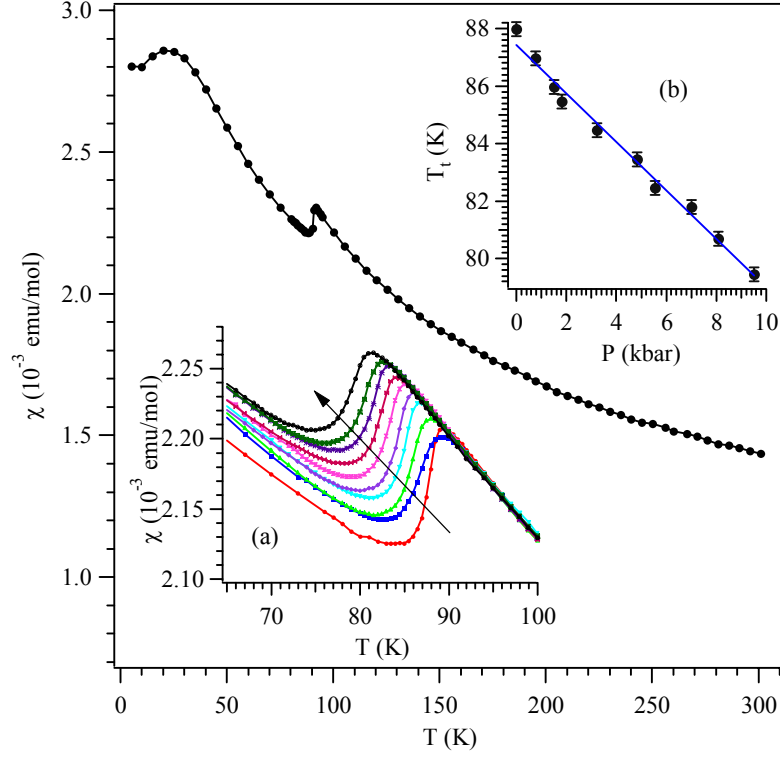
Figure 5.4: Temperature dependence of magnetic susceptibility $\chi(T)$ of the perovskite $PbRuO_3$. Inset (a): A zoom-in plot of $\chi(T)$ near the structural transition temperature T_t under pressure. The arrow points to the direction of increasing pressure. Inset (b): The pressure dependence of the transition temperature T_t.

In sharp contrast to what was observed by Kimber *et al*., our sample exhibits metallic conductivity down to 5 K in Fig. 5.5. Corresponding to the structural transition at T_t, R(T) shows a distinct anomaly that has a very small hysteresis loop between the cooling and warming measurements. The R(T) at ambient pressure was reproduced after releasing pressure. Similar to the pressure dependence of T_t from the magnetic susceptibility $\chi(T)$ in Fig. 5.4(a), T_t is reduced under pressure with a coefficient $dT_t/dP =$

−1.2(1) K/kbar. Both the hysteresis loop and the anomaly in R(T) at T_t become smaller under higher pressure.
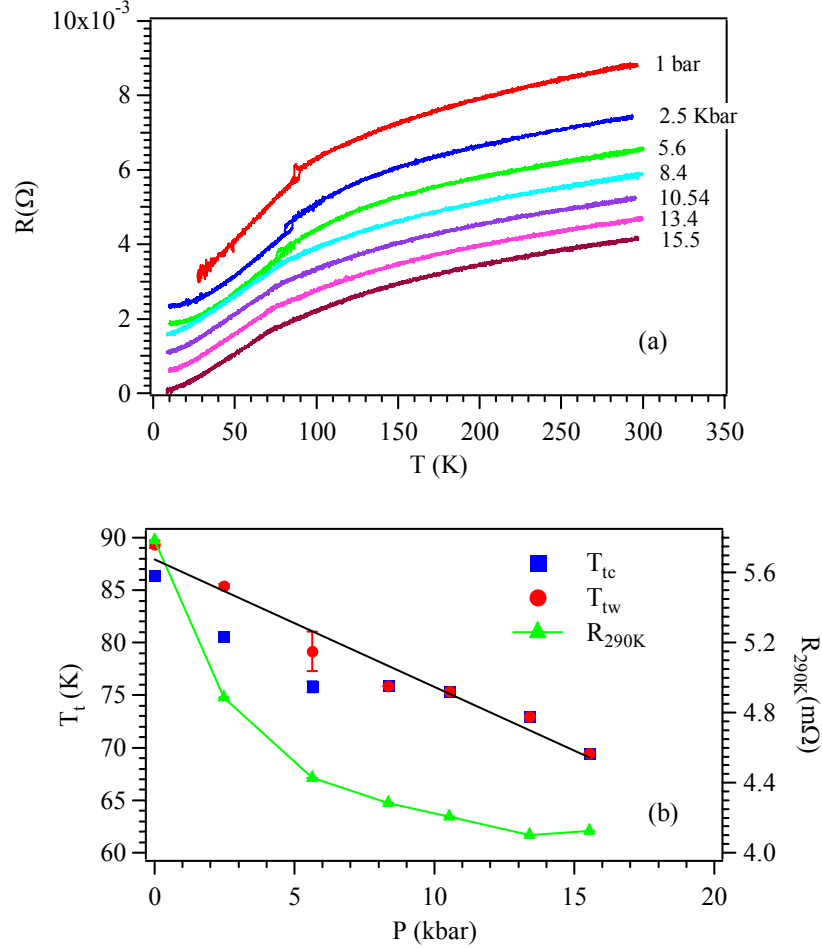
Figure 5.5:   (a) Temperature dependence of resistance R(T) of the perovskite $PbRuO_3$ under pressure; curves have been shifted vertically for clarification; (b) Pressure dependence of T_t obtained from (a) during the cooling down and warming up and the resistance at 290 K.

The thermoelectric power S(T) measurements of Fig. 5.6 provide more information about the low-temperature (LT) *Imma* phase and the high-temperature (HT)

Pbnm phase. S(T) in the HT phase is typical for a metal,[92] *i.e.* it follows the Mott diffusive thermoelectric power formula at sufficiently high temperature and shows the phonon drag effect at low temperature. Although S(T) of the HT phase is truncated by the phase transition at T_t, it approaches zero near 100 K, which indicates that the phonon-drag effect contributes a negative correction $\Delta S(T)$ to S(T). The phase transition at T_t brings about an abrupt change of S to a more negative value. The S(T) of the LT phase seems to have a large correction from the phonon-drag effect. The phonon-drag effect is much more enhanced in broad-band metals like Cu, Au, Pt [93]; it was barely seen in the narrow-band metal $LaCuO_3$ and is completely suppressed in Nd-doped $La_{1-x}Nd_xCuO_3$.[94] The relationship between the bandwidth and the phonon-drag effect is further proven by the S(T) measurements of $La_{1-x}Nd_xCuO_3$ under high pressure.[94] The strong phonon-drag effect found in the LT phase of $PbRuO_3$ signals that it is a broad-band metal. As shown in Fig. 5.6(a), whereas pressure changes slightly the S(T) in the *Pbnm* phase, it enhances significantly the phonon-drag effect in the LT *Imma* phase. Whether the correction to S(T) from the phonon-drag effect is positive or negative depends on the nature of the electron-phonon interactions that produce it; normal electron-phonon interactions contribute a negative correction whereas Umklapp processes give a positive one.[92] Whereas the S(T) of the HT phase is reproducible for different samples, the strong phonon-drag effect in the LT Phase, which is negative for the grain used in our high-pressure measurement, was found to be positive in some other samples, *i.e.* the S(T) showed a mirror symmetry around the S = 0 line of the S(T) in Fig. 5.6(a). It means that the sign of the correction from the phonon-drag effect is determined by the residual strain built into the high-pressure products. Given the same contact resistance, the noise level of S(T) is much reduced in the LT phase from that in the HT phase, which could also serve as an indicator for a more conductive LT phase. High pressure does not cause any

permanent change on the sample since the original S(T) under ambient pressure is fully recovered after releasing pressure.

As seen from S(T) at ambient pressure, a sharp transition at T_t becomes broader for P > 10 kbar, but T_t could still be defined as a shoulder of S(T). The pressure dependence of T_t defined in this way yields a $dT_t/dP = -1.19(6)$ K/kabr, which is nearly the same as that from R(T). However, as demonstrated in Fig. 5.6(b), another sharp transition develops at $T_t' < T_t$ under P ≥ 8 kbar. Although the resistance measurement R(T) and the thermoelectric measurement S(T) were made on the same grain, no anomaly has been found at T_t' in R(T). A large hysteresis loop in S(T) at T_t' indicates it is another first-order transition. Thermoelectric power is related to the asymmetric factor of a dispersion curve at the Fermi energy; it is more sensitive than the conductivity measurement to a phase transition in most cases. It remains unknown whether the transition at T_t' corresponds to a change in the magnetic susceptibility measurement since the maximum pressure of the cell for $\chi(T)$ measurement is below 1 GPa. A clear and important message from our results of transport and magnetic properties is that the conduction band of the HT *Pbnm* phase of perovskite $PbRuO_3$ is a little broader than that of the metallic perovskite $BaRuO_3$ phase and that it becomes broadened further in the LT phase to where long-range magnetic order is completely suppressed.
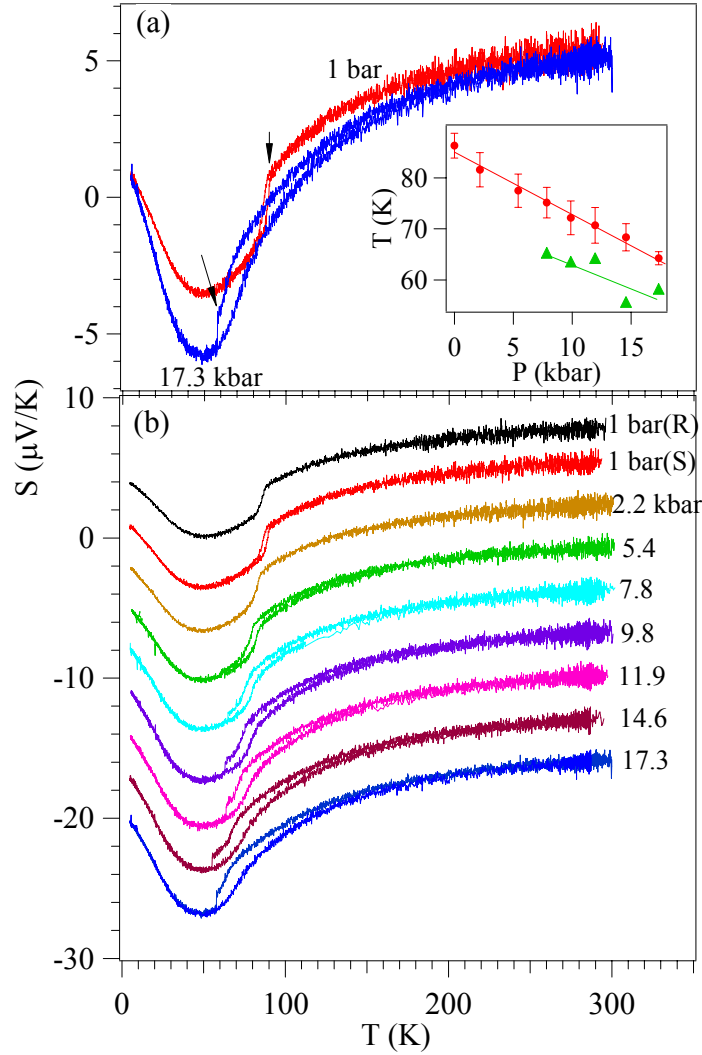
Figure 5.6:   Temperature dependence of thermoelectric power S(T) of the perovskite PbRuO$_3$. (a) S(T) at ambient pressure and the highest pressure in this study; the plot is to highlight the absolute change induced by high pressure. The arrow near the curve at 1 bar points the phase transition at T_t, which develops into a shoulder-like transition under high pressure. The arrow near the curve at 17.3 kbar points the sharp transition at T_t'. Inset: the pressure dependences of transition temperatures T_t and T_t'. (b) S(T) curves for all pressures. Curves have been shifted vertically for clarification.

It is highly unusual to find that the *Imma* phase with higher symmetry than *Pbnm* phase occurs at low temperature. One may wonder what is the difference between this *Imma* phase and that found in many perovskite oxides like $Sr_{1-y}Ba_yRuO_3$,[95] $Sr_{1-v}A_vSnO_3$ (A=Ca, Sr, and Ba),[96] $SrZrO_3$,[97] and $SrRuO_3$[98] where the geometric tolerance factor t is increased by either substituting a larger ion in the A site as in the first two systems or by raising temperature as in the latter two systems. In the tilting systems of the perovskite structure,[4] *Pbnm* is a subgroup of *Imma*. A series of structural transitions in the order of $Pbnm - Imma - I4/mcm$ ($R\bar{3}c$ in some cases) $- Pm\bar{3}m$ has been found as the t factor increases. As a precursor for the phase transition from *Pbnm* to *Imma*, a crossover from $b > a$ to $a > b$ and a continuous increase of $a - b$ are always found in the *Pbnm* phase near the *Pbnm-Imma* boundary. It has been shown that an increased octahedral-site distortion with O-M-O bond angle $\alpha < 90°$, where α subtends the axis of cooperative octahedral-site rotation, is the origin of the lattice-parameter crossover.[47] The structural transitions from *Pbnm* to *Imma* and to *I4/mcm* before the final cubic phase relieve this local distortion. Therefore, the maximum $a - b$ is found at the phase boundary between *Pbn*m and *Imma*. Since *Pbnm* is a subgroup of *Imma*, *i.e.* one tilting component of the *Pbnm* structure vanishes continuously at the phase boundary, the transition from *Pbnm* to *Imma* has been found to be second order. The first-order transition at T_t indicates that the *Imma* phase found in $PbRuO_3$ at low temperatures is not induced by the tolerance factor as occurs with the *Imma* phase that we have normally seen in the chain of phase transitions of perovskite structure. Moreover, an abrupt increase of $a - b$ has been found in the LT *Imma* phase at T_t whereas it should changes continuously in a phase transition from the *Pbnm* phase to the normal *Imma* phase.
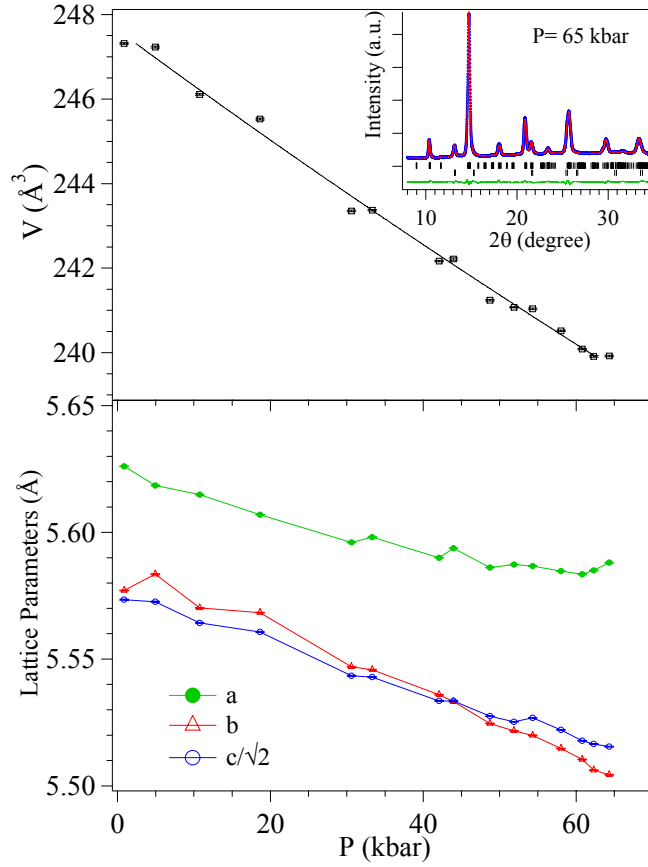
Figure 5.7:   Pressure dependences of lattice parameters of the perovskite $PbRuO_3$. Error bars are smaller than symbols. Lattice parameters were obtained from the profile fitting of XRD. An example of XRD (wavelength $\lambda = 0.71069$ Å) under high pressure and the profile fitting are shown as inset which includes diffractions from both the perovskite $PbRuO_3$ and CaF_2 to monitor the pressure.

Figure 5.7 shows room-temperature lattice parameters of the perovskite $PbRuO_3$ under pressure. The *Pbnm* phase is stable to 65 kbar, the highest pressure in this study. The bulk modulus obtained by fitting the V versus P curve with the Birch-Murnaghan equation is 185(4) GPa, which is in line with that of other perovskite ruthenates, 192 GPa in $SrRuO_3$[86] and 182 GPa in $BaRuO_3$[99] provided that the ion size of Pb^{2+} is located

between those of Sr^{2+} and Ba^{2+}. The bulk modulus has been found generally to be proportional to the inverse of the cell volume in the perovskite oxides. The lattice-parameter difference $a-b$ increases continuously with increasing pressure, which indicates that pressure increases the octahedral-site distortion by reducing further the angle α. This pressure-induced structural change would normally lead eventually to a phase transition to the *Imma* phase. In contrast, as shown by the physical properties under pressure, pressure reduces T_t, which implies that pressure suppresses the LT *Imma* phase in the perovskite $PbRuO_3$.

After highlighting the differences between the LT *Imma* phase of $PbRuO_3$ and the *Imma* phase normally found at high temperatures and high pressure, we take a closer look at the LT phase. Structural data from Kimber *et al.* [30] show that one of the O_1-Ru-O_2 angels, which is 91.35° in the *Pbnm* phase, increases abruptly to 91.71° in the LT *Imma* phase. As a result, this bond-angle change brings five Pb-O bonds falling to 2.5 Å. In comparison, there are only three Pb-O bonds with bond length less than 2.5 Å at 300 K. The coordination change appears to enhance the pathway for the hybridization between Pb-6s and Ru-4d orbitals so as to broaden the bandwidth of the Ru-O array. To increase the hybridization is likely the driving force for the first-order transition at T_t at the expense of the cell volume. High pressure prefers the *Imma* phase normally seen at high temperature but suppress the LT *Imma* phase in the $PbRuO_3$. The bond-length splitting at the octahedral site of Ru(IV) below T_t found by Kimber *et al.* is not a solid proof of an orbital ordering since a similar bond length splitting has been found in $SrRuO_3$ at 100 K.

5.3.2 Physical properties of the $Sr_{1-z}Pb_zRuO_3$ system

5.3.2.1 The crystal structure

The XRD patterns at room temperature of perovskites $Sr_{1-z}Pb_zRuO_3$ ($0.0 \leq z \leq$ 1.0) displayed in Fig. 5.8(a) are nearly identical and all major peaks can be indexed with the orthorhombic *Pbnm* space group. As marked by stars in Fig. 5.8(a), some samples contain a small amount of RuO_2 impurity (< 2%). The RuO_2 concentration versus z is shown in Fig. 5.8(c). No clear trend in RuO_2 impurity versus z was found, which indicates that the temperature window for synthesizing a phase-pure high-pressure product is very narrow in this case. Lattice parameters from refining XRD in Fig. 5.8(b) are in good agreement with that reported by Kafalas and Longo.[29] As illustrated systematically in the $A^{3+}M^{3+}O_3$ perovskites,[47] *b* deviates from the prediction with the SPuDs as the A-cation size r_A passes a critical value and eventually crosses with *a* as r_A further increases. The same situation occurs in $A^{2+}Ru^{4+}O_3$ (A = Ca, Sr, Ba) as shown in Fig. 4.3. The anomalous evolution of lattice parameters versus $\langle r_A \rangle$ is due to the octahedral-site distortion with an α angle less than 90°. There are two important consequences due to this kind of octahedral-site distortion: (a) the formula [46] based on rigid octahedron and lattice parameters for calculating the (180° -ϕ) Ru-O-Ru bond angle is no longer valid; (b) since the t-orbital degeneracy is lifted by the distortion, the orbital angular momentum in the localized t^4e^0 configuration on the octahedral-site Ru^{4+} is quenched. As shown below, the physical properties do not show any anomalies at the crossover of *b* and *a* since this kind local distortion already occurs in the end member $CaRuO_3$. As monitored by the difference $a-b$, the α angle decreases further as r_A increases. The phase transition to the *Imma* phase is a way for the structure to relieve this local strain. As a matter of fact, the maximum $a-b$ indeed occurs at the *Pbnm/Imma* phase boundary.[96, 97] Another remarkable change at the phase boundary is a crossover

117

from $c/\sqrt{2} > b$ in the *Pbnm* phase to $c/\sqrt{2} < b$ in the *Imma* phase. Since Pb^{2+} is slightly larger than Sr^{2+}, the effect of Pb substitution should be similar to that of Ba substitution, *i.e. a−b* increases continuously as z increases all the way to PbRuO$_3$. The high-pressure structural study of PbRuO$_3$ in Fig. 5.7 shows a continuous increase of *a−b* up to 7 GP, which indicates that PbRuO$_3$ at ambient pressure is far from the phase boundary to the *Imma* phase. An important observation from Fig. 5.8 is that in contrast to Ba substitution of Fig. 4.3, a crossover from $c/\sqrt{2} > b$ to $c/\sqrt{2} < b$ occurs between z = 0.9 and 1.0 within the *Pbnm* phase. As far as we know, a $c/\sqrt{2} < a\ and\ b$ cannot be the result of an intrinsic structural distortion of the orthorhombic perovskite structure with the *Pbnm* space group. In orthorhombic LaMnO$_3$, a $c/\sqrt{2} < a\ and\ b$ is due to the long-range cooperative Jahn-Teller distortion. The anomalously small $c/\sqrt{2}$ relative to *b* and *a* found in PbRuO$_3$ is most likely related to the hybridization between Pb-6s and Ru-4d orbitals. This structural anomaly also serves as a precursor to the unusual phase transition to the low-temperature *Imma* phase where $c/\sqrt{2}$ is further reduced.
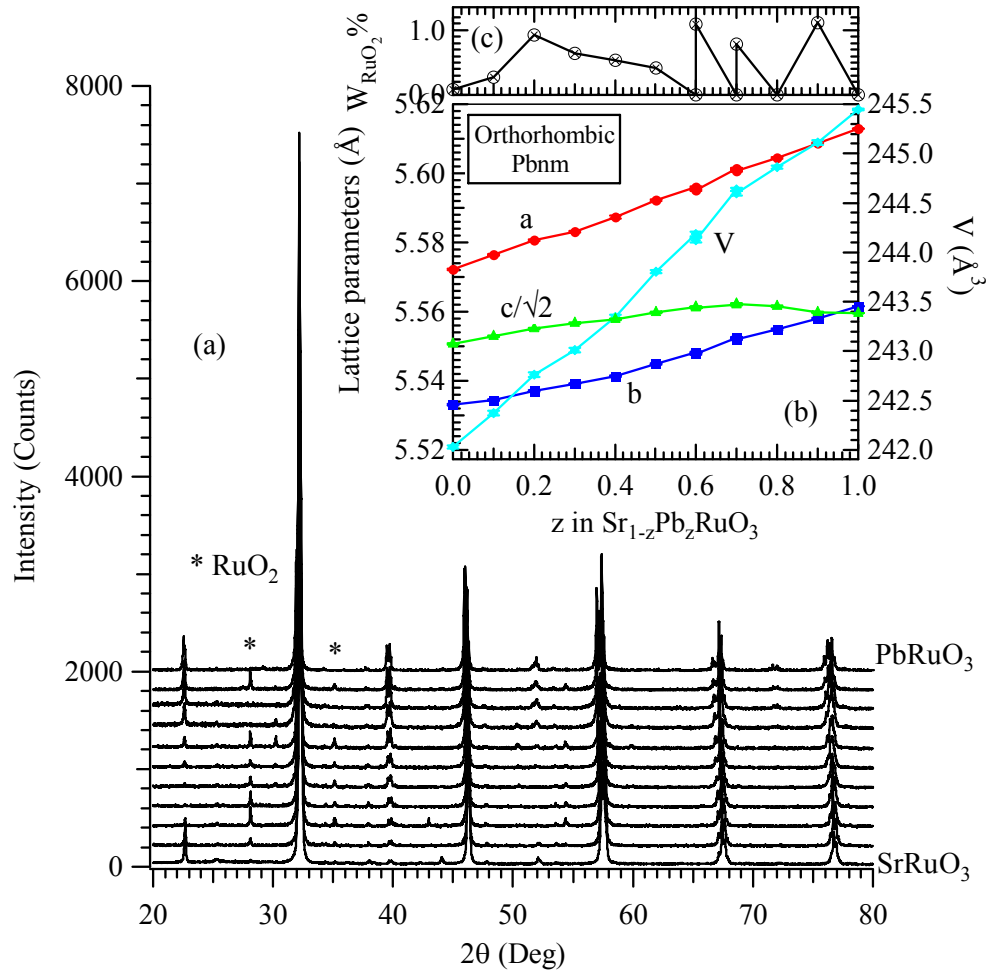
Figure 5.8: (a) X-ray powder diffraction of orthorhombic $Sr_{1-z}Pb_zRuO_3$; the peak locations marked by stars are from the RuO_2 phase; (b) Lattice parameters and cell volume as a function of z. (c) The concentration of RuO_2 in the high-pressure products as a function of z Pb.

5.3.2.2 Magnetic properties

The magnetic susceptibilities $\chi(T)$ and $\chi^{-1}(T)$ of the entire system $Sr_{1-z}Pb_zRuO_3$ are shown in Fig. 5.9. The $\chi(T)$ for both end members are consistent with that in the literature.[30, 71] Fitting these curves in the paramagnetic phase to the Curie-Weiss law gives the Weiss constant θ_{cw} and μ_{eff}; their evolutions as a function of z are plotted in Fig.

119

5.10. The Curie temperature T_c, determined from the minimum of $d\chi/dT$, is progressively reduced as z increases and vanishes near z = 0.5. Coincidently, θ_{cw} changes sign from positive to negative at the same composition and the μ_{eff}, which is slightly larger than the spin-only value at z = 0, exhibits a minimum near z = 0.5. The ultimate issue is why the ferromagnetic phase is suppressed while the structural distortion is gradually reduced as z increases. This issue is further addressed below in connection with the systematic studies of transport properties.

We introduce here a comparison of the magnetic properties among the Ca, Ba, and Pb substitutions. As shown in Fig. 4.1, an important feature developed for the Ca-doped $SrRuO_3$ is a downward curvature in the $\chi(T)$ curves at $T > T_c$, a characteristic of a Griffiths' phase.[73] The same feature for the Griffiths' phase also appears in the $\chi^{-1}(T)$ of Pb substituted samples with much reduced T_c. Although the characteristic $\chi^{-1}(T)$ for the Griffiths' phase appears in both Pb- and Ca-substituted $SrRuO_3$, their T_G does not match the maximum T_c in the system, which is different from the classic phase diagram drawn originally by Griffiths.[73] Nevertheless, there is no doubt that the suppression of the ferromagnetic phase in both Ca- and Pb-substituted $SrRuO_3$ is related to dilution by a nonmagnetic phase. In sharp contrast, Ba substitution in $SrRuO_3$ does not introduce any dilution-related feature in $\chi(T)$ of the paramagnetic phase. Instead, as shown in Fig. 4.1, the CW law is fulfilled in $\chi^{-1}(T)$ for all samples $Sr_{1-y}Ba_yRuO_3$ as T_c is reduced from 160 K in $SrRuO_3$ to about 60 K in $BaRuO_3$. Both Pb and Ba substitutions play a similar role in reducing the structural distortions. However, it is the orbital hybridization between Pb^{2+} and Ru^{4+} in Pb substituted samples that destroys ferromagnetic phase in $Sr_{1-z}Pb_zRuO_3$.

120
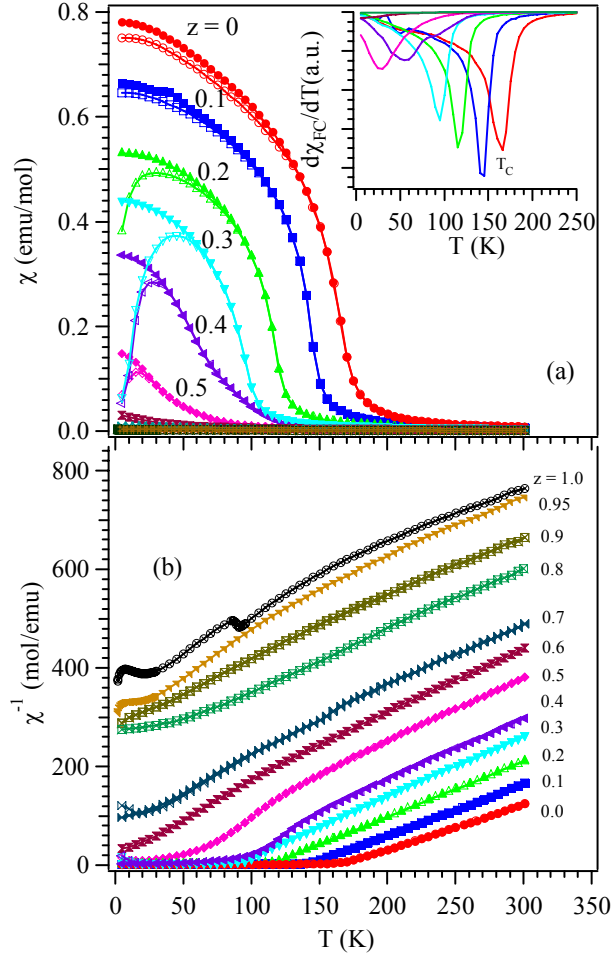
Figure 5.9: Temperature dependence of (a) the magnetic susceptibility χ and (b) χ^{-1} of $Sr_{1-z}Pb_zRuO_3$. T_cs are determined from the minimum of $d\chi_{FC}/dT$ as shown in the inset of (a). All plots of $\chi(T)$ for the samples $z > 0.5$ cannot be distinguished in (a).

121
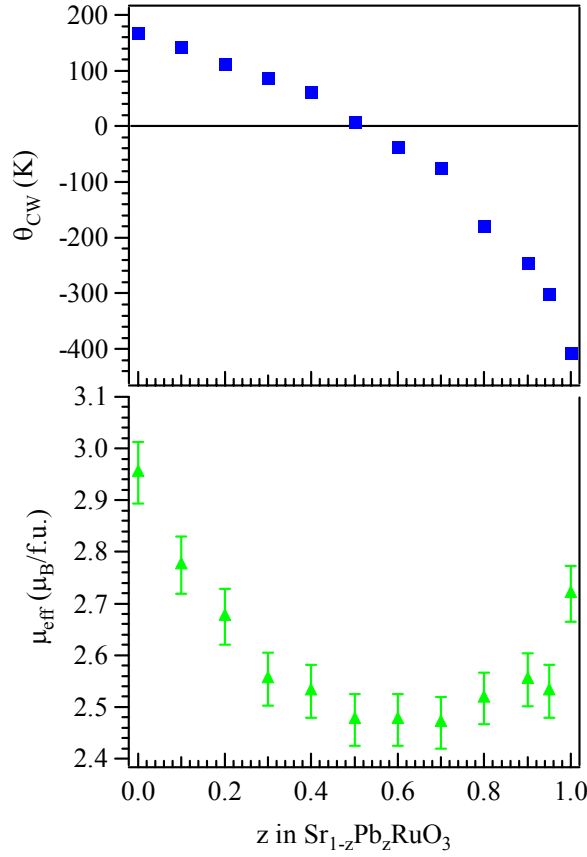
Figure 5.10: The Weiss constant θ_{cw} and the effective magnetic moment μ_{eff} as a function z in perovskites $Sr_{1-z}Pb_zRuO_3$.

5.3.2.3 Transport properties

Figure 5.11 shows the temperature dependence of resistivity $\rho(T)$ and its derivative with respect to temperature of samples of $Sr_{1-z}Pb_zRuO_3$. The result for $SrRuO_3$ is closer to that of a single crystal[71, 100] than to that of the ceramic samples[101] in the literature. All samples are metallic down to 5 K; a small upturn of resistivity at low temperatures for the z = 0.1 sample may be caused by some impurity phase. The ferromagnetic transition in $SrRuO_3$ induces a slope change in the curve of ρ vs T, which can be seen much more clearly in the curve of $d\rho/dT$ vs T. This anomaly moves to lower

122

temperatures and gradually fades away as z increases. On the other hand, the structural transition from the *Pbnm* to the *Imma* phase as temperature lowers through T_t causes an abrupt jump of the resistivity in $PbRuO_3$. The resistivity in the *Imma* phase exhibits a much steeper temperature dependence. The power law analysis of the low-temperature resistivity gives the dependence of the exponent n in $\rho = \rho_0 + T^n$ versus z shown as an inset of Fig. 5.11. Both end members show a well-defined Fermi-liquid behavior of $n = 2$. The non-Fermi-liquid behavior at the first minimum in the plot of n *vs* z near $z = 0.6$ appears to be associated with a quantum critical point as the Curie temperature is suppressed to zero. The second minimum in n *vs* z is perhaps related to critical fluctuations near the structural transition at T_t, which vanishes near $z = 0.9$.
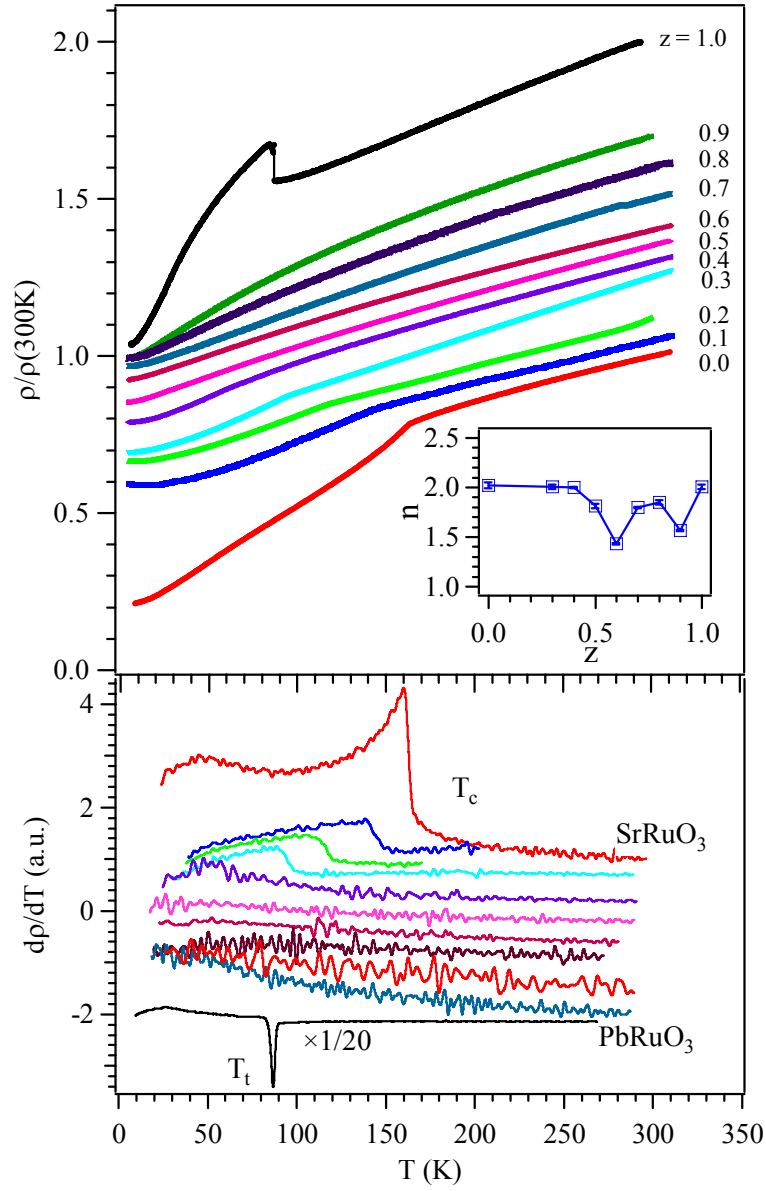
Figure 5.11: Temperature dependence of resistivity ρ and $d\rho/dT$ of perovskites $Sr_{1-z}Pb_zRuO_3$. All resistivity curves except for the sample $z = 0$ have been shifted vertically for clarification. The inset: exponential n in the power law $\rho = \rho_0 + T^n$ versus z.

The temperature dependence of thermoelectric power S(T) for samples $Sr_{1-v}A_vRuO_3$ (A = Ca, Pb, Ba) are shown in Fig. 5.12. As shown in Fig. 5.6, the structural transition at T_t induces an abrupt drop of thermoelectric power followed by a broad minimum in $PbRuO_3$. This broad minimum has been attributed to the phonon-drag effect. Similar features, which are characteristic of the *Imma* phase, can still be seen in the z = 0.95 samples of Fig. 5.12. The transition at T_t in the z = 0.95 sample, as monitored by an abrupt drop of S, is suppressed under high pressure, which is consistent with the T_t reduction under high pressure observed in $PbRuO_3$. For the samples z ≤ 0.8, the *Pbnm* phase remains stable to the lowest temperature and a positive hump with a maximum near 20 K appears; the enhancement persists over a broad range of the samples of $Sr_{1-z}Pb_zRuO_3$ and fades away in $SrRuO_3$. No such feature was observed in all Ca-substituted samples. The low-temperature enhancement of thermoelectric power in a metallic phase is normally due to the phonon-drag effect. However, it is significant that the enhancement near 20 K does not maximize at the end members where the Fermi-liquid behavior is well defined from the resistivity measurements, but occurs in the samples with compositions around the quantum critical point z ≈ 0.6 where T_c goes to zero. This observation suggests that the thermoelectric power enhancement near 20 K may be due to quantum critical fluctuations. Further verification of this argument will be done by the measurement of thermoelectric power under a magnetic field. On the side of Ca substitution, T_c is also reduced and vanishes near x = 0.7. Although a report has shown some quantum critical behavior associated with samples near z = 0.7,[102] no enhancement like that on the side of Pb substitution is observed. However, a dramatic upturn of S at low temperatures in $CaRuO_3$ indicates that another QCP is approached, which supports a similar argument from the measurement of specific heat.[103] The S(T) of Ba substituted samples resemble that of $SrRuO_3$; a slope change can be discerned at T_c.

The magnitude of thermoelectric power at a given temperature is not directly related to the bandwidth, but determined by the asymmetric energy dependent conductivity around the Fermi energy.[104] However, for the single-valence isostructural family $ARuO_3$, the evolution of |S| as a function of the tolerance factor t reflects the relative change of bandwidth. The thermoelectric power at room temperature as a function of the average A-cation size of Ca, Pb, and Ba substitutions are plotted in Fig. 5.13. S increases slightly on Ca substitution but drops much more steeply on Pb substitution. Pb substitution reduces S more dramatically than Ba substitution where the cubic phase $BaRuO_3$ with the highest symmetry in the system is reached. This plot indicates clearly that the orbital hybridization between Pb^{2+} and Ru^{4+} plays a more important role to broaden the bandwidth than the structural change in the Pb substituted samples $Sr_{1-z}Pb_zRuO_3.$
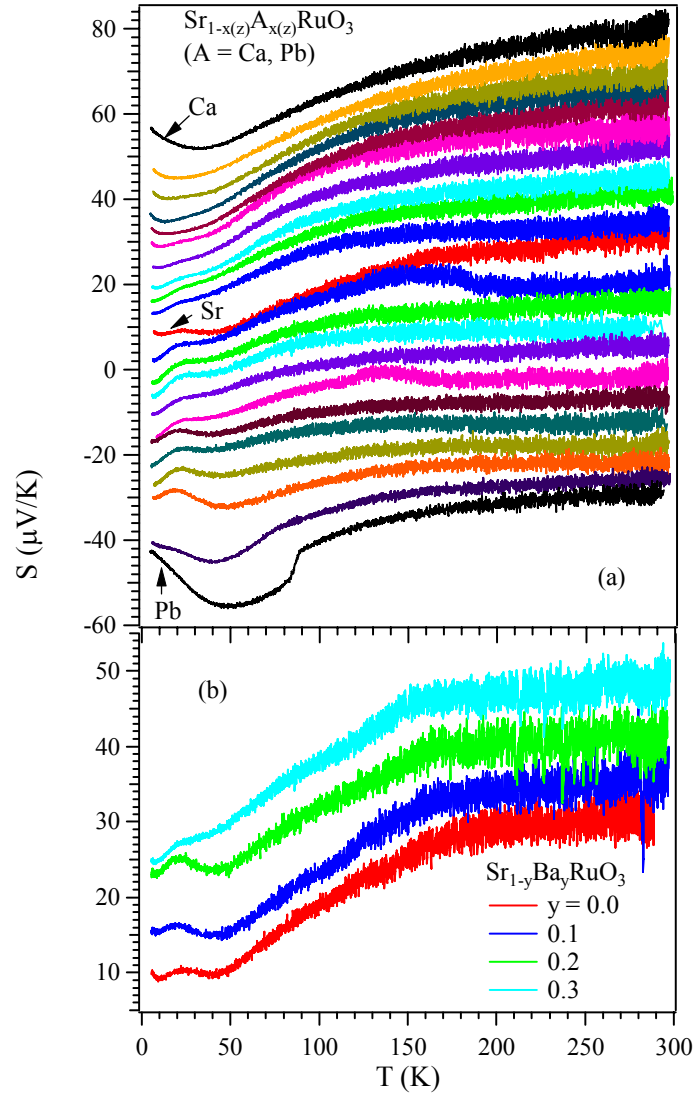
Figure 5.12: Temperature dependence of thermoelectric power S(T) for perovskites (a) $Sr_{1-x(z)}A_{x(z)}RuO_3$ (A = Ca and Pb) and (b) $Sr_{1-y}Ba_yRuO_3$. All curves except $SrRuO_3$ were shifted vertically for clarification.
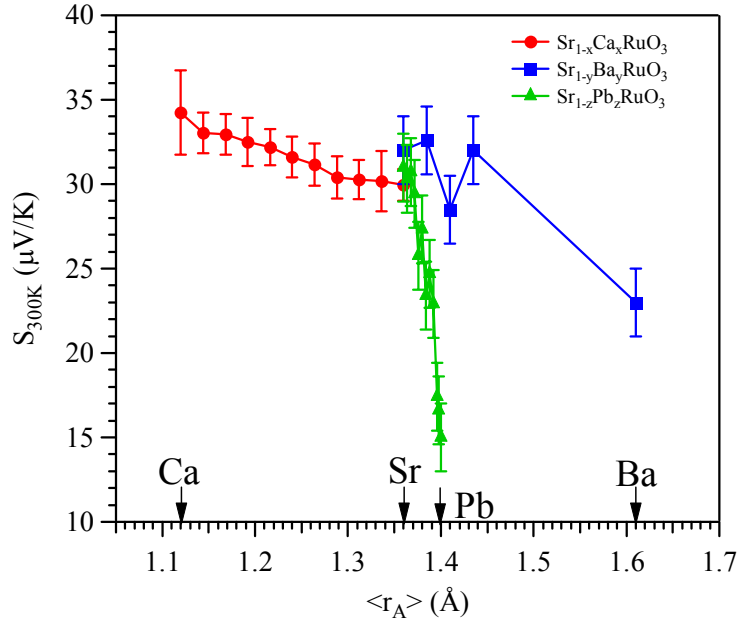
Figure 5.13: Thermoelectric power at room temperature as a function of average A-
cation size of the Ca, Pb and Ba substituted SrRuO$_3$.

5.4 CONCLUSION

The phase diagram of Fig. 5.14 for the Sr$_{1-z}$Pb$_z$RuO$_3$ system summarizes the major results of this study. The orthorhombic perovskite structure with the *Pbnm* space group has been found in all Pb substituted samples of Sr$_{1-z}$Pb$_z$RuO$_3$ to low temperatures, except in a narrow area below T$_t$ near PbRuO$_3$ in the phase diagram of T versus z, where a phase transition to another orthorhombic phase with the *Imma* space group takes place. Our results of transport properties show that the phase transition from the *Pbnm* to the *Imma* phase at T$_t$ ≈ 90 K in perovskite PbRuO$_3$ is a metal-metal transition. The Pb substitution does not alter the metallic conduction over the entire phase diagram, including both the *Pbnm* and the *Imma* phases. The Curie temperature T$_c$ in orthorhombic SrRuO$_3$ is gradually reduced as z increases and eventually vanishes near z = 0.6. All

samples with compositions $z > 0.6$ remain paramagnetic to lowest temperature. The influence of quantum critical fluctuations on the transport properties at low temperatures has been observed in compositions near a quantum critical point of $z \approx 0.6$. A comparison of the magnetic properties and thermoelectric power between Pb- and Ba-substituted samples shows conclusively that the orbital hybridization between Pb^{2+} and Ru^{4+} plays an important role to suppress ferromagnetism in Pb-substituted samples. An enhanced hybridization of the Pb-6s and Ru-4d orbitals below T_t that broadens the π^* conduction band of $Ru(IV):t^4$ parentage on the RuO_3 array is also supported by the structural data.
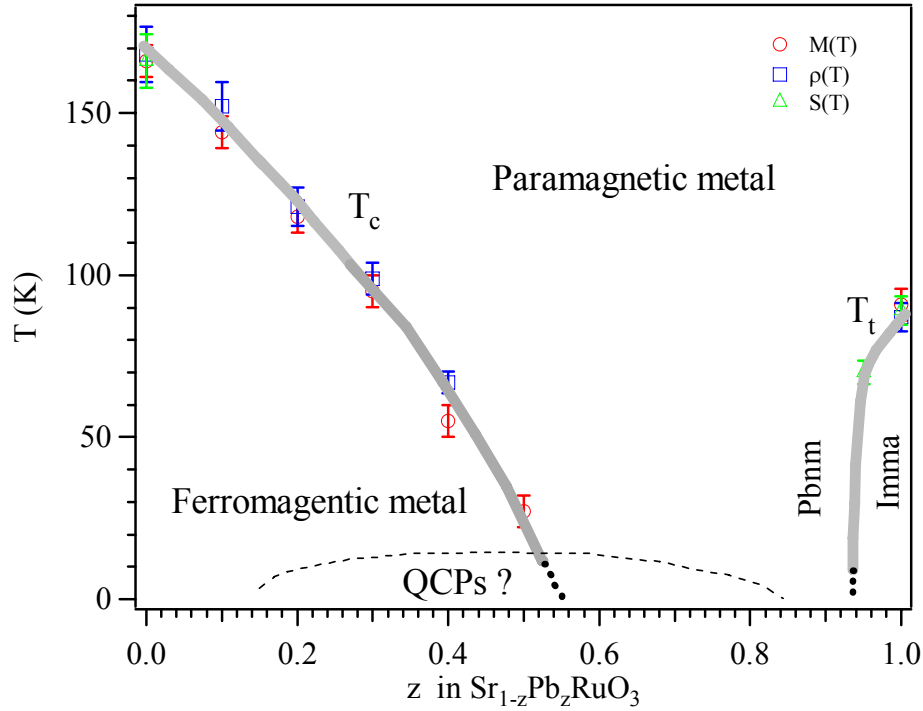
Figure 5.14: The phase diagram of perovskites $Sr_{1-z}Pb_zRuO_3$. Anomalous transport properties such as the extra enhancement in the thermoelectric power and non-Fermi-liquid behavior have been observed below the thin dashed line, that have been discussed in terms of quantum critical fluctuations (QCFs) as a quantum critical point near $z = 0.6$ is approached, see text for the detail.

Chapter 6 Evolution of the structural and physical properties in the BaIrO₃ polytypes

6.1 INTRODUCTION

Recently, BaIrO$_3$ has attracted much attention due to the observation of charge-density-wave (CDW) formation and weak ferromagnetism at the same temperature T$_c$ ≈ 180K.[33, 105, 106] In fact, it is the first known ferromagnet that contains a 5d transition-metal cation in a ternary oxide. The nonmetallic nature of BaIrO$_3$ makes the observation of a CDW quite unusual. In contrast to localized-spin magnetism,[107] Cao *et al.*[33] proposed a model of band magnetism due to a small exchange splitting with an associated CDW below T$_c$ that places a gap at the Fermi surface and induces a subtle lattice distortion at T$_c$. These arguments, based on measurements on a single-crystal sample, were subsequently supported by a tight-binding band-structure calculation,[105] which showed a sharp peak of the density of states at the Fermi level within its π* band of t$_{2g}$-block parentage and partially nested pieces of the Fermi surface. In addition, direct experimental evidence for a small Ir moment comes from a μSR measurement performed by Brooks *et al.*,[108] who observed clear oscillations below T$_c$ and found an extremely small internal field at the muon site, thus ruling out the possibility of a localized spin configuration. On the other hand, a high-resolution photoemission study[106] on BaIrO$_3$ revealed essentially localized electronic states forming a pseudogap at the Fermi energy ε_F for T > T$_c$; below T$_c$ a soft gap opens up at ε_F due to the CDW formation. This observation could also explain a semiconductor to insulator transition in the electrical resistivity. The scenario of a simultaneous onset of a CDW and a ferromagnetic transition was recently questioned by Nakano and Terasaki.[109] They carried out similar I-V measurements as in Ref. 33 on their single-crystal BaIrO$_3$ by using a pulsed current in

order to exclude the self-heating effects, and they observed the giant nonlinear conduction only below 20 K, well below $T_c \sim$ 180K. Instead of a sliding motion of the CDW, they proposed an interplay between two different bands is likely the origin of the nonlinear conduction observed in $BaIrO_3$. Moreover, the critical behavior of the ferromagnetic transition itself is unusual as revealed by the anomalous critical exponents $\beta = 0.82(3)$, $\gamma = 1.03(3)$, and $\delta = 2.20(1)$, which do not belong to any existing universality class.[87] Therefore, the nature of the ferromagnetic transition of $BaIrO_3$ is still under debate.

If prepared under ambient-pressure conditions, the crystal structure of $BaIrO_3$ is monoclinic (space group *C2/m*) and consists of vertex-linked Ir_3O_{12} trimers with three face-sharing $IrO_{6/2}$ octahedra forming columns roughly parallel to the *c* axis.[32] The monoclinic distortion in $BaIrO_3$ generates a twisting and buckling of the Ir_3O_{12} trimers that gives rise to zigzag chains along the *c* axis. Except for the monoclinic distortion, the $BaIrO_3$ is isostructural to the 9R $BaRuO_3$, which has been transformed to the 4H phase at 1.5 GPa, to the 6H phase at 3 GPa, and finally to the 3C phase at 18 GPa. Longo *et al.*[34] have reported that the ambient-pressure phase of $SrIrO_3$ has the monoclinically distorted 6H structure, which transforms to the orthorhombic perovskite structure under high pressure and high temperature. By using the precursor route, Chamberland *et al.*[110] have prepared various $BaIrO_3$ polytypes, such as 3H, 6H, and 18R. It is noteworthy that this 6H $BaIrO_3$ phase is different from the 6H $SrIrO_3$. Powell *et al.*[111] identified, by neutron diffraction, a significant number of oxygen vacancies in a sample of composition $BaIrO_{2.74}$, prepared by quenching the sample from 950°C, whereas an almost stoichiometirc material $BaIrO_{2.94}$ was synthesized by slow cooling the sample; both phases were structurally characterized as the monoclinically distorted polytype related to

9R BaRuO$_3$. To the best of our knowledge, no attempt has been made to characterize the high-pressure phases of BaIrO$_3$. In addition, it has been shown that the physical properties of BaRuO$_3$ polytypes exhibit a strong dependence on the stacking sequence of RuO$_{6/2}$ octahedra.[11] The 9R BaRuO$_3$ is a paramagnetic metal with an unusual temperature dependence of magnetic susceptibility. A calculation that includes a strong spin-orbit coupling can explain the anomalous $\chi(T)$ to a great extent.[31] The evolution from paramagnetic metal to ferromagnetic metal observed for the series of polytypes 9R-4H-6H-3C BaRuO$_3$ indicates an increasing bandwidth W that becomes broad enough to suppress the spin-orbit coupling, but not eliminate the spin-spin interaction as the population of the *C* layers increases. This work motivated us to explore further the evolution of the physical properties of the polytypes of BaIrO$_3$ if they do exist.

In this work, we first explored the structural evolution of BaIrO$_3$ under high pressure up to 10 GPa and 1000°C and identified a new 5H polytype within a very narrow pressure range 3 < P < 5 GPa, besides a 6H phase at P > 5 GPa and a 3C perovskite at 10 GPa as a minority phase. Then, we carried out systematic measurements of magnetic, electronic transport, thermodynamic, low-temperature structural as well as pressure effects on the phase-pure polytypes and showed that the ground states of BaIrO$_3$ evolve from a ferromagnetic insulator with $T_c \approx 180$ K in the 9R phase to a ferromagnetic metal with $T_c \approx 50$ K in the 5H phase, and finally to an exchange-enhanced paramagnetic metal near a quantum critical point (QCP) in the 6H phase.

6.2 EXPERIMENTAL DETAILS

The ambient-pressure phase, 9R BaIrO$_3$, was synthesized by using a conventional solid-state reaction. Stoichiometric mixtures of BaCO$_3$ and Ir metal were thoroughly

mixed in an agate mortar and sintered up to 1000°C for 4 days with several intermediate grindings. The thermal analysis (TGA curve) in reducing conditions (5%H_2/95%Ar flow) of the 9R phase was performed in a Perkin Elmer TGA 7 apparatus in the temperature range between 25 and 730°C with a heating rate of 1°C/min. About 50 mg of sample were used in the experiment. The total weight loss of 8.8% corresponds to 1.96(1) oxygen atoms, implying a starting composition of $BaIrO_{2.96(1)}$, close to the full oxygen stoichiometry. The HPHT experiments were performed in a Walker-type, multianvil pressure module under 10 GPa. XRD patterns were collected at 295 K with Cu K_α radiation in a Philips X'pert diffractometer by step-scanning from 10 to 120° in 2θ in increments of 0.02° and a counting time of 10 s each step. The neutron powder diffraction (NPD) diagram of 5H $BaIrO_3$ was collected at 295 K in the high-resolution D2B diffractometer at ILL-Grenoble. A wavelength of 1.594 Å was selected from a Ge monochromator. The counting time was 12 h with 0.4 g of sample contained in a vanadium can. The sample was obtained by gathering the product of 8 HPHT experiments (50 mg each).

The DC magnetic susceptibility and magnetization were measured with a commercial SQUID magnetometer (Quantum Design). A four-probe method was used to measure the resistivity. Thermoelectric-power measurements were performed in a home-made setup. The steady-state method was used in our thermal conductivity measurement. The specific-heat measurement was carried out on a PPMS (Quantum Design) with the two-τ relaxation method. The magnetic susceptibility under high pressure was measured with a miniature Cu-Be cell fitting the SQUID magnetometer. A piece of Pb as the pressure manometer, the sample, and a mixture of 3M Flourinert FC77 + FC 72 as the pressure medium were sealed in a Teflon capsule. Low-temperature XRD measurements

were carried out in a Schintag theta-theta diffractometer with Cu anode; samples were placed on a cryostat that was cooled down by flowing liquid nitrogen.

6.3 RESULTS AND DISCUSSIONS

6.3.1 High-pressure sequences of $BaIrO_3$

The high-pressure sequence of the perovskite polytypes of $BaIrO_3$ has been investigated in the pressure range up to 10 GPa. Four different polytypes of $BaIrO_3$ were identified as a function of the synthesis pressure. In the pressure range $0 \leq P \leq 3$ GPa the 9R polytype was found; in a narrow pressure interval around 4 GPa a new polytype, called hereafter 5H, was identified; finally, in the $5 \leq P \leq 10$ GPa range the 6H polytype could be stabilized, and at 10 GPa the cubic 3C perovskite could be identified as a minority phase. The crystal structure of the new 5H phase was resolved by direct methods with the EXPO program [112, 113] from XRD data. For the XRD and NPD profile refinements, a pseudo-Voigt function was chosen to generate the line shape of the diffraction peaks. The coherent scattering lengths in the NPD refinements for Ba, Ir, and O were 5.070, 10.60, and 5.803 fm. The neutron absorption of Ir was corrected considering a μr value of 1.90 estimated for the diameter of the sample cylinder. The location of oxygen atoms was performed by Fourier synthesis with the FOURIER programs included in the FULLPROF [70] suite. In the final refinement run the following parameters were refined: background coefficients, zero-point, half-width and pseudo-Voigt parameters for the peak shape; scale factor, positional parameters, occupancy factors for O (NPD data only) thermal isotropic factors and unit-cell parameters. The XRD and NPD patterns after the Rietveld refinements of these $BaIrO_3$ polytypes are shown in Fig. 6.1 and 6.2. The final atomic parameters and the main bond distances and

angles of these BaIrO$_3$ polytypes are given in Tables 6.1 to 6.6. A view of the crystal structures together with the pressure diagram is displayed in Fig. 6.3.
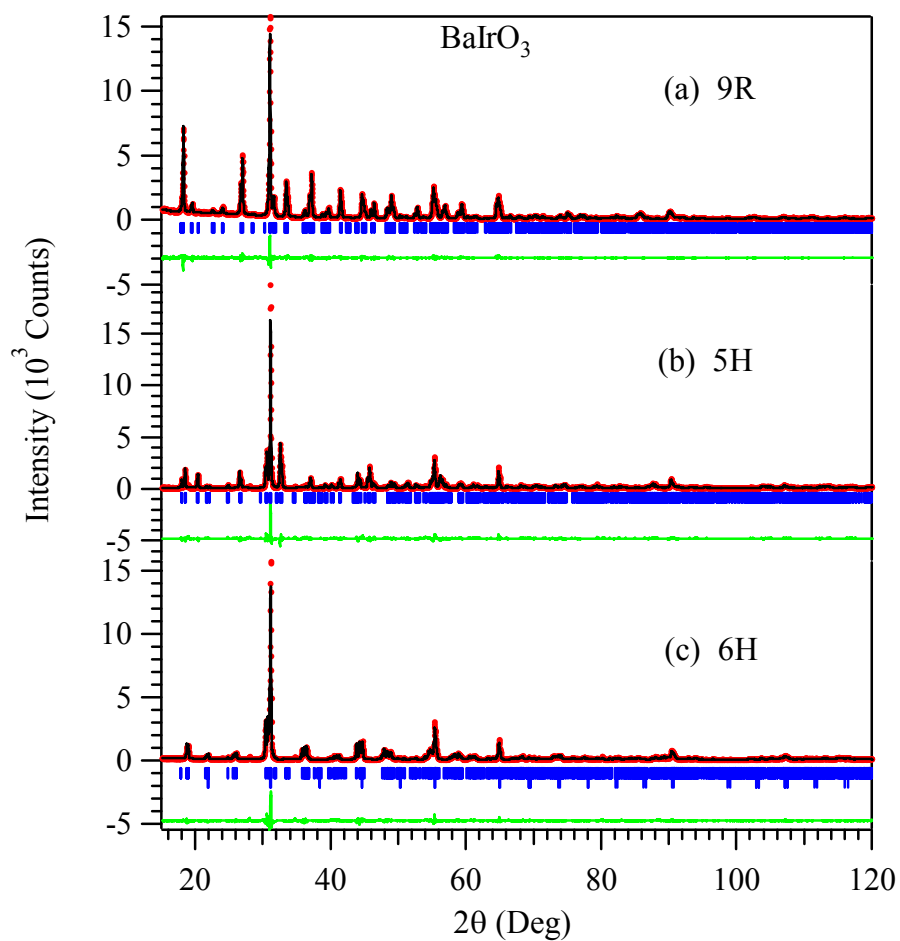
Figure 6.1:   Rietveld refinements of powder XRD patterns of the BaIrO$_3$ polytypes: (a) 9R, (b) 5H, and (c) 6H (5% 3C) phases.
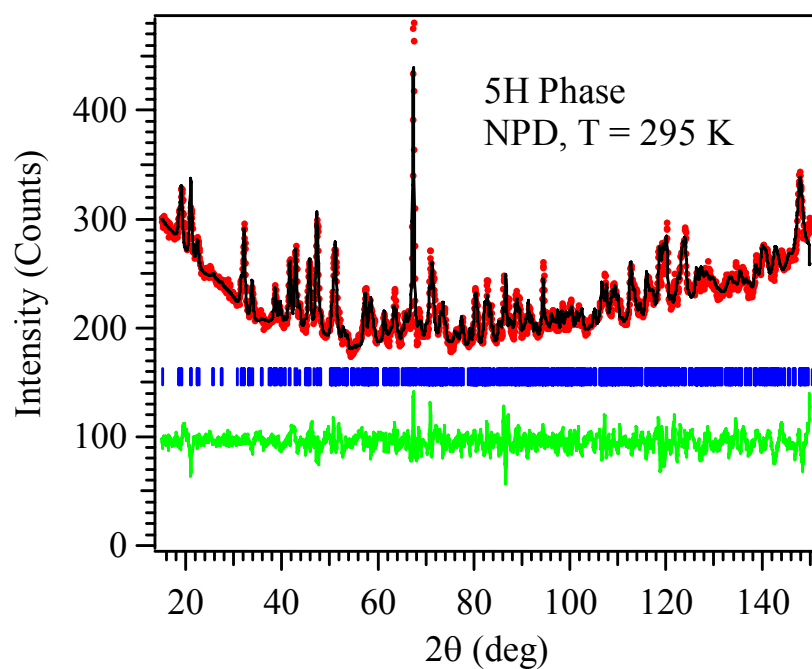
Figure 6.2: NPD pattern of the 5H BaIrO$_3$ at 295 K refined with the Rietveld method.
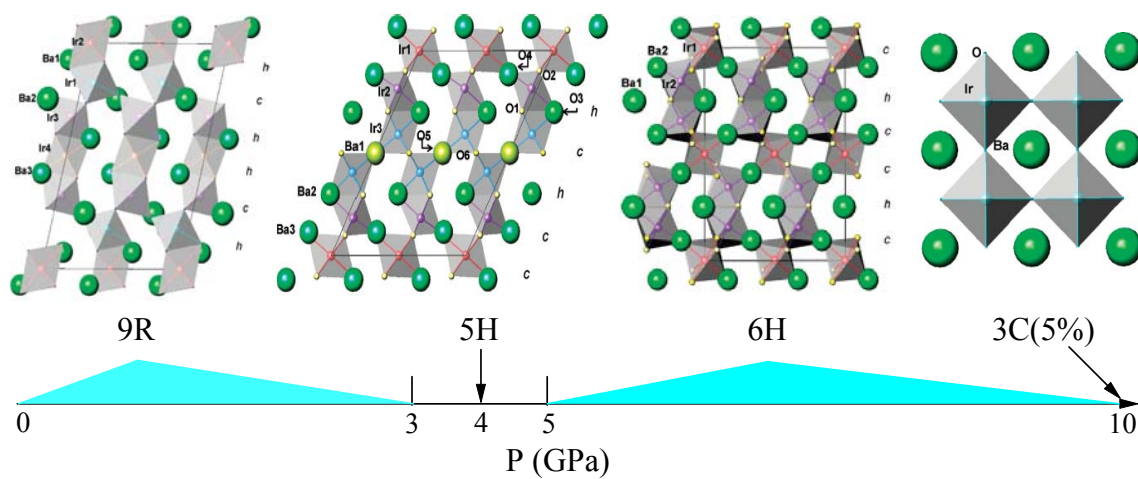
Figure 6.3: Crystal structures of the BaIrO$_3$ polytypes together with the pressure diagram.

9R BaIrO₃   The crystal structure of the 9R polytype is refined in the monoclinic *C2/m* space group with $a = 10.0046(3)$, $b = 5.75362(14)$, $c = 15.1839(4)$ Å, and $\beta = 103.27(1)°$. It contains trimers of face-sharing octahedra (or Ir_3O_{12} trioctahedra) that are linked by their vertices to form columns parallel to the *c* axis, with a stacking of layers of corner sharing (*C*) and face sharing (*h*) $IrO_{6/2}$ octahedra along the sequence *hhChhC*. The monoclinic distortion in $BaIrO_3$ results in a shifting and tilting of the columns relative to each other. Ir1-Ir2 and Ir3-Ir4 distances, of 2.622(3) and 2.644(3) Å, respectively, are very similar to those described for $BaIrO_{2.94}$,[111] of 2.618(4) and 2.627(4) Å, respectively, which supports a full oxygen stoichiometry for the present compound since these metal-metal distances are very sensitive to the oxygen contents of the sample: for oxygen deficient $BaIrO_{2.74}$, Ir1-Ir2 and Ir3-Ir4 distances were described to take the values 2.557(7) and 2.619(7) Å respectively. The observed Ir-Ir distances are even smaller than the separation of 2.72 Å found in Ir metal, which indicates significant interactions between iridium cations at the centre of face shared pairs of octahedra.

It was interesting to estimate the valence of the Ir cations by means of the Brown's bond valence model,[114, 115] which gives a phenomenological relationship between the formal valence of a bond and the corresponding bond length. The valence is the sum of the individual bond valences (s_i) for Ir-O bonds; the individual bond valences are calculated as $s_i = \exp[(r_0-r_i)/B]$; $B = 0.37$, $r_0 = 1.870$ for the $Ir^{4+}-O^{2-}$ pair. The bond valences of the four kinds of Ir cations were 2.91+, 2.74+, 3.91+ and 2.76+ for Ir1 to Ir4 atoms, respectively. They are significantly smaller than the expected value of 4+. This is a consequence of the metal-metal bonding within the trimers where a large fraction of the bonding power of Ir is used. In fact, the lowest valence is observed for Ir2 and Ir4, which

are located in the center of the trimers and therefore are expected to present a higher contribution of metal-metal bonding.

It is important to notice that, although this polytype has been compared to the 9R ambient pressure phase of $BaRuO_3$ with rhombohedral symmetry, unit-cell parameters a = 5.755, c = 21.621 Å [116] and a stacking sequence $(hhC)_3$, the monoclinic distortion described for ambient-pressure $BaIrO_3$ indeed involves a shorter periodicity, with a stacking sequence $(hhC)_2$ along the c axis, as is shown in Fig. 6.3(a). It is worth mentioning that Mn-doped $BaIrO_3$, prepared at ambient pressure, indeed exhibits the 9R structure, defined in the space group $R\bar{3}m$ with $a \approx 5.7$ and $c \approx 21.4$ Å, in the compositional range $BaIr_xMn_{1-x}O_3$, x = 0.3, 0.4 and 0.5. [117]

5H BaIrO₃ The 9R polytype is stable up to 3 GPa; at 4 GPa a new 5H polytype has been stabilized as a pure phase, stable in a narrow pressure range. The systematic absences were consistent with the *C2/m* space group. The estimated crystallographic density from that of the 9R polytype yielded Z = 10. The crystal structure was solved by direct methods from powder XRD data with the EXPO program, which enabled the localization of the Ba and Ir atoms. The oxygen atoms were located in successive Fourier synthesis. The exact positions of the oxygen atoms were refined from NPD data. The crystal structure was refined in the monoclinic *C2/m* space group with a = 9.9511(2), b = 5.7503(1), c = 13.71003(3) Å, β = 118.404(2)°. The structure contains chains of double dimer units of face-sharing octahedra; the twin dimers are connected to single layers of vertex-sharing octahedra, forming infinite chains along c. This polytype can be described as stacking $IrO_{6/2}$ octahedra along the sequence *hChCC*, Fig. 6.3(b). This is a unique

138

stacking sequence which, with this repetition length, had never been described before among the hexagonal polytypes of AMO_3 perovskites.

The occupancy factors of all the oxygen atoms were refined; those of O1, O3, O4, O5, and O6 converged to values slightly higher than unity and then they were fixed to 1.0; for O2 the occupancy factor converged to 0.923(4). This implies a crystallographic formula $BaIrO_{2.938(3)}$, slightly oxygen deficient in agreement with the thermal analysis data for the starting material (9R phase). Ir-O distances vary in the range 1.90 Å for Ir1-O4 to 2.23 Å for Ir2-O3. The average value, of 2.03 Å, is consistent with the ionic radii sum for Ir^{4+} (0.625 Å) and O^{2-} (1.40 Å).[27] It is noteworthy that the structure contains three kinds of octahedra with rather distinct average sizes: <Ir-O> are 1.985, 2.072 and 2.017 Å for Ir1, Ir2 and Ir3 octahedra. The two largest octahedra, Ir2 and Ir3, are those forming dimers, where the Ir-O bonds are weakened by the Ir-Ir bonds. Additionally, these Ir cations are linked to O2, for which a slight oxygen deficiency was detected. According to these bond distances, the bond valences for the three types of octahedra are 4.26(8)+, 3.35(8)+ and 4.06(9)+, indicating that Ir1 and Ir2 are under certain compressive and tensile stresses, respectively. Within the Ir_2O_9 dimers the Ir2-Ir3 bond lengths are 2.77 Å. This distance is conspicuously larger than the separation of 2.72 Å found in Ir metal, which suggests a weaker metal-metal bond between iridium cations across the shared faces of adjacent octahedra within the dimers.

6H BaIrO₃ The 5H polytype is stable in a narrow pressure range; at 5 GPa the 6H structure is formed, stable up to 10 GPa. The 6H-$BaIrO_3$ polytype is monoclinic, space group *C2/c* with *a* = 5.7483(2), *b* = 9.9390(3), *c* = 14.3582(5) Å, and *β* = 91.319(2)°. The structure consists of dimers of face-sharing octahedra separated by single

corner- sharing octahedra, showing the sequence *hCChCC* along the *c* axis. It is clear that it contains two distinct metal sites; Ir1 shares only vertices with adjacent octahedra whilst Ir2 shares both vertices and faces with neighbouring octahedra. The $Ir2O_{6/2}$ octahedra within the dimers are considerably more expanded than the $Ir1O_{6/2}$ octahedra with average Ir-O distances of 2.16 and 1.99 Å, respectively. This is probably a consequence of the metal-metal bond linking the couples of Ir2 atoms in the dimers with Ir2-Ir2 distances of 2.710(3) Å. As a result of the different octahedral sizes, the bond valences for Ir1 and Ir2 are 4.3(2)+ and 2.8(1)+, respectively.

3C BaIrO₃ The 6H polytype was identified at three pressures: 5, 7.5 and 10 GPa. During the refinement of the crystal structure of the 6H phase obtained at 10 GPa from XRD data, the disagreement observed in certain reflections, at Bragg positions corresponding to the perovskite aristotype, made it advisable to introduce as a second phase a perovskite model for $BaIrO_3$ defined in the space group $Pm\overline{3}m$, with Ir at 2*a* (0,0,0), Ba at 2*b* (0.5,0.5,0.5) and O at 3*c* (0.5,0,0) sites. The refinement converged with excellent discrepancy factors for both 6H (R_{Bragg} = 4.90%) and 3C (R_{Bragg} = 2.48%) polytypes. From the scale factors it was possible to estimate the amount of 3C phase as 5%. The unit-cell parameter of this ideal perovskite phase is 4.0611(7) Å. This is expected to be the high-pressure phase of $BaIrO_3$, which could not be stabilized pure under the maximum pressure conditions (P ≤ 10 GPa) but, at least, it could be identified as a minority phase at 10 GPa. The Ir-O distances are 2.0306(4) Å, with a corresponding bond valence for Ir cations of 3.89+, close to the expected value of 4+. Ba atoms are coordinated to 12 atoms at equal distances of 2.8717(5) Å.

Table 6.1: Atomic coordinates and isotropic thermal factors B_{iso} [Å^2] for 9R BaIrO$_3$ from powder XRD data[a] at 295 K; Space group $C2/m$, a = 10.0046(3), b = 5.75362(14), c = 15.1839(4) Å, β = 103.27(1)°, V = 850.69(4) Å^3, Z = 12.

atom	site	x	y	z	B_{iso}(Å)
Ba1	4i	0.7757(5)	0.0	0.2491(4)	1.33
Ba2	4i	0.3689(5)	0.0	0.0733(3)	1.39
Ba3	4i	0.1521(4)	0.0	0.4239(3)	1.52
Ir1	4i	0.0863(3)	0.0	0.17660(18)	0.87
Ir2	2a	0.0	0.0	0.0	1.19
Ir3	4i	0.4658(3)	0.0	0.32206(18)	0.60
Ir4	2d	0.5	0.0	0.5	0.64
O1	4i	0.301(3)	0.0	0.229(2)	1.4(2)
O2	8i	0.051(2)	0.264(4)	0.2608(17)	1.4(2)
O3	4i	0.879(4)	0.0	0.099(2)	1.4(2)
O4	8j	0.123(2)	0.272(5)	0.0790(17)	1.4(2)
O5	8j	0.386(2)	0.240(5)	0.4038(16)	1.4(2)
O6	4i	0.662(4)	0.0	0.424(2)	1.4(2)

[a] Discrepancy factors: R_p = 5.32%, R_{wp} = 6.71%, R_{exp} = 5.01%, χ^2 = 1.79, R_{Bragg} = 2.85%.

Table 6.2: Main interatomic distances (Å) and angles (°) of 9R BaIrO$_3$ from powder XRD data at 295 K.

IrO$_6$ octahedra			BaO$_{12}$ cuboctahedra		
Ir1	–O1	2.11(3)	Ba1	–O1	2.910(5) × 2
	–O2	2.07(2) × 2		–O2	3.11(2) × 2
	–O3	2.14(4)		–O2	2.67(2) × 2
	–O4	2.24(3) × 2		–O3	2.71(4)
<Ir1–O>		2.15		–O4	2.99(2) × 2
				–O5	2.79(2) × 2
Ir2	–O3	2.14(4) × 2		–O6	3.12(5)
	–O4	2.17(2) × 4	<Ba1–O >		2.90
<Ir2–O >		2.16			
			Ba2	–O1	2.61(3)
Ir3	–O1	1.91(3)		–O2	3.30(2) × 2
	–O2	1.95(2) × 2		–O3	3.16(3)
	–O5	2.13(3) × 2		–O3	2.902(4) × 2
	–O6	2.20(4)		–O4	2.93(2) × 2
<Ir3–O >		2.05		–O4	2.84(2) × 2
				–O4	2.68(3) × 2
Ir4	–O5	2.14(2) × 4	<Ba2–O >		2.92
	–O6	2.19(5) × 2			
<Ir4–O >		2.17	Ba3	–O2	2.88(2) × 2
				–O5	2.79(2) × 2
<Ir–O >		2.12		–O5	3.01(2) × 2
				–O5	3.11(3) × 2
Ir1	–Ir2	2.622(3)		–O6	2.61(4) × 2
Ir3	–Ir4	2.644(3)		–O6	2.88(1) × 2
			<Ba3–O >		2.90
Ir1–O1–Ir3		155.4(11)			
Ir1–O2–Ir3		164.2(10)	<Ba–O >		2.91
Ir1–O3–Ir2		75.7(14)			
Ir1–O4–Ir2		72.8(10)			
Ir3–O5–Ir4		76.5(10)			
Ir3–O6–Ir4		73.9(16)			

Table 6.3: Atomic coordinates and isotropic thermal factors B_{iso} [Å^2] for 5H BaIrO$_3$ from NPD data[a] at 295 K; Space group $C2/m$, $a = 9.9554(8)$, $b = 5.7434(6)$, $c = 13.8049(12)$ Å, $\beta = 119.231(6)°$, $V = 688.8(1)$ Å^3, $Z = 10$.

atom	site	x	y	z	B_{iso}(Å)	f_{occ}
Ba1	2c	0.5	0.5	0.5	1.2(5)	1.0
Ba2	4i	-0.191(2)	0.0	0.7139(12)	0.1(3)	1.0
Ba3	4i	-0.247(2)	0.5	0.8886(15)	0.9(3)	1.0
Ir1	2a	0.0	0.0	0.0	3.2(4)	1.0
Ir2	4i	-0.4529(12)	0.0	0.8215(8)	1.03(16)	1.0
Ir3	4i	-0.6046(14)	0.0	0.5920(10)	2.4(2)	1.0
O1	8j	0.053(2)	0.721(3)	0.7002(13)	2.3(3)	1.0
O2	8j	-0.0093(15)	-0.771(2)	0.1085(11)	1.2(3)	0.923(4)
O3	4i	0.703(4)	0.0	0.303(3)	4.0(6)	1.0
O4	4i	0.217(2)	0.0	0.0607(12)	0.6(2)	1.0
O5	2d	0.5	0.0	0.5	1.5(5)	1.0
O6	4f	0.75	0.75	0.5	3.9(5)	1.0

[a] Discrepancy factors: $R_p = 2.40\%$, $R_{wp} = 3.22\%$, $R_{exp} = 1.28\%$, $\chi^2 = 6.34$, $R_{Bragg} = 9.35\%$.

Table 6.4: Main interatomic distances (Å) and angles (°) of 5H BaIrO$_3$ from NPD data at 295 K.

IrO$_6$ octahedra			BaO$_{12}$ cuboctahedra		
Ir1	–O2	2.029(15) × 4	Ba1	–O1	3.010(18) × 4
	–O4	1.898(18) × 2		–O3	2.88(3) × 2
<Ir1–O>		1.985		–O5	2.8717(3) × 2
				–O6	2.8733(2) × 4
Ir2	–O1	2.12(2) × 2	<Ba1–O >		2.920
	–O2	1.963(17) × 2			
	–O3	2.23(3)	Ba2	–O1	2.99(3) × 2
	–O4	2.105(18)		–O1	2.77(3) × 2
<Ir2–O >		2.072		–O2	2.635(16) × 2
				–O3	2.879(3) × 2
Ir3	–O1	2.004(17) × 2		–O4	3.25(3)
	–O3	2.11(5)		–O5	3.051(13)
	–O5	1.997(17)		–O6	3.071(15) × 2
	–O6	1.994(7) × 2	<Ba2–O >		2.916
<Ir3–O >		2.017			
			Ba3	–O1	2.87(2) × 2
<Ir–O >		2.033		–O2	3.197(18) × 2
				–O2	2.97(2) × 2
Ir2	–Ir3	2.765(16)		–O2	2.78(3) × 2
				–O3	2.88(5)
Ir2–O1–Ir3		84.0(10)		–O4	2.936(5) × 2
Ir1–O2–Ir2		165.1(8)		–O4	2.57(3)
Ir2–O3–Ir3		79.1(17)	<Ba3–O >		2.915
Ir1–O4–Ir2		160.3(9)			
Ir3–O5–Ir3		180.0(15)	<Ba–O >		2.917
Ir3–O6–Ir3		180.0(6)			

Table 6.5: Atomic coordinates and isotropic thermal factors B_{iso} [Å^2] for 6H BaIrO$_3$ from powder XRD data[a] at 295 K; Space group $C2/c$, a = 5.7483(2), b = 9.9390(3), c = 14.3582(5) Å, β = 91.319(2)°, V = 820.12(5) Å^3, Z = 12.

atom	site	x	y	z	B_{iso}(Å)
Ba1	4e	0.0	-0.0052(6)	0.25	0.3(1)
Ba2	8f	0.0078(6)	0.3349(6)	0.0912(2)	0.25(8)
Ir1	4a	0.0	0.0	0.0	0.4(1)
Ir2	8f	0.9936(4)	0.3323(4)	0.8442(1)	0.27(5)
O1	4e	0.0	0.499(4)	0.25	-0.2(3)
O2	8f	0.218(5)	0.239(3)	0.2427(16)	-0.2(3)
O3	8f	0.036(5)	0.846(4)	0.0852(17)	-0.2(3)
O4	8f	0.286(6)	0.087(3)	0.049(2)	-0.2(3)
O5	8f	0.809(6)	0.090(3)	0.103(2)	-0.2(3)

[a] Discrepancy factors: R_p = 9.22%, R_{wp} = 12.2%, R_{exp} = 6.38%, χ^2 = 3.62, $R_{Bragg(6H)}$ = 4.90%, $R_{Bragg(3C)}$ = 2.48%.

Table 6.6: Main interatomic distances (Å) and angles (°) of 6H $BaIrO_3$ from powder XRD data at 295 K.

IrO_6 octahedra				BaO_{12} cuboctahedra			
Ir1	–O3	1.93(3)	× 2	Ba1	–O1	2.8743(3)	× 2
	–O4	2.02(3)	× 2		–O2	2.78(3)	× 2
	–O5	2.01(3)	× 2		–O2	2.97(3)	× 2
<Ir1–O>		1.99			–O3	2.76(3)	× 2
					–O4	3.52(3)	× 2
Ir2	–O1	2.19(4)			–O5	2.51(3)	× 2
	–O2	2.22(3)		<Ba1–O >		2.90	
	–O2	2.23(3)					
	–O3	2.10(4)		Ba2	–O1	2.77(3)	
	–O4	2.09(3)			–O2	2.65(3)	
	–O5	2.11(4)			–O2	2.88(3)	
<Ir2–O >		2.16			–O3	3.16(3)	
					–O3	2.73(3)	
<Ir–O >		2.10			–O3	3.03(3)	
					–O4	3.04(3)	
Ir2	–Ir2	2.710(3)			–O4	2.85(3)	
					–O4	2.44(3)	
Ir2–O1–Ir2		76.4(15)			–O5	2.77(3)	
Ir2–O2–Ir2		75.1(10)			–O5	3.00(3)	
Ir1–O3–Ir2		164.4(15)			–O5	3.40(3)	
Ir1–O4–Ir2		151.4(12)		<Ba2–O >		2.89	
Ir1–O5–Ir2		153.6(14)					

As a general trend, the A-O bond is more compressible than the M-O bond in AMO_3 perovskites; therefore, the A-O bond length decreases more rapidly with pressure, and so does the tolerance factor (dt/dP < 0), leading to the stabilization of the cubic *vs* hexagonal stacking. This is also consistent with pressure stabilizing preferentially the denser phase since in the 3C perovskite A cations exhibit 12-fold oxygen coordination whereas in hexagonal polytypes this coordination is reduced to (6+6) or lower. The observed crystallographic densities of the 9R, 5H, 6H and 3C phases of $BaIrO_3$ were 8.84, 9.08, 9.17 and 9.36 g/cm^3, respectively. They progressively increase as expected since these phases have been stabilized at increasing pressures; the 3C perovskite was identified as a minority phase together with the 6H polytype at 10 GPa. This sequence corresponds, therefore, to denser packings of the BaO_3 layers along the *c* axis, showing an evolution to structures with more corner-sharing and fewer face-sharing octahedra, corresponding to a decreasing value of the tolerance factor under pressure. In fact, the Ba coordination polyhedra become progressively more regular with lower deviations from the average distances.

It is evident that the application of external pressure destabilizes the structure with multiple face-sharing octahedra as the cations are forced closer together. Eventually, the cation repulsion exceeds the metal-metal bonding involved in the octahedral face-sharing. In general, the intermediate polytypes occur only in a narrow transitional interval of the tolerance factor. Because Δt is small, it is possible to find examples where the various polytypes are stabilized successively with increasing pressure. The classical sequence 2H→9R→4H→6H→3C was described by Longo *et al.*[16] and Dance *et al.*[118] The paradigmatic example of $BaRuO_3$ has been intensively investigated; it shows a pressure evolution along the sequence 9R-4H-6H-3C.[6] Similar behavior has been described for

many oxides, fluorides and chlorides; for instance $CsMnCl_3$ transforms from the ambient pressure 9R structure to the cubic 3C polytype via a 6H structure.

The interval of pressure stability of the 5H polytype of $BaIrO_3$ is probably smaller than 1 GPa. Experiments performed at 3 GPa yielded the pure 9R polytype, at 4 GPa the 5H phase was stabilized as a pure phase, whereas at 5 GPa the 6H polytype was formed. The stability range of 5H $BaIrO_3$ is, therefore, very narrow, which explains why it was not described before. There is a reference to the formation of 6H $BaIrO_3$ at 5 GPa, in agreement with our observation, but no details on this polytype have been published.[119] On the other hand, the synthesis of 5H $BaIrO_3$ was shown to be perfectly reproducible under the same conditions, as verified when preparing the large sample for the NPD study obtained from 8 HPHT experiments yielding single-phase products with identical XRD patterns.

In order to understand the sequence of transitions observed in $BaIrO_3$, comparison with the $BaRuO_3$ case is enlightening. In this compound the 9R ambient-pressure structure, with a stacking sequence $(hhC)_3$, containing 1/3 of cubic *vs* hexagonal stacking, transforms at 3 GPa into the 4H ($hChC$) polytype, having equal amounts of cubic and hexagonal stackings. Finally, at 5 GPa there is a phase transition to the 6H (hCC)$_2$ polytype, containing 2/3 of cubic stacking. In spite of the slightly smaller tolerance factor of $BaIrO_3$ (t = 1.051) with respect to $BaRuO_3$ (t = 1.054), which would normally require a lower external pressure to induce the first phase transition, $BaIrO_3$ does not undergo a structural transformation up to 4 GPa where the pressure stabilizes a 4H-6H hybrid polytype 5H ($hChCC$) with a higher proportion of cubic stacking (3/5) than the 4H structure. The reason for this different behavior is certainly related to a

higher stability of 9R BaIrO$_3$ with respect to 9R BaRuO$_3$. Let us recall that BaRuO$_3$ crystal structure is defined in the rhombohedral space group $R\overline{3}m$ whereas BaIrO$_3$ exhibits a monoclinic distortion with the same basic stacking sequence. The main difference between both crystal structures is that whereas the Ru-Ru distance in BaRuO$_3$ is relatively short, 2.55 Å,[116] the Ir-Ir distance in 9R BaIrO$_3$ is considerably longer, 2.622(3) Å for Ir1-Ir2 and 2.644(3) Å for Ir3-Ir4. These longer distances are associated with the larger radial extension of the Ir 5d orbitals, accounting for a higher equilibrium distance for the metal-metal bonding, even though the ionic sizes of Ir^{4+} (0.625 Å) and Ru^{4+} (0.620 Å) are very similar [27] in octahedral coordination. Also, a greater number of d electrons on the Ir^{4+} ions than the Ru^{4+} ions lead to weaker, longer bonds to oxygen and to estimated bond valences for Ir significantly smaller than 4+. Despite the longer Ir-Ir distances across the face-sharing octahedra, stronger Ir-Ir bonding makes this structure considerably more stable toward an external applied pressure, in a range P < 4 GPa. At 4 GPa, stabilization of a polymorph with a greater proportion of cubic stacking than that of the 4H phase is required, leading to the formation of the 5H polymorph where the size of the three kinds of IrO$_{6/2}$ octahedra are more similar and the charge distribution corresponds more precisely to the expected 4+ value. This intermediate phase has the particularity of showing a considerably larger Ir-Ir distance within the dimers of face-sharing octahedra, 2.76 Å, implying a weaker metal-metal bonding and a stronger Ir-O bonding. Finally, the subsequent application of increasing external pressure leads to the collapse of this phase, giving rise to the 6H polymorph with smaller Ir-Ir bond lengths of 2.71 Å. It is a delicate balance between the external pressure and the Ir-Ir repulsion across the face-sharing octahedra and the trend to decrease the hexagonal *vs* cubic packing ratio that makes possible the formation of this unreported polymorph in an extremely narrow range of pressures.

Another clue for understanding the significant stability of the ambient pressure 9R $BaIrO_3$ phase can be related to the particular stability of $SrIrO_3$; despite a tolerance factor below unity (t = 0.97), it prefers to adopt the hexagonal 6H polytype instead of the 3C perovskite structure at ambient pressure [34] whereas most of the remaining $SrBO_3$ compounds (B = Ti, Zr, Hf, Mo, Cr, Ru, Fe, Sn, Pb) form 3C perovskites. It would appear that the hexagonal polytype is stabilized by the cubic-field outer electron configuration $t_{2g}^5 e_g^0$ for low-spin Ir(IV). In the trigonal field of the hexagonal polytype the t_{2g}^5 orbitals become $e_{g\sigma}^0 e_{g\pi}^4 a_{1g}^1$, which allow for metal-metal bonding along the c axis via the half-filled a_{1g} orbitals. Simultaneously, the 90º Ir-O-Ir π-σ-bond interactions are strengthened. The reinforcement of the Ir-O bonds as well as the formation of stable Ir-Ir bonds seem to stabilize the hexagonal polytypes for $AIrO_3$ compounds, thus accounting for the pressure stability of the 9R BaIrO3 phase containing a large ratio of hexagonal vs cubic packing.

It is noteworthy that the three polytypes 9R, 5H and 6H exhibit a monoclinic symmetry. Whereas for the 6H structures the monoclinic β angles are close to 90°, implying that the chains of face-sharing octahedra are almost perpendicular to the ab plane, the 5H polytype presents a β angle of 119.23°, involving an arrangement where the chains of octahedra are extremely shifted and leaned with respect to the ab plane. This particular arrangement involves a reduced tilting of the IrO_6 octahedra as far as corner sharing is concerned, giving 180° angles for Ir3-O5-Ir3 and Ir3-O6-Ir3 (Table 6.4), which promotes a full overlap between $Ir-e_{g\sigma}^0$ and O-2p orbitals. The formation of these strong σ bonds between Ir atoms of adjacent chains could be the driving force for the exceptional monoclinic distortion. The mentioned overlap suggests improved transport properties for the 5H polytype with respect to the ambient-pressure phase, containing

150

more bent tilting angles interconnecting the chains of octahedra, of 155.4(11)° for Ir1-O1-Ir3 and 164.2(10)° for Ir1-O2-Ir3 (Table 6.2).

The 5H-BaIrO$_3$ phase is the first example of a 5H polytype of a stoichiometric, single-valent perovskite showing *hChCC* stacking. Other phases with a so-called 5H structure have been described in different systems, but they correspond to defective perovskites with different octahedral stackings than that observed in 5H BaIrO$_3$. Compounds of stoichiometry BaIr$_{1-x}$Co$_x$O$_{3-\delta}$ (x = 0.5, 0.7 0.8) [120] have been reported to adopt 12R, 10H, and 5H perovskite structures, respectively, where the distribution of Co and Ir cations over corner-sharing and face-sharing sites has been determined and the Co/Ir-O bond lengths have been used to assign the cation oxidation states as Ir^{5+} and Co^{3+}/Co^{4+}. The 5H polytype of BaIr$_{0.2}$Co$_{0.8}$O$_{2.84}$ is characterized by *hhCCC* stacking, where (Co/Ir)$_3$O$_{12}$ trimers of face-sharing octahedra are separated by two layers of corner-sharing octahedra exclusively occupied by Co. Moreover, some oxygen deficiency is found between the two Co layers of octahedra containing a [BaO$_2$] layer instead of a [BaO$_3$] layer, as observed in 12H BaCoO$_{2.6}$.[121] The reduction of this layer results in the replacement of two corner-sharing octahedra by two unconnected tetrahedra. Something similar is observed in the defective perovskite BaMn$_{0.2}$Co$_{0.8}$O$_{2.80}$,[122] the structure of which can be described as a *CC'Chh* 5H hexagonal polytype with ordered oxygen vacancies where the cubic *C'* layer corresponds to a composition of [BaO$_2$] as opposed to [BaO$_3$]. The resulting layer structure consists of [MnCo$_2$O$_{12}$] blocks of three face-sharing octahedra linked by corners to two unconnected [CoO$_4$] tetrahedra. This stacking sequence is in contrast with that observed in the present work for 5H BaIrO$_3$, characterized by the *hChCC* sequence, in the sense that (i) no oxygen deficiency has been detected in 5H BaIrO$_3$ by neutron diffraction so the octahedral connection is complete

along the c axis and (ii) although both sequences involve the same proportion of h and C stackings, $hhCCC$ present a lower number of changes from hexagonal to cubic and thus it would, in principle, exhibit a higher thermodynamic stability.[6]

A polytypoid 5H with the stacking sequence $ChhCC$ has also been described for a well-known family of defective perovskites of general stoichiometry $A_5B_4O_{15}$ (for instance $Ba_5Nb_4O_{15}$ or $Ba_5Ta_4O_{15}$), defined in the space group $P\bar{3}m1$ and characterized by the presence of a fully ordered distribution of cations and vacancies at the B sublattice.[123] In this structure, which contains chains of three face-sharing octahedra, the vacancies are located in the central octahedron, leading to a maximum separation of the highly charged (e.g. Nb^{5+} or Ta^{5+}) cations.

Finally, very few compounds have been found to crystallize in the rare 15R modification. A paradigmatic example is $BaIr_{0.3}Fe_{0.7}O_{2.95}$, defined in the space group $R\bar{3}m$ with $a \approx 5.73$, $c \approx 35.55$ Å. There are two possible stacking sequences that yield such a cell; these correspond to the $(hhhhC)_3$ which has been reported for the system $BaMnO_{3-\delta}$,[124] and the $(hChCC)_3$ as observed for $SrFe_{0.085}Mn_{0.915}O_{2.979}$ [125] and $BaIr_{0.3}Fe_{0.7}O_{2.949(7)}$.[126] This stacking is similar to that of the 5H polytype described in the present work, but it acquires a triple periodicity. The 15R structure comprises dimers of face-sharing octahedra as well as octahedra that share only vertices with their neighbors. For $BaIr_{0.3}Fe_{0.7}O_{2.949(7)}$,[126] the delicate balance between the stabilities of the 6H and 15R polytypes was highlighted by the presence of a small amount of the 6H phase together with the main 15R phase. This observation is in full agreement with the present findings for the 5H $BaIrO_3$ polytype, which shows a precarious range of stability, giving way to the 6H phase upon a small increment of the external pressure.

6.3.2 Physical properties of the BaIrO₃ polytypes

6.3.2.1 Magnetic properties

Figure 6.4 summarizes the magnetic properties of the three phase-pure $BaIrO_3$ polytypes. The temperature dependence of the dc magnetic susceptibilities $\chi(T)$ were measured with increasing temperature from 5 to 360 K under a magnetic field H = 1 T after zero-field cooling (ZFC) and field cooling (FC). As shown in Fig. 6.4(a), the $\chi(T)$ curves of both 9R and 5H phases exhibit a sharp increase corresponding to a ferromagnetic transition at T_c. From the sharp minimum of the $d\chi_{FC}/dT$ curves, inset of Fig. 6.4(a), values of T_c were determined to be 180 K and 50 K for the 9R and 5H phases, respectively. For both phases, the ZFC and FC $\chi(T)$ curves split at a temperature slightly below T_c, which implies the presence of magnetocystalline anisotropy. The similar change of $\chi(T)$ at $T \leq T_c$ found in the 5H and 9R phases makes the 5H phase a new weak ferromagnetic iridate. The observed T_c = 180 K of the 9R phase is in excellent agreement with those reported in the literature.[33, 107] On the other hand, the 6H phase does not show any magnetic ordering down to 5 K with complete overlapping of the ZFC and FC $\chi(T)$ curves. Thus, with increasing ratio of corner-shared to face-shared $IrO_{6/2}$ octahedra, the magnetic ordering temperature is reduced dramatically from 180 K in the 9R phase to below 5 K in the 6H phase. As shown in Fig. 6.4(b), the $\chi^{-1}(T)$ curves in the paramagnetic region exhibit very weak temperature dependences, suggesting the presence of a large, temperature-independent term, χ_0. Therefore, we have fit the $\chi^{-1}(T)$ in the paramagnetic region with a modified Curie-Weiss (C-W) law, $viz.$ $\chi = \chi_0 + C/(T-\theta)$ and extracted the effective spin-only paramagnetic moment ($\mu_{eff} = \sqrt{8C}$) of the Ir(IV) ions and the Weiss temperatures θ. As shown by the solid lines in Fig. 6.4(b), the fitting is reasonably good. The fitting parameters are given in Table 6.7. The μ_{eff} values increase gradually from 9R to 5H to 6H, but they are much lower than the expected value for the

low-spin Ir(IV) with S = ½. A reduced μ_{eff} is commonly observed in most iridates,[33, 127, 128] and has been attributed to the strong hybridization between iridium 5d and oxygen 2p orbitals. The χ_0 falls into a narrow range 2.08 to 2.88 $\times 10^{-4}$ emu/mol Ir(IV) in these three polytypes. The results for the 9R phase are consistent with those reported by Cao *et al.* [33] on a single-crystal sample.

Figure 6.4(c) displays the hysteresis loops, M(H), measured at T = 5 K after ZFC from 300 K, which indicates that a weak ferromagnetism takes place below T_c in the 9R and 5H phases. Although the remanant field has been checked and balanced carefully during ZFC, M(H) does not start from the origin as H increases from zero and the coercive field is unusually large. The offset of M at H=0 becomes smaller in the 5H phase but it is still visible. On the other hand, any hysteresis loop for the 6H phase is negligible and is symmetric about the origin. The magnetic moment per Ir(IV) site at 5 K and 5 T is rather small in all three phases; it increases from 0.006 μ_B (6H) to 0.007 μ_B (5H) to 0.015 μ_B (9R). It has been argued [33] that the small ordered moment of Ir(IV) is due to the d-p hybridization and a small exchange splitting rather than a canted-spin in the localized spin configuration. If the intrinsic d-p hybridization is assumed to be the same for the three phases, then the evolution of $M_{5K,5T}$ suggests a decreased exchange splitting from the 9R to the 6H phases. The displaced magnetization curve of the 9R phase has also been reported before.[107] The origin of the internal field causing this shift remains unknown.

We note that this band model does not take into consideration the ordering of holes at the face-shared octahedral into *c*-axis orbitals to give three *c*-axis electron/Ir in the trimer in the 9R phase where the Ir-Ir distance is short. With S = 1/2 per trimer in the

9R phase, the ferromagnetic coupling would be between trimers and the moment would be reduced.
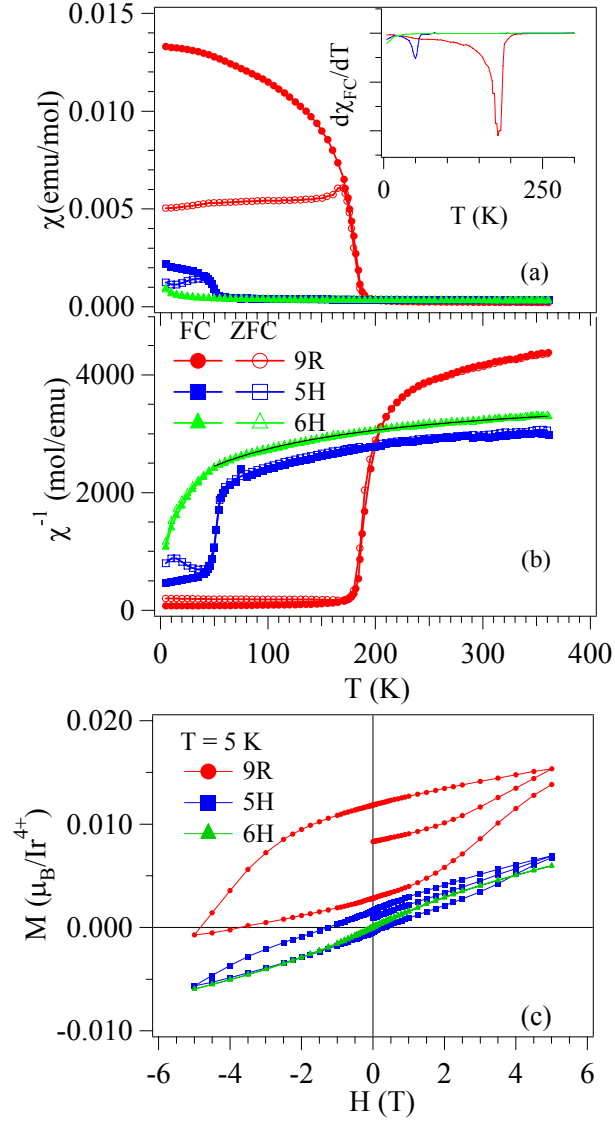
Figure 6.4:   (a) Temperature dependence of the dc magnetic susceptibility χ, (b) χ^{-1}; (c) isothermal magnetization M(H) at 5 K for the three BaIrO$_3$ polytypes: 9R, 5H and 6H. Inset of (a) shows the temperature derivative of the χ_{FC}. Modified Curie-Weiss fitting curves are shown in (b) as the solid lines.

Table 6.7:   Physical properties and fitting parameters of the BaIrO$_3$ polytypes.

		9R	5H	6H
T_c (K)		180(5)	50(3)	/
θ_{CW} (K)		162.9(2.8)	-22.3(1.9)	-64.9(3.5)
μ_{eff} (μ_B/Ir)		0.186(6)	0.346(4)	0.364(6)
χ_0 (10^{-4} emu/mol Ir^{4+})		2.08(1)	2.88(1)	2.64(1)
$M_{5K,\,5T}$ (μ_B/Ir^{4+})		0.015(1)	0.007(1)	0.006(1)
ρ_{300K} (mΩ cm)		12.586	6.92	4.07
ρ_{10K} (mΩ cm)		>35000	3.22	1.62
S_{300K} (μV/K)		6.9	5.1	13.6
γ (10^{-3} J/molK^2)		1.15(8)	6.15(6)	8.99(8)
β (10^{-4} J/molK^4)		5.04(5)	2.23(4)	1.85(5)
δ (10^{-6} J/molK^6)		0.95(5)	1.77(4)	1.27(4)
Θ_D (K)		268.2	351.9	374.5
α_a (10^{-5} K^{-1})	$T > T_c$	1.8(1)	/	/
	$T < T_c$	1.2(2)		
α_b (10^{-5} K^{-1})	$T > T_c$	2.3(1)	/	/
	$T < T_c$	1.9(2)		
α_c (10^{-5} K^{-1})	$T > T_c$	0	/	/
	$T < T_c$	-1.9(2)		
α_V (10^{-5} K^{-1})	$T > T_c$	4.1(4)	/	/
	$T < T_c$	1.1(3)		

6.3.2.2 Transport properties

Figure 6.5 shows the temperature dependence of the resistivity ρ(T) of the BaIrO$_3$ polytypes measured from 8 to 310 K under zero field. The 9R phase of Fig. 6.5(a) is nonmetallic over the entire temperature range. The ferromagnetic transition causes a sharp anomaly as seen in the derivative dlnρ/dT. This result is consistent with the opening up of a soft gap at ε_F due to the CDW formation as reported previously.[33, 106] The weak temperature dependence of ρ(T) at T > T$_c$ does not distinguish whether it is due to a hopping conduction of localized electrons or band conduction with the Fermi energy located in a gap. However, the thermoelectric power at T > T$_c$ in Fig. 6.6 indicates that there are thermally excited carriers, which suggests that it is a semiconductor with a

gap as small as 0.025 eV. The formation of a CDW phase at $T < T_c$ would normally result in a band reconstruction with ε_F remaining in the gap if the CDW wavelength commensurates with the lattice distortion. In this case, a jump of the $S(T)$ at T_c followed by an exponential increase to infinity as T decreases is expected. However, the observed $S(T)$ in Fig. 6.6(a) peaks out at 70 K. The $S(T)$ at low temperatures behaves like the hopping conduction of small polarons. On the other hand, the structural changes of the polytypes make both the 5H and 6H metallic. For the 5H phase, a weak kink anomaly can be discerned in the $\rho(T)$ of Fig. 6.5(b) near $T_c \sim 50$ K, which can be seen more clearly from the $dln\rho/dT$ curve. Similar to the ferromagnetic transition at T_c in Ni [129] or the antiferromagnetic transition at T_N in $Nb_{12}O_{29}$,[130] the anomaly of $\rho(T)$ at the magnetic transition temperatures is due to the critical scattering of the conduction electrons from the short-range spin fluctuations. While the phase transition between different polytype structures just quenches the spin-orbit coupling in the $BaRuO_3$ phase with greater C stacking, the same structural change enlarges the bandwidth so as to induce a semiconductor-metal transition in the $BaIrO_3$ polytypes. The 5H $BaIrO_3$ becomes the first ferromagnetic metal in iridium oxides. As shown in Fig. 6.5(c), the paramagnetic 6H phase is a metal down to 8 K. The structural difference between the 5H phase and the 6H phase is so small that the ferromagnetic transition should be just suppressed in the 6H phase, so a non-Fermi-liquid behavior is expected. In order to check out this possibility, we have fit the $\rho(T)$ below $T < 60$ K with a power-law formula $\rho = \rho_0 + AT^n$, which gives the fitting parameters $\rho_0 = 1.588(1)$ $m\Omega$ cm, A $= 5.7(1) \times 10^{-4}$ $m\Omega$ $cm/$ $K^{1.68}$ and n $=$ 1.68(1) $\sim 5/3$. A straight line in the ρ vs $T^{5/3}$ plot shown in the inset of Fig. 6.5(c) confirms the non-Fermi-liquid (NFL) behavior, which has also been found in systems like $PrNiO_3$ [64] and $ZrZn_2$ [65] in the vicinity of a quantum critical point (QCP). It is interesting to note that the exponents for the $\rho(T)$ curves of the 6H and perovskite $SrIrO_3$ are 3/2 and 2,

respectively.[131] Therefore, the exponent 5/3 suggest that the 6H phase is located near a QCP between the ferromagnetic metallic state of the 5H phase and a Fermi-liquid state of the perovskite phase. Quantum critical fluctuations at low temperatures in the 6H phase have been further confirmed by our thermoelectric power measurement in Fig. 6.6. A superconductive phase has been stabilized at a much lower temperature in some cases in the vicinity of a QCP. We have checked the resistivity of the 6H phase down to 0.05 K in an Oxford dilution refrigerator. No superconductive transition was found. However, we did observe an anomalous temperature dependence of resistance in the 5H phase within the temperature range of a ^{3}He refrigerator. Fig. 6.5(b) shows a steep resistivity drop at T_c followed by a nearly temperature independent $\rho(T)$ down to 8 K. This sample was loaded in a high-pressure chamber mounted on an Oxford Heliox probe and measured to 0.355 K under pressure to 16 kbar. As shown in Fig. 6.7, the resistance undergoes a sharp drop at 3.4 K followed by a semiconducting temperature dependence as temperature further decreases. The transition temperature T_t is reduced slightly under pressure; but the resistance drop becomes sharper under pressure. Since no anomaly of the magnetic susceptibility was found, the sharp drop of resistance at T_t is likely caused by superconductive pair fluctuations. The transition to a bulk superconductive phase is truncated by a charge density wave phase at T_t-δT. The origin of this transition deserves further study.
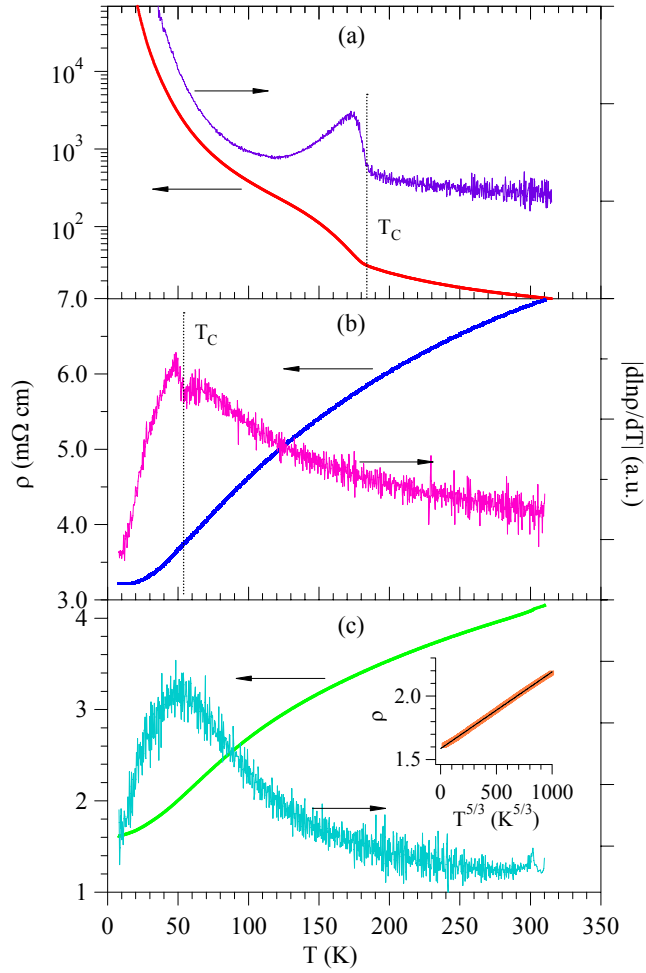
Figure 6.5: Temperature dependence of the resistivity ρ and its derivative $|d\ln\rho/dT|$ of the BaIrO$_3$ polytypes: (a) 9R, (b) 5H, and (c) 6H. A plot of ρ vs T$^{5/3}$ for the 6H BaIrO$_3$ was shown in the inset of (c).

The overall temperature dependence of the thermoelectric powers of the 5H and 6H phases are similar, $i.e.$ they increase gradually with decreasing temperature and exhibit a broad maximum around 50-60 K as shown in Fig. 6.6(b). An inflection point near 50 K in the 5H phase appears to correlate with the ferromagnetic transition. However, the magnitude of S(T), especially the enhancement at low temperatures in the

159

6H phase, is much larger than that of the 5H phase. The 6H phase has a smaller resistivity, but a much higher S(T) than that of the 5H phase. The NFL behavior of the ρ(T) at low temperatures indicates that the 6H phase may be located at a QCP at the boundary between a ferromagnetic phase and a paramagnetic phase. We can test this possibility by the plot of S/T *vs* lnT since a linear relationship has been predicted theoretically [132] and observed in other systems [133] close to the QCP. As shown in Fig. 6.6(c), a linear fit can be made in the plot of S/T *vs* lnT over a wide temperature range below 90 K in the 6H phase, which supports the argument of a QCP. In contrast, the linear fitting is not valid in the S/T *vs* lnT plot of the 5H phase in Fig. 6.6(c). Since the π^* bandwidth changes in a small step between two neighboring phases in a series of polytype structures, we have fortunately found a QCP, which is normally located only by fine tuning the bandwidth with hydrostatic pressure, magnetic field, and/or chemical substitution. Further measurements of the electrical resistivity and thermoelectric power under high pressure for the 6H phase are in progress in order to check whether a Fermi-liquid phase can be restored by broadening the bandwidth. Although we have not yet synthesized the pure 3C phase sample, the sample synthesized under 10 GPa includes 5% 3C phase. Its thermoelectric power, shown in Fig. 6.6(b), is smaller than that of the 6H phase sample. The thermoelectric power is dominated by the most conductive phase in case of a multiphase coexistence. A reduced S(T) observed in the sample with 5% 3C phase indicates that the 3C phase may have an S(T) without the enhancement seen in the 6H phase.
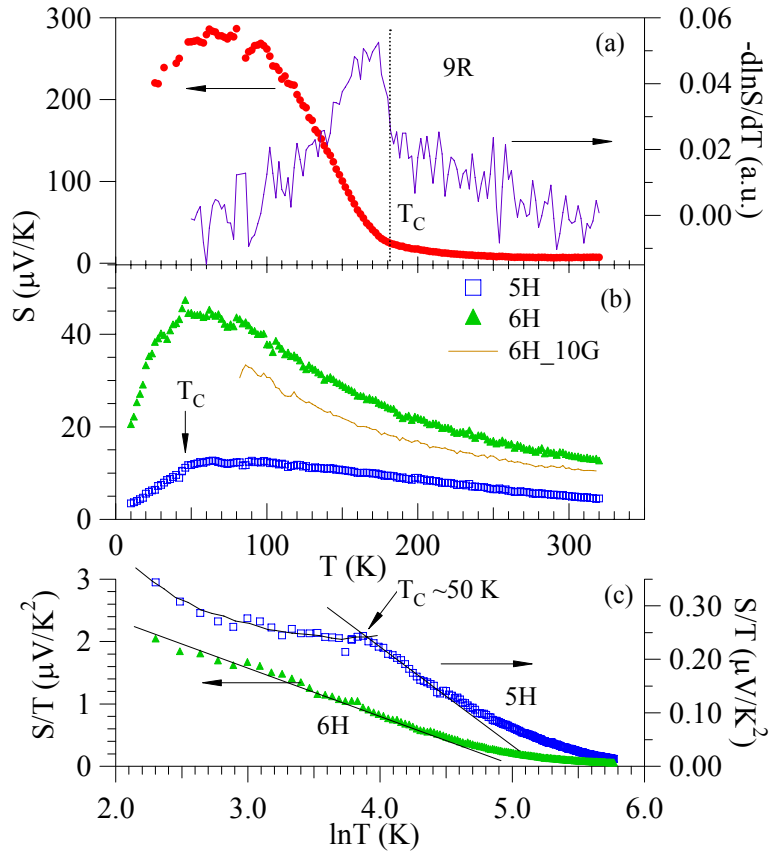
Figure 6.6: Variation with temperature of the thermoelectric power S(T) for (a) 9R and (b) 5H and 6H phases. For the 9R phase, the ferromagnetic transition T_c can be seen more clearly in the -dlnS/dT curve. The S(T) data of the 5H and 6H phases were replotted in the form of S/T *vs* lnT in (c).
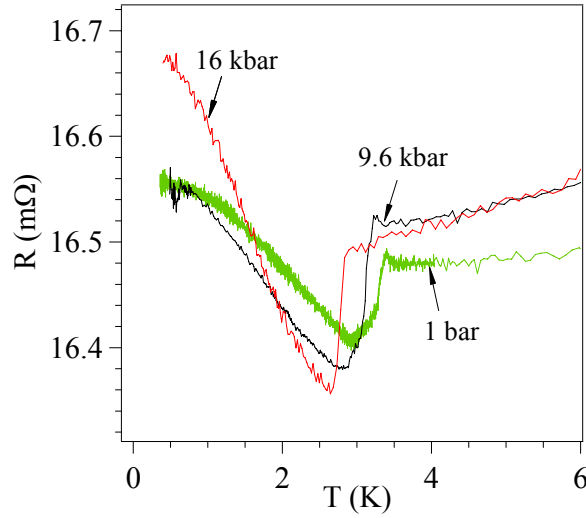
Figure 6.7:   Temperature dependence of the resistance for the 5H phase under different pressures. Curves under pressure have been shifted to the level of that at ambient pressure for clarification.

6.3.2.3 Specific heat

The specific-heat data for these three polytypes are shown in Fig. 6.8. Weak anomalies can be discerned near T_c in the C/T *vs* T curves of the 9R and 5H phases. No specific heat anomaly could be observed down to 2 K in the 6H phase. Although the $\chi(T)$, $\rho(T)$, and S(T) curves all exhibit obvious anomalies at T_c, the impact of magnetic ordering on C(T) is rather weak in both the 9R and the 5H phases. A similar anomaly near T_c in the 9R phase has been reported in the literature.[134, 135] Normally, a sharp λ-shaped anomaly is observed in the C(T) near a second-order magnetic transition associated with ordering of localized spins. As in $ZrZn_2$,[136] a weak anomaly in C(T) at T_c of the 9R and 5H phases may signal that band ferromagnetism is taking place.

162

In order to characterize the contributions from electrons and lattice to the specific heat in these polytypes, we have made a plot of C/T versus T^2 and fitted it with the formula:

$$C/T = \gamma + \beta T^2 + \delta T^4, \qquad (6.1)$$

where the first term describes the electronic contribution and the second and third terms represent the lattice contribution. The Debye temperatures Θ_D can be calculated from β through $\Theta_D = (12\pi^4 nR/5\beta)^{1/3}$, where n = 5 is the number of atoms in the chemical formula and R is the ideal gas constant. The fitting curves are shown in Fig. 6.8(b) as the solid lines and the fitting parameters are given in Table 6.7. It was found that Θ_D increases gradually from 268.2 K (9R) through 351.9 K (5H) to 374.5 K (6H) with increasing fraction of corner-shared $IrO_{6/2}$ octahedra. The electronic specific heat coefficients γ also increase systematically, *i.e.* 1.15(8), 6.15(6) and 8.99(8) mJ/mol K^2 for 9R, 5H and 6H, respectively. Since γ is proportional to the density of states at ε_F, $N(\varepsilon_F)$, at low temperatures, the increased γ is consistent with the evolution from an insulator to metals. In contrast, as derived from the high-temperature susceptibility χ_0, the difference of $N(\varepsilon_F)$ near room temperature between these polytypes is very small. The dramatic change of $N(\varepsilon_F)$ on crossing T_c is consistent with a gap opening due to the formation of a CDW below T_c, which is also supported by measurements of $\rho(T)$ and S(T). At this point, it is interesting to estimate the Sommerfeld-Wilson ratio R_w:[137]

$$R_w = \frac{\pi^2}{3}\left(\frac{\kappa_B}{\mu_B}\right)^2 \frac{\chi_0}{\gamma} \qquad (6.2)$$

for these polytypes. An $R_w = 1$ is obtained in a non-interacting electron system. In a strongly correlated system, however, it has been argued that R_w could be as high as 2 at the limit U/W = ∞.[137] We were not able to derive χ_0 in the 9R and 5H phases since they are ferromagnetic at low temperatures where γ is obtained. For the 6H phase, the R_w is

2.14(3). Therefore, the 6H BaIrO$_3$ is an exchange-enhanced paramagnetic metal as the QCP is approached from the paramagnetic metal side.
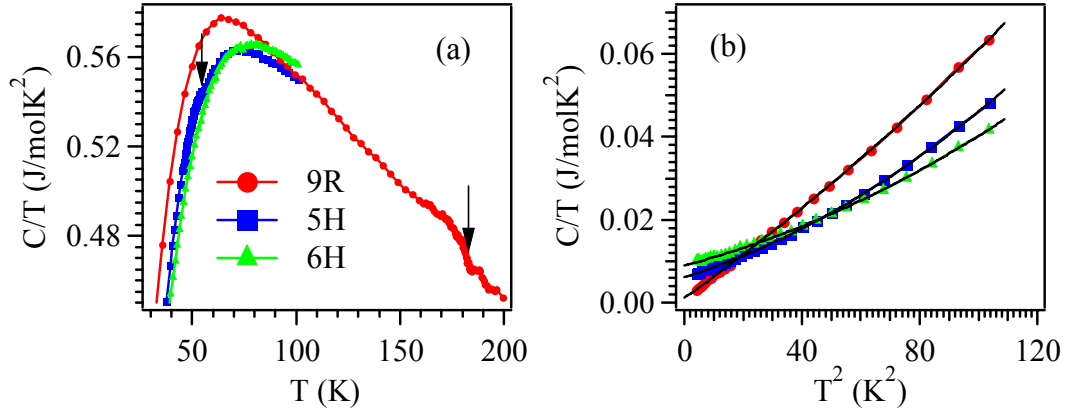
Figure 6.8: (a) Specific heat data of the BaIrO$_3$ polytypes showing the anomalies corresponding to the ferromagnetic transitions; (b) the low-temperature specific heat data in the plot of C/T *vs* T^2. Solid lines in (b) are the fitting curves.

6.3.2.4 Thermal conductivity and low-temperature structure

Figure 6.9 shows the thermal conductivity $\kappa(T)$ of three BaIrO$_3$ polytypes and CaFeO$_3$. The phonon thermal conductivities κ_p were obtained by subtracting from the total $\kappa(T)$ the electronic contributions κ_e according to the Wiedemann-Franz law, *viz.* $\kappa_e = L_0 T/\rho$, where $L_0 = 2.44 \times 10^{-8}$ WΩK^{-2} is the Lorenz constant. The phonon thermal conductivity follows a roughly 1/T law and peaks out at a low temperature depending on the sample's quality. The peak in $\kappa(T)$, or a hump in some cases, moves to higher temperatures in sintered polycrystalline samples. It is clear from Fig. 6.9 that the 5H BaIrO$_3$ sample has larger grains and an improved contact between grains. All other samples show an essentially glassy κ. However, several interesting features can still be

observed. For 9R $BaIrO_3$, a jump of κ, which can be seen more clearly in the inset of Fig. 6.9, occurs at T_c. The influence of spin ordering on κ is normally modest relative to the lattice contribution as in the case of the 5H phase and other magnets.[138, 139] On the other hand, we have shown that the $\kappa(T)$ will undergo a dramatic change at T_c or T_N if the magnetic transition is accompanied by a lattice change as, for example, in the hexagonal $RMnO_3$ (R = Y, Ho-Lu) manganites [49] or the perovskite $RTiO_3$.[140] The perovskite $CaFeO_3$ undergoes a charge disproportionation ($Fe^{4+} \rightarrow Fe^{3+} + Fe^{5+}$) transition at $T_{CD} \sim$ 290 K.[141] As shown in Fig. 6.9, a small increase of κ can be seen at T_{CD} in $CaFeO_3$. Therefore, a dramatic increase of κ at T_c in the 9R phase supports the scenario of forming a CDW phase below T_c.
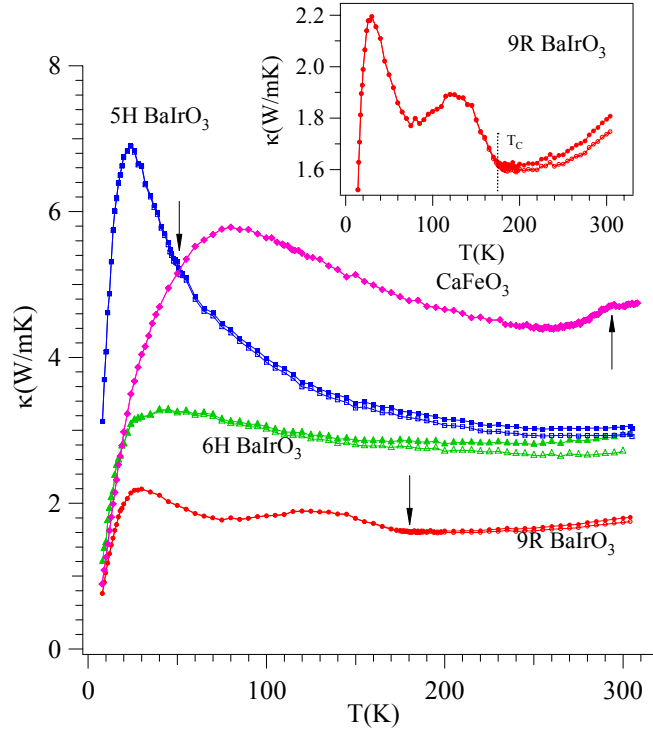
Figure 6.9: Temperature dependence of the thermal conductivity $\kappa(T)$ of the BaIrO$_3$ polytypes and the perovskite CaFeO$_3$. The $\kappa(T)$ of the 9R BaIrO$_3$ is enlarged in the upper inset in order to see clearly the anomaly around T_c. Open symbols represent $\kappa(T)$ after correcting the electronic contribution.

In order to confirm the structural change crossing T_c, we have measured the low-temperature XRD of the 9R BaIrO$_3$ from 300 down to 100 K. The unit cell parameters, a, b, c, β, and V as a function of temperature are shown in Fig. 6.10. It can be seen that all parameters except β indeed show discontinuous changes near T_c. Because the sensor position relative to the sample is different between the LT-XRD and other measurements of physical properties, T_c obtained from the LT-XRD is slightly higher. The thermal expansion coefficients $\alpha_A \equiv \mathrm{d}\ln A/\mathrm{d}T$ ($A = a$, b, c, β and V) were calculated by linear fitting to data below and above T_c and are given in Table 6.7. The most striking change is

166

in α_c, which shows an abrupt drop from $\alpha_c = 0$ above T_c to $\alpha_c = -1.9(2) \times 10^{-5}$ K^{-1} below T_c. Due to the abnormal thermal contraction of the c axis, the α_V below T_c is much smaller than that above T_c.
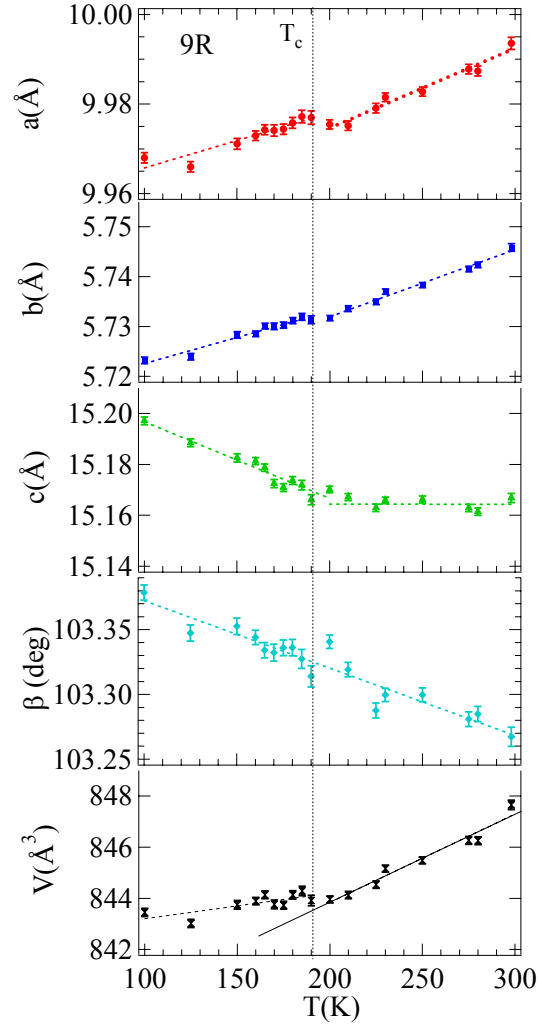
Figure 6.10: Temperature dependence of the unit cell parameters, a, b, c, β, and V of the 9R BaIrO$_3$ from 100 to 300K. The vertical line marks the ferromagnetism transition temperature T_c. The dashed lines represent the linear fitting to data below and above T_c, yielding the thermal expansion coefficients α.

6.3.2.5 The pressure effects on the ferromagnetic transitions

There are two reports in the literature about the pressure effect on T_c of 9R BaIrO$_3$.[142, 143] Although the resistivity anomaly at T_c has been used to monitor the change of T_c under pressure, quite different pressure coefficients were obtained in the two cases, *i.e.* −6.1(2) versus −29 K/GPa. The coefficients could be sample dependent. Moreover, the magnitude of the resistivity change at T_c and the definition of T_c from the $\rho(T)$ curve can also alter the dT_c/dP. This issue becomes more complicated in 9R BaIrO$_3$ since there are two close transitions, spin ordering and charge ordering. The magnetization measurement picks up signal from spins, which is the same for polycrystalline and single-crystal samples. Therefore we have chosen the magnetization measurement under high pressure to study the pressure effect on T_c. The T_c was defined as the minimum of the dM/dT curve for each pressure. It can be seen in Fig. 6.11 that T_c decreases linearly with increasing pressure, with $dT_c/dP = −14.5(4)$ K/GPa and $d\ln T_c/dP = −0.086(2)$ GPa^{-1}. The pressure coefficient is in the middle between the two values obtained by resistivity measurements,[142, 143] but it is still unusually large compared to other known ferromagnetic perovskite oxides, for example, BiMnO$_3$,[95] YTiO$_3$,[95] Sr$_{1-x}$Ba$_x$RuO$_3$ [95] and ZrZn$_2$.[81] A negative pressure coefficient of T_c has been normally found for both localized-spin and band ferromagnets.
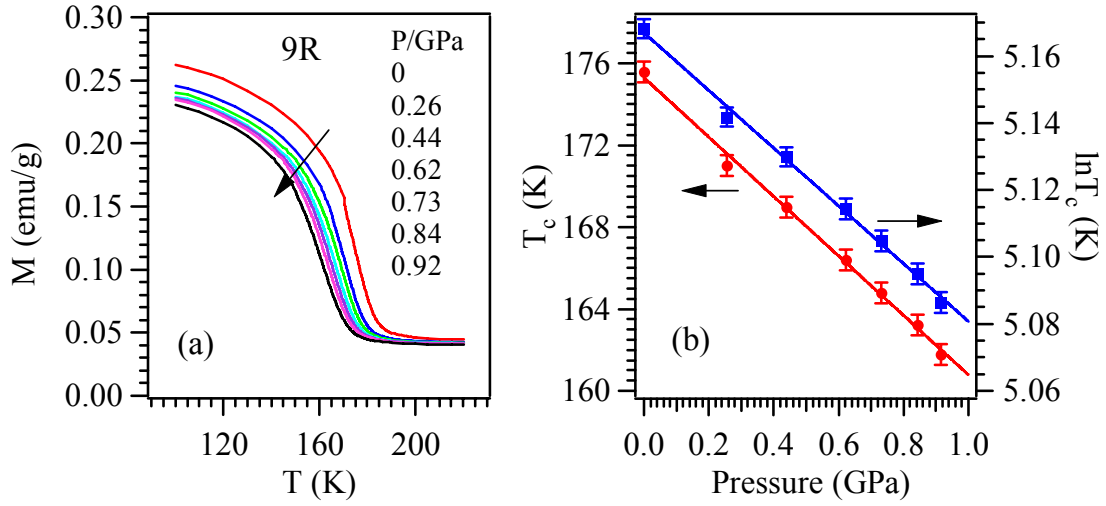
Figure 6.11: (a) M(T) curves of the 9R BaIrO$_3$ under high pressure up to 1 GPa. (b) Pressure dependence of the ferromagnetic transition T$_c$ (left) and lnT$_c$ (right) as well as the linear fitting curves.

For the 5H phase, measuring M(T) under high pressure is not feasible because the signal from the Be-Cu pressure chamber is at the same level as that of the sample. Thus, we carried out resistivity measurements under high pressure to study the pressure effect on T$_c$ shown in Fig. 6.12. With the same definition of T$_c$ as shown in Fig. 6.6(b), *i.e.* a narrow minimum in dR/dT, T$_c$ is suppressed under pressure; but T$_c$ versus P is no longer linear. The initial slope near ambient pressure is much smaller than that in the 9 R phase. However, without a structural transition at T$_c$, the suppression of T$_c$ of the 5H phase under pressure is much more dramatic than what has been normally seen in ferromagnets, which signals that the ferromagnetic 5H phase is near the edge of its collapse.
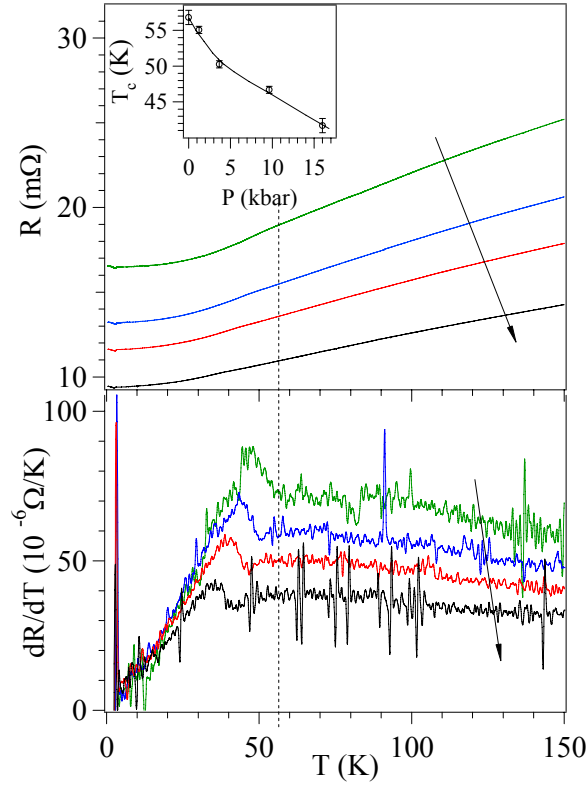
Figure 6.12: Temperature dependence of the resistance for the 5H phase in the temperature range of ferromagnetic transition T_c. Inset shows the pressure dependence of T_c. Arrows in the plot point the direction of increasing pressure.

It is interesting to correlate the dramatic change of transport properties observed in the 9R versus 5H phases with structural and bonding peculiarities of the polytypes. As seen in Fig. 6.3, the important electron transfer pathway between two adjacent C layers is through face-shared octahedra. In the 5H phase, not only is the fraction of C layer stacking increased, which reduces the distance between C layers by 1/3 from that in the 9R structure, but also a single perovskite layer is introduced in every four octahedra along the c axis. These structural changes are important to broaden the bandwidth. An

insulator to metal transition was not induced in the 9R phase under pressure to 12 GPa.[143] Moreover, we have found the Ir-Ir distances within trimers in the 9R structure are 2.622 and 2.644Å. Shrinking the Ir-Ir distance within a trimer takes place at the expense of expanding the important Ir-O-Ir bond length at *C* layer. The change of monoclinic distortion between 9R phase and the 5H phase results in a straight Ir-O-Ir bond angle in the 5H phase whereas it is bent from 180° in the 9R phase. These structural and local bonding changes insure a broader bandwidth in the 5H phase than that in the 9R phase. A schematic diagram is made in Fig. 6.13, which organizes all polytype phases of $BaIrO_3$ and their physical properties presented in this study as a function of their bandwidth.
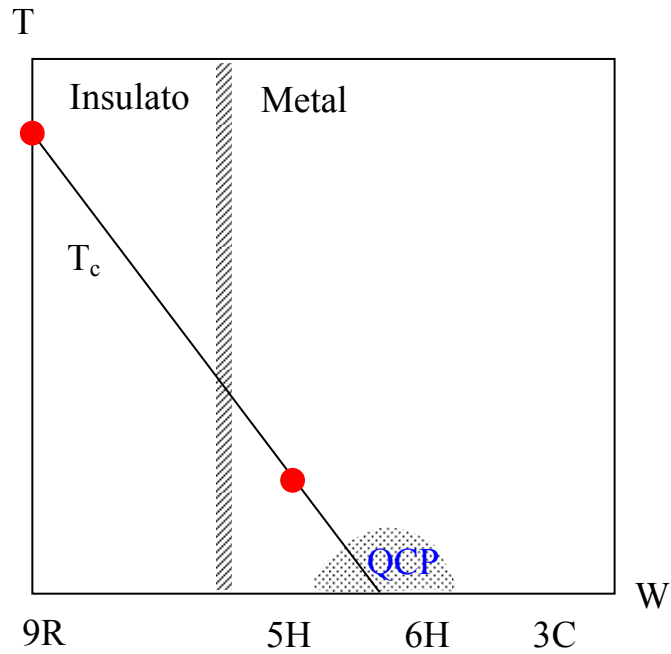
Figure 6.13: A schematic phase diagram of transition temperature versus bandwidth W of $BaIrO_3$ polytypes. QCP denotes a quantum critical point.

6.4 CONCLUSION

In summary, the sequence of pressure-induced transitions of $BaIrO_3$ has been studied in the pressure range up to 10 GPa. Four phases have been identified, the 9R, 5H, 6H and 3C structures. The 5H BaIrO3 phase is the first example of a 5H polytype of a stoichiometric, single-valent perovskite showing *hChCC* stacking. The significant stability found for the 9R polytype, identified up to 3 GPa, accounts for the formation of this new 5H polytype at 4 GPa; the *hChCC* sequence has a higher ratio of cubic stacking, than the commonly found 4H phase with a *hChC* sequence. The pressure stability of the 9R phase is related to the strong metal-metal bonding, in spite of the long Ir-Ir distances observed within the trimers of face-sharing octahedra, of 2.67 Å, given the spatial extension of the 5d orbitals involved in the metal-metal bonding. The Coulombic repulsion between the Ir^{4+} ions is responsible for the displacement of Ir3 and Ir1 away from Ir2 and Ir4 at the center of the trimers, but the Ir-Ir bonding reduces the magnitude of that displacement and allows pressure to decrease this distance before a new polytype is stabilized. The intermediate 5H phase relieves the Coulombic repulsion by giving an even larger Ir-Ir distance within the dimers of face-sharing octahedra, of 2.77 Å, implying a weaker metal-metal bonding and a stronger Ir-O bonding; the stability pressure range of this phase is small (less than 1 GPa), and the subsequent application of increasing external pressure leads to the collapse of this phase to the 6H polytype with a smaller Ir-Ir bond length of 2.71 Å. A delicate equilibrium between the increased Ir-Ir bonding with the external pressure and the Ir-Ir repulsion across the face-sharing octahedra, as well as the trend to decrease the hexagonal *vs* cubic packing ratio, makes possible the formation of this unreported 5H polymorph in an extremely narrow range of pressures. Finally, the cubic 3C perovskite was identified as a minority phase at 10 GPa, but it was not possible to isolate it as a pure phase in the available pressure range.

172

Systematic studies of the physical properties of three phase-pure $BaIrO_3$ polytypes show that with increasing fraction of corner-shared relative to face-shared layer stacking along the c axis in the order 9R (*hhChhChhC*) → 5H (*hChCC*) → 6H (*hCChCC*), the ground states of $BaIrO_3$ evolve from a ferromagnetic insulator with $T_c \approx 180$ K through a ferromagnetic metal with $T_c \approx 50$ K to an exchange-enhanced paramagnetic metal near a quantum critical point. All measurements of resistivity, thermoelectric power, thermal conductivity, thermal expansion from the structural study, and the pressure dependence of T_c confirm that the ferromagnetic transition of the 9R $BaIrO_3$ is accompanied by a structural change, perhaps forming a CDW phase below T_c. In contrast, the 5H $BaIrO_3$ becomes ferromagnetic at a significantly reduced $T_c \approx 50$ K and metallic down to 3.4 K. The highly unusual behavior of $\rho(T)$ near 3.4 K deserves further study. The paramagnetic 6H phase remains metallic to 0.05 K. However, the non-Fermi-liquid behavior of the $\rho(T)$ and a much enhanced $S(T)$ at low temperature show a quantum critical point is approached in the 6H phase where ferromagnetism is suppressed by bandwidth broadening.

Chapter 7 High-pressure synthesis and physical properties of a new 6H SrRhO$_3$

7.1 INTRODUCTION

As mentioned before, high-pressure synthesis has the advantage of maintaining a very high oxygen pressure inside the sample cell so as to stabilize unusual formal oxidation states, such as Fe^{4+}, Ni^{3+} and Cu^{3+}. By sealing KClO$_4$ and the sample in the high-pressure cell, Yamaura et al.[35] recently stabilized Rh^{4+} and synthesized a new orthorhombic perovskite SrRhO$_3$ under 6 GPa and 1500ºC. It was found to be a Fermi-liquid metal with enhanced Pauli paramagnetism. Since then, they have also obtained several novel Rh(IV) oxides with perovskite-related structures, including bi- and tri-layered perovskite Sr$_{n+1}$Rh$_n$O$_{3n+1}$ (n=2, 3) [144, 145] as well as perovskite and post-perovskite CaRhO$_3$.[146] CaRhO$_3$ is the fourth known oxide after CaMO$_3$ (M = Ir, Pt, Ru) that is quenchable under ambient condition with a post-perovskite structure. Siegrist et al.[147] have reported the synthesis of two hexagonal 9R and 4H BaRhO$_3$ polytypes under 6-6.5 GPa and 1175°C.

We have noticed that although the tolerance factor is t = 0.96 < 1, SrIrO$_3$ adopts at ambient condition a monoclinically distorted 6H polytype, which transforms to an orthorhombic perovskite structure under high pressure.[34] This unusual stability of the 6H polytype with t < 1 has been attributed to strong Ir-Ir bonding in the 6H phase via half-filled $a_1{}^1$ orbitals of the $e_\pi{}^4 a_1{}^1 e_\sigma{}^0$ configuration in trigonal site symmetry. As a sister compound with the same electron configuration as SrIrO$_3$ and even larger tolerance factor t, SrRhO$_3$ is also expected to crystallize into a 6H polytype under lower pressures. However, no effort has been made to search for this unknown phase except for the

synthesis of perovskite $SrRhO_3$ at 6 GPa and 1500ºC. In addition, the inverse magnetic susceptibility of perovskite $SrRhO_3$ has been found [35] to exhibit an unusual upturn, or hump-like feature at low temperatures, which results in a particular quadratic temperature dependence, *i.e.* $\chi^{-1}(T) \propto T^2$, instead of the linear Curie-Weiss behavior. This behavior could not be reasonably explained with the 3D spin fluctuation models. Density-functional calculations [36] for $SrRhO_3$ suggested that it is near a quantum critical point and that the properties are substantially affected by quantum critical fluctuations. On the other hand, we have learned from the magnetic susceptibility of 9R $BaRuO_3$ that the competition between the spin-orbit coupling $\lambda\mathbf{L}\cdot\mathbf{S}$ and the spin-spin exchange interaction can also result in an up-turn, or hump-like feature in the $\chi^{-1}(T)$ at low temperatures.[31] However, the effect of spin-orbit coupling has not been invoked to explain the unusual magnetic behavior of the perovskite $SrRhO_3$ even though a strong spin-orbit coupling $\lambda\mathbf{L}\cdot\mathbf{S}$ should be expected in the 4d transition-metal oxides, especially for the Rh^{4+} ions with the ground term $^2T_{2g}$. As seen from the evolution of the magnetic susceptibility of $BaRuO_3$ polytypes,[11] the spin-orbit coupling weakens gradually as the bandwidth broadens with increasing ratio of corner-sharing $RuO_{6/2}$ octahedra. If the 6H polytype exist, studies of the evolution of the magnetic susceptibility in the $SrRhO_3$ polytypes would enable us to understand further the peculiar magnetic behavior of the perovskite phase. Therefore, in this work we have mapped out a pressure-temperature phase diagram of $SrRhO_3$ in order to search for the unknown low-pressure 6H phase. Since they are structurally and electronically closely related, we have also made a side-by-side comparison between the $SrRhO_3$ and $SrIrO_3$ polytypes.

7.2 EXPERIMENTAL DETAILS

The precursor of $SrRhO_3$ for the HPHT experiments was prepared by conventional solid-state reaction. Thoroughly mixed $SrCO_3$ and Rh powders in a 1:1 ratio were pressed into pellets, sintered at 1000ºC for 24 h, and then 1200ºC for 48 h in an oxygen flow. These pellets were well-sintered as judged from the almost melted surface. In order to have a better solid-state reaction, the as-sintered sample was cold pressed into pellets under a loading force of 20 T over an area of ~7 mm^2. The ambient-pressure phase of $SrIrO_3$ was also prepared by sintering a stoichiometric mixture of $SrCO_3$ and Ir powders at 900-1000ºC for 4 days with several intermediate grindings. The HPHT experiments were performed in a Walker-type multianvil pressure module. In order to produce a high oxygen pressure in the Pt capsule for $SrRhO_3$, we have used a thin YSZ pellet (~ 0.3 mm) to separate the precursor and the oxygen source, $KClO_4$, with the volume ratio of ~ 1:1. Such a split-cell arrangement prevents the contamination of KCl and thus makes the high-pressure product suitable for physical measurements.

Any leakage on the Pt capsule leads to impurity phases ($Sr_{0.75}Rh_4O_8$ + Sr_2RhO_4) on the surface of the pellets, whereas the inner part is $SrRhO_3$. The color difference between the $SrRhO_3$ phase and impurity phases helps to identify them easily under a microscope; the impurity phases on the surface can be polished out. Phase purity was examined with powder X-ray diffraction (XRD) at room temperature with a Philips X'pert diffractometer (Cu Kα radiation). The XRD data were collected by step-scanning from 15 to 120° in 2θ in increments of 0.02° and a counting time of 10 seconds at each step. The XRD patterns were refined with the Rietveld method by using the FullProf program.[70] Scanning electron microscopy (SEM) and energy dispersive spectroscopy (EDS) were carried out on three selected samples in a commercial apparatus (JEOL JSM-

5610 equipped with INCA Energy, Oxford Instruments). Magnetic properties were measured with a SQUID magnetometer (Quantum Design). A four-probe method was used to measure the resistivity. Thermoelectric power was measured with a home-made setup.

7.3 RESULTS AND DISCUSSIONS

7.3.1 Pressure-temperature phase diagram of SrRhO$_3$ polytypes

The XRD pattern of the as-sintered precursor for SrRhO$_3$ shows that it consists of a mixture of Sr$_6$Rh$_5$O$_{15}$ and SrRh$_2$O$_4$, indicating that the Rh(IV) is hard to stabilize under moderate oxygen pressure. The high oxygen pressure maintained in the high-pressure cell is thus essential to stabilize the Rh(IV) cation and obtain novel rhodium(IV) oxides. Since the temperature of 1500ºC used by Yamaura *et al.* [35] is currently beyond the limit of our high-pressure apparatus, we only undertook HPHT experiments up to 1400ºC. The XRD pattern of our first experiment carried out at 6 GPa and 1400ºC was totally different from that of the perovskite phase reported by Yamaura *et al.*, but it was very similar to that of the ambient 6H phase of SrIrO$_3$. By using the structural model of 6H SrIrO$_3$ given by Longo *et al.*[34], almost all of the XRD peaks could be indexed very well. However, Rietveld refinement to the XRD data shows a large discrepancy at certain reflections corresponding to a perovskite phase. After we introduced as a second phase an orthorhombic perovskite structure defined in the space group *Pbnm*, the Rietveld refinement converged very well and showed that the obtained sample consisted of ~80% 6H phase and ~20% Perovskite (Pv) phase as shown in Fig. 7.1. This result is consistent with that of Yamaura *et al.*, who prepared the perovskite phase at 6 GPa and 1500ºC. We believed that the 6H polytype must be a low-temperature phase of SrRhO$_3$ and the

177

temperature of 1400°C is just located at the phase boundary between these two phases under 6 GPa. Therefore, we carried out a number of HPHT experiments in order to obtain pure phases of both products and to map out a pressure-temperature phase diagram. As shown in Fig. 7.2, the phase relationship between 6H and Pv polytypes of SrRhO$_3$ was determined for $4 \leq P \leq 8$ GPa and $1200 \leq T \leq 1400$°C. Pure 6H SrRhO$_3$ can be synthesized at lower pressures or temperatures and a pure Pv phase was obtained at high pressures or temperatures. EDS measurements at several positions of three selected samples, one 6H and two Pv phases, revealed that the Sr: Rh ratio is very close to the stoichiometric 1: 1 without any contamination from YSZ or KCl. Due to the small quantity of the obtained samples, we did not determine the oxygen content by thermogravimetric analysis. Fortunately, as shown by Yamaura *et al.* in the Sr$_{n+1}$Rh$_n$O$_{3n+1}$ (n=2, 3, and ∞) [35, 144, 145] family, the oxygen stoichiometry can always be guaranteed in these samples prepared under high oxygen pressure.
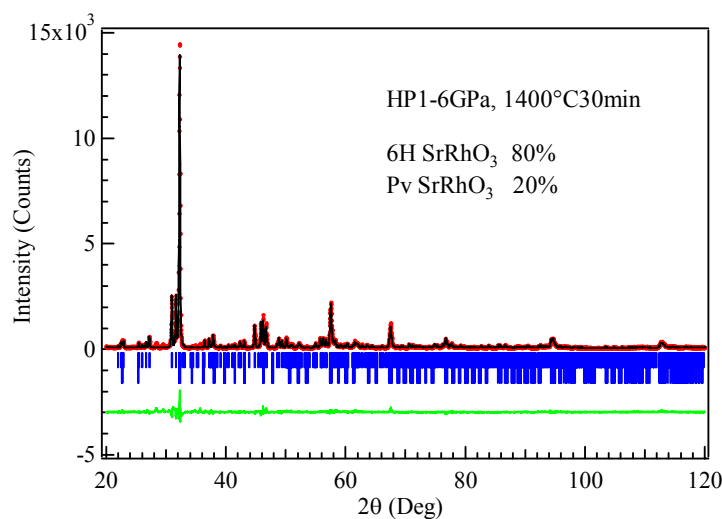
Figure 7.1: Rietveld refinement of the XRD pattern of SrRhO$_3$ obtained at 6 GPa and 1400°C.
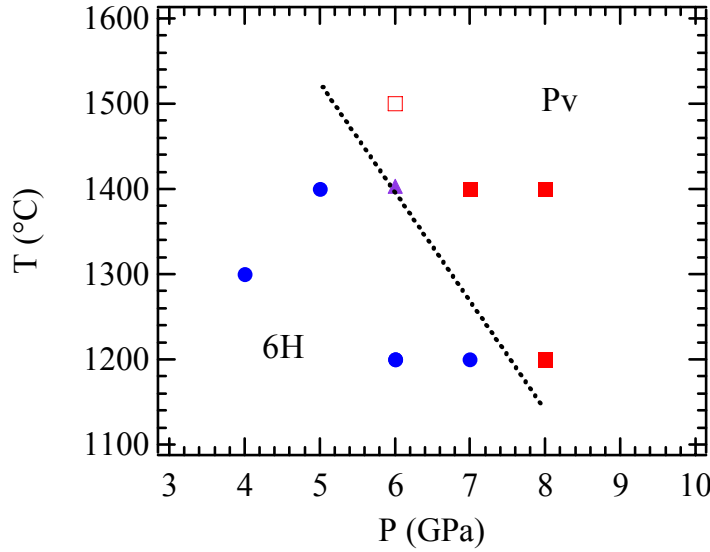
Figure 7.2:   Pressure-temperature phase diagram for the 6H to Pv SrRhO$_3$ transformation. The solid circle denotes the 6H phase and the solid square stands for the Pv phase, while the triangle represents the mixed phase. The open square is after Yamaura *et al.*[35]

7.3.2 Crystal structure

6H SrRhO$_3$ The XRD pattern of the sample obtained at 6 GPa and 1200°C is shown in Fig. 7.3(a), which can be indexed in a monoclinic unit cell with $a = 5.5650(1)$, $b = 9.5967(2)$, $c = 14.0224(4)$ Å, and $\beta = 92.846(2)°$. The crystal structure was refined from the powder XRD data in the space group *C2/c* of ambient SrIrO$_3$ as starting model. The two kinds of Sr atoms are placed at 4*e* (0, y, 1/4) and 8*f* (x, y, z) positions; Rh1 was located at 4*a* (0, 0, 0) and Rh2 at 8*f* sites; and five independent positions for oxygen atoms, O1 at 4*e*, O2-O5 were put at 8*f* positions. The final atomic parameters and the main interatomic distances and angles after the refinement are listed in Tables 7.1 and 7.2. A view of the crystal structure of 6H SrRhO$_3$ is shown in Fig. 7.4(a). It consists of

179

dimers of face-sharing Rh2 octahedra linked by their vertices to single corner-sharing Rh1 octahedra along the c axis. Alternatively, it can be described as a stacking of layers of corner-sharing (C) and face-sharing (h) RhO$_6$ octahedra in the sequence $hCChCC$ along the c axis. It is clear that Rh1 shares only vertices with adjacent octahedra while Rh2 shares both vertices and faces with neighboring octahedra. Rh-O distances for the two Rh atoms vary in the range from 1.91 Å for Rh2-O3 to 2.25 Å for Rh2-O1. The longest Rh2-O1 bond is due to a strong buckling of the face-sharing Rh$_2$O$_9$ dimer. The average Rh1-O distance, 2.00 Å, is consistent with the ionic radii sum for Rh^{4+} (0.60 Å) and O^{2-} (1.40 Å).[27] Relative to the Rh1O$_{6/2}$ octahedra, however, the Rh2O$_{6/2}$ octahedra show a significant expansion with an average Rh2-O distance of 2.06 Å. A strong metal-metal bonding across the shared face within the Rh$_2$$_2O_9$ dimer, as evidenced by the short Rh2-Rh2 distances, 2.673(3) Å, which are even shorter than the separation of 2.69 Å found in Rh metal. It is interesting to evaluate the Rh valences within the different coordination polyhedra. Brown's bond valence model [114, 115] gives a phenomenological relationship between the formal valence of a bond and the corresponding bond length. The valence is the sum of the individual bond valences (s_i) for Rh-O bonds and the individual bond valances are calculated as $s_i = \exp[(d_0-d_i)/B]$, where B = 0.370, d_0 = 1.793 for the Rh^{3+}-O^{2-} pair were used. As a consequence of the strong Rh2-Rh2 bond, the bonding power of Rh2 to the oxygen atoms within the dimer is weakened, thus enlarging the Rh2O$_{6/2}$ octahedra compared to the Rh1O$_{6/2}$ octahedra: in fact, the valence of the Rh2 cations, 3.1(1)+, is smaller than the 3.5(1)+ of Rh1 as calculated by the Brown's bond valence model. Significantly smaller valences of Ir cations have also been observed in the face-sharing octahedra of various BaIrO$_3$ polytypes. However, it should be mentioned that the calculated valences of Rh cations here are underestimated compared to the

nominal 4+ due to the lack of a bond valence parameter, d_0, for the Rh^{4+}-O^{2-} pair in the internal table of FullProf software.[70]

Pv SrRhO₃   Figure 7.3(b) shows the XRD pattern of the perovskite phase prepared at 8 GPa and 1400°C; it refines very well in the space group *Pbnm* with the Sr atom at 4*c* (*x*, *y*, ¼), the Rh atom at 4*b* (1/2, 0, 0), and two kinds of O atoms at 4*c* and 8*d* (*x*, *y*, *z*) sites. The lattice parameters, *a* = 5.5673(1), *b* = 5.5399(2), and *c* = 7.8550(2) Å are in excellent agreement with those reported by Yamaura *et al.* [35] of *a* = 5.5394(2), *b* = 7.8539(3), and *c* = 5.5666(2) Å defined in the space group *Pnma*. The final atomic parameters and the main interatomic distances and angles are listed in Tables 7.3 and 7.4. As shown in Fig. 7.4(b), the crystal structure consists of a 3D network of corner-sharing RhO₆ octahedra with the large Sr cations in the interstitial positions. The orthorhombic distortion arises from a cooperative rotation of the $RhO_{6/2}$ octahedra about the cubic [110] axis, which results in the deviation from ideal Rh-O-Rh angles of 180°, *i.e.* Rh-O1-Rh = 159.1(2)° and Rh-O2-Rh = 157.7(6)°. On the other hand, the $RhO_{6/2}$ octahedra are not rigid, with O-Rh-O angles 88.2°, 89.9° and 88.7° deviating from 90°. It has been demonstrated thoroughly in the $R^{3+}M^{3+}O_3$ perovskites [47] that the O-M-O angle α reduced from 90° subtends the orthorhombic *b* axis, converting from *b* > *a* to *a* > *b*. Such a crossover has been argued to occur for $\alpha = (90° - \delta)$ as small as 1°. Thus, a $\delta = 1.3$ ° for the O2-Rh-O2 angle is in accordance with the observed *a* > *b* in the Pv SrRhO₃. The average Rh-O distance, 2.00 Å, is the same as that of <Rh1-O> in the 6H phase and is also consistent with the ionic radii sum for Rh^{4+} (0.60 Å) and O^{2-} (1.40 Å).[27]

Before the present study of SrRhO₃, SrIrO₃ [34] was the only compound among known SrMO₃ (M = 3d, 4d and 5d transition metals) that exhibits the monoclinic 6H

181

structure and transform to an orthorhombic perovskite phase under HPHT. In addition, $Rh^{IV}(4d^5)$ and $Ir^{IV}(5d^5)$ share the same electronic configurations in the outermost shell. Therefore, it will be of high value to make a direct comparison of the structural features of $SrRhO_3$ and $SrIrO_3$ polytypes. For this purpose, we also prepared the ambient 6H and high-pressure Pv phases of $SrIrO_3$ and refined their crystal structures by the Rietveld method from XRD data. It should be mentioned that both the 6H and 3C phases of $SrMnO_3$ have been obtained by different methods; no transformation from the 6H to the 3C phase under high pressure has been observed as far as we know.[148]

6H SrIrO₃   This phase can be obtained at ambient pressure. The XRD pattern, shown in Fig. 7.3(c), was refined in the space group *C2/c* with a = 5.5970(4), b = 9.6197(6), c = 14.167(1) Å, and β = 93.184(3)°. These parameters match well with those reported by Longo *et al.* [34] of a = 5.604, b = 9.618, c = 14.174(9) Å, and β = 93.26°. Table 7.5 lists the final atomic parameters and Table 7.6 gathers the main interatomic distances and angles after the refinement. The crystal structure is the same as 6H $SrRhO_3$, Fig. 7.4(a). Ir-O distances for the two Ir atoms vary in the range from 1.94(3) Å for Ir1-O5 to 2.285(3) Å for Ir2-O1, with the longest one corresponding to the buckling of the Ir_2O_9 dimer. In the same manner as in 6H $SrRhO_3$, the $Ir2O_{6/2}$ octahedra are expanded compared to the $Ir1O_{6/2}$ octahedra with average Ir-O distances of 2.08 Å and 2.03 Å, respectively. The Ir2-Ir2 distance, 2.724(3) Å, is almost the same separation as the 2.72 Å found in Ir metal, suggesting a strong Ir-Ir bonding. As a result of the different sizes of octahedra, the bond valences of Ir atoms are calculated to be 4.0(1)+ and 3.5(1)+ for Ir1 and Ir2, respectively.

Pv SrIrO₃   Figure 7.3(d) displays the XRD pattern of the perovskite $SrIrO_3$ obtained at 6 GPa and 1000ºC, which contains a tiny amount of IrO_2 impurity. Thus, in addition to the orthorhombic perovskite phase, we also included an IrO_2 phase defined in the space group *P4₂/mnm* with Ir at 2*a* (0, 0, 0) and O at 4*f* (*x*, *x*, 0) sites in the Rietveld refinement. From the scale factors, the wight fraction of the IrO_2 phase was estimated to be ~ 0.7%. The atomic parameters and the main interatomic distances and angles are given in Tables 7.7 and 7.8. The lattice parameters, *a* = 5.5979(1), *b* = 5.5669(1), *c* = 7.8909(1) Å are consistent with those reported by Longo *et al.*[34] of *a* ≈ 5.60, *b* ≈ 5.58, and *c* ≈ 7.89 Å, or by Zhao *et al.*[149] of *a* = 5.5909(1), *b* = 5.5617(1) and *c* = 7.8821(1) Å. As the Pv $SrRhO_3$, *a* > *b* is also observed in $SrIrO_3$ due to the intrinsic distortion of the $IrO_{6/2}$ octahedra, having δ = 1.3º for the O2-Ir-O2 = 88.7º. The orthorhombic distortion also results in the deviation from 180º of the Ir-O-Ir angles, *i.e.* Ir-O1-Ir = 151.6(2)º and Ir-O2-Ir = 156.6(7)º. The average Ir-O distance, 2.02 Å, is consistent with the ionic radii sum for Ir^{4+} (0.625 Å) and O^{2-} (1.40 Å).[27] The tolerance factor calculated from the average Sr-O and Ir-O bond lengths is t = 0.984.
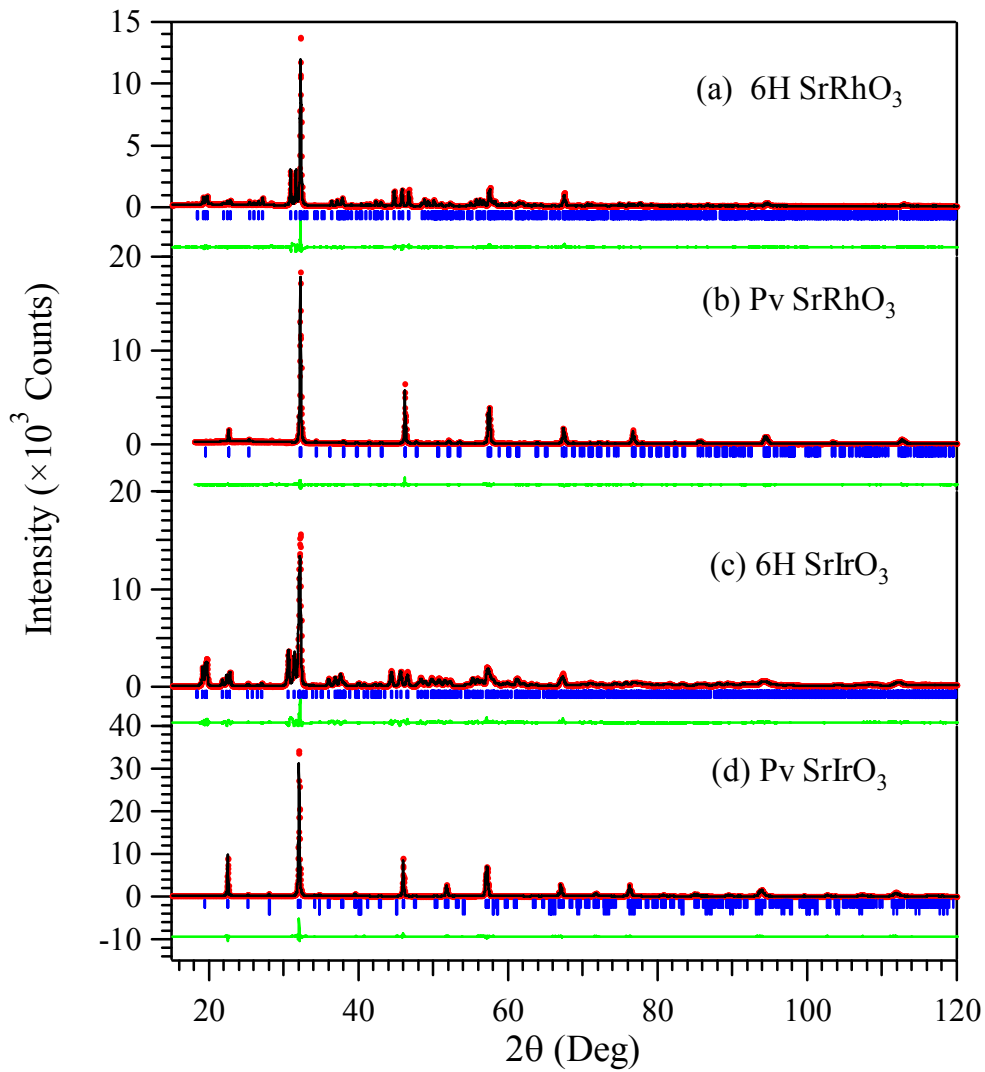
Figure 7.3: Observed (red dots), calculated (black lines), and difference (green lines) XRD profiles after the Rietveld refinements of the (a) 6H SrRhO$_3$, (b) Pv SrRhO$_3$, (c) 6H SrIrO$_3$ and (d) Pv SrIrO$_3$. The Bragg reflections are shown by the blue vertical marks.
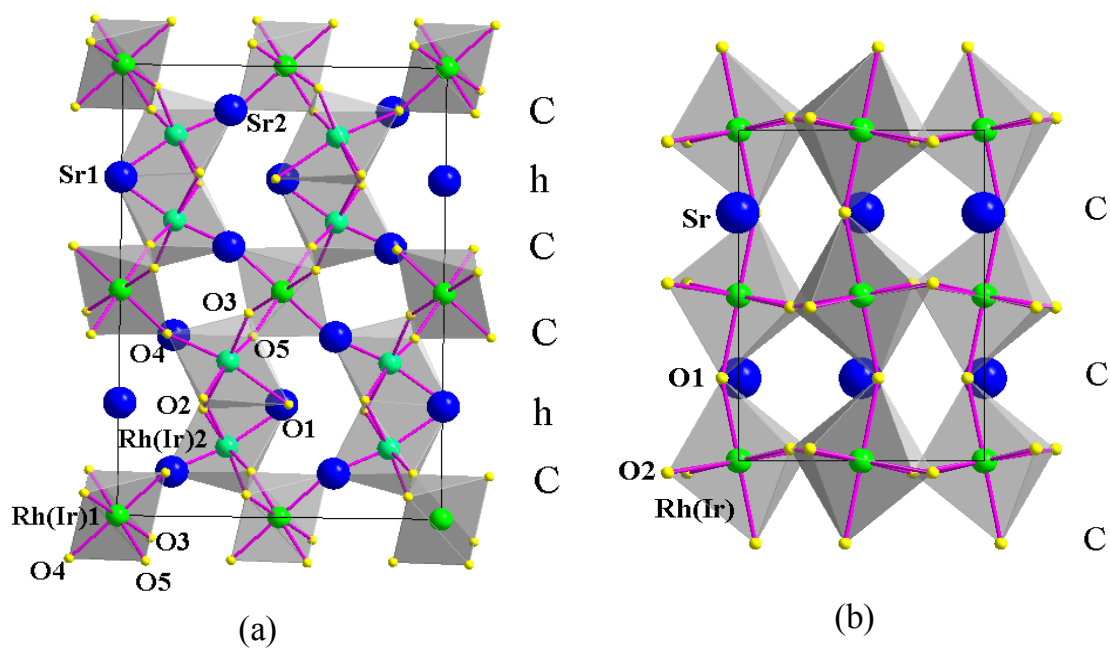
Figure 7.4: Projection of crystal structures of (a) 6H-SrRh(Ir)O$_3$ along [1 0 0] direction and (b) Pv SrRh(Ir)O$_3$ along [0 1 0] direction.

Table 7.1: Atomic coordinates and isotropic thermal factors B_{iso} [Å^2] for 6H SrRhO$_3$ from powder XRD data[a] at 295 K; Space group $C2/c$, a = 5.5650(1), b = 9.5967(2), c = 14.0224(4) Å, β = 92.846(2)$^\circ$, V = 747.96(3) Å^3, Z = 12.

atom	site	x	y	z	B_{iso}(Å)
Sr1	4e	0.0	0.0029(6)	0.25	1.26(14)
Sr2	8f	0.0095(6)	0.6666(5)	0.0986(2)	1.97(9)
Rh1	4a	0.0	0.0	0.0	1.44(12)
Rh2	8f	0.9841(5)	0.6642(4)	0.8448(2)	1.45(6)
O1	4e	0.0	0.525(3)	0.25	2.4(2)
O2	8f	0.244(3)	0.260(2)	0.2618(11)	2.4(2)
O3	8f	0.817(3)	0.397(2)	0.0486(12)	2.4(2)
O4	8f	0.939(3)	0.147(3)	0.4040(11)	2.4(2)
O5	8f	0.331(4)	0.411(2)	0.0999(13)	2.4(2)

[a] Discrepancy factors: R$_p$ = 9.10%, R$_{wp}$ = 12.1%, R$_{exp}$ = 6.92%, χ^2 = 3.03, R$_{Bragg}$ = 8.45%.

Table 7.2: Main interatomic distances (Å) and angles (°) of 6H $SrRhO_3$ from powder XRD data at 295 K.

RhO$_6$ octahedra			SrO$_{12}$ cuboctahedra		
Rh1	–O3	2.106(17) × 2	Sr1	–O1	2.791(2) × 2
	–O4	1.97(2) × 2		–O2	2.819(17) × 2
	–O5	1.925(20) × 2		–O2	2.740(17) × 2
<Rh1–O>		2.000		–O3	3.552(17) × 2
				–O4	2.60(2) × 2
Rh2	–O1	2.25(2)		–O5	2.428(19) × 2
	–O2	2.045(16)	<Sr1–O >		2.822
	–O2	2.035(17)			
	–O3	1.908(17)	Sr2	–O1	2.523(16)
	–O4	2.01(3)		–O2	2.926(17)
	–O5	2.08(2)		–O2	2.501(16)
<Rh2–O >		2.055		–O3	2.874(19)
				–O3	2.401(18)
<Rh–O >		2.028		–O3	2.903(19)
				–O4	3.27(2)
Rh2	–Rh2	2.673(3)		–O4	2.501(17)
				–O4	3.077(17)
Rh2–O1–Rh2		72.7(8)		–O5	3.04(2)
Rh2–O2–Rh2		81.9(7)		–O5	3.372(19)
Rh1–O3– Rh2		147.4(7)		–O5	2.55(2)
Rh1–O4– Rh2		155.0(1)	<Sr2–O >		2.828
Rh1–O5– Rh2		151.2(9)			

Table 7.3: Atomic coordinates and isotropic thermal factors B_{iso} [Å^2] for Pv SrRhO$_3$ from powder XRD data[a] at 295 K; Space group *Pbnm*, a = 5.5673(1), b = 5.5399(2), c = 7.8550(2) Å, V = 242.267(9) Å^3, Z = 4.

atom	site	x	y	z	B_{iso}(Å)
Sr	4c	0.9985(13)	0.00275(3)	0.25	1.51(5)
Rh	4b	0.5	0.0	0.0	1.22(3)
O1	4c	0.065(4)	0.498(2)	0.25	1.9(3)
O2	8d	0.714(2)	0.279(3)	0.0369(19)	1.9(3)

[a] Discrepancy factors: R_p = 6.61%, R_{wp} = 9.24%, R_{exp} = 6.94%, χ^2 = 1.77, R_{Bragg} = 4.57%.

Table 7.4: Main interatomic distances (Å) and angles (°) of Pv $SrRhO_3$ from powder XRD data at 295 K.

RhO$_6$ octahedra			SrO$_{12}$ cuboctahedra		
Rh	–O1	1.997(4) × 2	Sr	–O1	2.957(11)
	–O2	1.973(15) × 2		–O1	2.633(12)
	–O2	2.029(13) × 2		–O1	3.14(2)
<Rh–O>		2.000		–O1	2.44(2)
				–O2	2.693(15) × 2
Rh–O1–Rh		159.11(16)		–O2	2.428(19) × 2
Rh–O2–Rh		157.7 (6)		–O2	2.769(15) × 2
O1–Rh–O2		88.2(9)		–O2	3.244(15) × 2
O1–Rh–O2		89.9(9)			
O1–Rh–O2		88.7(9)	<Sr–O >		2.793

Table 7.5: Atomic coordinates and isotropic thermal factors B_{iso} [Å^2] for 6H $SrIrO_3$ from powder XRD data[a] at 295 K; Space group $C2/c$, a = 5.5970(4), b = 9.6197(6), c = 14.167(1) Å, β = 93.184(4)°, V = 761.59(9) Å^3, Z = 12.

atom	site	x	y	z	B_{iso}(Å)
Sr1	4e	0.0	0.0042(8)	0.25	0.62(16)
Sr2	8f	0.0122(7)	0.6656(7)	0.0994(3)	0.59(11)
Ir1	4a	0.0	0.0	0.0	0.80(7)
Ir2	8f	0.9796(4)	0.6639(3)	0.8454(1)	0.54(4)
O1	4e	0.0	0.527(4)	0.25	1.1(3)
O2	8f	0.246(4)	0.269(2)	0.2621(15)	1.1(3)
O3	8f	0.818(5)	0.385(3)	0.0368(15)	1.1(3)
O4	8f	0.914(4)	0.144(3)	0.4014(14)	1.1(3)
O5	8f	0.321(5)	0.413(3)	0.0981(17)	1.1(3)

[a] Discrepancy factors: R_p = 11.30%, R_{wp} = 14.7%, R_{exp} = 5.41%, χ^2 = 7.41, R_{Bragg} = 7.93%.

Table 7.6:   Main interatomic distances (Å) and angles (°) of 6H $SrIrO_3$ from powder XRD data at 295 K.

	IrO$_6$ octahedra				SrO$_{12}$ cuboctahedra		
Ir1	−O3	2.14(3)	× 2	Sr1	−O1	2.807(6)	× 2
	−O4	2.01(2)	× 2		−O2	2.90(2)	× 2
	−O5	1.94(3)	× 2		−O2	2.69(2)	× 2
<Ir1−O>		2.03			−O3	3.77(2)	× 2
					−O4	2.60(2)	× 2
Ir2	−O1	2.285(3)			−O5	2.48(3)	× 2
	−O2	2.03(2)		<Sr1−O >		2.87	
	−O2	2.06(2)					
	−O3	2.02(2)		Sr2	−O1	2.521(5)	
	−O4	2.05(3)			−O2	2.98(2)	
	−O5	2.05(3)			−O2	2.53(2)	
<Ir2−O >		2.08			−O3	3.02(2)	
					−O3	2.25(2)	
< Ir −O >		2.055			−O3	2.89(2)	
					−O4	3.37(2)	
Ir 2	−Ir 2	2.724(3)			−O4	2.39(2)	
					−O4	3.22(2)	
Ir2−O1−Ir2		73.2(1)			−O5	2.99(3)	
Ir2−O2−Ir2		83.7(9)			−O5	3.36(3)	
Ir1−O3−Ir2		137.9(10)			−O5	2.61(3)	
Ir1−O4−Ir2		148.2(11)					
Ir1−O5−Ir2		154.4(11)		<Sr2−O >		2.84	

Table 7.7:   Atomic coordinates and isotropic thermal factors B_{iso} [Å^2] for Pv $SrIrO_3$ from powder XRD data[a] at 295 K; Space group *Pbnm*, $a = 5.5979(1)$, $b = 5.5669(1)$, $c = 7.8909(1)$ Å, $V = 245.904(7)$ Å^3, Z= 4.

atom	site	x	y	z	B_{iso}(Å)
Sr	4c	0.9970(12)	0.0314(3)	0.25	1.24(3)
Ir	4b	0.5	0.0	0.0	0.996(16)
O1	4c	0.089(4)	0.498(3)	0.25	1.74(16)
O2	8d	0.711(3)	0.289(3)	0.034(2)	1.74(16)

[a] Discrepancy factors: R_p= 6.92%, R_{wp}= 9.33%, R_{exp}= 5.75%, χ^2= 2.63, R_{Bragg}= 3.90%.

Table 7.8:   Main interatomic distances (Å) and angles (°) of Pv $SrIrO_3$ from powder XRD data at 295 K.

IrO_6 octahedra			SrO_{12} cuboctahedra		
Ir	–O1	2.035(5) ×2	Sr	–O1	3.014(17)
	–O2	2.014(17) ×2		–O1	2.648(17)
	–O2	2.017(17) ×2		–O1	3.29(2)
<Ir–O>		2.022		–O1	2.32(2)
				–O2	2.743(17) ×2
				–O2	2.731(16) ×2
Ir–O1–Ir		151.6(2)		–O2	2.466(17) ×2
Ir–O2–Ir		156.6(7)		–O2	3.298(17) ×2
O1–Ir–O2		88.9(9)			
O1–Ir –O2		86.3(9)			
O1–Ir –O2		88.7(9)	<Sr–O >		2.812

As pointed out in Chapter 2, pressure induces a 6H to 3C transition for AMO_3 compounds with a tolerance factor t > 1. However, both $SrIrO_3$ and $SrRhO_3$ have a t < 1 in the perovskite phase with the normal distortion of the 3C phases to orthorhombic symmetry; yet, they each have a 6H polytype structure at lower temperatures and pressures. As pointed out by Longo *et al.* [34] for 6H $SrIrO_3$, this unusual stability of the 6H polytype with $t < 1$ can be attributed to the low-spin t^5e^0 d-electron configuration and the larger radial extension of the 4d and 5d orbitals relative to that of the 3d orbitals. Strong M-M bonding stabilizes the dimers of the 6H phase via half-filled $a_1{}^1$ orbitals of the $e_\pi{}^4a_1{}^1e_\sigma{}^0$ configuration in the trigonal site symmetry. Displacement of the M2 cations of a dimer leaves the M1 ions unable to find a partner for bonding, so the M1 cations occupy sites whose small distortion to orthorhombic symmetry does not completely quench the orbital angular momentum by complete ordering of the t^5 hole into the O4-M1-O5 plane. Thus, the appearance of a 6H structure with a tolerance factor t < 1 can be understood, and the sequence 6H → Pv under pressure is consistent with the smaller volume

189

associated with all-cubic-stacking of the SrO_3 planes. The observed crystallographic densities of the 6H and Pv polytypes are 6.35 and 6.54 g/cm^3 for $SrRhO_3$, and 8.58 and 8.86 g/cm^3 for $SrIrO_3$, respectively. They represent an increase in density of 3.0% and 3.3% from the 6H to Pv phase for $SrRhO_3$ and $SrIrO_3$, respectively.

Among the known $SrMO_3$ (M = 3d, 4d, and 5d transition metals) compounds, $SrRhO_3$ and $SrIrO_3$ are the only two compounds that adopt a monoclinic distortion of the 6H structure at lower pressure and transform to an orthorhombic *Pbnm* perovskite rather than the cubic 3C perovskite under higher pressures. Rietveld refinements on their crystal structures revealed great similarities: for example, in the 6H polytypes, the $M2O_{6/2}$ octahedra are expanded with a smaller valence sum relative to the $M1O_{6/2}$ octahedra; the M2-M2 distances are short, implying strong metal-metal bonding; and the M2-O1 bond lengths are stretched due to the buckling of the $M2_2O_9$ dimers. Similar features have also been observed recently in the 6H $Ba_{0.4}Sr_{0.6}RuO_3$ with a monoclinic distortion,[150] *i.e.* the average distance of Ru2-O, 2.109 Å, is much larger than that of Ru1-O with 2.00 Å; the Ru2-Ru2 distance, 2.596(2) Å, is shorter than the separation of 2.65 Å found in ruthenium metal; the Ru2-O1 bond length, 2.319 Å, is the longest among the Ru-O bonds. To our knowledge, the perovskite $Ba_{0.4}Sr_{0.6}RuO_3$ has not been obtained below 10 GPa, but it may not adopt the orthorhombic *Pbnm* structure because we have shown before that another orthorhombic *Imma* phase emerges for $0.1 < y < 0.3$ in the $Sr_{1-y}Ba_yRuO_3$ system. The high-pressure forms of both $SrRhO_3$ and $SrIrO_3$ exhibit an orthorhombic *Pbnm* perovskite structure, which is consistent with the tolerance factors, ~ $0.98 < 1$, as calculated from the average Sr-O and Rh/Ir-O bond lengths. The same structure is also found in $SrRuO_3$, which can be prepared at ambient pressure. Defined in the space group *Pbnm*, all of them show lattice parameters $a > b$, which can be inverted

to $b > a$ with decreasing average size of the A-site cation by Ca^{2+} doping. The crossover occurs at ~30%,[151] ~10%,[152] and ~15% Ca^{2+} doping for $SrRuO_3$, $SrRhO_3$, and $SrIrO_3$, respectively. Such a lattice-parameter anomaly has been demonstrated thoroughly in the $R^{3+}M^{3+}O_3$ (R = rare earth and Y; M = 3d transition metals and Ga) perovskites arising from an intrinsic octahedral-site distortion.[47] It consists of a deviation from 90° of the O-M-O angle subtending the site-rotations with increasing A-site cation size radius above 1.11 Å; the $MO_{6/2}$ octahedra are not rigid and b decreases while a increases until they cross. We have seen this distortion in perovskite phases of both $SrRhO_3$ and $SrIrO_3$. Examination of the evolution of the lattice parameters a and b in the $Sr_{1-x}Ca_xMO_3$ (M=Ru and Rh) system indicates that such an intrinsic octahedra-site distortion has already taken place for $CaMO_3$, and the A-cation size for the $A^{2+}M^{4+}O_3$ perovskites must be smaller than the 1.18 Å of Ca^{2+}.

The ideal hexagonal 6H structure is found where the perovskite phase has a t >1, as is typified by $RbNiF_3$ [153] and $TlNiF_3$.[154] The 6H polytypes transform to the cubic perovskite 3C polytype under high pressure. However, the monoclinic distortion of the 6H phases of $SrRhO_3$ and $SrIrO_3$ indicates that a compressive stress on the A-O bond due to an equilibrium M-O *vs* A-O bond-length mismatch remains in a 6H polytype stabilized by strong M-M bonding for a tolerance factor t < 1 rather than a t > 1. Consistent with this deduction is the observation that the monoclinic distortion of 6H $SrIrO_3$ decreases from β = 93.184(4)° to β = 91.319(2)° in $BaIrO_3$. However, retention of a monoclinic distortion in 6H $BaIrO_3$ indicates that the M-M bonding also plays an important role in creating a compressive stress on the A-O bond in $BaIrO_3$. We also note the following: (1) With increasing pressure, the ambient-pressure 9R $BaRuO_3$ transforms to the 4H polytype at 3 GPa and to the 6H phase at 5 GPa and finally to the cubic 3C phase at 18

GPa; both the 4H and 6H phases have hexagonal symmetry with space group $P6_3/mmc$. Interestingly, Zhao *et al.*[150] have re-investigated the structural evolution of the 6H $Ba_{1-x}Sr_xRuO_3$ system and shown that the hexagonal $P6_3/mmc$ structure forms for $0 \le x \le 0.3$ whereas the monoclinic $C2/c$ structure, which is the same as that of $SrIrO_3$ and $SrRhO_3$, is found for $0.4 \le x \le 0.6$. The monoclinic distortion in the $Ba_{1-x}Sr_xRuO_3$ system also increases as the average A-cation size decreases. (2) In the 1:2 B-site ordered 6H $Ba_3(MSb_2)O_9$ (M = Mg, Ca, Sr), [155, 156] the symmetries are also lowered successively from hexagonal $P6_3/mmc$ to monoclinic $C2/c$, and then to triclinic $P\text{-}1$ on going from Mg^{2+}(0.72 Å) through Ca^{2+}(1.00 Å) to Sr^{2+} (1.18 Å), as the bond-length mismatch with Sb^{5+} (0.60 Å) increases. We examined this relationship further in the large family of 1:2 B-site ordered 6H $Ba_3(MRu_2)O_9$ compounds with M = Li, Na, Mg, Ca, Sr, Ti, Fe, Co, Ni, Cu, Zn, Cd, In, Sb, Y, Bi, La-Lu.[157] The hexagonal space group $P6_3/mmc$ was found for all compounds except M = Sr and Bi, which are monoclinic $C2/c$. The Sr^{2+} ionic radius, 1.18 Å, is the largest of the M cations; all the others have ionic radii in the range 0.6 Å for Sb^V to 1.032 Å for La^{3+}. Although Bi^{3+}(1.30 Å), is a little smaller than that of La^{3+}, the presence of the $6s^2$ lone pair on Bi^{3+} may play an important role in lowing the symmetry.

7.3.3 Magnetic properties

Figure 7.5 summarizes the magnetic properties of the 6H and Pv phases for both $SrRhO_3$ and $SrIrO_3$, including the magnetic susceptibilities, $\chi(T)$ and $\chi^{-1}(T)$, as a function of temperature up to 750 K, and magnetization curves, M(H), at T = 5 K and up to 5 T. Below 300 K, the $\chi(T)$ curves were measured under H = 1T except for the 6H $SrRhO_3$, which was measured under H = 5 T due to the small sample and weak signal; for all of them, the measurements were performed with increasing temperatures after both zero

field cooling (ZFC) and field cooling (FC). Above 300 K, all $\chi(T)$ curves were measured under H = 5 T.

First of all, no long-range magnetic ordering was observed down to 5 K for all samples. The absence of magnetic ordering in the 6H and Pv $SrIrO_3$ is consistent with the evolution of the ground states of the $BaIrO_3$ polytypes; *i.e.* the ferromagnetic transition temperature T_c decreases from 180 K for the 9R phase to 50 K for the 5H phase, and finally disappears for the 6H phase with increasing portion of corner-sharing $IrO_{6/2}$ octahedra or bandwidth. The $\chi(T)$ curve of the Pv $SrRhO_3$ is essentially the same as that reported by Yamaura *et al.*; the unusual quadratic temperature dependence of $\chi^{-1}(T)$, *i.e.* $\chi^{-1} \propto T^2$, was also observed up to 400 K as is shown in the inset of Fig. 7.5(b). However, our measurement extended to 750 K reveals a clear deviation from the linearity of χ^{-1} *vs* T^2. Instead, a Curie-Weiss like behavior is restored in the temperature range 400-750 K as shown in Fig. 7.5(b). It is interesting to note that the unusual quadratic temperature dependence of $\chi^{-1}(T)$ in the Pv $SrRhO_3$ reported by Yamaura *et al.* arises from the hump-like feature in the $\chi(T)$ curves or an upturn in the $\chi^{-1}(T)$ curves, which is also observed in the Pv $SrIrO_3$, Fig. 7.5(d) and (e). Similar features in the $\chi(T)$ curve have also been observed in the 9R $BaRuO_3$ [31] and $Ca_3Co_2O_6$;[158] in both cases the spin-orbit coupling plays an important role in addition to the spin-spin interactions. Drillon *et al.*[31] have undertaken quantitative calculations taking into account the spin-orbit coupling $\lambda\mathbf{L}\cdot\mathbf{S}$ and reproduced the characteristic features of $\chi(T)$ curve for the 9R $BaRuO_3$. It is the competition between the spin-orbit coupling $\lambda\mathbf{L}\cdot\mathbf{S}$ and the spin-spin exchange interaction that results in an up-turn, or hump-like feature, in the $\chi(T)$ curve at low temperatures. A strong spin-orbit coupling $\lambda\mathbf{L}\cdot\mathbf{S}$ is commonly found in the 4d and 5d transition-metal oxides, especially for the ions with the ground term $^2T_{2g}$ or $^3T_{1g}$. The much stronger

193

enhancement of the upturn feature observed in the of $\chi^{-1}(T)$ curve of Pv SrIrO$_3$ than that of Pv SrRhO$_3$ is consistent with the fact that the spin-orbit coupling in the 5d Ir is much stronger than that in the 4d Rh. The Curie-Weiss like behavior can only be restored at sufficiently high temperatures, ~400 K for Pv SrRhO$_3$, for instance, where the spin-orbit coupling becomes dominated by the spin-spin exchange interaction. Therefore, our $\chi(T)$ measurements up to 750 K and comparison with Pv SrIrO$_3$ have resolved the puzzle in explaining the unusual quadratic temperature dependence of $\chi^{-1}(T)$ for the Pv SrRhO$_3$.

The $\chi^{-1}(T)$ curves of the SrRhO$_3$ polytypes show a stronger temperature dependence than those of the SrIrO$_3$ polytypes. The Curie-Weiss (CW) law is applicable at high temperatures. As shown by the solid lines in Fig. 7.5(b), CW fitting to the $\chi^{-1}(T)$ curves above 400 K yields $\mu_{eff} = 2.65$ μ_B/Rh^{IV} and $\theta_{CW} = -519$ K for the 6H SrRhO$_3$ and $\mu_{eff} = 2.48$ μ_B/Rh^{IV} and $\theta_{CW} = -279$ K for the Pv SrRhO$_3$. The μ_{eff}s are larger than that expected spin-only value of 1.73 μ_B for Rh^{IV} with S = ½, while the large negative θ_{CW} implies antiferromagnetic interactions between Rh^{IV} cations. On the other hand, CW fitting to the $\chi^{-1}(T)$ curves of SrIrO$_3$ polytypes yields unphysical parameters. The M(H) curves for all samples increase almost linearly with increasing magnetic fields and no remanence was observed. At T = 5 K and H = 5 T, the magnetic moments are 0.011 μ_B and 0.017 μ_B for 6H and Pv SrRhO$_3$, and 0.04 and 0.037 μ_B for 6H and Pv SrIrO$_3$. The observed smaller paramagnetic moment of Ir^{IV} compared to Rh^{IV} can be understood considering the more extended nature of the 5d orbitals relative the 4d orbitals.

194
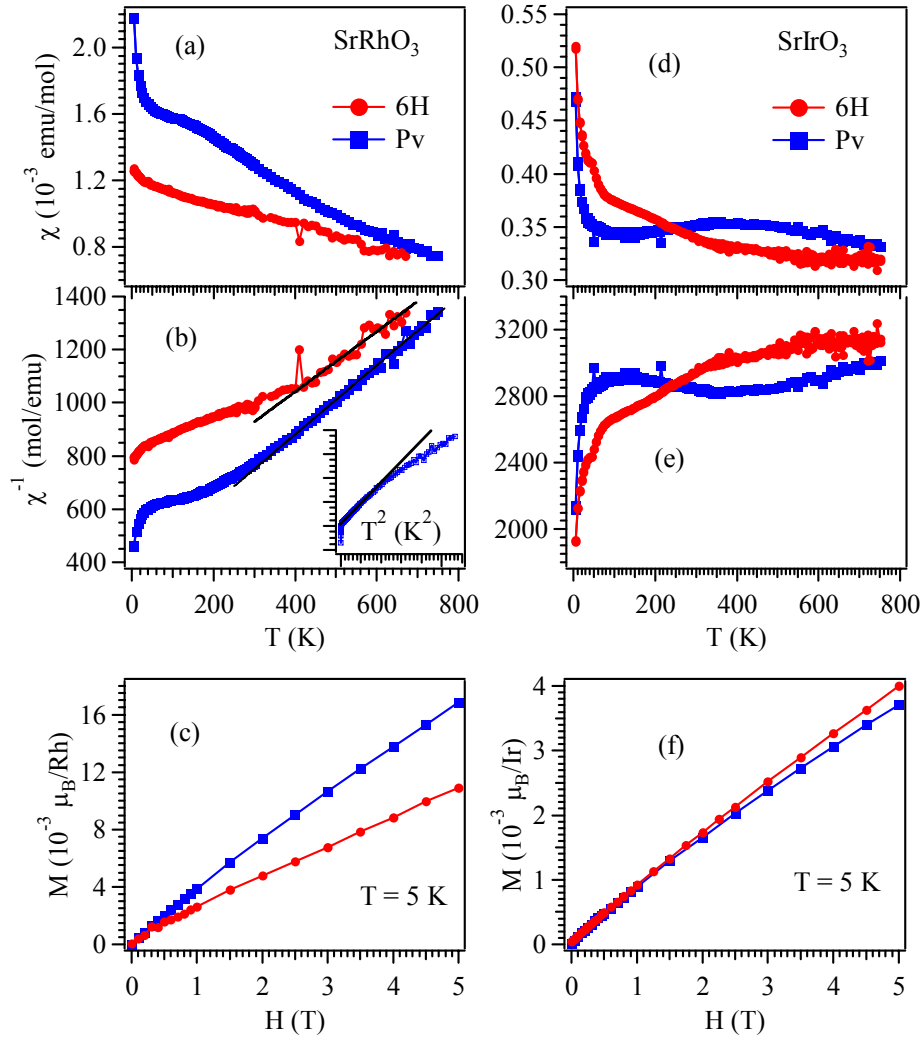
Figure 7.5:   Summary of the magnetic properties of the 6H and Pv polytypes of SrRhO$_3$ and SrIrO$_3$ polytypes: (a) and (d) χ *vs* T; (b) and (e) χ^{-1} *vs* T; (c) and (f) M *vs* H at T = 5 K. Inset of (b) shows the plot of χ^{-1} *vs* T^2 for Pv SrRhO$_3$.

7.3.4 Transport properties

The temperature dependence of resistivity $\rho(T)$ for the SrRhO$_3$ and SrIrO$_3$ polytypes are shown in Fig. 7.6(a) and (d), respectively. Despite the polycrystalline

nature of the samples, a metallic conductivity is observed for all of them. For Pv SrIrO$_3$, a weak upturn of resistivity was observed below ~40K, which has also been reported recently by Zhao *et al.* [149] and attributed to a pseudogap opening. ρ(T) data at low temperatures are replotted as a function of T^2 (upper) and T$^{3/2}$ (lower) in Fig. 7.6(b), (c), (e), and (f). It is interesting to find that the ρ(T) curves of the 6H phases follow a T$^{3/2}$ dependence whereas a good linearity can be realized in the plot of ρ *vs* T^2 for the Pv phases in a wide temperature range. Cao *et al.* [131] have shown that 6H SrIrO$_3$ is close to a magnetic instability, characterized by an enhanced specific heat and a $\rho \propto$ T$^{3/2}$ dependence in a single-crystal sample. Such a non-Fermi-liquid behavior has also been found in the 6H BaIrO$_3$ that is located near a quantum critical point between a ferromagnetic and a paramagnetic phase. A similar situation should also occur in the 6H SrIrO$_3$, which is further tested by the thermoelectric power measurement. As in the case of 6H BaIrO$_3$, a linear relationship is indeed observed in the plot of S/T *vs* lnT, Fig. 7.7(c).

Figure 7.7 displays the temperature dependence of thermoelectric power S(T) for (a) SrRhO$_3$ and (b) SrIrO$_3$ polytypes. For both 6H and Pv SrRhO$_3$, the thermoelectric power is positive and follows a similar temperature dependence, *i.e.* S(T) increases gradually with temperature. However, the situation in the SrIrO$_3$ polytypes is more complicated: (i) the sign of S(T) changes from positive for the 6H phase to negative for the Pv phase; (ii) a broad hump in |S(T)| centered at 170 K is observed in the Pv SrIrO$_3$. Since the thermoelectric power is determined by the unsymmetric energy dependent conductivity around the Fermi energy in metals, the band structure of SrIrO$_3$ should undergo a dramatic change as the structure changes from the 6H to the Pv polytype.
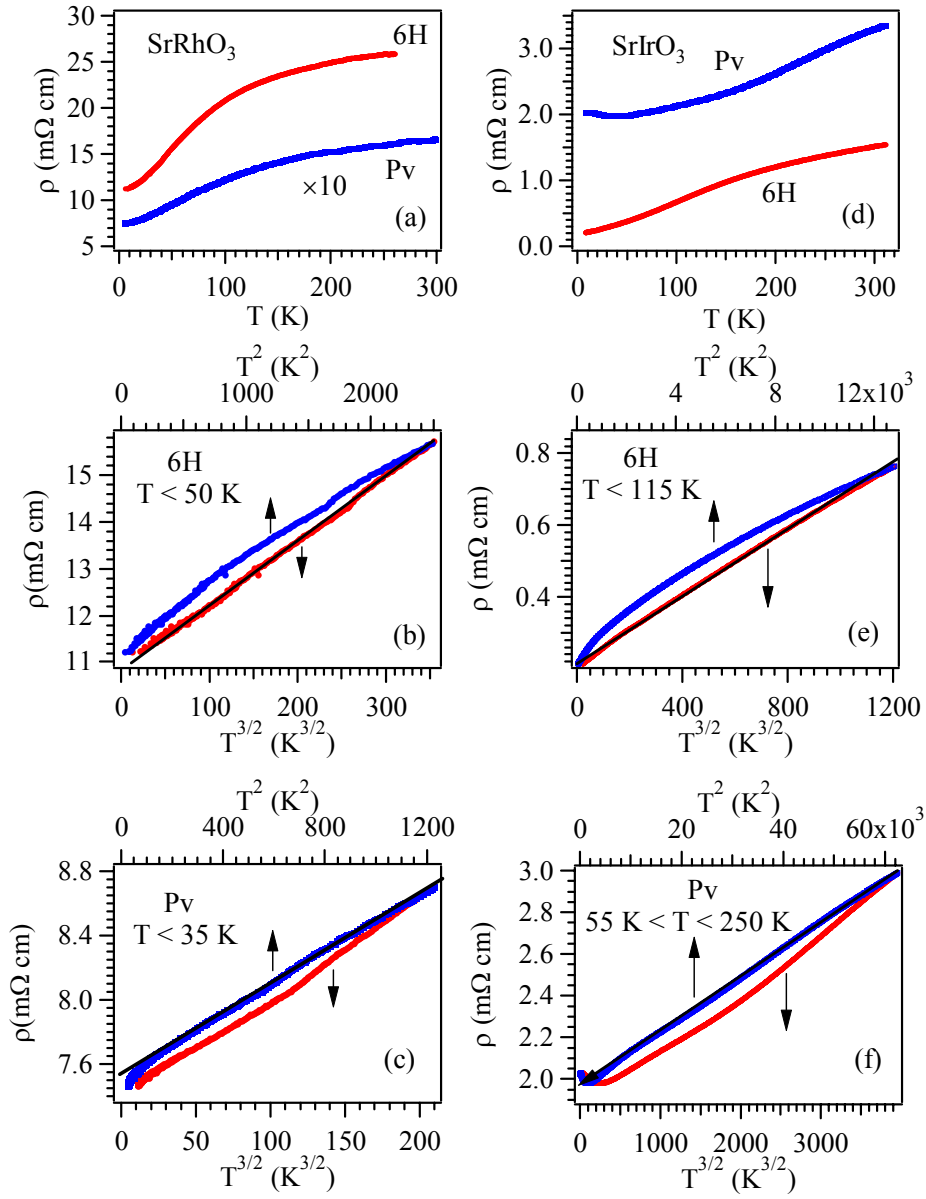
Figure 7.6: Temperature dependences of resistivity for (a) 6H and Pv SrRhO$_3$ and (d) 6H and Pv SrIrO$_3$. The resistivity data at low temperatures are replotted as a function of T^2 (upper) and T$^{3/2}$ (lower) for each sample in (b), (c), (e) and (f).
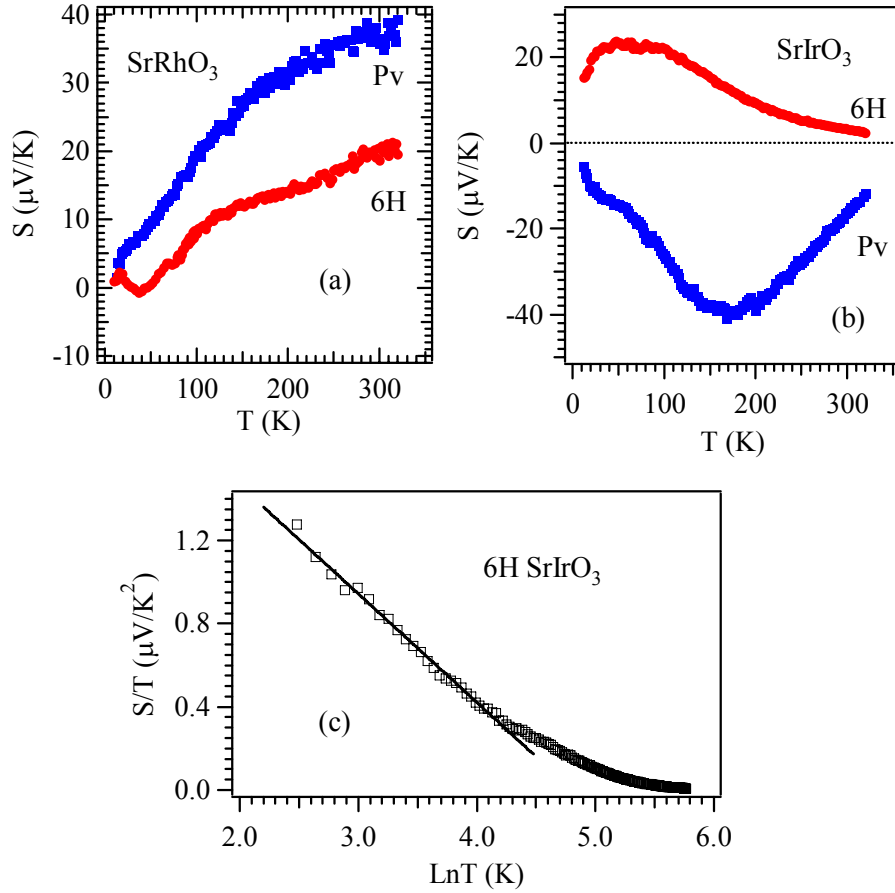
Figure 7.7:   Temperature dependences of the thermoelectric power S(T) for (a) $SrRhO_3$ and (b) $SrIrO_3$ polytypes. S(T) of the 6H $SrIrO_3$ is replotted in the form of S/T *vs* lnT in (c).

The metallic conductivity of the perovskite $SrMO_3$ phases (M = Rh and Ir) with Fermi-liquid behavior, *i.e.* $(\rho-\rho_0) \sim T^2$, can be expected for the low-spin 4d and 5d configurations; in these perovskites, oxygen covalent bonding with the d orbitals of larger radial extension than that of 3d orbitals gives M:t-O:$2p_\pi$-M:t interactions that are strong enough to transform localized t orbitals into itinerant π^* orbitals. On the other hand, in the

6H polytypes, we should expect the M-M bonding in the dimers to split the half-filled a_1 molecular orbital into filled bonding and empty antibonding states, so we are left to consider only M1:t-O-O-M1:t interactions. As has been demonstrated in the double perovskite $Sr_2MgMoO_{6-\delta}$, for example, t-orbital interatomic interactions via a two-O^{2-}-ion bridge can be strong enough with 4d orbitals to give itinerant-electron behavior, but the π^* bands of the M1 sites would be significantly narrower than those of the M sites in the perovskite phase where interaction is across a single O^{2-}-ion bridge. Therefore, the conductivity of the 6H phase is much reduced relative to that of the perovskite phase. Moreover, a $(\rho-\rho_0) \sim T^{3/2}$ indicates a non-Fermi-liquid behavior on the approach to a quantum critical point from the itinerant-electron side. In this region we should expect to find stronger evidence of strong-correlation fluctuation in the paramagnetic state.

7.4 CONCLUSION

In summary, we have synthesized a new 6H polytype of $SrRhO_3$ under high pressure and high temperature. The crystal structure was refined from the XRD data in the monoclinic space group *C2/c* with lattice parameters $a = 5.5650(1)$, $b = 9.5967(2)$, $c = 14.0224(4)$ Å, and $\beta = 92.846(2)°$. It is isostructural with the ambient phase of $SrIrO_3$ and consists of dimers of face-sharing $Rh2O_{6/2}$ octahedra connected by their vertices to single corner-sharing $Rh1O_{6/2}$ octahedra along the *c* axis with a stacking of SrO_3 layers in the sequence *hCChCC*. The dimers are buckled to give a monoclinically distorted 6H structure. With increasing pressures and/or temperatures, the 6H $SrRhO_3$ transforms to an orthorhombic perovskite phase having $a = 5.5673(1)$, $b = 5.5399(2)$, $c = 7.8550(2)$ Å in the space group *Pbnm*. A pressure-temperature phase diagram shows the 6H to Pv phase boundary moves to lower temperatures with increasing pressure. Comparative studies on

the crystal structures of $SrMO_3$ (M=Rh and Ir) have revealed several similar features: (1) for 6H polytypes, the face-sharing $M2O_{6/2}$ octahedra are expanded relative to the $M1O_{6/2}$ octahedra due to the strong M-M metal bonding within the $M2_2O_9$ dimers, which leads to a smaller bond valence for the M2 cations than for the M1 cations; (2) the M2-O1 bond length is always the longest one due to the strong buckling of the $M2_2O_9$ dimers; (3) the $MO_{6/2}$ octahedra of the orthorhombic perovskite phase are not rigid with O2-M-O2 angles deviating from 90º, giving rise to $a > b$. It is argued that a chemical pressure on the A-O bonds induces the monoclinic distortion in the low-pressure 6H form, which was stabilized by metal-metal bonding. All the samples were metallic with a Pauli paramagnetism enhanced by strong-correlation fluctuations. No long-range magnetic order was observed, but a $(\rho - \rho_0) \sim T^2$ in the perovskite phases changes to a $(\rho - \rho_0) \sim T^{3/2}$ dependence in the 6H phases, which have a narrower π^* band. It is clear that all samples, especially the 6H phases, approach a QCP from the itinerant-electron side.

References

[1] J. G. Bednorz and K. A. Muller, Z. Phys. B **64**, 189 (1986).

[2] R. von Helmolt, J. Wecker, B. Holzapfel, et al., Phys. Rev.Lett. **71**, 2331 (1993).

[3] S. Jin, T. H. Tiefel, M. McCormack, et al., Science **264**, 413 (1994).

[4] R. H. Mitchell, *Perovskites, Modern and Ancient* (Almaz Press Inc., 2002).

[5] J. B. Goodenough and J. M. Longo, *Crystallographic and magnetic properties of perovskite and perovskite related compounds. Landolt-Bornstein Numerical Data and Functional Relastionships in Science and Technology.* (Springer, Berlin, 1970).

[6] J. B. Goodenough, J. A. Kafalas, and J. M. Longo, *High-Pressure Synthesis. Preparative Methods in Solid State Chemistry* (Academic Press, Inc., New York and London, 1972).

[7] D. Walker, M. A. Carpenter, and C. M. Hitch, Am. Mineral. **75**, 1020 (1990).

[8] D. Walker, Am. Mineral. **76**, 1092 (1991).

[9] S.-H. Shim, Annu. Rev. Earth Planet. Sci. **36**, 569 (2008).

[10] H. Huppertz, Z. Kristallogr. **219**, 330 (2004).

[11] C.-Q. Jin, J.-S. Zhou, J. B. Goodenough, et al., PNAS **105**, 7115 (2008).

[12] A. Callaghan, C. W. Moeller, and R. Ward, Inorg. Chem. **5**, 1572 (1966).

[13] J. M. Longo, P. M. Raccah, and J. B. Goodenough, J. Appl. Phys. **39**, 1327 (1968).

[14] I. I. Mazin and D. J. Singh, Phys. Rev. B **56**, 2556 (1997).

[15] P. C. Donohue, L. Katz, and R. Ward, Inorg. Chem. **4**, 306 (1965).

[16] J. M. Longo and J. A. Kafalas, Mater. Res. Bull. **3**, 687 (1968).

[17] J. P. Attfield, Chem. Mater. **10**, 3239 (1998).

[18] J. P. Attfield, Int. J. Inorg. Mater. **3**, 1147 (2001).

[19] J. P. Attfield, Crystal Engineering **5**, 427 (2002).

[20] L. M. Rodriguez-Martinez and J. P. Attfield, Phys.Rev. B **54**, R15622 (1996).

[21] J. P. Attfield, A. L. Kharlanov, and J. A. McAllister, Nature **394**, 157 (1998).

[22] J. A. McAllister and J. P. Attfield, Phys. Rev. Lett. **83**, 3289 (1999).

[23] D. Kim, B. L. Zink, F. Hellman, et al., Phys. Rev. B **67**, R100406 (2003).

[24] E. P. Wohlfarth, J. Appl. Phys. **39**, 1061 (1968).

[25] J.-S. Zhou, K. Matsubayashi, Y. Uwatoko, et al., Phys. Rev. Lett. **101**, 077206 (2008).

[26] Y. Itoh, T. Mizoguchi, and K. Yoshimura, J. Phys. Soc. Jpn **77**, 123702 (2009).

[27] R. D. Shannon, Acta. Cryst. **A32**, 751 (1976).

[28] S. Munzo Perez, R. Cobas, and J. Albino Aguiar, Phys. C **435**, 50 (2006).

[29] J. A. Kafalas and J. M. Longo, Mat. Res. Bull **5**, 193 (1970).

[30] S. A. J. Kimber, J. A. Rodgers, H. Wu, et al., Phys. Rev. Lett. **102**, 046409 (2009).

[31] M. Drillon, L. Padel, and J.-C. Bernier, J. Chem. Soc. Faraday Transcation 2 **75**, 1193 (1979).

[32] T. Siegrist and B. L. Chamberland, J. Less-Common Metals **170**, 93 (1991).

[33] G. Cao, J. E. Crow, R. P. Guertin, et al., Solid State Comm. **113**, 657 (2000).

[34] J. M. Longo, J. A. Kafalas, and R. J. Arnott, J. Solid State Chem. **3**, 174 (1971).

[35] K. Yamaura and E. Takayama-Muromachi, Phys. Rev. B **64**, 224424 (2001).

[36] D. J. Singh, Phys. Rev. B **67**, 054507 (2003).

[37] F. Kanamaru, H. Miyamoto, Y. Mimura, et al., Mat. Res. Bull. **5**, 257 (1970).

[38] J. A. Alonso, J. L. Garcia-Munoz, M. T. Fernandez-Diaz, et al., Phys. Rev. Lett. **82**, 38713874 (1999).

[39] J. A. Alonso, M. J. Martinez-Lope, M. T. Casais, et al., J. Am. Chem. Soc. **121**, 4754 (1999).

[40] G. Demazeau, C. Parent, M. Pouchard, et al., Mat. Res. Bull. **7**, 913 (1972).

[41] J. S. Zhou, W. Archibald, and J. B. Goodenough, Phys. Rev. B **61**, 3196 (2000).

[42] J. B. Goodenough and J.-S. Zhou, J. Mater. Chem. **17**, 2394 (2007).

[43] A. M. Glazer, Acta Cryst. B **28**, 3384 (1972).

[44] A. M. Glazer, Acta Cryst. A **31**, 756 (1975).

[45] C. J. Howard and H. T. Stokes, Acta Cryst. B **54**, 782 (1998).

[46] M. O'Keeffe and B. G. Hyde, Acta Cryst. B **33**, 3802 (1977).

[47] J.-S. Zhou and J. B. Goodenough, Phys. Rev. Lett. **94**, 065501 (2005).

[48] J.-S. Zhou and J. B. Goodenough, Phys. Rev. B **77**, 132104 (2008).

[49] J.-S. Zhou, J. B. Goodenough, J. M. Gallardo-Amores, et al., Phys. Rev. B **74**, 014422 (2006).

[50] J. B. Goodenough, J. M. Longo, and J. A. Kafalas, Mater. Res. Bull. **3**, 471 (1968).

[51] B. L. Chamberland, Solid State Commun. **5**, 663 (1967).

[52] A. Munoz, J. A. Alonso, M. J. Martinez-Lope, et al., Phys. Rev. B **73**, 104442 (2006).

[53] J. B. Goodenough, *Localized to Itinerant Electronic Transition in Perovskite Oxides, In Structure and Bonding, Vol. 98* (Springer, Berlin, Germany, 2001).

[54] T. Moriya, *Spin Fluctuations in Itinerant Electron Magnetism* (Springer-Verlag, Berlin, 1985).

[55] A. Arrott, Phys. Rev. **108**, 1394 (1957).

[56] A. Arrott and J. E. Noakes, Phys. Rev. Lett. **19**, 786 (1967).

[57] F. Y. Yang, C. L. Chien, X. W. Li, et al., Phys. Rev. B **63**, 092403 (2001).

[58] H. Yanagihara, W. Cheong, M. B. Salamon, et al., Phys. Rev. B **65**, 092411 (2002).

[59] K. Ghosh, C. J. Lobb, R. L. Greene, et al., Phys. Rev. Lett. **81**, 4740 (1998).

[60] E. C. Stoner, Proc. Roy. Soc. London **165**, 372 (1938).

[61] K. H. Kim, N. Harrison, M. Jaime, et al., Phys. Rev. Lett. **91**, 256401 (2003).

[62] N. Doiron-Leyraud, I. R. Walker, L. Taillefer, et al., Nature **425**, 595 (2003).

[63] J. Custers, P. Gegenwart, H. Wihelm, et al., Nature **424**, 524 (2003).

[64] J.-S. Zhou, J. B. Goodenough, and B. Dabrowski, Phys. Rev. Lett. **94**, 226602 (2005).

[65] R. P. Smith, M. Sutherland, G. G. Lonzarich, et al., Nature **455**, 1220 (2008).

[66] J. A. Rodgers, A. J. Williams, and J. P. Attfield, Z. Naturforsch. **61b**, 1515 (2006).

[67] V. E. Bean, S. Akimoto, P. M. Bell, et al., Phys. B **139-140**, 52 (1986).

[68] C. M. Bertka and Y. W. Fei, J. Geophys. Res. **102**, 5251 (1997).

[69] M. J. Walter, Y. Thibault, K. Wei, et al., Can. J. Phys. **73**, 273 (1995).

[70] J. Rodriguez-Carvajal, Physica B **192**, 55 (1993).

[71] G. Cao, S. McCall, M. Shepard, et al., Phys. Rev. B **56**, 321 (1997).

[72] K. Yoshimura, T. Imai, T. Kiyama, et al., Phys. Rev. Lett. **83**, 4397 (1999).

[73] R. B. Griffiths, Phys. Rev. Lett. **23**, 17 (1969).

[74] M. W. Lufaso and P. M. Woodward, Acta. Cryst. B **57**, 725 (2001).

[75] T. Kiyama, K. Yoshimura, KosugeK., et al., J. Phys. Soc. Jpn **68**, 3372 (1999).

[76] M. Shikano, T.-K. Huang, Y. Inaguma, et al., Solid State Comm. **90**, 115 (1994).

[77] J. J. Neuneier, A. L. Cornelius, and J. S. Schilling, Physica B **198**, 324 (1994).

[78] J. J. Hamlin, S. Deemyad, J. S. Schilling, et al., Phys. Rev. B **76**, 014432 (2007).

[79] E. P. Wohlfarth, J. Phys. C: Solid State Phys. **2**, 68 (1969).

[80] F. M. Grosche, C. Pfleiderer, G. J. McMullan, et al., Physica B **206-207**, 20 (1995).

[81] S. Takashima, M. Nohara, H. Ueda, et al., J. Phys. Soc. Jpn **76**, 043704 (2007).

[82] K. Koyama, T. Goto, T. Kanomata, et al., Phys. Rev. B **62**, 986 (2000).

[83] P. G. Niklowizt, F. Beckers, G. G. Lonzarich, et al., Phys. Rev. B **72**, 024424 (2005).

[84] J. Grewe, J. S. Schilling, K. Ikeda, et al., Phys. Rev. B **40**, 9017 (1989).

[85] D. Bloch, J. Phys. Chem. Solids **27**, 881 (1966).

[86] M. K. Jacobsen, R. S. Kumar, G. Cao, et al., J. Phys. Chem. Solids **69**, 2237 (2008).

[87] T. Kida, A. Senda, S. Yoshii, et al., Eur. Phys. Lett. **84**, 27004 (2008).

[88] A. P. Mackenzie, J. W. Reiner, A. W. Tyler, et al., Phys. Rev. B **58**, R13318 (1998).

[89] K. Fujioka, J. Okamoto, T. Mizokawa, et al., Phys. Rev. B **56**, 6380 (1997).

[90] M. J. Rozenberg, G. Kotliar, and X. Y. Zhang, Phys. Rev. B **49**, 10181 (1994).

[91] Y. J. Uemura, T. Goko, I. M. Gat-Malureanu, et al., Nature Physics **3**, 29 (2007).

[92] S. J. Blatt, P. A. Schroeder, C. L. Foiles, et al., *Thermoelectric power of Metals* (Plenum, New York, 1976).

[93] D. K. C. MacDonal, *Thermoelectricity: An Introduction to the Principles* (Wiley, New York, 1962).

[94] J. S. Zhou, W. Archibald, and J. B. Goodenough, Phys. Rev. B **57**, R2017 (1998).

[95] J.-G. Cheng, J. S. Zhou, and J. B. Goodenough, (unpublished).

[96] E. H. Mountstevens, J. P. Attfield, and S. A. T. Redfern, J. Phys.: Condens. Matter **15**, 8315 (2003).

[97] C. J. Howard, K. S. Knight, B. J. Kennedy, et al., J. Phys.: Condens. Matter **12**, L677 (2000).

[98] B. J. Kennedy, B. A. Hunter, and J. R. Hester, Phys. Rev. B **65**, 224103 (2002).

[99] J. S. Zhou, Unpublished.

[100] P. B. Allen, H. Berger, O. Chauvet, et al., Phys. Rev. B **53**, 4393 (1996).

[101] T. He, Q. Huang, and R. J. Cava, Phys. Rev. B **63**, 024402 (2000).

[102] Y. Itoh, T. Mizoguchi, and K. Yoshimura, J. Phys. Soc. Jpn **77**, 123702 (2008).

[103] G. Cao, O. Korneta, S. Chikara, et al., arXiv: 0805.0741 (2008).

[104] H. Fritzsch, Solid State Comm. **9**, 1813 (1971).

[105] M.-H. Whangbo and H.-J. Koo, Solid State Comm. **118**, 491 (2001).

106 K. Maiti, R. S. Singh, V. R. R. Medicherla, et al., Phys. Rev. Lett. **95**, 016404 (2005).

107 R. Lindsay, W. Strange, B. L. Chamberland, et al., Solid State Comm. **86**, 759 (1993).

108 M. L. Brooks, S. J. Blundell, T. Lancaster, et al., Phys. Rev. B **71**, 220411(R) (2005).

109 T. Nakano and I. Terasaki, Phys. Rev. B **73**, 195106 (2006).

110 B. L. Chamberland, J. Less-Common Metals **171**, 377 (1991).

111 A. V. Powell and P. D. Battle, J. Alloy. Comp. **232**, 147 (1996).

112 A. Altomare, G. Cascarano, C. Giacovazzo, et al., J. Appl. Cryst. **27** (1994).

113 A. Altomare, M. C. Burla, G. Cascarano, et al., J. Appl. Cryst. **28**, 842 (1995).

114 N. E. Brese and M. O'Keeffe, Acta. Cryst. **B47**, 192 (1991).

115 I. D. Brown, Z. Kristallogr. **199**, 255 (1992).

116 M. L. Foo, Q. Huang, J. W. Lynn, et al., J. Solid State Chem. **179**, 563 (2006).

117 N. A. Jordan and P. D. Battle, J. Mater. Chem. **13**, 2220 (2009).

118 J. M. Dance and A. Tressaud, Mater. Res. Bull **14**, 37 (1979).

119 J. G. Zhao, L. X. Yang, Y. Yu, et al., J. Solid State Chem. **182**, 327 (2009).

120 J. F. Vente and P. D. Battle, J. Solid State Chem. **152**, 361 (2000).

121 A. J. Jacobson and J. L. Hutchison, J. Solid State Chem. **35**, 334 (1980).

122 L. Miranda, A. Feteira, D. C. Sinclair, et al., Chem. Mater. **20**, 2818 (2008).

123 J. M. De Paoli, J. A. Alonso, and R. E. Carbonio, J. Phys. Chem. Solid. **67**, 1558 (2006).

124 T. Negas and R. S. Roth, J. Solid State Chem. **3**, 323 (1979).

125 E. J. Cussen, J. Sloan, J. P. Vente, et al., Inorg. Chem. **37**, 6071 (1998).

126 N. A. Jordan, P. D. Battle, J. Sloan, et al., J. Mater. Chem. **13**, 2617 (2003).

127 G. Cao, J. Bolivar, S. McCall, et al., Phys. Rev. B **57**, R11039 (1998).

128 G. Cao, Y. Xin, C. S. Alexander, et al., Phys. Rev. B **66**, 214412 (2002).

129 F. C. Zumsteg and R. D. Parks, Phys. Rev. Lett. **24**, 520 (1970).

130 R. J. Cava, B. Batlogg, J. J. Krajewski, et al., Nature **350**, 598 (1991).

131 G. Cao, V. Durairaj, S. Chikara, et al., Phys. Rev. B **76**, 100402(R) (2007).

132 I. Paul and G. Kotliar, Phys. Rev. B **64**, 184414 (2001).

133 R. Daou, O. Cyr-Choiniere, F. Laliberte, et al., Phys. Rev. B **79**, 180505 (2009).

134 G. Cao, G. Shaw, and J. W. Brill, J. Phys. IV France **12**, 91 (2002).

135 N. S. Kini, A. Bentien, S. Ramakrishnan, et al., Physica B **359-361**, 1264 (2005).

136 E. A. Yelland, S. J. C. Yates, O. Taylor, et al., Phys. Rev. B **72**, 184436 (2005).

137 K. Wilson, Rev. Mod. Phys. **47**, 773 (1975).

138 H. Stern, J. Phys. Chem. Solids **26**, 153 (1965).

139 J. J. Martin and G. S. Dixon, Phys. Status Solidi B **54**, 707 (1972).

140 J.-G. Cheng, Y. Sui, J.-S. Zhou, et al., Phys. Rev. Lett. **101**, 087205 (2008).

141 M. Takano, S. Nasu, T. Abe, et al., Phys. Rev. Lett. **67**, 3267 (1991).

142 J. G. Zhao, L. X. Yang, K. Mydeen, et al., Solid State Comm. **148**, 361 (2008).

143 T. Nakano, Koatsuryoku no Kagaku to Gijutsu **18**, 62 (2008).

144 K. Yamaura, Q. Huang, D. P. Young, et al., Phys. Rev. B **66**, 134431 (2002).

145 K. Yamaura, Q. Huang, D. P. Young, et al., Chem. Mater. **16**, 3424 (2004).

146 K. Yamaura, Y. Shirako, H. Kojitani, et al., J. Am. Chem. Soc. **131**, 2722 (2009).

[147] T. Siegrist, E. M. Larson, and B. L. Chamberland, J. Alloy. Comp. **210**, 13 (1994).

[148] B. L. Chamberland, A. W. Sleight, and J. F. Weiher, J. Solid State Chem. **1**, 506 (1970).

[149] J. G. Zhao, L. X. Yang, Y. Yu, et al., J. Appl. Phys. **103**, 103706 (2008).

[150] J. G. Zhao, L. X. Yang, Y. Y., et al., J. Solid State Chem. **182**, 1524 (2009).

[151] H. Kobayashi, M. Nagata, R. Kanno, et al., Mat. Res. Bull. **29**, 1271 (1994).

[152] K. Yamaura, Q. Huang, D. P. Young, et al., Physica B **329-333**, 820 (2003).

[153] J. A. Kafalas and J. M. Longo, Mat. Res. Bull. **3**, 501 (1968).

[154] Y. Syono, S. Akimoto, and K. Kohn, J. Phys. Soc. Jpn. **26**, 993 (1969).

[155] B. Rowda, M. Avdeev, P. L. Lee, et al., Acta. Cryst. **B64**, 154 (2008).

[156] C. D. Ling, B. Rowda, M. Avdeev, et al., J. Solid State Chem. **182**, 479 (2009).

[157] E. Quarez, M. Huve, F. Abraham, et al., Solid State Sci. **5**, 951 (2003).

[158] J.-G. Cheng, J.-S. Zhou, and J. B. Goodenough, Phys. Rev. B **79**, 184414 (2009).

Vita

Jinguang Cheng was born to Meiying Pang and Gan Cheng on July 24, 1982 in Weifang, Shandong province, People's Republic of China. Upon graduation from Weifang 4th High School in 1999, he pursued studies in Physics at Harbin Institute of Technology and obtained his Bachelor's Degree in 2003 and Master's Degree in 2005. In August 2006, He began to pursue a doctoral degree in Materials Science and Engineering from the University of Texas at Austin, where his research interests include synthesis and study of transition-metal oxides with novel structural and electronic properties.

Permanent address (or email): Xiaowujia Village, Fangzi District, Weifang, Shandong 261206, People's Republic of China.

This dissertation was typed by the author.